UNIVERSITÀ DEGLI STUDI DI PADOVA

DIPARTIMENTO DI FISICA E ASTRONOMIA

SCUOLA DI DOTTORATO DI RICERCA IN FISICA

XXX CICLO

TOWARD A FULLY AUTOMATED AND DIGITALLY CONTROLLED SQUEEZED VACUUM SOURCE FOR GRAVITATIONAL WAVE DETECTORS

Dottorando:
Marco Vardaro

Supervisore:
Jean-Pierre Zendri

Marzo 2018

Contents

Chapter 1

Introduction

1.1 Gravitational wave detection with laser interferometers

The present generation of interferometric gravitational wave detectors is based on the Michelson-Moreley interferometer design. A Michelson-Moreley interferometer is composed by a laser source, two mirrors and a beam splitter. The beam splitter divides the main laser beam in two beam traveling back and forth through the two different arm of the instrument. When the two beams recombine at the beam splitter they are detected with a photodiode. Fig. 1.1 shows the effect of a "+" polarized gravitational wave that propagates in the direction perpendicular to the interferometer plane: the length of each arm is alternatively increased/decreased with opposite phase between them.

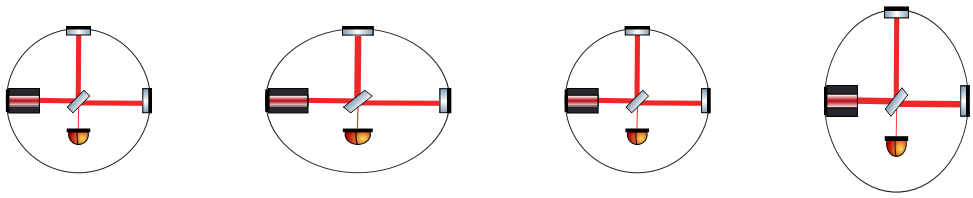

Figure 1.1: Effect of a gravitational wave that pass trough a Michelson-Morley interferometer.

Thus the net effect is a phase shift between the two fields that propagate in the arms and this can be detected as a change of the interference pattern at the output port of the beam splitter. The induced phase shift $\Delta\phi$ is equal to:

$$\Delta\phi = h_{GW}(t)\frac{2\pi}{\lambda}L,$$

where λ is the laser wavelength and h is called the *gravitational wave strain* and L

the unperturbed arm length. The gravitational wave induced phase shift reflects on a power fluctuation at the detection photodiode [1][2].

1.1.1 The Advanced Virgo Interferometer

Virgo is a ground based gravitational wave detector built in Cascina, near Pisa. This project was born in 1985 when Adalberto Giazzotto and Alain Brillet, who have worked both in the development of gravitational wave detector technologies, started to collaborate attracting numerous groups in the following years. In 1990 the collaboration presented the project of the detector which was approved in 1994, whereas its construction stared in 1996 and was completed in 2003. From 2007 to 2011, conjointly with other interferometers (LIGO and GEO600), Virgo acquires scientific data. This represents the birth of the the world-wide collaboration for the gravitational wave research, based on exchange of scientific data and technical knowledge. Simultaneously to the data taking period, in 2005 was written the Advanced Virgo White paper effort for the development of a new detector that will be 10 times more sensitive: Advanced Virgo [3]. This project was approved by the French and Italian government in 2009 and the upgrades stared at the end of 2011. Today the Virgo collaboration is composed by 250 people, 20 laboratories spread of 6 European countries: Italy, France, Holland, Poland Hungary and Spain [4]. Advanced Virgo shares the same infrastructure of the Initial Virgo detector, but most of its components are upgraded. The final design will be reached in many steps. Initially the interferometer is locked in a configuration similar to the one used in the previous version, i.e. without the signal recycling cavity and with an input power below 40 W. The final configuration planned for 2019 in which the laser power will be 200 W and all the upgrade are installed. In August 2017 the instrument enters in the joint observational run with the two Ligo interferometers. The 14 of August was observed for the first time the merging of two black holes with a network of three interferometers [5].

The optical setup of Advanced Virgo, in its final configuration, is a dual recycled Michelson interferometer with 3 km long Fabry-Perot arm cavities as it is shown in Fig. 1.2. The optical scheme is divided in 4 principal block that are briefly summarized here below [4] [6].

Injection block It is composed by a 1064 nm laser source with output power up to 200 W in the final design (2019). Its output beam is stabilized in frequency and in amplitude. Between the lasers and the interferometer is placed a 150 m long triangular cavity, the input mode cleaner, that acts on the laser beam as a spatial filter.

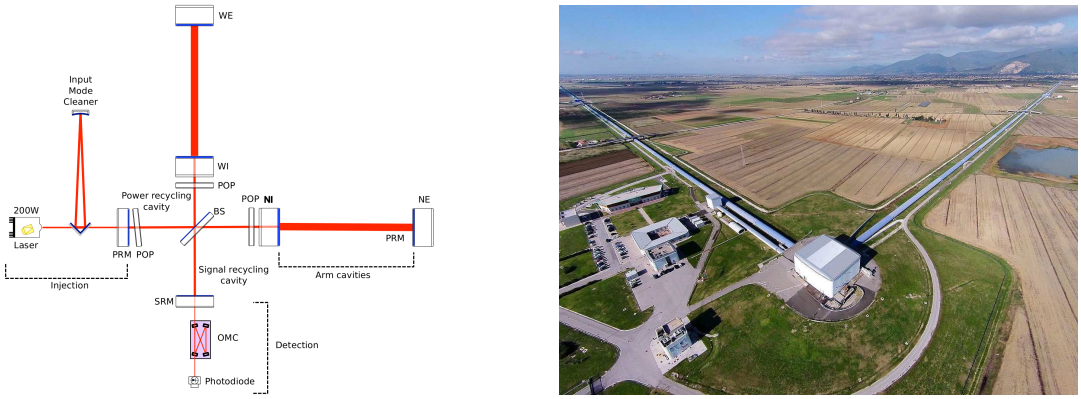

Figure 1.2: Left: Schematic of the Advanced Virgo Optical setup [4]. Right: aerial view of the Virgo detector.

Detection block In this block the interferometer output light beam, which phase contains the gravitational wave signal, is converted to a voltage signal that can be recorded.

Arm cavities The two perpendicular 3 km long Fabry-Perot arm cavities are formed each one by two mirrors. The mirrors are made of fused silica and have a mass of about 40 kg, cylindrical shape with diameter of 35 cm and a thickness of 20 cm. The mirror polishing is performed at atomic level and the multilayer coating allows to reach a reflectivity higher than 99.999% [7]. The mirrors are suspended by means of the superattenuator in order to filter the the ground motion. This system is a cascade of pendulum stadiums with a total height of 8 m. The last stadium of the superattenuator is suspended with monolithic suspensions, made with the same low losses material of the mirrors, with the aim to minimize the thermal noise contribution [8] [9]. The superattenuator attenuates the seismic noise by ten orders of magnitude in the frequency range above few Hertz in the six degrees of freedom.

Recycling cavities two additional cavities are composed one by the arm cavities and the power recycling mirror and the other by the arm cavity and the signal recycling mirror. The former cavity is used to enhance the light power circulating in the interferometer by a factor 40, whereas the latter changes the optical response of the instrument and hence increases the sensitivity of the instrument in some frequency regions [10] [11] [12]. The initial version of Virgo is equipped with the power recycling cavity but not with the signal recycling cavity.

1.1.2 Classical noise sources in an interferometric wave detector

The gravitational wave induced deformation of the two arms of a 3 kilometer ground based interferometer is very tiny. Thus to reach high detection probabilities these interferometer must be able to measure differential length variations of less than 10^{-18}m. Therefore all the noise disturbance of a gravitational wave detector must be minimized. In the following, the main noise sources are briefly described.

Seismic noise The earth's ground continuously moves with an amplitude of the order of few microns. The causes of this motion are many: in the spectral region between 1 and 10 Hz it origins from human activities or local phenomena such as winds. Moreover a micro-seismic background exists that affects the detector in term of surface waves that moves the free falling mirrors of the interferometer. This noise is orders of magnitude larger than the gravitational wave signals [1], thus it must be must be attenuated and in Virgo this is realized with a system of pendulums in cascade [8].

Newtonian noise This noise origins from the Newtonian gravitational attraction between masses, in particular between the detector test masses and nearby moving masses. The most important Newtonian effect is induced by the micro-seismic noise that causes mass density fluctuations and therefore variation of the gravitational field of the earth that couple directly with the detector test masses [13]. This effect can not easily be eliminated because the gravitational field can not be shielded. While strategies exist to estimate this noise contribution from seismic data and subtract them from the interferometer output, a way to directly reduce its impact is the development of underground detectors as KAGRA in Japan or in the future the next generation of ground based interferometer.

Thermal noise This noise sources can be divided in two main groups: the suspension thermal noise and the test mass thermal noise [14] [15]. The former group encloses any thermal vibration in the superattenuator system, i.e. pendulum thermal fluctuations, vertical thermal fluctuations and violin modes. The latter group includes Brownian motion of the mirrors, thermo-elastic fluctuations and thermo-refractive fluctuations [16] [1]. This noise can be reduced either improving the quality of the coating and fiber materials or heading to low temperature operations [17].

1.1.3 Quantum noise sources in an interferometric wave detector

In addition to the classical noise sources that causes a displacement noise of the test masses, the detector sensitivity is limited by the photon quantum noise due to the Heisenberg uncertainty principle. As it will be shown in Sec. 2.8 this kind of noise is due to the electromagnetic field vacuum fluctuations that enter in the interferometer dark port and manifests with two different phenomena: the the photon shot noise and the quantum radiation pressure noise.

Shot Noise

The shot noise is a consequence of the light quantum nature: the laser source emits photons with a Poisson statistic, therefore the number of detected photons varies in the time and this induces fluctuations in the measured laser power that is directly proportional to the number of photons that reach the photodetector. These fluctuations are called *shot-noise fluctuations* and their contribution to the detector strain amplitude h_{sn} is given by [18]:

$$h_{sn}(\Omega) = \frac{1}{L}\sqrt{\frac{\hbar c\lambda}{2\pi P}},$$

where L is the interferometer arm length, λ is the laser wavelength and P is the laser power. By increasing the circulating laser power this contribution decreases as the square root of the power.

Quantum radiation pressure noise

The radiation pressure noise is another consequence of the light quantization. Each photon that reaches an end mass of the detector transferrers to it a momentum equal to $2\hbar\omega/c$. Here, the variations in the number of incident photons causes a fluctuation in the transferred momentum to the test masses and in the mirror position. This induced noise is called *radiation pressure* and its contribution to the interferometer strain sensitivity is described by: [18]:

$$h_{rp}(\Omega) = \frac{1}{m\Omega^2 L}\sqrt{\frac{8\pi\hbar P}{c\lambda}},$$

where m is the mirrors mass. Therefore the contribution of this noise source to the interferometer sensitivity increases with the square root of the injected laser power.

Standard quantum limit

The total quantum noise is computed as the square sum of the shot noise and the radiation pressure noise strain sensitivity:

$$h_{qn}(\Omega) = \sqrt{h_{sn}^2(\Omega) + h_{rp}^2(\Omega)},$$

that can be minimized with respect the total power P. The resulting minimal noise, calculated at the optimal frequency in which the radiation pressure noise and the shot noise contributions are equal, is called *standard quantum limit* and is given by

$$h_{sql} = \sqrt{\frac{4\hbar}{m\Omega^2 L^2}}$$

that is reached with an optimal power P_{opt} given by

$$P_{opt} = \frac{c\lambda m\Omega^2}{4\pi}.$$

1.1.4 Quantum noise reduction

A method to decrease the shot noise contribution is to increase the laser power, but this can produce several technical issues in general difficult to deal with, like for example thermal lensing or parametric instabilities [19]. Another approach is the one proposed by Caves in 1981 [20] that is the main topic of this thesis, i.e. the replacement of the electromagnetic vacuum fluctuations that enters in the interferometer dark port with a phase squeezed vacuum state. Squeezed states will be introduced in the next chapter and are states of light with one of the two quadrature fluctuations reduced compared to the one of a vacuum state, whereas the other is increased. Fig. 1.3 shows the effect of this technique. The blue trace represents the quantum noise of a Michelson interferometer assuming the input laser power equal to 25 W, the laser wavelength equal to 1064 nm, the mass of the mirrors equal to 50 kg, the length of the arms equal to 3 km and their finesse equal to $\mathcal{F} = 100$. If 20 dB of phase squeezing are injected into the detector (red trace), the shot noise contribution to the interferometer strain sensitivity will be decrease by a factor 10, whereas the radiation pressure contribution will increase by the same factor. The generation of the phase squeezed vacuum states in the audio frequency region is the main topic of this work. Obviously the injection of phase squeezed states can only improve the detector sensitivity at frequencies where it is limited by quantum shot noise. In the last scientific run of the interferometers they where limited by shot noise at frequencies above several hundred Hertz, whereas the radiation pressure noise was not the limiting factor in the low frequency region because at such frequencies the instruments was limited

by seismic and Newtonian noises. Thus, with the current detector configuration, an increase of the radiation pressure contribution will not decrease the sensitivity of the instrument at low frequencies.

In the future the sensitivity of the detectors will be increased also at lower frequencies, therefore the injection of frequency independent phase squeezing would decrease the sensitivity in the low frequency band. The green line in Fig. 1.3 represents the future perspective of squeezed light injection in GW interferometers: i.e. the injection of *frequency dependent squeezing*. This technique consists in an improvement of the frequency independent squeezing experiment in which the squeezing ellipse is rotated in a certain frequency band. Unuruh has shown that the injection of frequency dependent squeezed field into a GW detector allows a quantum noise reduction over the complete detector bandwidth, as it is shown by the green trace. Using these optimal prepared squeezed vacuum states even the standard quantum limit can be beaten in a certain bandwidth [21] [22]. Nowadays two technique for the generation of frequency dependent squeezed states are proposed: squeezing ellipse angle rotation by means of the filter cavity, already tested, but requiring substantial infrastructure modifications [23], or by exploiting the EPR entanglement [24].

1.2 Structure of this thesis

The goal of this thesis is the description of a squeezed vacuum source which is fully digitally controlled and Virgo compatible. Chap. 2 provides a theoretical introduction of quantum optics. It gives the definition of coherent and squeezed light states, describes the quantum noise measurement techniques and finally the principal sources of squeezed light degradation. Chap. 3 is a brief introduction of nonlinear optics. It starts from the description of all the second order nonlinear phenomena, the phase matching condition. Then it describes before with a semiclassical point of view and after with a quantum approach an Optical Parametric Oscillator and why it can be used for squeezed vacuum states generation. The optical layout of the vacuum source, developed in the Virgo site from September 2015, is fully described in Chap. 4. The first section gives to the reader a general view of the layout and then a section is dedicated for the description of each single subsystem and its performances. The last three chapters, i.e. Chap. 5, Chap. 6, Chap. 7 are dedicated to the description of the electronics and the control loops that ensures the squeezer operation. Chap. 5 describes the digital generation of radiofrequency signals based on DDS chip. Chap. 6 describes how the phase lock between two laser sources with a fixed frequency offset is performed. Finally Chap. 7 treats the temperature controller boards, the servo loop

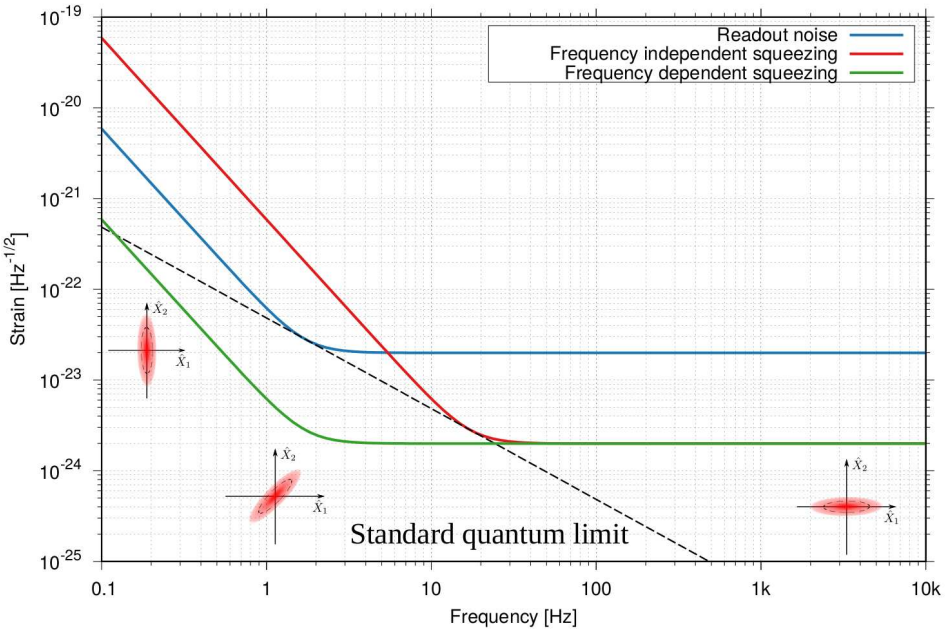

Figure 1.3: Quantum noise strain sensitivity in a Michelson-Moreley interferometer, assuming P = 25 W, $\lambda = 1064\,\text{nm}$, m = 50 kg, L = 3000 m and $\mathcal{F} = 100$. Blue trace the detector quantum readout noise. Red trace: effect of the injection of 20 dB of frequency independent phase squeezing into the detector. The shot noise is reduced of an order of magnitude, whereas the radiation pressure noise is enhanced. Green trace: effect of the injection of 20 dB of frequency dependent squeezed states into the interferometer: both the quantum noises are decreased and the standard quantum limit is beaten in a certain bandwidth.

for cavity locking and pump power stabilization, the high voltage piezoelectric driver and the photodetector amplifier. Each of these chapter is divided in three part: first a theoretical introduction, then the developed board description, implementation and performances and finally how a software interface is written with the aim to integrate each board in the Virgo DAQ environment and to remote manage the optical system.

Part I

Quantum and non-linear optics

Chapter 2

Behoynd the classical light

This chapter introduces the quantum nature of light and it is structured as follows: Sec. 2.1 describes the quantization of the electromagnetic field; Sec. 2.2 introduces the Fock States, i.e. eigenstates of the number operator, that are not good descriptor of laser fields; therefore Sec. 2.3 introduces the coherent states i.e. the eigenstates of the annihilation operator. Sec. 2.5 introduces the squeezed states, whereas Sec. 2.6 describes some measurement techniques of quantum light states and Sec. 2.7 describes the squeezing degradation mechanism. Finally Sec. 2.8 describes a pure quantum mechanical treatment of the Michelson interferometer and shows how the injection of squeezed states in its dark port causes a quantum noise reduction.

2.1 Electromagnetic field quantization

A rigorous treatment of the quantization of the electromagnetic field is based on the Lagrange formalism [25], but it exceeds the aim of this thesis. Therefore, in this paragraph, this topic is approached by exploiting the analogies between the electromagnetic field an the harmonic oscillator [26],[27],[28]. This analysis treats the most simple situation: the electromagnetic field that propagates in the vacuum, which is described by the Maxwell equations:

$$\begin{aligned} \vec{\nabla} \cdot \vec{E} &= 0 & \vec{\nabla} \times \vec{E} + \frac{\partial \vec{B}}{\partial t} &= 0 \\ \vec{\nabla} \cdot \vec{B} &= 0 & \vec{\nabla} \times \vec{B} - \mu_0 \epsilon_0 \frac{\partial \vec{E}}{\partial t} &= 0, \end{aligned} \tag{2.1}$$

where $\vec{E}$ and $\vec{B}$ are respectively the magnetic and the electric field. The wave equation is obtained by applying the curl operator to the equation in the first row right and

by substituting in it the first and the fourth equations. It follows that:

$$\nabla^2 \vec{E} - \mu_0 \epsilon_0 \frac{\partial^2 \vec{E}}{\partial t^2} = 0. \tag{2.2}$$

Let we take a linear cavity of length L with perfectly reflective mirrors oriented along the field propagation axis z. A class of solutions of Eq. 2.2 are standing waves confined in the cavity. The boundary conditions implies that the allowed frequencies of the standing waves are $\omega_m = c(m\pi/L)$ where $m = 1, 2, \ldots$. The solution with $m = 1$ of the Eq. 2.2 is:

$$\vec{E}(\vec{r}, t) = \hat{e}_x E_x(z, t) = \hat{e}_x \sqrt{\left(\frac{2\omega_m^2}{V\epsilon_0}\right)} q(t) \sin(kz), \tag{2.3}$$

where the electric field polarization vector is considered, without loss of generality, along the x direction orthogonal to z. In Eq. 2.3 ω_m is the frequency of the standing wave, k is the wave vector, related to the frequency with $k_m = \omega_m/c$, V is the effective volume of the cavity and finally $q(t)$ is a time-dependent factor with the dimension of a length. The expression of the magnetic field $\vec{B}$ in the cavity is obtained by applying the second of the Eq. 2.1 to Eq. 2.3. It follows that:

$$\vec{B}(\vec{r}, t) = \hat{e}_y B_y(z, t) = \hat{e}_y \left(\frac{\mu_0 \epsilon_0}{k}\right) \sqrt{\left(\frac{2\omega^2}{V\epsilon_0}\right)} \dot{q}(t) \cos(kz), \tag{2.4}$$

where the polarization vector is oriented along the y axis. The total energy, or Hamiltonian, of the fields in the cavity is:

$$H = \frac{1}{2} \int_V \left(\epsilon_0 \vec{E}^2(\vec{r}, t) + \frac{1}{\mu_0} \vec{B}^2(\vec{r}, t)\right) dV. \tag{2.5}$$

By substituting $\vec{E}$ and $\vec{B}$ in Eq. 2.5 with Eq. 2.3 and Eq. 2.4 and by performing the integration; it is straightforward to obtain the following expression of the Hamiltonian:

$$H = \frac{1}{2} \left[\dot{q}^2(t) + \omega^2 q^2(t)\right],$$

which has the same form of the Hamiltonian of an harmonic oscillator. Therefore $q(t)$ and $\dot{q}(t)$ behave respectively as the canonical position and momentum of a particle with unit mass. It is shown heuristically that a single mode field has a similar behaviour of an harmonic oscillator with unit mass in which the electric and the magnetic fields plays respectively the roles of the canonical position and momentum. Having identified the canonical variables of the classical system the correspondence rule is used to replace them by their equivalent operator [29]:

$$q(t) \to \hat{q}(t) \qquad\qquad \dot{q}(t) \to \hat{p}(t)$$

that satisfies the standard commutation rule $[\hat{q}, \hat{p}] = \imath\hbar\hat{I}$. Because of the operators $\hat{q}$ and $\hat{p}$ are Hermitian, the quantized electric and magnetic field operators become observable and have the following form:

$$\hat{E}_x(z,t) = \sqrt{\left(\frac{2\omega^2}{V\epsilon_0}\right)}\hat{q}(t)\sin(kz) \qquad \hat{B}_y(z,t) = \left(\frac{\mu_0\epsilon_0}{k}\right)\sqrt{\left(\frac{2\omega^2}{V\epsilon_0}\right)}\hat{p}(t)\cos(kz).$$

The Hamiltonian of the system becomes:

$$H = \frac{1}{2}\left[\hat{p}^2(t) + \omega^2\hat{q}^2(t)\right].$$

Until now an intuitive process is used to rewrite the electromagnetic field in a quantized form, but for a more rigorous computation the reader is addressed to a standard textbook of quantum electrodynamic.

Now the obtained results are rewritten by introducing the non-Hermitian annihilation ($\hat{a}$) and creation ($\hat{a}^\dagger$) operators defined as:

$$\hat{a} = \frac{1}{\sqrt{2\hbar\omega}}(\omega\hat{q} + \imath\hat{p}) \qquad \hat{a}^\dagger = \frac{1}{\sqrt{2\hbar\omega}}(\omega\hat{q} - \imath\hat{p}).$$

It is easy to show that the commutator $[\hat{a}, \hat{a}^\dagger] = \hat{I}$. The electric field and the magnetic field operator becomes:

$$\hat{E}_x(z,t) = E_0(\hat{a} + \hat{a}^\dagger)\sin(kz) \qquad \hat{B}_y(z,t) = B_0(\hat{a} - \hat{a}^\dagger)\cos(kz), \tag{2.6}$$

where $E_0 = (\hbar\omega/\epsilon_0 V)^{1/2}$ and $B_0 = (\mu_0/k)(\epsilon_0\hbar\omega^3/V)^{1/2}$. With this formalism the Hamiltonian of the single mode in the cavity can be rewritten in the following simplified form:

$$\hat{H} = \hbar\omega\left(\hat{a}^\dagger\hat{a} + \frac{1}{2}\right).$$

2.2 Fock states

This section will show how the creation and annihilation operators allow to find easily the eigenstates $|n\rangle$ of a single mode field with energy E_n in a cavity. In this treatment the number operator $\hat{n}$, defined as $\hat{a}^\dagger\hat{a}$, plays a determinant role. Its eigenstates are the eigenstates of the Hamiltonian of the system:

$$\hat{H}|n\rangle = \hbar\omega\left(\underbrace{\hat{a}^\dagger\hat{a}}_{\hat{n}} + \frac{1}{2}\right)|n\rangle = E_n|n\rangle. \tag{2.7}$$

From Eq. 2.7 it is easy to explain why $\hat{a}^\dagger$ and $\hat{a}$ are respectively called the creation and annihilation operators. Multiplying Eq. 2.7 for $\hat{a}^\dagger$ it follows that:

$$\hat{a}^\dagger\hat{H}|n\rangle = \hbar\omega\left(\hat{a}^\dagger\hat{a}^\dagger\hat{a} + \frac{1}{2}\hat{a}^\dagger\right)|n\rangle = E_n\hat{a}^\dagger|n\rangle. \tag{2.8}$$

With the commutation relationship Eq. 2.8 can be rewritten as:

$$\begin{aligned}\hbar\omega\left((\hat{a}^\dagger\hat{a}-\hat{a}^\dagger)\hat{a}^\dagger+\frac{1}{2}\hat{a}^\dagger\right)|n\rangle &= \hat{H}\hat{a}^\dagger|n\rangle-\hbar\omega\hat{a}^\dagger|n\rangle = E_n\hat{a}^\dagger|n\rangle \\ \hat{H}\hat{a}^\dagger|n\rangle &= (E_n+\hbar\omega)\hat{a}^\dagger|n\rangle\end{aligned} \tag{2.9}$$

Eq. 2.9 describes the eigenvalue problem for the eigenstates $\hat{a}^\dagger|n\rangle$ with energy equal to $E_n+\hbar\omega$. From this equation one can understand why $\hat{a}^\dagger$ is called creation operator, in fact it generates a quantum of energy $\hbar\omega$. In the same way, it is possible to show that the annihilation operator destroys a quantum of energy $\hbar\omega$ and its eigenvalues problem for the eigenstates $\hat{a}|n\rangle$ is the following:

$$\hat{H}\hat{a}|n\rangle = (E_n-\hbar\omega)\hat{a}|n\rangle\,.$$

Thus for the electromagnetic field the following two statements are equivalent: a quantum of energy is created/destroyed and a photon with energy $\hbar\omega$ is created/destroyed.

If the annihilation operator is iteratively applied to an eigenstate $|n\rangle$ it lowers each time the energy of the system. But the energy of the harmonic oscillator is always positive therefore a state with minimum energy, called *ground state*, must exists and is indicated with $|0\rangle$. It follows that:

$$\hat{H}(\hat{a}|0\rangle) = (E_0-\hbar\omega)(\hat{a}|0\rangle) \equiv 0$$

The ground state eigenvalue can be found from its eigenvalues equation:

$$\hat{H}|0\rangle = \hbar\omega\left(\hat{a}^\dagger\hat{a}+\frac{1}{2}\right)|0\rangle = \frac{1}{2}\hbar\omega|0\rangle = E_0|0\rangle\,.$$

Since $E_{n+1} = E_n+\hbar\omega$ the energy eigenvalues can be rewritten in the same way of the harmonic oscillator eigenvalues:

$$E_n = \hbar\omega\left(n+\frac{1}{2}\right) \qquad \text{with} \quad n=1,2,\ldots.$$

The eigenstates $|n\rangle$ of the number operator $\hat{n}$ are called *Fock states* and form an orthogonal and complete set such that:

$$\hat{n}|n\rangle = n|n\rangle\,, \qquad \sum_{n=0}^{+\infty}|n\rangle\langle n| = 1 \qquad \text{and} \quad \langle m|n\rangle = \delta_{m,n}. \tag{2.10}$$

With this definitions it is easy to show that:

$$\hat{a}|n\rangle = \sqrt{n}\,|n-1\rangle \qquad \hat{a}^\dagger|n\rangle = \sqrt{n+1}\,|n+1\rangle\,.$$

From last results it is straightforward to show that a generic Fock state $|n\rangle$ can be obtained by applying recoursively the creation operator to the ground state:

$$|n\rangle = \frac{(\hat{a}^\dagger)^n}{\sqrt{n!}}|0\rangle\,, \tag{2.11}$$

where n is the number of photons contained in the state of the single mode field.

2.2.1 Quantum fluctuations of the field steady states on Fock basis

A Fock state has a well defined energy but the same does not happen for the electric field. Starting from Eq. 2.6 and Eq. 2.10, the average value of the electric field on a Fock State $|n\rangle$ is equal to:

$$< \hat{E}_x(z,t) >_n = \langle n| \hat{E}_x(z,t) |n\rangle = E_0 \sin(kz) \langle n| \hat{a} + \hat{a}^\dagger |n\rangle = 0,$$

i.e. the electric field oscillations have a null average value. Moreover their fluctuations, that are characterized by the variance on the state $|n\rangle$, are equal to:

$$\left\langle (\Delta \hat{E}_x(z,t))^2 \right\rangle_n = < \hat{E}_x^2(z,t) > - < \hat{E}_x(z,t) >^2 = 2E_0^2 \sin^2(kz) \left(n + \frac{1}{2} \right).$$

Therefore for all the Fock states the fluctuations of the electromagnetic field are greater than zero.

2.3 Coherent states

The results presented in Sec. 2.2.1 evince that the Fock states are not the best candidates for the quantum description of a real field such as a laser beam. In fact, in the classical limit, i.e. when the number n of photons is very high and the number operator can be approximated as a continuous variable, the mean of the electric field remains equal to zero. This property is not in agreement with the classical description of light in which, chosen a fixed point in the space, the electric field oscillates sinusoidally in time. Therefore a new set of states must be introduced to transpose the classical physics of laser fields in the quantum world. These states, called *coherent states*, are the eigenstates of the annihilation operator:

$$\hat{a} |\alpha\rangle = \alpha |\alpha\rangle ,$$

where the eigenvalue α are complex numbers because of the annihilation operator is not Hermitian. The coherent states can be expanded in the Fock basis:

$$|\alpha\rangle = \sum_{n=0}^{+\infty} C_n |n\rangle . \tag{2.12}$$

The coefficients C_n of the expansion are found by acting with the operator $\hat{a}$ on Eq. 2.12:

$$\hat{a} |\alpha\rangle = \sum_{n=0}^{+\infty} C_n \hat{a} |n\rangle = \sum_{n=1}^{\infty} C_n \sqrt{n} |n-1\rangle, \tag{2.13}$$

where $C_n\sqrt{n} = \alpha C_{n-1}$ and with an iterative process it follows that:

$$C_n = \frac{\alpha}{\sqrt{n}}C_{n-1} = \frac{\alpha^2}{\sqrt{n(n-1)}}C_{n-2} = \cdots = \frac{\alpha^n}{\sqrt{n!}}C_0.$$

Therfore the Eq. 2.12 becomes:

$$|a\rangle = C_0 \sum_{n=0}^{\infty} \frac{\hat{a}^n}{\sqrt{n!}} |0\rangle.$$

The C_0 coefficient is easily find using the normalization condition i.e. $\langle\alpha|\,|\alpha\rangle = 1$. Finally a coherent state in the Fock basis is expressed as:

$$|a\rangle = \exp\left(-\frac{|\alpha|^2}{2}\right) \sum_{n=0}^{\infty} \frac{\hat{a}^n}{\sqrt{n!}} |0\rangle.$$

In the following it will be shown that the coherent states represent a good quantum description of a laser field. The mean value of the electric field, on a coherent state, is thus equal to:

$$< \hat{E}_x(z,t) >_\alpha = \langle\hat{\alpha}|\,\hat{E}_x(z,t)\,|\hat{\alpha}\rangle = 2|\alpha|\sqrt{\frac{\hbar\omega}{2\epsilon_0 V}}\sin\left(\omega t - \vec{k}\cdot\vec{r} - \vartheta\right), \tag{2.14}$$

where the complex eigenvalue α is written in polar coordinates $\alpha = |\alpha|\exp(\imath\vartheta)$. In this basis the expectation value of the electric field operator does not vanish but it oscillates sinusoidally as the classical field. Moreover its fluctuations are identical to those of the vacuum state:

$$\left\langle(\Delta\hat{E}_x(z,t))^2\right\rangle_\alpha = \frac{\hbar\omega}{2\epsilon_0 V}. \tag{2.15}$$

In the last part of this section the results 2.14 and 2.15 are rewritten in terms of the quantum number operator. In Eq. 2.14 the real part of the parameter α is related to the electric field amplitude and coincides with the expectation value of the number of state operator:

$$< \hat{n} >_\alpha = \langle\hat{\alpha}|\,\hat{n}\,|\hat{\alpha}\rangle = |\alpha|^2$$

that describes the number of photons in a mode of the electric field. The fluctuations of the number operator are given by the following relationship:

$$\sqrt{< (\Delta\hat{n})^2 >_\alpha} = \sqrt{\langle\hat{\alpha}|\,\hat{n}^2\,|\hat{\alpha}\rangle - (\langle\hat{\alpha}|\,\hat{n}\,|\hat{\alpha}\rangle)^2}.$$

By computing

$$\langle\hat{\alpha}|\,\hat{n}^2\,|\hat{\alpha}\rangle = \langle\hat{\alpha}|\,\hat{a}^\dagger\hat{a}\hat{a}^\dagger\hat{a}\,|\hat{\alpha}\rangle = \langle\hat{\alpha}|\,(\hat{a}^\dagger\hat{a}^\dagger\hat{a}\hat{a} + \hat{a}^\dagger\hat{a})\,|\hat{\alpha}\rangle = |\alpha|^4 + |\alpha|^2 =< \hat{n} >_\alpha^2 + < \hat{n} >_\alpha$$

it follows that:

$$\sqrt{< (\Delta\hat{n})^2 >_\alpha} = \sqrt{< \hat{n} >_\alpha} := \sqrt{\bar{n}}$$

which is characteristic of a Poisson process. Finally the probability to detect n photons is given by:

$$P_n = |\langle\alpha|\,|n\rangle|^2 = e^{-|\alpha|^2}\frac{|\alpha|^{2n}}{n!} = e^{\bar{n}}\frac{\bar{n}^n}{n!}$$

which is a Poisson distribution with mean $\bar{n}$.

Another method used to obtain a coherent state from the vacuum state $|0\rangle$ consists in the introduction of the *displacement operator*. It is defined as:

$$\hat{D}(\alpha) = \exp(\alpha\hat{a}^\dagger + \alpha^*\hat{a}) \qquad \text{with} \qquad \hat{D}^\dagger(\alpha) = \hat{D}(-\alpha).$$

A coherent state can be obtained by "displacing" the vacuum state applying the displacement operator $\hat{D}$:

$$|\alpha\rangle = \hat{D}(\alpha)\,|0\rangle\,.$$

2.4 Quadrature Operators

Sec. 2.2 showed that the annihilation and creation operators are not Hermitian and therefore are not observables. With s linear combination of these operators ($\hat{a}$, $\hat{a}^\dagger$), two new Hermitian operators are introduced:

$$\hat{X_1} = \frac{1}{2}\left(\hat{a} + \hat{a}^\dagger\right) \qquad\qquad \hat{X_2} = \frac{1}{2\imath}\left(\hat{a} - \hat{a}^\dagger\right). \tag{2.16}$$

By introducing the time dependence of the creation and annihilation operator, the electric field operator is rewritten as:

$$\hat{E}_x(z,t) = E_0(\hat{a}e^{\imath\omega t} + \hat{a}^\dagger e^{-\imath\omega t})\sin(kz),$$

that can be rearranged in term of the $\hat{X}_{1,2}$ operators as follows:

$$\hat{E}_x(z,t) = 2E_0\sin(kz)\left[\hat{X}_1\cos(\omega t) + \hat{X}_2\sin(\omega t)\right] \tag{2.17}$$

From Eq. 2.17 it is clear that the $\hat{X}_1$ and $\hat{X}_2$ are associated with field amplitudes that are out of phase with each other of 90°. For this reason these two operators are called *quadrature operators*. Moreover by inverting Eq. 2.16 one obtains that:

$$\hat{a} = \hat{X}_1 + \imath\hat{X}_2 \qquad\qquad \hat{a}^\dagger = \hat{X}_1 + \imath\hat{X}_2,$$

Since a coherent state is an eigenstate of the annihilation operator and $\hat{X}_1$ and $\hat{X}_2$ are respectively its real and imaginary part, they are called the *amplitude quadrature* operator and *phase quadrature* operator [20].

2.4.1 The Heisenberg uncertainty principle

The Heisenberg uncertainty principle states that for two non commuting and Hermitian operators $\hat{P}$ and $\hat{Q}$ it is not possible to measure simultaneously their quantities with arbitrary precision. This theorem can be expressed in a mathematical form as

$$< (\Delta\hat{P})^2 >< (\Delta\hat{Q})^2 >\geq \frac{1}{2}\left[\hat{P},\hat{Q}\right]^2. \tag{2.18}$$

From Eq. 2.18 follows that much smaller is the uncertainty on the observable $\hat{P}$ much greater is the uncertainty on the observable $\hat{Q}$ and vice-versa. The commutator for the two quadrature operators is given by

$$\left[\hat{X}_1,\hat{X}_2\right] = \frac{\imath}{2}$$

and therefore it follows that:

$$< (\Delta\hat{X}_1)^2 >< (\Delta\hat{X}_2)^2 >\geq \frac{1}{16}.$$

Minimum uncertainty for a Fock state

The mean value of the quadrature operators on a Fock state are equal to $\langle n|\,\hat{X}_1\,|n\rangle = \langle n|\,\hat{X}_2\,|n\rangle = 0$, whereas their fluctuations on a Fock state are equal to:

$$< (\Delta\hat{X}_1)^2 >= \langle n|\,\hat{X}_1^2\,|n\rangle = \frac{1}{4}\langle n|\,\hat{a}^{\dagger^2} + \hat{a}^2 + \hat{a}^\dagger\hat{a} + \hat{a}\hat{a}^\dagger\,|n\rangle = \frac{1}{4}(2n+1),$$

$$< (\Delta\hat{X}_2)^2 >= \langle n|\,\hat{X}_2^2\,|n\rangle = -\frac{1}{4}\langle n|\,\hat{a}^{\dagger^2} + \hat{a}^2 - \hat{a}^\dagger\hat{a} - \hat{a}\hat{a}^\dagger\,|n\rangle = \frac{1}{4}(2n+1).$$

Therefore the uncertainty is equally distributed on the two quadrature; moreover when $n = 0$ the Heisenberg Uncertainty is minimized, so the vacuum state correspond to the Fock state with minimum uncertainty.

Minimum uncertainty for a Coherent state

It is interesting to compare the uncertainty of a coherent state with the uncertainty of a vacuum state. The fluctuations of a coherent state are given by:

$$\begin{aligned}
< (\Delta\hat{X}_1)^2 >_\alpha &= \langle\alpha|\,\hat{X}_1^2\,|\alpha\rangle + \langle\alpha|\,\hat{X}_1\,|\alpha\rangle^2 = \frac{1}{4}\left[\langle\alpha|\,(\hat{a}^\dagger+\hat{a})^2\,|\alpha\rangle - \langle\alpha|\,(\hat{a}^\dagger+\hat{a})\,|\alpha\rangle^2\right] \\
&= \frac{1}{4}\left[\langle\alpha|\,((\hat{a}^\dagger)^2 + (\hat{a})^2 + 2\hat{a}^\dagger\hat{a} + 1)\,|\alpha\rangle - \langle\alpha|\,(\hat{a}^\dagger+\hat{a})\,|\alpha\rangle^2\right] \\
&= \frac{1}{4}\left[(\alpha^2 + \alpha^{*^2} + 2|\alpha|^2 + 1 - (\alpha^2 + \alpha^{*^2} + 2|\alpha|^2)\right] = \frac{1}{4}
\end{aligned}$$

With a similar calculation one obtains the same result for the fluctuations, on a coherent state, of the other quadrature operator $\hat{X}_2$. Therefore this short computation

shows that both the coherent states and the vacuum state are minimum uncertainty states.

A coherent state, can be represented as an "error circle" centred in $< \hat{a} >= \alpha$ and radius equal to $\sqrt{< (\Delta \hat{X}_1)^2 >} = 1/2$ in the complex-amplitude plane, in which the axis are the two quadrature operators $\hat{X}_1$ and $\hat{X}_2$. Fig. 2.1 shows a coherent state $|\alpha\rangle$ and the vacuum state in this representation [20].

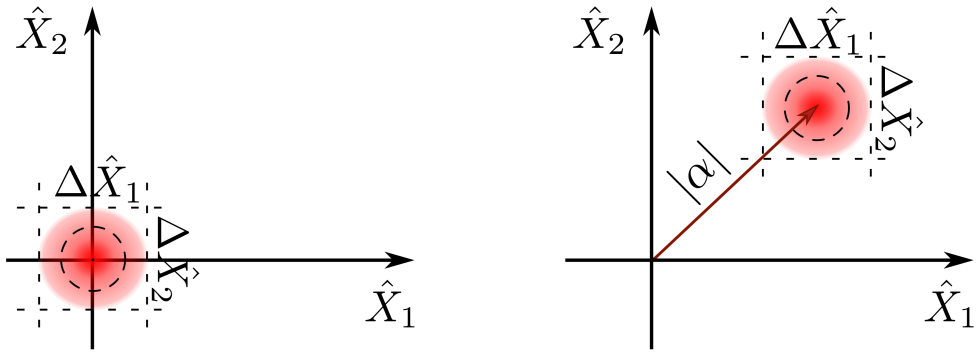

Figure 2.1: Representation of light states in the quadrature operators plane. Left: a vacuum state. Right: a coherent state with eigenvalue α

2.5 Squeezed states

This section introduces the *squeezed states*, i.e. another class of minimum uncertainty states. A minimum uncertainty state is defined as a state in which the fluctuation of two non commuting observable satisfies, with the equal sign, the relationship in Eq. 2.18. If the two observable are the quadrature operators it follows that:

$$< (\Delta \hat{X}_1)^2 >< (\Delta \hat{X}_2)^2 >= \frac{1}{16}.$$

The last expression sets a lower limit to the product between the fluctuations of the two quadrature operators but it does not forbid that an observable has fluctuations greater than the other one. Therefore a *squeezed quadrature* is defined as a quadrature that has fluctuations lower than vacuum state fluctuations, i.e.:

$$< (\Delta \hat{X}_1)^2 >< \frac{1}{4} \qquad \text{or} \qquad < (\Delta \hat{X}_2)^2 >< \frac{1}{4}.$$

At the same time if one of the quadrature is squeezed the other must be *anti-squeezed*, i.e. its fluctuations are larger than the ones of the vacuum state:

$$< (\Delta \hat{X}_1)^2 >> \frac{1}{4} \qquad \text{or} \qquad < (\Delta \hat{X}_2)^2 >> \frac{1}{4}.$$

A squeezed state is obtained by applying the squeezing operator on a coherent state. The squeezing operator $\hat{S}(R,\vartheta)$ is defined as:

$$\hat{S}(r,\vartheta) = \exp\left[\frac{1}{2}re^{-\imath\vartheta}\hat{a}^2 - \frac{1}{2}re^{\imath\vartheta}\hat{a}^{\dagger^2}\right] \tag{2.19}$$

where r is called *squeezing parameter* ($0 < r < \infty$) and ϑ is called *squeezing angle* ($0 < \vartheta < 2\pi$). It is possible to distinguish two kind of squeezed states, the first is obtained by applying the squeezing operator to a vacuum state

$$|r,\vartheta,0\rangle := \hat{S}(r,\vartheta)\,|0\rangle$$

and it is called *squeezed vacuum state*; whereas the second is obtained by applying the squeezing operator to a generic coherent state

$$|r,\vartheta,\alpha\rangle := \hat{S}(r,\vartheta)\,|\alpha\rangle = \hat{S}(r,\vartheta)\hat{D}(\alpha)\,|0\rangle$$

and it is called *bright squeezed state*. In the following the quadrature fluctuations of a squeezed state are computed. The result is obtained from the expectation value of $\hat{a}^2$ and $\hat{a}^{\dagger^2}$ over a squeezed state. To do this, the following results, obtained with the Baker Hausdorf lemma are exploited [27]:

$$\begin{aligned}\hat{S}^\dagger(r,\vartheta)\hat{a}\hat{S}(r,\vartheta) &= \hat{a}\cosh(r) - \hat{a}^\dagger e^{\imath\vartheta}\sinh(r)\\ \hat{S}^\dagger(r,\vartheta)\hat{a}^\dagger\hat{S}(r,\vartheta) &= \hat{a}\cosh(r) - \hat{a}^\dagger e^{-\imath\vartheta}\sinh(r).\end{aligned} \tag{2.20}$$

From these two relationships, the variances of the two quadrature operators over a squeezed vacuum state are easily computed:

$$\begin{aligned}\left\langle\Delta\hat{X}_1\right\rangle^2_{r,\vartheta,0} &= \frac{1}{4}\left[\cosh^2(r)^2 + \sinh^2(r) - 2\sinh(r)\cosh(r)\cos(\vartheta)\right]\\ \left\langle\Delta\hat{X}_2\right\rangle^2_{r,\vartheta,0} &= \frac{1}{4}\left[\cosh^2(r) + \sinh^2(r) + 2\sinh(r)\cosh(r)\cos(\vartheta)\right].\end{aligned} \tag{2.21}$$

Substituting $\vartheta = 0$ in Eq. 2.21 one obtains that:

$$\begin{aligned}\left\langle\Delta\hat{X}_1\right\rangle^2_{r,0,0} &= \frac{1}{4}e^{-2r}\\ \left\langle\Delta\hat{X}_2\right\rangle^2_{r,0,0} &= \frac{1}{4}e^{+2r}.\end{aligned} \tag{2.22}$$

Thus a squeezed state with $\vartheta = 0$ is a minimum uncertainty state whose amplitude quadrature operator fluctuations are suppressed, (squeezed) by a factor e^{-r}, with respect to the coherent state fluctuations and whose phase quadrature operator fluctuations are increased, (anti-squeezed) by a factor e^{r}, respect to the coherent state

fluctuations. This result can be generalized for any value of the squeezing angle ϑ, by defining rotated quadrature operator as:

$$\begin{bmatrix} \hat{Y}_1 \\ \hat{Y}_2 \end{bmatrix} = \begin{bmatrix} \cos(\vartheta/2) & \sin(\vartheta/2) \\ -\sin(\vartheta/2) & \cos(\vartheta/2) \end{bmatrix} \times \begin{bmatrix} \hat{X}_1 \\ \hat{X}_2 \end{bmatrix}, \tag{2.23}$$

therefore Eq. 2.24 can be rewritten as:

$$\begin{aligned} \left\langle \Delta \hat{Y}_1 \right\rangle^2_{r,\vartheta,0} &= \frac{1}{4} e^{-2r} \\ \left\langle \Delta \hat{Y}_2 \right\rangle^2_{r,\vartheta,0} &= \frac{1}{4} e^{+2r}. \end{aligned} \tag{2.24}$$

In most of the case the squeezing level is expressed in dB by means the following relationship:

$$V[dB] = 10 \log \left(\frac{\left\langle \Delta \hat{X}_1 \right\rangle^2}{\left\langle \Delta \hat{X}_2 \right\rangle^2} \right) = 20 \log \left(e^{-2r} \right).$$

Fig. 2.2 is a plot of the quadrature noise variance as function of the of the quadrature angle ϑ.

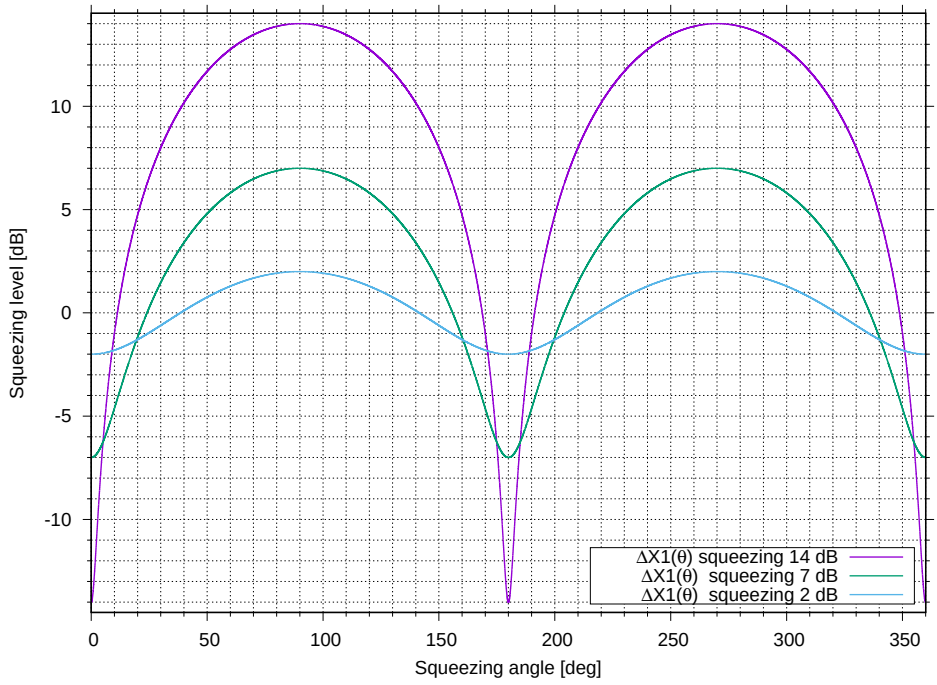

Figure 2.2: Quadrature noise variance as function of the quadrature angle ϑ. The violet line represents a squeezed state of 15dB, the green line is the trend of a squeezed state of 7dB and the blue line a squeezed state of 2dB.

As explained above a bright squeezed state is obtained by applying the the displacement operator $\hat{D}(\alpha)$ on a squeezed vacuum state. These states have fluctuations

of the quadratures operators equal to those of a vacuum squeezed state. However the mean value of the number operator over a bright squeezed state is equal to:

$$< \hat{n} >_{r,\vartheta,\alpha} = |\alpha|^2 + \sinh^2(r)$$

which is slightly increased compared to the photon number of a coherent state. This expression evinces that a squeezed vacuum state contains photons and has higher energy than the vacuum state, therefore during the squeezing process photons are generated and the energy of the state is increased. Fig. 2.3 shows in the quadrature planes a vacuum squeezed state in the left side and a bright squeezed state in the right side.

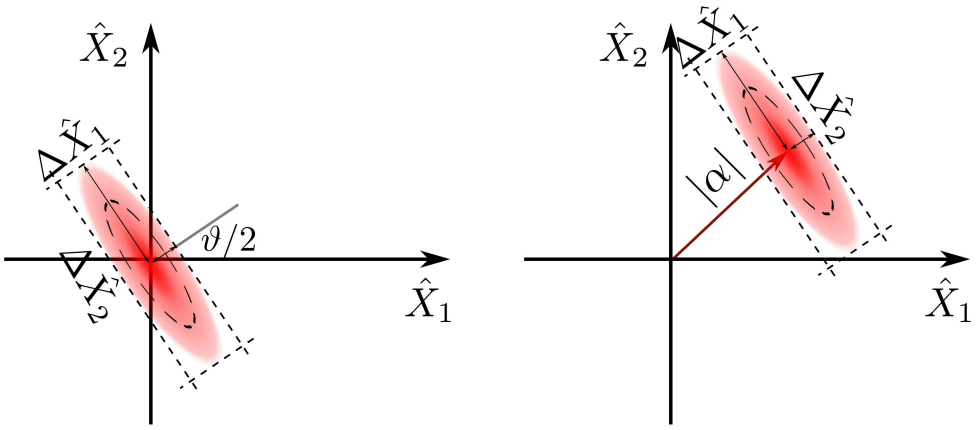

Figure 2.3: Representation of squeezed states in the quadrature operators plane. Left: a vacuum squeezed state Right: a bright squeezed state

2.6 Detection of squeezed states

A key instrument used in optical experiments for the measurements of light states is the photodetector. It converts photon in free electrons generating a photocurrent proportional to the incident light power on its active surface. An intuitive way to describe, in the quantum world, the behaviour of photodetectors consist in the linearization of operators. This method describes well bright beams which have an amplitude much larger than their fluctuations. To linearize an operator it is decomposed in two components: the former, represented by a complex number, is the steady state amplitude and the latter, described by an operator, represents the time dependent fluctuations. For example the annihilation and the creation operators are rewritten as:

$$\hat{a} = \alpha + \delta\hat{a} \qquad \hat{a}^\dagger = \alpha^* + \delta\hat{a}^\dagger$$

where the mean value of the time dependent fluctuations is equal to zero ($< \delta\hat{a} >=< \delta\hat{a}^\dagger >= 0$). The linearization of the number operator is interesting:

$$\hat{n} = \hat{a}^\dagger\hat{a} = (\alpha + \delta\hat{a})(\alpha^* + \delta\hat{a}^\dagger) = |\alpha|^2 + \alpha\delta\hat{a}^\dagger + \alpha^*\delta\hat{a} + \delta\hat{a}^\dagger\delta\hat{a}.$$

By neglecting the second order fluctuations and assuming that the α parameter is real, the number operator $\hat{n}$ is linearized as follows:

$$\hat{n} = \hat{n} + \delta\hat{n} \approx \alpha^2 + 2\alpha\delta\hat{X}_1,$$

therefore fluctuations of the number of photons are related to the quadrature $\hat{X}_1$ that is referred as *amplitude quadrature*.

2.6.1 Direct photons detection

The simplest scheme of light detection is the direct detection with a photodiode that converts the photons in electrons with a quantum efficiency η_q and it generates a current $\hat{i}$ that is equal to

$$\hat{i} = \eta_q e\hat{n} = \eta_q e\alpha^2 + 2\eta_q e\delta\hat{X}_1(t).$$

The left part of Fig. 2.4 shows a scheme of direct photodetection. In it the photocurrent is composed by a classical DC terms,proportional to the intensity of the field, and by an AC current. Thus this technique is sensitive only to the fluctuations of the amplitude quadrature $\hat{X}_1$ and a direct measurement can be used to detect only amplitude squeezed states.

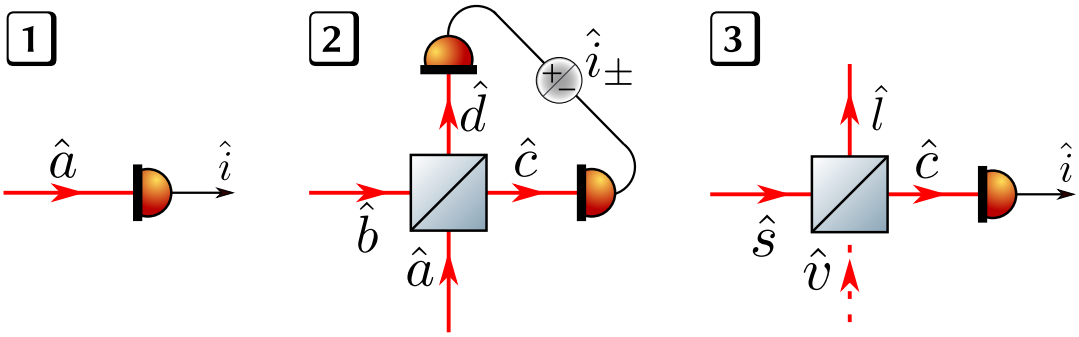

Figure 2.4: Scheme of light photodetection. 1. represents the direct photodetection of light, 2. represents the photodetection with an homodyne detector, 3. represents the direct photodetection of light when the optical losses are considered.

2.6.2 Homodyne detection

The homodyne photodetection setup is shown in the middle part of Fig. 2.4. It is composed by a beam-splitter (BS) and two photodetectors. If the splitting ratio of the beam-splitter is 50/50, this technique is called *balanced homodyne detection*. This technique exploits the interference phenomenon between the two input fields of the BS that are: the field under measurement, represented in the figure with the operator $\hat{a}$ and a reference field, called *local oscillator* (LO), represented in the figure with the operator $\hat{b}$. The two output of the BS are respectively the transmitted field, represented by the operator $\hat{c}$, and the reflected field, represented by the operator $\hat{d}$. The following expression is the BS input output relationship:

$$\begin{bmatrix} \hat{c} \\ \hat{d} \end{bmatrix} = \begin{bmatrix} r & t \\ t & -r \end{bmatrix} \times \begin{bmatrix} \hat{a} \\ \hat{b} \end{bmatrix}, \tag{2.25}$$

where r and t are respectively its reflectance and transmittance. The signal field $\hat{a}$ and the LO field $\hat{b}$ are linearized as: $\hat{a} = \alpha + \delta\hat{a}$ and $\hat{b} = (\beta + \delta\hat{b})e^{\imath\varphi}$, where φ is an arbitrary phase between the local oscillator field and the field under measurement, whereas α and β are real coefficients. The two BS outputs are detected by two different photodiodes. Remembering that the photocurrent is expressed as $\hat{i} = \eta_q e\hat{n}$; the generated photocurrent by the field $\hat{c}$ is equal to:

$$\begin{aligned}\hat{i}_c &= \eta_q e \left(r\hat{a}^\dagger + t\hat{b}^\dagger\right)\left(r\hat{a} + t\hat{b}\right) \\ &\approx \eta_q e \left[r^2\alpha^2 + 2rt\alpha\beta\cos(\varphi) + t^2\beta^2 + 2r\alpha\left(r\delta\hat{X}_{a,1} + t\delta\hat{X}_{b,-\varphi}\right) + 2t\beta\left(t\delta\hat{X}_{b,1} + r\delta\hat{X}_{a,\varphi}\right)\right].\end{aligned}$$

At the same time the photocurrent generated by the the reflected field $\hat{d}$ is equal to:

$$\begin{aligned}\hat{i}_d &= \eta_q e \left(t\hat{a}^\dagger - r\hat{b}^\dagger\right)\left(t\hat{a} - r\hat{b}\right) \\ &\approx \eta_q e \left[r^2\alpha^2 - 2rt\alpha\beta\cos(\varphi) + t^2\beta^2 + 2r\alpha\left(r\delta\hat{X}_{a,1} - t\delta\hat{X}_{b,-\varphi}\right) - 2t\beta\left(t\delta\hat{X}_{b,1} - r\delta\hat{X}_{a,\varphi}\right)\right],\end{aligned}$$

where in both the expressions the high order terms are neglected and the following notation is introduced:

$$\hat{X}_{a,\vartheta} = \frac{1}{2}\left[\hat{a}e^{-\imath\vartheta} + \hat{a}^\dagger e^{\imath\vartheta}\right] = \hat{X}_{a,1}\cos(\vartheta) + \hat{X}_{a,2}\sin(\vartheta). \tag{2.26}$$

The two photodiodes are mounted on an electronic circuit that computes the sum ($\hat{i}_+$) and the difference ($\hat{i}_-$) of their output currents:

$$\begin{aligned}\hat{i}_+ &= \hat{i}_c + \hat{i}_d \approx 2\eta_q e\left[r^2\alpha^2 + t^2\beta^2 + 2r\alpha\delta\hat{X}_{a,1} + 2t\beta\delta\hat{X}_{b,1}\right] \\ \hat{i}_- &= \hat{i}_c - \hat{i}_d \approx 4rt\eta_q e\left[\alpha\beta\cos(\varphi) + \alpha\delta\hat{X}_{b,-\varphi} + \beta\delta\hat{X}_{a,\varphi}\right]\end{aligned}$$

If the signal field has an intensity α negligible with respect to the intensity of the local oscillator field β, the last two expressions can be simplified as:

$$\hat{i}_+ \approx 2\eta_q e \left[t^2\beta^2 + 2t^2\beta\delta\hat{X}_{b,1} \right]$$
$$\hat{i}_- \approx 4rt\eta_q e \left[\alpha\beta\cos(\varphi) + \beta\delta\hat{X}_{a,\varphi} \right].$$

The sum signal contains only the information on the local oscillator field and on the fluctuations of its quadrature $\hat{X}_1$, whereas the difference signal is composed by two terms: the former describes the interference between the two fields and the latter contains the fluctuations of a quadrature of the signal beam rotated by an angle φ respect to the $\hat{X}_1$, $\hat{X}_2$ plane. Using the expression in Eq. 2.26 the last expression becomes:

$$\hat{i}_- \approx 4rt\eta_q e \left[\alpha\beta\cos(\varphi) + \beta\left(\delta\hat{X}_{a,1}\cos(\vartheta) + \delta\hat{X}_{a,2}\sin(\vartheta) \right) \right],$$

thus the difference signal is composed by a DC component and its fluctuations. In order to obtain the information on the rotated quadrature, the power spectral density of the difference signal is acquired with a spectrum analyzer. By virtue of the Wiener Khinchin theorem, the power spectrum of a stationary process is equal to the Fourier transform of its auto-correlation function; so by measuring the difference signal with a spectrum analyzer, the information about the quadrature fluctuations is extracted. If in the homodyne detection, the signal field is a squeezed vacuum states one measures the squeezing level with this technique. In particular, the fluctuations of the amplitude quadrature $\hat{X}_1$ are measured by setting the relative phase between the local oscillator and the signal field equal to 0; whereas the fluctuations of the phase quadrature are measured by setting the relative phase equal to $\pi/2$. The relative phase between the two beams is set by changing the optical beam paths. Usually in squeezing experiments the detection is performed with the balance homodyne detector, thus the beam splitter has a 50/50 splitting ratio and the expressions of the currents can be simplified by inserting $r = t = 1/\sqrt{2}$. In this thesis the homodyne detector is designed with a self-subtracting scheme: this means that the two photocurrents are directly subtracted before applying electronic conditioning of the two photodode signals. The aim of this design is to avoid gain difference between the two signal that will cause a discrepancy between the generated squeezing level and the measured squeezing level [30].

2.7 Squeezing degradation

This section analyzes the degradation processes of a squeezed state due to the optical losses and the phase noise.

2.7.1 Optical losses

In most classical experiment an optical loss can be compensated by increasing the light power, but this is not true in a squeezing experiment, where any optical loss reduces the squeezing level. In quantum optics, a simple method to describe the optical losses is the *beam splitter model* that is shown in the right part of Fig. 2.4. It describes an optical loss ϵ with a beam splitter with power reflectivity $\sqrt{\epsilon}$ and power transmittivity $\sqrt{1-\epsilon}$. In the unused BS input port enters a vacuum state, that has an high effect on the squeezing level and has low impact on the anti-squeezing level. Mathematically, this problem is described starting from the beam splitter matrix shown in Sec. 2.6.2.

This computations refers to the right part of Fig. 2.4, where the two input fields of the BS are the signal field $\hat{s}$ and the vacuum field $\hat{v}$. The transmitted beam ($\hat{c}$) is detected with a photodetector. The tree fields are linearized as:

$$\hat{s} = \sigma + \delta\hat{a} \qquad \hat{v} = \delta\hat{v} \qquad \hat{c} = \gamma + \delta\hat{c},$$

where $\hat{v}$ is composed only by fluctuation because it is a vacuum state. If the photodetector quantum effciency is supposed equal to one, the measured photocurrent is:

$$\begin{aligned}\hat{c} &= \left(\sqrt{\epsilon}\hat{v}^{\dagger} + \sqrt{1-\epsilon}\hat{s}^{\dagger}\right)\left(\sqrt{\epsilon}\hat{v} + \sqrt{1-\epsilon}\hat{s}\right) \\ &\approx (1-\epsilon)\sigma^2 + 2\sqrt{1-\epsilon}\sigma(\sqrt{1-\epsilon}\delta\hat{X}_{s,1} + \sqrt{\epsilon}\delta\hat{X}_{v,1})\end{aligned}$$

where the second order fluctuations are neglected. Now the mean value of the output field fluctuations is computed:

$$< (\Delta\delta\hat{X}_{c,1})^2 >= 4\sigma^2(1-\epsilon)(< (1-\epsilon)\delta\hat{X^2_{s,1}} > + < \epsilon\delta\hat{X}^2_{v,1} >) + 2 < \sqrt{\epsilon(1-\epsilon)}\delta\hat{X}_{1,s}\delta\hat{X}_{1,v} > .$$

The last term is equal to zero because the fluctuations of the vacuum field and the signal field are independent processes. If the signal field $\hat{s}$ has fluctuations equal to x expressed in dB, i.e. ($< (\Delta\delta\hat{X}_{a,1})^2 >= x$ [dB]), the last expression can be rewritten as:

$$< (\Delta\delta\hat{X}_{c,1})^2 >= 10\log\left[(1-\epsilon)10^{\frac{x[\mathrm{dB}]}{10}} + \epsilon\right] \tag{2.27}$$

Fig. 2.6 shows the effect of the optical losses on the generated squeezing/anti-squeezing level.

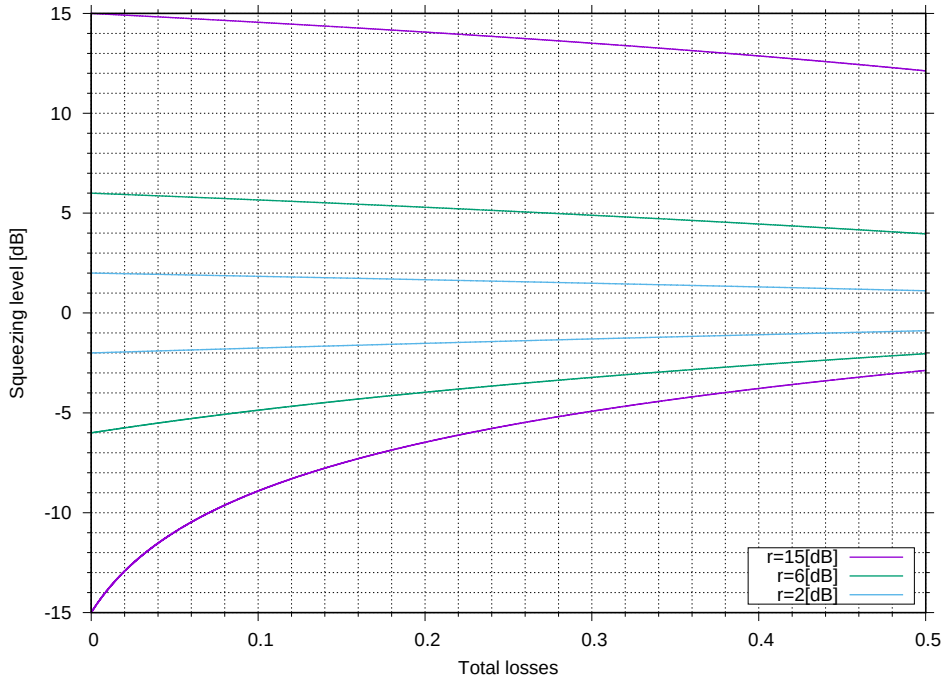

Figure 2.5: Degradation of the squeezing level due to the optical losses. The violet curve represents a squeezed state of 15 dB, the green curve represents a squeezed state of 6 dB and the blue curve represents a squeezed state of 2 dB.

A particular source of losses: homodyne mismatch

As said above, the homodyne detection is performed by overlapping the signal field and the local oscillator field on a beam splitter. In a real experiment the interference phenomenon is not perfect. To obtain the maximum interference the two beams must have the same frequency, spatial modes, waist dimension, waist position and polarization. A mismatch of this quantities, between the two beams, causes a degradation of the interference phenomenon. An estimator of the interference level between the two beams is the *fringe visibility* $\mathcal{V}$ that is measured by scanning the relative phase between them and measuring the intensity of the fringes with a photodetector. In particular the visibility is defined as:

$$\mathcal{V} = \frac{I_{max} - I_{min}}{I_{max} + I_{min}},$$

where I_{max} adn I_{min} are respectively the minimum and the maximum of the fringes. The mismatch is an optical loss in the squeezing measurement and it contributes quadratically to the detection efficiency that is equal to:

$$\eta_{eff} = \eta_{prop} \cdot \eta_q \cdot \mathcal{V}^2$$

where η_q is the quantum efficiency of the photodiode and η_{prop} are the propagation losses of the squeezing field from its generation to its detection. Eq. 2.27 can be rewritten in terms of the detection efficiency as:

$$< (\Delta\delta\hat{X}_{c,1})^2 >= 10\log\left[\eta 10^{\frac{x[\mathrm{dB}]}{10}} + (1-\eta)\right].$$

2.7.2 Ellipse phase fluctuations

In the homodyne detection, the relative phase between the local oscillator beam and the measured beam determines the quadrature under observation. This angle must be fixed and its residual fluctuations can be treated as the jitter of the squeezing ellipse respect to the observed quadrature. The effect of these fluctuation on the generated squeezing states consists in a mixing of the two quadrature variances $< (\Delta\hat{X}_1)^2 >$ and $< (\Delta\hat{X}_2)^2 >$ that is given by:

$$< (\Delta\hat{X}_{1,2})^2 >' = < (\Delta\hat{X}_{1,2})^2 > \cos^2(\delta\vartheta) + < (\Delta\hat{X}_{2,1})^2 > \sin^2(\delta\vartheta)$$

where the variable $\delta\vartheta$ represents the residual phase fluctuations. This relationship is valid only for small residual fluctuations and is obtained with the projection of the two rotated quadrature variances on the two Cartesian axis, see the left side of Fig. 2.6. The right side of the same figure shows how a state with squeezing level equal to 15 dB is affected by the optical losses and the residual phase noise.

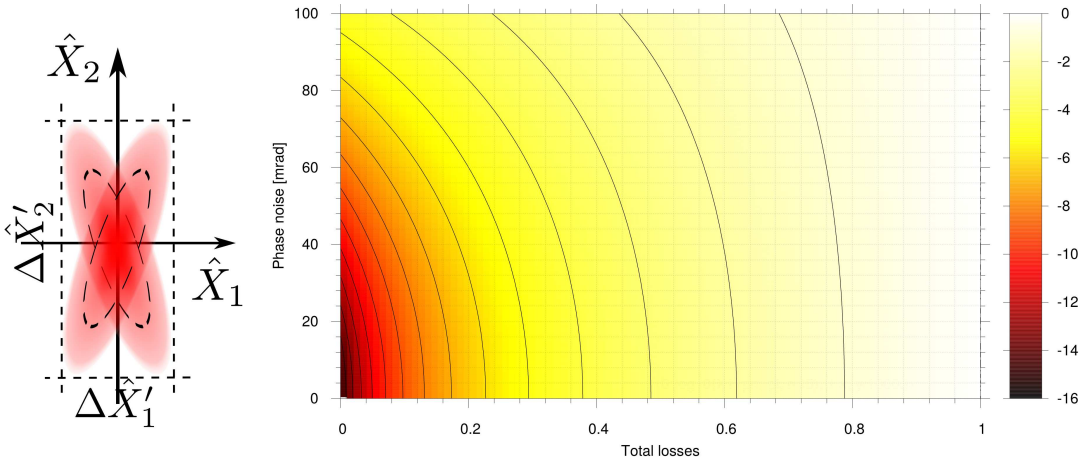

Figure 2.6: Left: effect of the phase noise on the squeezing ellipse. Right: degradation of the squeezing level due to the optical losses (x axis), and to the residual phase noise (y axis)

2.8 Quantum-mechanic analysis of an interferometer

This section describes a Michelson-Morley interferometer with a quantum mechanical approach that allows to understand how the Heisenberg uncertainty prin-

ciple limits the sensitivity of the detector. As said in Chap. 1 this kind of detector measures the difference in length between its two arms. The most simple scheme of a Michelson interferometer is shown in Fig. 2.7. The light emitted by the laser enters in

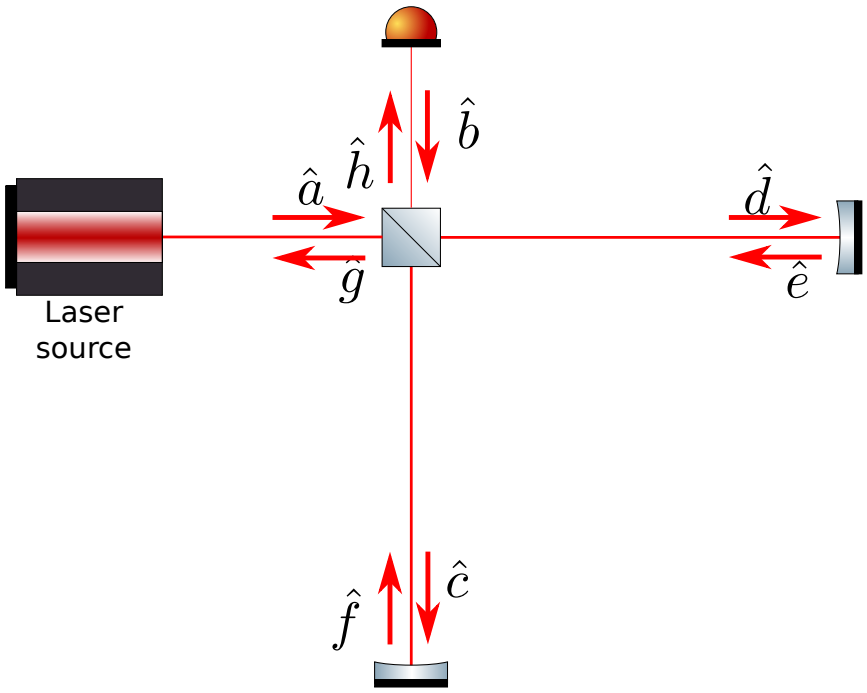

Figure 2.7: Scheme of the most simple configuration of a Michelson Morley interferometer

the interferometer trough the 50/50 beam splitter, is reflected by the two end mirrors and finally it recombines at the beam splitter. The mass of the two end mirrors is denoted with m whereas the mass of the beam splitter with M. It is assumed $m \ll M$ so it is considered the contribution of the radiation pressure of the field only on the end mirror, whereas the beam splitter is considered as at rest. The length of the two arms is identified with ℓ and the displacement of the two test masses respect to their rest position is defined respectively with z_1 and z_2. The interference signal between the beams in the two arms is measured with a photodetector placed in front of the BS output port. This signal contains the information about the relative phase of the light in the two arms. It is given by $\Delta\phi = 2kz$ where k is the wave vector. A gravitational wave that pass through the interferometer plane induced a phase shift $\Delta\phi$. Its measured value is not an instantaneous value but it is an average during the time that the light is stored in each arm of the interferometer $\tau_s = 2\ell c$. Therefore τ_s is linked with the temporal resolution of the instrument. Using the quantum mechanical formalism introduced in this chapter, one will see that the precision of a measurement of z is limited by the Heisenberg uncertainity principle and in particular the two quantum

mechanical noise sources are the fluctuations of the radiation pressure on the mirrors and the fluctuations of the number of photons at the BS output port. Now these two contributions are separately analyzed and their total effect is obtained with a square sum of them [20].

2.8.1 Radiation pressure

In a Michelson interferometer, the contribution to the radiation pressure due to the light emitted by the laser is zero, but it is also possible to observe that its sensitivity at low frequency is limited by the radiation pressure noise. In 1980, Caves shows that this contribution is due to the fluctuations of the vacuum field that enters in the interferometer from the unused BS port [31]. These fluctuations interferes with the laser light. Their contribution to the interferometer sensitivity is obtained by computing the momentum transferred to the test masses m, that are assumed initially at rest in order to neglect the Doppler effect on the reflected light. Then, to compute the perturbation of z this assumption must be clear and the masses can move again. The transferred momentum is computed starting from the beam splitter matrix (see Eq. 2.25). If the beam splitter ratio is 50/50 ts two output fields are:

$$\hat{c} = \frac{1}{\sqrt{2}}\left(\hat{a} + \hat{b}\right) \qquad \hat{d} = \frac{1}{\sqrt{2}}\left(-\hat{a} + \hat{b}\right).$$

Each photon, that reaches one of the two end mirrors, transfers to it a momentum equal to $|p| = 2\hbar\omega/c$. The difference between the momenta transferred to the end masses is proportional to the difference between the number of photons in the field $\hat{c}$ and $\hat{d}$. The total transferred momentum is equal to:

$$\mathcal{P} = \frac{2\hbar\omega}{c}\left(\hat{d}^\dagger\hat{d} - \hat{c}^\dagger\hat{c}\right);$$

it can be rewritten in term of the two input fields of the beam splitter:

$$\mathcal{P} = -\frac{2\hbar\omega}{c}\left(\hat{a}^\dagger\hat{b} + \hat{b}^\dagger\hat{a}\right).$$

Even if the mode $\hat{a}$ is a coherent state of the interferometer laser and the mode $\hat{b}$ is a vacuum state, in this analysis the mode $\hat{b}$ is treated as a squeezed vacuum state because this leads to a more general result. The light mode in the interferometer is:

$$|\psi\rangle = \hat{S}_b(r,\vartheta)\hat{D}_a(\alpha)\,|0\rangle\,. \tag{2.28}$$

From the properties of choerent and squeezed states it follows that:

$$\langle\psi|\,\mathcal{P}\,|\psi\rangle = 0 \qquad \text{and} \qquad <(\Delta\mathcal{P})^2> = \left(\frac{2\hbar\omega}{c}\right)^2(\alpha^2 e^{2r} + \sinh^2(r)).$$

Therefore if a measurement requires a time τ the disturbance due to the radiation pressure noise on the relative position of the test masses is given by:

$$(\Delta z)_{rp} = \frac{\sqrt{<(\Delta \mathcal{P})^2>}}{2m}\tau = \left(\frac{\hbar\omega\tau}{mc}\right)\sqrt{\alpha^2 e^{2r} + \sinh^2(r)}. \tag{2.29}$$

With this result it is possible to understand both the effect of the fluctuations of the vacuum field that enter in the interfermeter and their suppression by replacing them with squeezed states. The radiation pressure noise contribution is obtained by substituting r=0 in Eq. 2.29. Otherwise, when $r \neq 0$, the term $\alpha^2 e^{2r}$ expresses the effect of the replacement of the vacuum state with a squeezed vacuum state: if the amplitude quadrature is squeezed the radiation pressure noise is suppressed whereas if the phase quadrature is squeezed the radiation pressure fluctuations are enhanced.

2.8.2 Shot noise

The second contribution is due to the fluctuations of the number of photons that reach the photodetector. As for the radiation pressure, the analysis starts form the beam splitter, but now the two input fields are the reflected beams by the end mirrors. The two output fields can be written in term of the beam fields in its arms [32]:

$$\begin{bmatrix} \hat{f} \\ \hat{e} \end{bmatrix} = e^{\imath\Phi} \begin{bmatrix} \cos(\Delta\phi/2) & \imath\sin(\Delta\phi/2) \\ \imath\sin(\Delta\phi/2) & \cos(\Delta\phi/2) \end{bmatrix} \times \begin{bmatrix} \hat{h} \\ \hat{g} \end{bmatrix}, \tag{2.30}$$

where $\Delta\phi$ is the phase difference between the light from the two arms and Φ is the average phase:

$$\Delta\phi = \left[\pi + 2\frac{\omega z}{c}\right] \qquad \text{and} \qquad \Phi = \frac{2\omega}{c}(z_1 + z_2) + const.$$

If the two fields are detected with two different photodiodes the difference of their photons number can be expressed as:

$$\hat{n} = \left[\hat{h}^\dagger\hat{h} - \hat{g}^\dagger\hat{g}\right] = \left[\hat{f}^\dagger\hat{f} - \hat{e}^\dagger\hat{e}\right]\cos(\Delta\phi) + \imath\left[\hat{f}^\dagger\hat{f} - \hat{e}^\dagger\hat{e}\right]\sin(\Delta\phi).$$

The circulating field inside the interferometer is defined in Eq. 2.28 as in the previous case. The mean value and the variance of the operator $\hat{n}$ can be computed as [20]:

$$\begin{aligned} <\hat{n}> &= \left[\alpha^2 - \sinh^2(r)\right]\cos(\Delta\phi) \\ <(\Delta\hat{n})^2> &= \left[\alpha^2 + 2\cosh^2(r)\sinh^2(r)\right]\cos^2(\Delta\phi) + \left[\alpha^2 e^{-2r} + \sinh^2(r)\right]\sin^2(\Delta\phi) \end{aligned}$$

From the first result we obtain that a small variation of the relative position of the two test masses δz causes a small variation of the photon number $\delta\hat{n}$ that is given by:

$$\delta\hat{n} \approx -\frac{2\omega}{c}\sin(\Delta\phi)\delta z,$$

where we have assumed $\alpha^2 \gg \sinh^2(r)$ that is always true for the squeezed vacuum state injected in an interferometer for the gravitational waves detection. Finally the net effect of the photon number fluctuations can be rewritten as a disturbance of the relative position z of the mirrors:

$$(\Delta z)_{sn} \approx \frac{c}{2\omega}\sqrt{\left[\frac{\cot^2(\Delta\phi)}{\alpha^2} + \frac{2\cot^2(\Delta\phi)\cosh^2(r)\sinh^2(r)}{\alpha^4} + \frac{e^{-2r}}{\alpha^2} + \frac{\sinh^2(r)}{\alpha^2}\right]}.$$

The value of $\Delta\phi$ depends on the relative position between the two photodiodes, therefore it is chosen such that $\cot(\Delta\phi) = 0$ and the last expression becomes:

$$(\Delta z)_{sn} \approx \frac{c}{2\omega\alpha^2}\sqrt{\left[\alpha^2 e^{-2r} + \sinh^2(r)\right]}. \tag{2.31}$$

As in the radiation pressure case, by substituting $r = 0$ Eq. 2.31 shows the effect of the fluctuations of a coherent vacuum state that enters in the unused interferometer port. Moreover for $r \neq 0$ the term $\alpha^2 e^{-2r}$ express the effect of the replacement of the vacuum state with a squeezed vacuum state. If the amplitude quadrature is squeezed, the shot noise is enhanced ,whereas if the phase quadrature is squeezed the shot noise fluctuations are depleted.

With this quantum mechanical treatment of an interferometer it is understood that the quantum noises, i.e. radiation pressure noise and shot noise, are induced by electromagnetic vacuum fluctuations that enter in the detector from its dark port. In addition, by injecting a squeezed quadrature, one of these two noises can be depleted, whereas the other increased. The next chapter briefly introduces non linear optics and shows how squeezed light is generated by using non linear cavities.

Chapter 3

A small compendium of non linear optics

The nonlinear optics is the field of optics that studies the behaviour of the light in nonlinear medium. A medium is called nonlinear when its response to an applied optical field depends in a nonlinear manner on its strength [33]. In a nonlinear medium the polarization vector $\vec{P}$ responds to the incident electrical field $\vec{E}(t)$ as follows:

$$\begin{aligned} P(t) &= \epsilon_0 \left[\chi^{(1)} E(t) + \chi^{(2)} E^2(t) + \chi^{(3)} E^3(t) + \dots \right] \\ &= P^{(1)}(t) + P^{(2)}(t) + P^{(3)}(t) + \dots, \end{aligned} \tag{3.1}$$

where ϵ_0 is the permittivity of the vacuum and $\chi^{(n)}$ is the n-th order optical susceptibility. In "standard" linear optics the susceptibility $\chi^{(n)}$ with $n > 1$ are negligible and the polarization vector depends linearly to the incident field strength. Eq. 3.1 assumes that:

- the polarization vector and the electric field are scalar quantities;
- the nonlinear medium is lossless and dispersionless, thus the polarization vector at time t depends only on the instantaneous value of the electric field;
- the susceptibility does not depend on the frequency of the input field.

The work in this thesis, i.e. the development of the Virgo squeezer is based only on second order nonlinear processes therefore this chapter is focused on them. In a second order nonlinear process, Eq. 3.1 becomes:

$$P(t) = \epsilon_0 \chi^{(2)} E^2(t). \tag{3.2}$$

In a material with a strong second order nonlinear susceptibility, the typical range of $\chi^{(2)}$ is $\times 10^{-13} \div 10^{-9} \mathrm{m\,V^{-1}}$.

3.1 Classical description of second order nonlinear processes

This section describes in an intuitive manner all the second order nonlinear processes. Let us consider an electric field, oscillating at two different frequencies, incident on a second order nonlinear medium:

$$E(t) = E_1 e^{-\imath\omega_1 t} + E_1^* e^{\imath\omega_1 t} + E_2 e^{-\imath\omega_2 t} + E_2^* e^{\imath\omega_2 t}. \tag{3.3}$$

The polarization vector is given by Eq. 3.2:

$$\begin{aligned} P(t) = {} & 2\epsilon_0\chi^{(2)}\left[|E_1|^2 + |E_2|^2\right] && \text{(OR)} \\ & + \epsilon_0\chi^{(2)}\left[E_1^2 e^{-2\imath\omega_1 t} + E_1^{2^*} e^{2\imath\omega_1 t}\right] && \text{(SHG)} \\ & + \epsilon_0\chi^{(2)}\left[E_2^2 e^{-2\imath\omega_2 t} + E_2^{2^*} e^{2\imath\omega_2 t}\right] && \text{(SHG)} \\ & + 2\epsilon_0\chi^{(2)}\left[E_1 E_2 e^{-\imath(\omega_1+\omega_2)t + E_1^* E_2^* e^{\imath(\omega_1+\omega_2)t}}\right] && \text{(SFG)} \\ & + 2\epsilon_0\chi^{(2)}\left[E_1^* E_2 e^{-\imath(\omega_1-\omega_2)t} + E_1^* E_2 e^{\imath(\omega_1-\omega_2)t}\right] && \text{(DFG)} \end{aligned} \tag{3.4}$$

where each term is labelled with the name of the physical process that it describes: the optical rectification (OR), the second harmonic generation (SHG), the sum frequency generation (SFG) and the difference frequency generation (DFG). Therefore each second order nonlinear process should generate four components at difference frequency; however no more than one of these phenomenon has a non negligible amplitude. Sec. 3.1.4 will explain that a non linear medium shows a non-negligible conversion efficiency only if certain phase-matching conditions are satisfied and usually this happens for one kind of nonlinear process. The Virgo squeezer is based on two of these nonlinear processes: the second harmonic generation (SHG) and a special class of the difference frequency generation, i.e. the optical parametric oscillation (OPO).

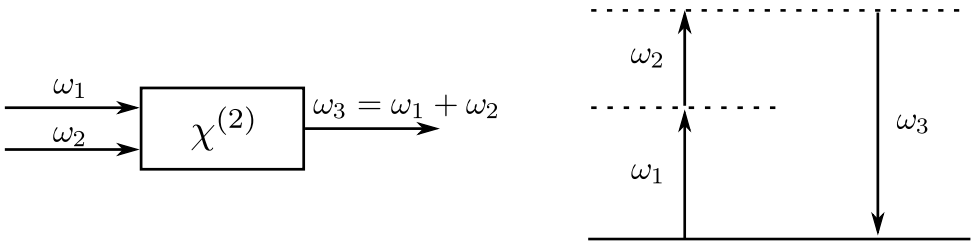

Figure 3.1: Sum frequency generation. Left: geometry of the interaction. Right: energy level scheme of the process.

Fig. 3.1 shows a scheme of the Sum Frequency Generation (SFG) process: the two input fields are oscillating respectively at frequency ω_1 and ω_2. Due to the nonlinear

interaction, each atom of the medium has an oscillating dipole moment that contains also the component $\omega_3 = \omega_1 + \omega_2$. Therefore each of them radiate an electric field oscillating at this frequency. The nonlinear material contains N atoms oscillating at the same frequency but the phase of the emitted radiation depends on the one of the input fields. If a particular condition is satisfied all the dipole radiations interfere constructively. Thus the electric field strength of the emitted radiation will be N time larger than the one generated by a single atom. This condition is called *phase matching*.

This chapter is structured as follows: Sec. 3.1.1 shows the wave equations in a nonlinear medium; Sec. 3.1.2 shows the coupled wave equations in the SFG and SHG processes; Sec. 3.1.3 and Sec. 3.1.4 explains the phase matching condition; Sec. 3.1.5 explains the quasi-phase matching condition; Sec. 3.1.6 describes the DFG and the OPO processes and how squeezed light can be generated by OPO process; finally Sec. 3.2 shows the behaviour of non linear cavities under a quantum mechanical point of view.

3.1.1 Waves equation in non linear medium

The Maxwell equation in presence of matter are:

$$\begin{aligned} \vec{\nabla} \cdot \vec{D} &= \rho & \vec{\nabla} \times \vec{E} + \frac{\partial \vec{B}}{\partial t} &= 0 \\ \vec{\nabla} \cdot \vec{B} &= 0 & \vec{\nabla} \times \vec{B} - \frac{\partial \vec{D}}{\partial t} &= \vec{J} \quad . \end{aligned} \tag{3.5}$$

This chapter treats only the solutions of Eq. 3.5 in regions of space without free charge and free currents: $\vec{J} = 0$ and $\rho = 0$ and the medium is assumed as non magnetic, i.e. $\vec{B} = \mu_0 \vec{H}$. The nonlinear effect is described by the polarization vector $\vec{P}$ that is related to the electric displacement vector $\vec{D}$ as follows:

$$\vec{D} = \epsilon_0 \vec{E} + \vec{P} = \underbrace{\epsilon_0 \vec{E} + \vec{P}^{(1)}}_{\vec{D}^{(1)}} + \vec{P}^{(NL)} = \vec{D}^{(1)} + \vec{P}^{(NL)}$$

Considering the medium as isotropic, from Eq. 3.5 the wave equation is obtained:

$$\nabla^2 \vec{E} - \frac{\epsilon^{(1)}}{c^2} \frac{\partial^2 \vec{E}}{\partial t^2} = \frac{1}{\epsilon_0 c^2} \frac{\partial^2 \vec{P^{(NL)}}}{\partial t^2} \tag{3.6}$$

where $\epsilon^{(1)}$ is the dielectric constant of the medium that is related to the refraction index by $n = \sqrt{\epsilon^{(1)}}$. Eq. 3.6, with the term in the right-hand side, differs from the wave equations in vacuum (see Eq. 2.2). This term is the non linear response of the medium and acts as a source term.

3.1.2 The coupled wave equation for SFG

Let assume two collimated, monochromatic, continuous plane wave input beams propagating along the z-direction that are normally incident on the surface of a non-linear medium (see Fig. 3.1). The two fields are oscillating respectively at frequency ω_1 and ω_2:

$$\begin{aligned} E_1(z,t) &= A_1 e^{\imath(k_1 z-\omega_1 t)} + A_1^* e^{-\imath(k_1 z-\omega_1 t)} \\ E_2(z,t) &= A_2 e^{\imath(k_2 z-\omega_1 t)} + A_2^* e^{-\imath(k_2 z-\omega_2 t)}. \end{aligned} \tag{3.7}$$

The nonlinear interaction generates the sum frequency component at $\omega_3 = \omega_1 + \omega_2$ that is a solution of Eq. 3.6:

$$E_3(z,t) = A_3(z) e^{\imath(k_3 z-\omega t)} + A_3^*(z) e^{-\imath(k_3 z-\omega t)} \tag{3.8}$$

where

$$k_3 = \frac{n_3\omega_3}{c} \qquad \text{and} \qquad n_3 = \sqrt{\epsilon^{(1)}(\omega_3)}.$$

The amplitude of the nonlinear polarization can be written as [33]:

$$P_3(z,t) = P_3 e^{\imath\omega_3 t} + P_3^* e^{-\imath\omega_3 t} \quad \text{where} \quad P_3 = 2\epsilon_0 \chi^{(2)} A_1 A_2 e^{\imath(k_1+k_2)z} \tag{3.9}$$

and its effect on $E_3(z,t)$ is that its amplitude $A_3(z)$ is a slow varying function of z. Substituting Eq. 3.7, Eq. 3.8 and Eq. 3.9 in the wave equations Eq. 3.6 and assuming that the field amplitudes varies slowly, a set of couple equations, that describe the spatial dependence of the field amplitudes A_i, is find [33]:

$$\begin{aligned} \frac{dA_1}{dz} &= \frac{\imath\chi^{(2)}\omega_1^2}{k_1 c^2} A_3 A_2^* e^{-\imath\Delta k z} \\ \frac{dA_2}{dz} &= \frac{\imath\chi^{(2)}\omega_2^2}{k_2 c^2} A_3 A_1^* e^{-\imath\Delta k z} \\ \frac{dA_3}{dz} &= \frac{\imath\chi^{(2)}\omega_3^2}{k_3 c^2} A_1 A_2 e^{-\imath\Delta k z}, \end{aligned} \tag{3.10}$$

where the quantity Δk is called *phase mismatch*:

$$\Delta k = k_1 + k_2 - k_3 \tag{3.11}$$

3.1.3 Means of the phase mismatch

Let us consider the special case, called *weak conversion*, in which the amplitude of the two incident fields E_1 and E_2 are not depleted during the non-linear conversion. The amplitude of the sum-frequency field, at the exit of the non linear medium, is equal to:

$$A_3(L) = \frac{\imath\chi^{(2)}\omega_3^2 A_1 A_2}{k_3 c^2} \int_0^L e^{\imath\Delta k z}\, dz = \frac{\imath\chi^{(2)}\omega_3^2 A_1 A_2}{k_3 c^2} \left(\frac{e^{\imath\Delta k L} - 1}{\imath\Delta k} \right), \tag{3.12}$$

where the length of the crystal is equal to L and it starts at the position $z = 0$. The intensity of the sum-frequency field is obtained from the magnitude of the time-averaged Poynting vector:

$$I_3 = 2n_3\epsilon_0 c|A_3|^2 = \frac{4n_3\epsilon_0\chi^{(2)^2}\omega_3^4|A_1|^2|A_2|^2}{k^2c^3}L^2\mathrm{sinc}^2\left(\frac{\Delta kL}{2}\right). \tag{3.13}$$

Fig. 3.2 shows how the efficiency of the three wave mixing process decreases when

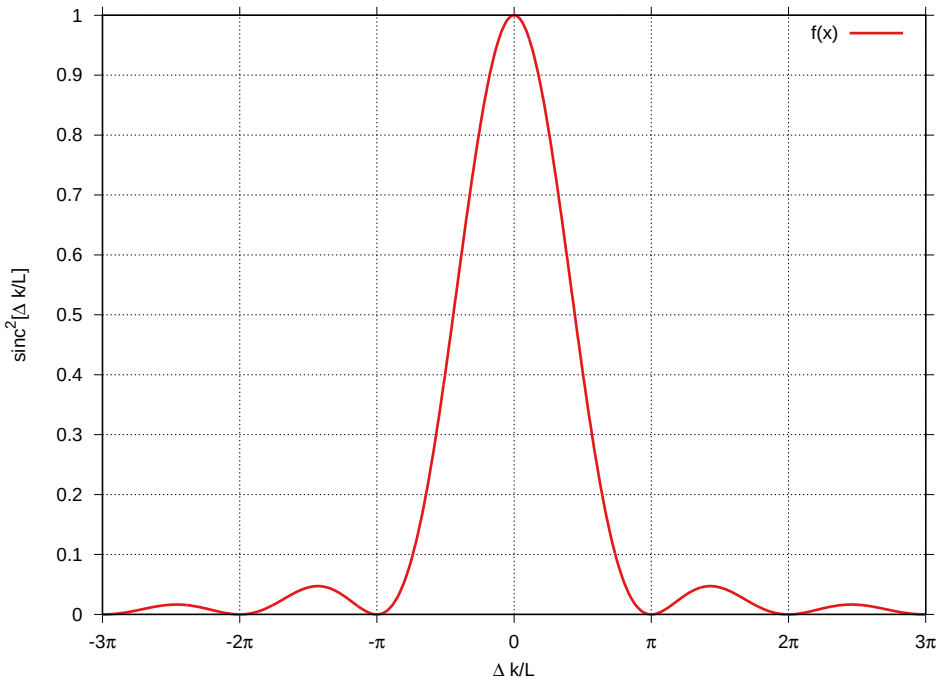

Figure 3.2: Effects of wavevector mismatch on the efficiency of SFG process.

$\Delta k/L$ increases and has a maximum when $\Delta k = 0$. This condition is satisfied only if each the dipole that constitutes the non linear medium generates an electric field that sum coherently with the field generated by the other dipoles.

Second Harmonic Generation

The second harmonic generation is a particular SFG process where: the two input fields oscillate at the same frequency $\omega_1 = \omega_2 = \omega$ and the generated field oscillates at frequency 2ω.

3.1.4 Phase matching

The phase matching condition holds for all the nonlinear optical processes and can be expressed as follows:

$$0 = \Delta k = \frac{n(\omega_1)\omega_1}{c} + \frac{n(\omega_2)\omega_2}{c} - \frac{n(\omega_3)\omega_1}{c}. \tag{3.14}$$

In the SHG process Eq. 3.14 can be simplified as follows:

$$n(\omega) = n(2\omega).$$

This condition can not be satisfied because the refractive index of a lossless material is a monotonically increasing function of the frequency.

The most elegant solution for this problem exploits the birefringent behaviour of many crystals. The birefringence is a property of materials in which the refraction index depends on the direction of the polarization of the applied electric field. The simplest type of birefringent medium are *uniaxial materials* that are characterized by a crystal axis, i.e. a single direction governing the optical anisotropies, whereas all the perpendicular directions are equivalent. Light whose polarization is perpendicular to the optic axis is governed by the *ordinary refractive index*, whereas light whose polarization is parallel to the optical axis is governed by the *extraordinary refractive index*. In SFG process the phase matching condition can be obtained when the highest frequency wave (ω_3) is polarized in the direction governed by the lowest of the two refraction indices.

There are two possible choices for the incident field polarizations:

- **Type I phase matching:** the two input fields at frequency ω_1 and ω_2 have the same polarization, whereas the generated field at frequency ω_3 is orthogonally polarized;

- **Type II phase matching:** the two input fields at frequency ω_1 and ω_2 have orthogonal polarization and the generated field has the same polarization of one of them.

Exploiting the birefringence, tipically the phase matching condition can be achieved with two different techniques: the angular tuning and the temperature tuning. The first method consists in a precise angular orientation of the crystal axis with respect to the propagation direction of the incident light; the second is a fine tuning of the two refraction indices of the material that exploits their temperature dependence.

3.1.5 Quasi phase matching

The quasi phase matching is a kind of phase matching obtained exploiting a periodically poled material. The periodically poling is a structure in which the orientation of the crystal axis is inverted periodically as a function of the position within the material (see Fig. 3.3). An inversion of the crystal axis causes an inversion of the sign of

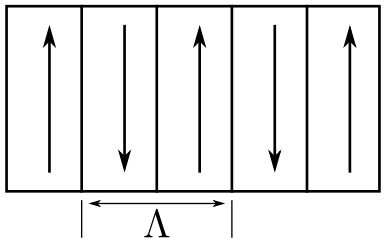

Figure 3.3: Schematic representation of a periodically poled material. Its crystal axis alternates in orientation with period Λ.

the non linear coupling coefficient $\chi^{(2)}/2$. If the poling period is equal to Λ the non linear coupling coefficient is given by:

$$d(z) = \frac{\chi^{(2)}}{2}\text{sign}\left(\frac{2\pi}{\Lambda}z\right).$$

When the nonlinear medium is a periodically poled material, the phase matching condition can be rewritten as [33]:

$$\Delta K_{qpm} = k_1 + k_2 - k_3 + \frac{2\pi}{\Lambda};$$

therefore the optimal poling period becomes:

$$\Lambda = \frac{2\pi}{k_1 + k_2 - k_2}.$$

3.1.6 Difference frequency generation

Fig. 3.4 is a scheme of difference frequency generation process. This process seems similar to SFG, but the comparison of the two energy level diagrams (right part of Fig. 3.1 and Fig. 3.4) evinces an important difference in the two phenomena.

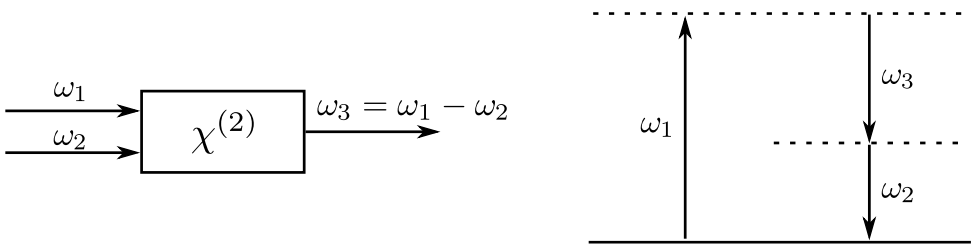

Figure 3.4: Difference frequency generation. Left: geometry of the interaction. Right: energy level scheme of the process

In the SFG process the two photons of frequency ω_1 and ω_2 are destroied and a photon at frequency $\omega_1 + \omega_2$ is simultaneously crated. However, in DFG process for every photon created at frequency $\omega_3 = \omega_1 - \omega_2$, a photon at ω_1 is annihilated and

an additional one at frequency ω_2 is created. Therefore the field at frequency ω_2 is amplified by this process that is also known as *optical parametric amplification*.

This phenomenon is described mathematically starting from the coupled equations in nonlinear medium. Let us consider that the ω_1 field is not depleted by the DFG process, so the coupled equations are obtained by a method similar to the one used in Sec. 3.1.2:

$$\begin{aligned} \frac{dA_2}{dz} &= \frac{\imath\chi^{(2)}\omega_2^2}{k_2c^2}A_1A_3^*e^{-\imath\Delta kz} \\ \frac{dA_3}{dz} &= \frac{\imath\chi^{(2)}\omega_3^2}{k_3c^2}A_1A_2^*e^{-\imath\Delta kz}, \end{aligned} \tag{3.15}$$

where the phase mismatch is defined as $\Delta k = k_1 - k_2 - k_3$. In the perfect phase matching condition the solution of the two equations become [33]:

$$\begin{aligned} A_2(z) &= A_2(0)\cosh(\sigma z) \\ A_3(z) &= \imath\left(\frac{n_2\omega_3}{n_3\omega_2}\right)\frac{A_1}{|A_1|}A_2^*(0)\sinh(\sigma z) \\ \sigma &= \frac{2\chi^{(2)^2}\omega_2^2\omega_3^2}{k_2k_3c^4}|A_1|^2. \end{aligned} \tag{3.16}$$

Fig. 3.5 shows the amplitude of the two solution as function of z: both the two field experience a monotonic growth as expected.

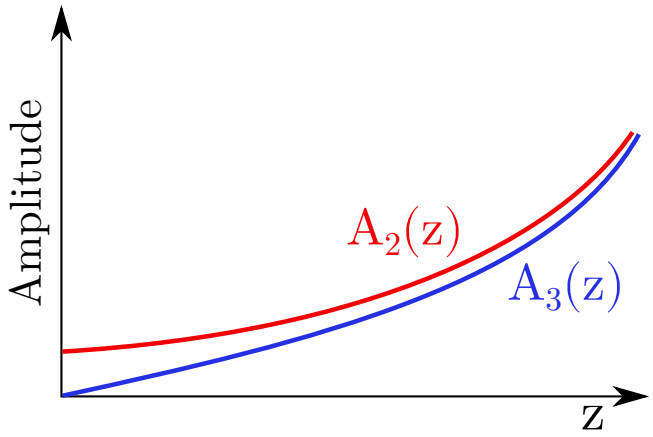

Figure 3.5: Spatial evolution of field amplitudes $A_2(z)$ and $A_3(z)$ in the DFG process, where the system is considered in the phase matching condition and in the constant pump approximation.

OPO and squeezing generation - semiclassical point of view

Let us consider again the DFG phenomenon, but with the non linear crystal placed in an optical cavity. This kind of device is called *Optical Parametric Oscillator* (OPO). In this device the length of the interaction increases, so an higher

amplification factor can be reached. One application of this device is the generation of frequency tunable laser light. In addition, this process leads to the coupling between the quantum noise of the two field quadratures, thus it can be used to generates squeezed light states. In the following it is shown how the two quadtatures are coupled by this process.

In an optical parametric oscillator conventionally the ω_1 field is called pump ω_p, the amplified field ω_2 is called signal ω_s and the difference frequency field ω_3 is called idler ω_i. Let us consider a degenerate optical parametric oscillator in which the frequency of the signal and the idler is the same $\omega_s = \omega_i = \omega$. This condition is obtained only when the pump frequency is twice the signal frequency. The frequency difference amplitude A_ω is rewritten as:

$$\frac{dA_s}{dz} = \imath g A_p A_i^* e^{\imath \Delta k z} \qquad \text{where} \qquad g = \frac{\chi^{(2)} \omega_s}{k_s c^2}.$$

Since the signal and the idler are indistinguishable the amplitude of the ω field and its complex conjugate can be simplified as:

$$\frac{dA_\omega}{dz} = \imath g A_p A_\omega^* \qquad\qquad \frac{dA_\omega^*}{dz} = -\imath g A_p^* A_\omega, \tag{3.17}$$

where a perfect phase matching condition $\Delta k = 0$ and a lossless medium ($g \in \mathbb{R}$) are considered. In the "parametric approximation" the pump is in a coherent state with large amplitude and is not depleted by the DFG process. Therefore the pump amplitude is rewritten as: $\beta e^{\imath\varphi}$, where β is a real number and φ is the relative phase between the pump and the signal field. Eq. 3.17 becomes:

$$\frac{dA_\omega}{dz} = \imath g \beta A_\omega^* e^{\imath\varphi} := \gamma A_\omega^* e^{\imath(\varphi+\pi/2)} \qquad\qquad \frac{dA_\omega^*}{dz} = -\imath g \beta A_\omega e^{-\imath\varphi} := \gamma A_\omega e^{-\imath(\varphi-\pi/2)} \tag{3.18}$$

Using simple algebra from Eq. 3.18 it follows that:

$$\begin{aligned} \frac{1}{2}\frac{d}{dz}\left(A_\omega + A_\omega^*\right) &= \frac{\gamma}{2}\left(A_\omega e^{-\imath(\varphi+\pi/2)} + A_\omega^* e^{\imath(\varphi+\pi/2)}\right) \\ \frac{1}{2\imath}\frac{d}{dz}\left(A_\omega - A_\omega^*\right) &= \frac{\gamma}{2}\left(A_\omega e^{-\imath\varphi} + A_\omega^* e^{\imath\varphi}\right) \end{aligned} \tag{3.19}$$

Chap. 2 shows that in the second quantization formalism the real part and the complex part of the electric field amplitude can be respectively transposed in the annihilation and in the creation operators. Therefore, using the quantum formalism, Eq. 3.19 can be rewritten as:

$$\begin{aligned} \frac{d\hat{X}_1}{dz} &= \frac{\gamma}{2}\left(\hat{a}_\omega e^{-\imath(\varphi+\pi/2)} + \hat{a}_\omega^\dagger e^{\imath(\varphi+\pi/2)}\right) = \gamma \hat{X}_{\varphi+\pi/2} \\ \frac{d\hat{X}_2}{dz} &= \frac{\gamma}{2}\left(\hat{a}_\omega e^{-\imath\varphi} + \hat{a}_\omega^\dagger e^{\imath\varphi}\right) = \gamma \hat{X}_\varphi, \end{aligned}$$

where $\hat{X}_\varphi$ is a quadrature operator rotated by an angle φ with respect to the $\hat{X}_1$, $\hat{X}_2$ plane. For simplicity the angle φ is fixed equal to $\pi/2$, thus:

$$\begin{aligned} \frac{d\hat{X}_1}{dz} &= -\gamma \hat{X}_1 \qquad \Rightarrow \qquad \hat{X}_1 = \hat{X}_1(0)e^{-\gamma z} \\ \frac{d\hat{X}_2}{dz} &= +\gamma \hat{X}_2 \qquad \Rightarrow \qquad \hat{X}_2 = \hat{X}_2(0)e^{+\gamma z}. \end{aligned} \tag{3.20}$$

This result shows that the non linear process amplifies one of the two quadrature whereas the other is suppressed by the same factor. This means that a degenerate optical parametric oscillator can be used for the squeezed light generation [26].

OPO and squeezing generation - quantum point of view

The nonlinear interaction in an optical parametric oscillator is described by the following Hamiltonian:

$$\hat{H} = \hbar\omega_a \hat{a}^\dagger \hat{a} + \hbar\omega_b \hat{b}^\dagger \hat{b} + \imath\hbar\chi^{(2)} \left(\hat{a}^2 \hat{b}^\dagger - \hat{a}^{\dagger 2} \hat{b} \right), \tag{3.21}$$

where $\hat{a}$ is the mode of the signal field, and $\hat{b}$ refers to the pump field [27]. In the parametric approximation, the pump field is not depleted by the process and the operator $\hat{b}$ can be replaced by $\beta e^{-\imath 2\omega t}$, where ω is the frequency of the signal/idler field. The time evolution of the operator $\hat{a}$ can be represented as $\hat{a} \to \hat{a}e^{\imath\omega t}$, thus the Hamiltonian of the system becomes time independent [27].

$$\hat{H} = \imath\hbar\chi^{(2)} \left(\beta^* \hat{a}^2 + \beta \hat{a}^{\dagger 2} \right).$$

Its associated time evolution operator is:

$$\hat{U}(t,0) = \exp\left(-\frac{\imath\hat{H}t}{\hbar} \right) = \exp\left(\chi^{(2)}\beta^* \hat{a}^2 t - \chi^{(2)}\beta \hat{a}^{\dagger 2} t \right)$$

that has the same form of the squeezing operator, see Eq. 2.21. Therefore the signal field of an optical parametric oscillator is a squeezed state.

3.2 Quantum description of non linear cavities

An optical cavity is an arrangement of partially transmissive mirrors that allow to an optical beam to circulate in a closed path. This section summarizes the Langevin approach to derive the motion equation of a nonlinear optical cavity. The used formalism is developed by Gardiner and Collet in [34]. Fig. 3.6 shows the model of a nonlinear ring optical cavity including all the fields and the coupling constants. This model can be easily extended to a linear cavity. The various optical fields are:

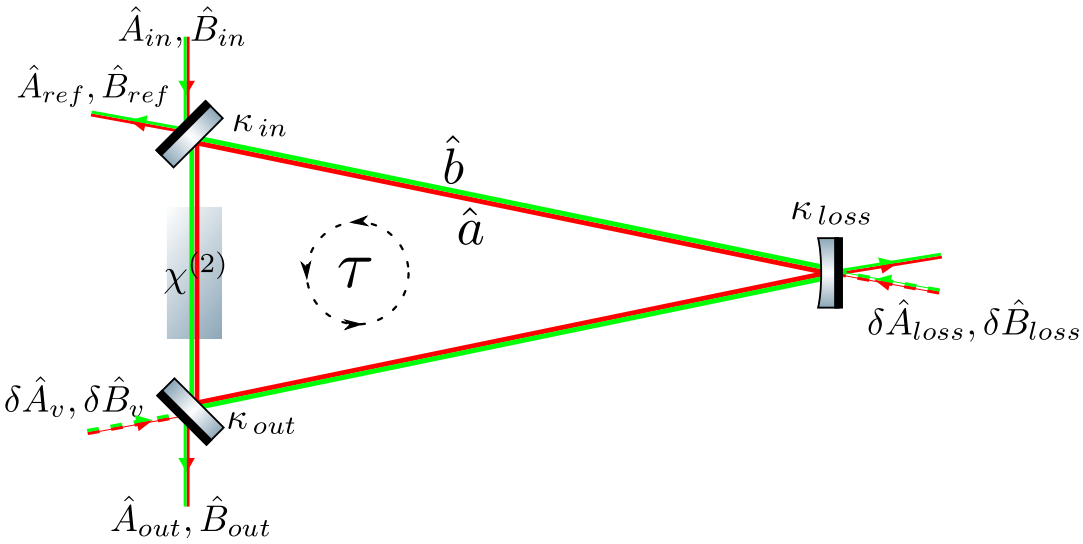

Figure 3.6: A nonlinear triangular optical cavity with various input and output fields.

- the cavity mode $\hat{a}$;
- $\hat{A}_{in}$ and $\hat{B}_{in}$ the the fundamental and the harmonic input field to the cavity;
- $\hat{A}_{out}$ and $\hat{B}_{out}$ the fundamental and the harmonic output field from the cavity;
- $\delta\hat{A}_{loss}$ and $\delta\hat{B}_{loss}$ the fundamental and the harmonic vacuum-modes coupled in by intra-cavity losses;
- $\delta\hat{A}_v$ and $\delta\hat{B}_v$ the fundamental and the harmonic vacuum modes at the output mirror;
- $\hat{a}$ and $\hat{b}$ the fundamental and the harmonic cavity modes.

The connection between the intracavity field and the input/output field is modelled with the coupling rates κ_j where:

- κ^a_{in} and κ^b_{in} are the coupling rates through the input mirror;
- κ^a_{out} and κ^b_{out} are the coupling rates through the output mirror;
- κ^a_{loss} and κ^b_{loss} are the coupling rates for the intracavity losses.

Each coupling term is the ratio between the transmittivity of the mirror t_j and the round trip time τ of the light in the cavity: $\tau = \mathrm{OPL}/c$ where OPL is the round trip optical path length. Using the formalism introduced by Gardiner and Collett the

quantum Langevin equation of motion for a cavity modes are:

$$\begin{aligned}\dot{\hat{a}} &= -(\kappa^a + \imath\omega_c^a)\hat{a} + \epsilon\hat{a}^\dagger\hat{b} + \sqrt{2\kappa_{in}^a}\hat{A}_{in}e^{-\imath\omega_A t} + \sqrt{2\kappa_{out}^b}\delta\hat{A}_v + \sqrt{2\kappa_{loss}^b}\delta\hat{A}_{loss} \\ \dot{\hat{b}} &= -(\kappa^b + \imath\omega_c^b)\hat{b} - \frac{\epsilon}{2}\hat{a}^2 + \sqrt{2\kappa_{in}^b}\hat{B}_{in}e^{-\imath\omega_B t} + \sqrt{2\kappa_{out}^b}\delta\hat{B}_v + \sqrt{2\kappa_{loss}^b}\delta\hat{B}_{loss}\end{aligned} \tag{3.22}$$

where ω_A and ω_B are respectively the frequency of the field $\hat{A}_{in}$ and $\hat{B}_{in}$; ω_c^a and ω_c^b are the cavity resonant frequencies related to the two input fields, κ^a and κ^b are the total cavity damping rate given by $\kappa = \kappa_{in} + \kappa_{out} + \kappa_{loss}$ and ϵ is the nonlinear coupling coefficient. In a rotating frame with the input field, Eq. 3.22 is rewritten as:

$$\begin{aligned}\dot{\hat{a}} &= -(\kappa^a + \imath(\omega_c^a - \omega_A))\hat{a} + \epsilon\hat{a}^\dagger\hat{b} + \sqrt{2\kappa_{in}^a}\hat{A}_{in} + \sqrt{2\kappa_{out}^b}\delta\hat{A}_v + \sqrt{2\kappa_{loss}^b}\delta\hat{A}_{loss} \\ \dot{\hat{b}} &= -(\kappa^b + \imath(\omega_c^b - \omega_B))\hat{b} - \frac{\epsilon}{2}\hat{a}^2 + \sqrt{2\kappa_{in}^b}\hat{B}_{in} + \sqrt{2\kappa_{out}^b}\delta\hat{B}_v + \sqrt{2\kappa_{loss}^b}\delta\hat{B}_{loss}.\end{aligned} \tag{3.23}$$

Eq. 3.23 shows that the motion equation of the harmonic and the fundamental field are coupled between them by means of the term containing ϵ, i.e. the nonlinear coupling coefficient. These expressions can be simplified if the cavity is held on resonance: $\omega_c^a = \omega_A$ and $\omega_c^b = \omega_B$. In the parametric approximation the term $\frac{\epsilon}{2}\hat{a}^2$ is assumed equal to zero, i.e. the pump harmonic field is not depleted during the nonlinear process. Eq. 3.23 becomes:

$$\begin{aligned}\dot{\hat{a}} &= -\kappa^a\hat{a} + \epsilon\hat{a}^\dagger\hat{b} + \sqrt{2\kappa_{in}^a}\hat{A}_{in} + \sqrt{2\kappa_{out}^b}\delta\hat{A}_v + \sqrt{2\kappa_{loss}^b}\delta\hat{A}_{loss} \\ \dot{\hat{b}} &= -\kappa^b\hat{b} + \sqrt{2\kappa_{in}^b}\hat{B}_{in} + \sqrt{2\kappa_{out}^b}\delta\hat{B}_v + \sqrt{2\kappa_{loss}^b}\delta\hat{B}_{loss}.\end{aligned} \tag{3.24}$$

In the following the Optical Parametric Oscillator (OPO) process is treated with a classical and a semiclassical model, where in both the pump field $\hat{b}$ is assumed as a classical field: $\hat{b} \to \beta$. The combination between this field and the nonlinearity term ϵ is called *total nonlinear gain* $g = \beta\epsilon$.

3.2.1 Classical behaviour of OPO cavity

In the classical world ,the fluctuations are neglected and the intracavity field is a steady state is:

$$\dot{\hat{a}} = 0 \qquad \text{and} \qquad < \hat{a} >= \alpha.$$

In this approximation the Langevin equation of the intracavity field $\hat{a}$ is:

$$\begin{aligned}0 = \dot{\hat{a}} &= -\kappa^a\hat{a} + g\hat{a}^\dagger + \sqrt{2\kappa_{in}^a}\hat{A}_{in} \\ 0 = \dot{\hat{a}}^\dagger &= -\kappa^a\hat{a}^\dagger + g^*\hat{a} + \sqrt{2\kappa_{in}^a}\hat{A}_{in}^\dagger.\end{aligned}$$

If the classical amplitude of the input field is real, from the last expressions it is easy to find:

$$\alpha =< \hat{a} >= \frac{\left(1 + \frac{g}{\kappa^a}\right)\sqrt{2\kappa_{in}^a}}{\kappa^a\left(1 - \frac{|g|^2}{\kappa^{a2}}\right)} < A_{in} > . \tag{3.25}$$

The classical amplitude of the transmitted field $\hat{A}_{out}$ is equal to $< A_{out} >= \sqrt{2\kappa_{in}^{a}}\alpha$ [34]. The amplification gain of the process is defined as the ratio between the cavity output power and the cavity output power when the gain g is equal to zero:

$$\frac{P_{out}}{P_{out}|_{g=0}} = \left(\frac{A_{out}}{A_{out}|_{g=0}}\right)^2 = \frac{\left(1+\frac{g}{\kappa^a}\right)^2}{\left(1-\frac{|g|^2}{\kappa^{a2}}\right)^2}, \tag{3.26}$$

where the term g/κ^a is known as the normalized pump parameter and is equivalent to the ratio of the pump field amplitude B to the pump field amplitude at the threshold B_{th} [35].

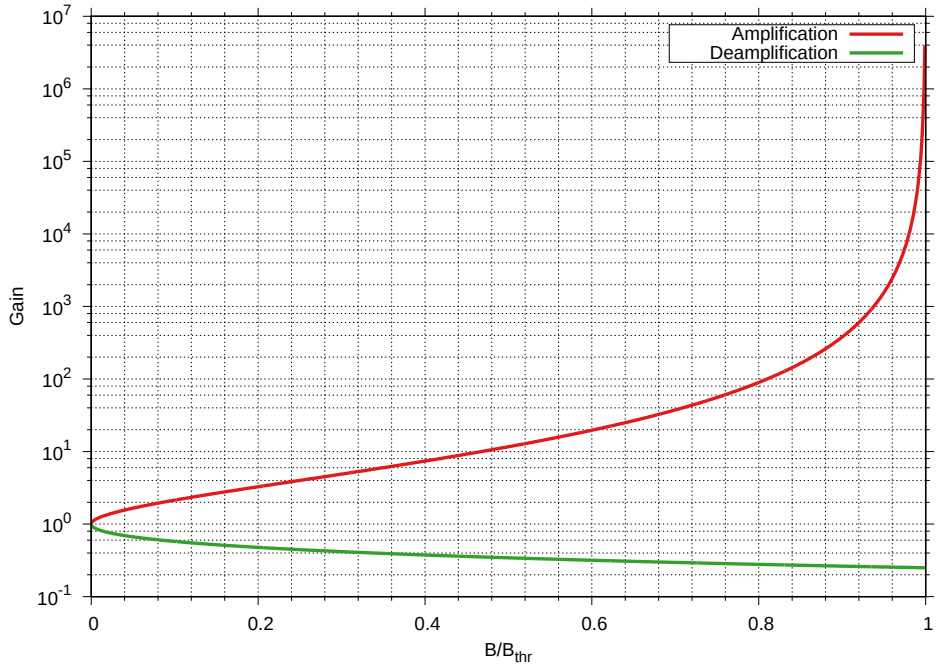

Figure 3.7: Gain of an optical parametric amplifier

The parametric gain can be rewritten as:

$$\frac{P_{out}}{P_{out}|_{g=0}} = \frac{\left(1+\frac{B}{|B_{th}|}\right)^2}{\left(1-\frac{|B|^2}{|B_{th}|^2}\right)^2}. \tag{3.27}$$

Fig. 3.7 shows the parametric gain of an OPO cavity as a function of $|B/B_{th}|$. Two different behaviour are shown: the amplification and the deamplification of the input beam. If the phase of the pump field is such that it is real and positive the input signal is amplified, whereas when the pump field is real and negative the input field is deamplified. A measurement of the amplification-deamplification gain of the cavity allows to determine the pump threshold power.

3.2.2 Semiclassical behaviour of OPO cavity

The classical model of the cavity helps in the understanding on its quantum behaviour. When it is in the deamplification regime the quantum fluctuation of the amplitude quadrature are also deamplified and this phenomenon is the amplitude squeezing. Otherwise , when it is in the amplification regime, the amplitude quadrature is amplified (anti-squeezed) and the phase quadrature is squeezed. With a computation similar to the one made in the classical case, starting from Eq. 2.16 and Eq. 3.24, it is possible to compute the spectrum of the two quadrature of the field $\hat{a}$ at the output of the cavity:

$$\begin{aligned} V_{out,1}(\omega) &= 1 + \eta_{loss}\eta_{esc}\frac{4\frac{B}{|B_{th}|}}{\frac{\omega^2}{{\kappa^a}^2} + (1 - \frac{B}{|B_{th}|}^2)} \\ V_{out,2}(\omega) &= 1 - \eta_{loss}\eta_{esc}\frac{4\frac{B}{|B_{th}|}}{\frac{\omega^2}{{\kappa^a}^2} + (1 + \frac{B}{|B_{th}|}^2)} \end{aligned} \tag{3.28}$$

where η_{esc} is the escape efficiency defined as $\eta_{esc} = \kappa^a_{in}\kappa^a$, η_{loss} are the total detection losses and the input field is considered in a coherent state [36][35]. η_{esc} determines the efficiency with which the squeezing exits from the cavity. The efficiency is high when the output coupling rate κ^a_{out} is large, i.e. when the output mirror transmission coefficient is high and the intracavity losses are low. κ^a_{out} can not be arbitrarily large while, if the total coupling rate κ^a is too big ,the pump power needed to generate an high nonlinear gain becomes excessive (see Eq. 3.27).

Part II

The squeezing vacuum source

Chapter 4

Overview of the squeezing vacuum source

A squeezed light source for an interferometric gravitational wave detector must show a long term stability in the frequency region interested to the detector. A system with these features has already been implemented in the GEO 600 interferometer [37] and its application has been demonstrated in one of the LIGO interferometers [38] .

This part of the thesis describes the squeezing optical bench and its electronic/control system that was initially designed to be installed in the Virgo interferometer. The layout of the bench is similar to the one installed in the GEO 600 detector [30] [39], whereas the electronics and controls are designed in order to be integrated in the Virgo Data Acquisition system [40] [41] and in the system Methatron for the controls automation in the Virgo framework [42].

The bench is under construction in a clean room placed in the building at the middle of the West arm of the Virgo interferometer (1500W). This project is a collaborative effort involving many Italian laboratories, i.e. the INFN sections of: Napoli, Roma 1 (La Sapienza), Roma 2 (TorVergata), Pisa, Genova, Perugia, Padova, TIFPA (Trento) and the Optics and Electronics group of the EGO staff. This part of the thesis is organized as follows: Chap. 4.1 describes the optical layout of the squeezer, the feature of its principal components and their performances; the next three chapters will describe the electronic developed to control all the bench components. In particular Chap. 5 is dedicated to the radiofrequency signals generation, Chap. 6 describes the optical phase locked loops and Chap. 7 treats the temperature controller boards, the boards used to lock the active optical components, the high voltage amplifiers and the photodiode amplifiers.

On the basis of the results obtained by injecting the squeezed light in LIGO and

in GEO 600, the Virgo squeezing working group set up the following requirements:

- 12 dB of produced frequency independent squeezed vacuum states between 10 Hz and 10 kHz;
- less than 10 mrad rms phase noise;
- less than 5% optical losses.

The requirement on the squeezing parameter must be intended before the action of the optical losses. On the other hand the electronics must be compatible with the Virgo tools for data acquisition and controls management. This is realized by implementing the following choices:

- the developed boards must be remotely controlled, thus each of them is equipped by an intelligent unit such as a DSP, a microcontroller or a Linux Embedded PC and a routine for the USB/ethernet communication;
- the boards are all managed by a server of instruments developed with the Tango Controls Toolkit as for the other Virgo subsystems (Vacuum, SAT, etc.);
- the servo loops that act on a piezoelectric actuator are based on the UDSPT board, that are developed for the control of the Virgo superattenuators and are already prepared to be interfaced with the DAQ system.

4.1 Overview of the squeezer

The top part of Fig. 4.1 shows a block scheme of the optical setup of the squeezer developed in the clean room at the Virgo site. For clarity reasons in the scheme are neglected the steering mirrors, lenses, wave plates and most part of the servo loops. The complete optical layout is shown in App. C and the layout of each control loop will be shown, below in this chapter, when the controlled optical component is described. The bottom part of Fig. 4.1 is a picture of the optical bench taken before the installation of the AUX1 laser. The bench is covered by an anodized black enclosure in order to screen it from air turbulence, dust, etc.. This enclosure is divided in three parts with the aim to decrease the scattered light in the OPO and in the detection region. The optical beams pass from a zone to the other with holes in the bulkheads.

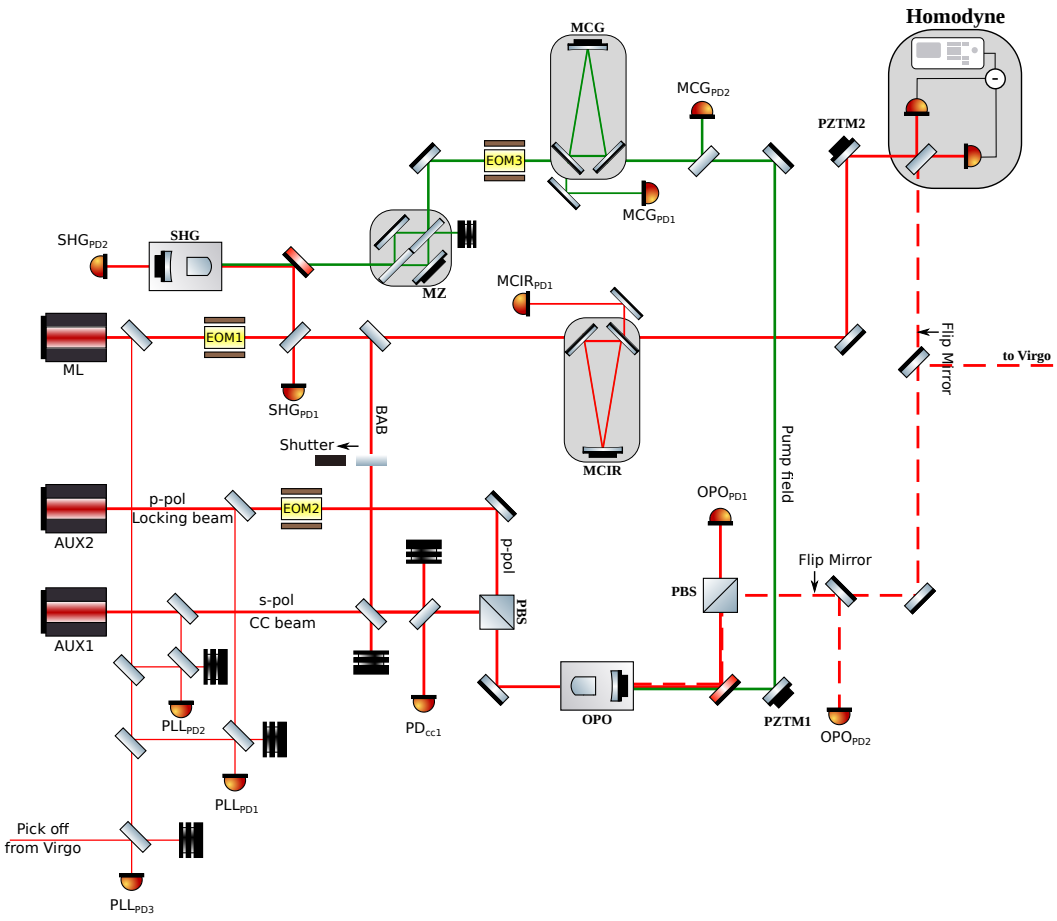

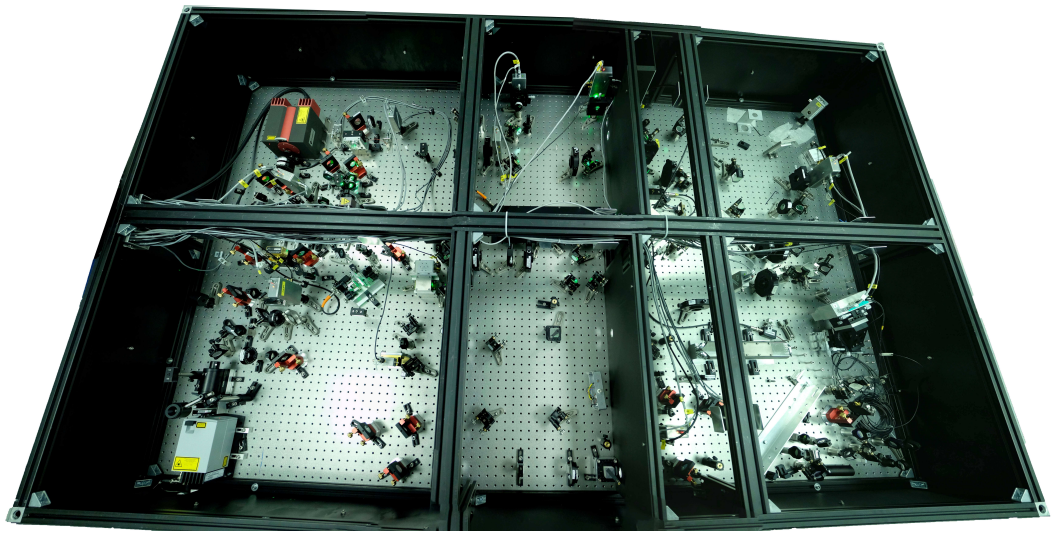

Figure 4.1: Top: simplified scheme of the squeezer. Bottom: picture of the squeezer before the installation of the AUX1 laser

4.1.1 Laser sources

The generation of squeezed state in the audio-frequency region for gravitaional wave detection is based on two different wavelength: the fundamental field with a wavelength of 1064 nm, which frequency is identified as ω_0, and its harmonic field with a wavelength of 532 nm, which frequency is identified as $2\omega_0$. On the bench are installed three different laser sources. Each of them is followed by an half wave-plate and a quarter wave-plate with the aim to clean the output polarization of its generated light and by a Faraday opto-isolator.

The main laser source (ML) is a 1 W Nd:YAG Non Planar Ring Oscillator (NPRO) at frequency ω_0. It is the model Mephisto produced by Coherent company [43]. This source provides: the input field of the second harmonic generator cavity, the local oscillator field for the homodyne photodetection and the auxilliary beam, called bright aligment beam (BAB), used for the alignment of the generated squeezed light toward the homodyne detector or toward the interferometer. The two cavities driven by ML are held on resonance exploiting the Pound-Drever-Hall technique (PDH), therefore the ML output field is phase modulated with a resonant electro-optic modulator (EOM1) at a frequency of 80 MHz.

The second Nd:YAG NPRO laser source (AUX2) is the model Mephisto S of Coherent company. It has an output power of 200 mW at frequency ω_0. This source is used for the active length control of the Optical Parametric Oscillator, which is locked on the laser line at frequency ω_0 in the p-polarization. The OPO length locking is performed with the PDH technique, thus the AUX2 laser beam must be phase modulated, at a frequency of 78 MHz with a resonant electro-optic modulator (EOM2), before it is injected in the cavity. The choice on the polarization of this locking beam is made in order to avoid additional technical noises on the s-polarized squeezed beam. Moreover as the OPO nonlinear crystal is birefringent, the two orthogonal polarizations resonates in the OPO at different frequencies, thus the AUX2 frequency must be shifted in a way that the cavity resonates simultaneously for both the polarizations. This frequency shift is obtained with an Optical Phase Locked Loop (OPLL) that will be described in Chap. 6. Its input, the beat note signal between ML and AUX2, is taken from the photodetector PD_{PLL1}. Finally in order to held on resonance the OPO cavity, with the PDH technique, the AUX2 output field is phase modulated with (EOM2) at a frequency of 78 MHz.

A third Nd:YAG NPRO laser source (AUX1), identical to AUX2, is installed on the bench. This is used for the generation of the coherent control beam required to stabilize the squeezing ellipse orientation angle. This laser is frequency locked on

the ML with an OPLL servo loop, which beat note input signal is detected by the PD_{PLL2} photodetector.

4.1.2 The squeezed light source - OPO cavity

The main optical cavity of the bench is the squeezed light source, i.e. the OPO cavity, which is driven below threshold. As described in Sec. 4.6 it is a single-resonant, linear hemilitc cavity in which the nonlinear medium is a periodically poled KTP (PPKTP) crystal. The cavity is held on resonance by acting on the piezoelectric transducer that is mechanically connected to its incoupling mirror. The cavity length locking, achieved with the PDH technique, is performed using as error signal the demodulated output of the photodetector PD_{OPO1} placed in transmission to the cavity.

As it is shown in Fig. 4.25 the squeezer proper operation is achieved by injecting simultaneously three beam into the OPO cavity:

- the green pump field at frequency $2\omega_0$ which is used as pump field of the DFG nonlinear process. The generation and the stabilization of the green field will be described in Sec. 4.2, in Sec. 4.3 and in Sec. 4.4;

- a frequency shifted, with respect to ML frequency, and p-polarized infrared field used for the cavity length stabilization. This field is generated by the AUX2 laser.

- an s-polarized infrared beam, that is called the *coherent control beam* (CC beam). It is used for the stabilization of the squeezed light ellipse orientation. The CC beam is generated by the AUX1 laser and is frequency shifted respect to the ML output frequency ω_0. It interacts with the pump field and is involved in the nonlinear DFG process. Due to this nonlinear process, a frequency shifted beam is generated in the cavity and its phase is related to the phase of the green pump field. Thus, this field contains the information on the green pump field phase fluctuations and it is used for the error signal generation of the loop used to stabilize these fluctuations. Moreover, because of the AUX2 beam is frequency shifted, its injection inside the OPO cavity does not add technical noises to the squeezed beam. The phase of the green pump field is controlled, by changing the green path length, with a mirror placed on a piezoelectric actuator (PZTM1) and the error signal is extracted from the photodetector PD_{COH1} placed in reflection to the OPO respect to the AUX1 laser. The stabilization of the green pump field is not enough, in fact when the squeezing level is measured

with the homodyne detector, the phase difference between the squeezed beam and the LO beam must be also stabilized. This is achieved with another mirror placed on a piezoelectric transducer (PZTM2) and the error signal is extracted from the radiofrequency difference channel of the homodyne detector.

An additional s-polarized pick-off of the main laser, the bright alignment beam (BAB), is used for alignment purposes. The BAB resonates inside the OPO cavity and thus, in transmission to the OPO, it shares the same optical properties of the squeezed beam. For this reason, the BAB is used for the alignment of the squeezed beam both on the homodyne detector and on the interferometer. When the BAB is not used it is damped.

4.1.3 Green pump generation and stabilization

The green pump field at frequency $2\omega_0$ is generated exploiting the second harmonic generation nonlinear process. This frequency doubled field is generated by injecting the ML beam into an SHG cavity. As the OPO, the SHG cavity is a single resonant, linear and hemilitic cavity based on a PPKTP nonlinear crystal and it is held on resonance with a piezoelectric actuator linked to its incoupling mirror. This cavity is described in Sec. 4.2. The PDH error signal is taken in reflection to the cavity using the demodulated output signal of the photodetector PD_{SHG1}. Moreover an additional photodetector PD_{SHG2} is placed in transmission to the cavity and it is used to detect when it is near the resonance. Exploiting PD_{SHG2} signal, an SHG cavity auto-locking procedure is developed. After the SHG cavity are mounted a Faraday Opto-isolator and three harmonic beam-splitters (HBS) which are used to remove the IR component from the green beam.

Before its injection inside the squeezer cavity, the green pump field is cleaned, exploiting a triangular cavity, from the light high order modes. This is performed to avoid the interactions between the green field high order modes and any fundamental field high order modes inside the OPO. The used triangular cavity, the green mode cleaner (MCG), acts on the green laser as a spatial filter and attenuates the contributions of high order modes. Its input and output mirrors are plano-plano mirrors while the third one is a plano concave mirror and has a radius of curvature of 1000 mm. The cavity is held on resonance with the PDH technique by acting on a piezoelectric actuator linked to the plano-concave mirror. The PDH error signal is taken from the photodetector PD_{MCG1} placed in refection to the cavity. The additional photodiode PD_{MCG2}, placed in transmission to the cavity, is used to detect if the MCG is near the resonance and it is used to implement the PDH auto-locking routine. This cavity

is described in Sec. 4.3.

The fluctuations of green power DC level are a source of squeezing degradation. Therefore, in this setup, they are stabilized by exploiting a Mach-Zehnder interferometer (MZ), placed in the green path. The active control on the green power is performed by acting on the MZ arm lengths by means of a piezoelectric actuator linked to one of the MZ mirrors. The error signal for this loop is taken in reflection to the MCG cavity from the photodetector PD_{MCG2}. The MZ interferometer is described in Sec. 4.4.2.

4.1.4 Balanced homodyne detector

As discussed in Sec. 2.6.2 the homodyne detector is composed by a 50/50 beam splitter and two photodetectors. Sec. 2.7.1 will show how an high fringe visibility minimizes the detection losses. Moreover the local oscillator beam is filtered with another triangular cavity, the infrared mode cleaner (MCIR), that is described in Sec. 4.5.1. MCIR is held on resonance as MCG with a piezoelectric actuator placed on its curved mirror. The error signal of the PDH servo loop is taken from the output of PD_{MCIR1} placed in reflection to MCIR. The homodyne electronic board is based on the self subtracting scheme and it is briefly described in Sec. 4.5.2.

4.2 Second Harmonic Generator cavity

The aim of the SHG cavity is the generation of the green field used as pump field in the DFG nonlinear process inside the OPO cavity. The green field has to fulfill the following requirements:

- the maximum green power produced must be at least equal to the OPO threshold 115 mW in our case (see Sec. 4.6.2);
- the IR contamination of the green field must be as little as possible in order to avoid squeezed light contamination[44].

The IR contamination is reduced by inserting a cascade of three harmonic beam splitters (HBS) on the green path after SHG cavity. In this setup are used three dichroic BS model HBSY11 of Thorlabs manufacturer. These components exhibit very low IR transmittivity with a minimum of 56(5) ppm for vertically polarized field at 45°of incident angle[1]. With this setup the IR contamination of the green field should be below of 2×10^{-14} W when the power of the SHG IR pump field is 1 W.

[1] further information at `https://www.thorlabs.com/newgrouppage9.cfm?objectgroup_id=7035&pn=HBSY11`

This section describes briefly the SHG cavity installed in the squeezer in the Virgo site, for further information I remand the reader to the Matteo Leonardi thesis [45].

4.2.1 Cavity description and mechanics

Fig. 4.2 shows a sketch of the SHG cavity optical elements. It is composed by:

- a PPKTP crystal with dimension equal to 1 mm×1.5 mm×9.3 mm. Its back surface has a radius of curvature of 8 mm with an high reflection coating (R=99.975%) for both the wavelength (green and IR). The other crystal surface is flat and has an AR coating different for the two wavelengths: $R < 0.2\%$ @ 1064 nm and $R < 2\%$ @532 nm;
- a partially reflective meniscus lens. Its inner part has a radius of curvature of 25 mm, a reflectivity @ 1064 nm $R = 90\%$ and $R < 0.2\%$ @ 532 nm. The outer surface has a radius of curvature of 20 mm, an infrared reflectivity $R < 0.2\%$ and a green reflectivity of $R < 0.3\%$.

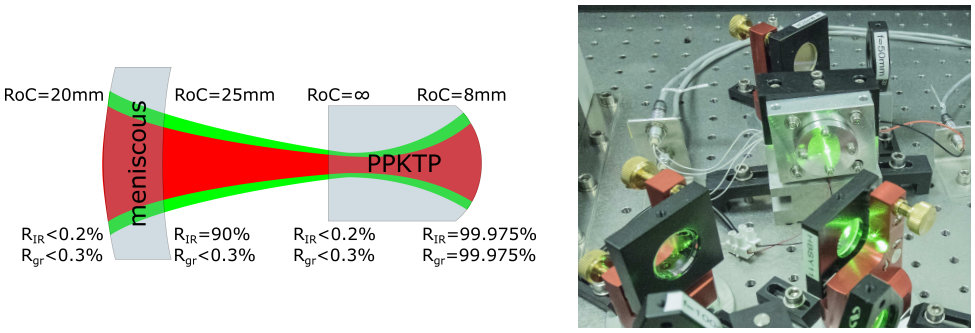

Figure 4.2: Left: SHG optical component scheme. All the reflectivity and curvature radii are reported. Right: photo of the SHG cavity installed in the optical bench in Pisa.

With these components the resulting cavity has the following properties: a finesse equal to $\mathcal{F} = 54$ at the fundamental wavelength, a free spectral range (FSR) of approximatively 3.8 GHz and a full width half maximum (FWHM) of approximatively 71 MHz. The SHG optical components are hosted in a mechanical mount that provides a mechanically stable housing for the meniscus and the crystal. This condition is mandatory because the cavity length variations can produce a phase fluctuations on the generated green beam. Sec. 3.1.4 shows that, in a nonlinear process, to obtain an high conversion efficiency the phase matching condition must be achieved. In this SHG, it is obtained with a thermal tuning of the PPKTP crystal refraction index, thus the cavity must be equipped with an high performance temperature stabilization system. This system is described in Sec. 7.1 and is composed by two NTC sensors,

a Peltier cell actuator and a digital controller board based on the Arduino microcontroller unit. To have an high performance temperature controller system, a good thermal contact between the thermometers, the actuator and the crystal is required. This is ensured in the following manner: the crystal is placed on an Oxygen-free High Conductivity copper element (OFHC) that is thermally connected to the Peltier cell with an indium foil; in addition the crystal is surrounded by another indium foil in order to thermally connect it with the OFHC element. The two NTC thermistors are mechanically attached to the copper element exploiting two copper berillium springs. This choice was made to avoid glues and greases which could affect the crystal performances [46]. Fig. 4.3 shows a vertical section of the SHG cavity in which are represented all the optical, mechanical and thermal components.

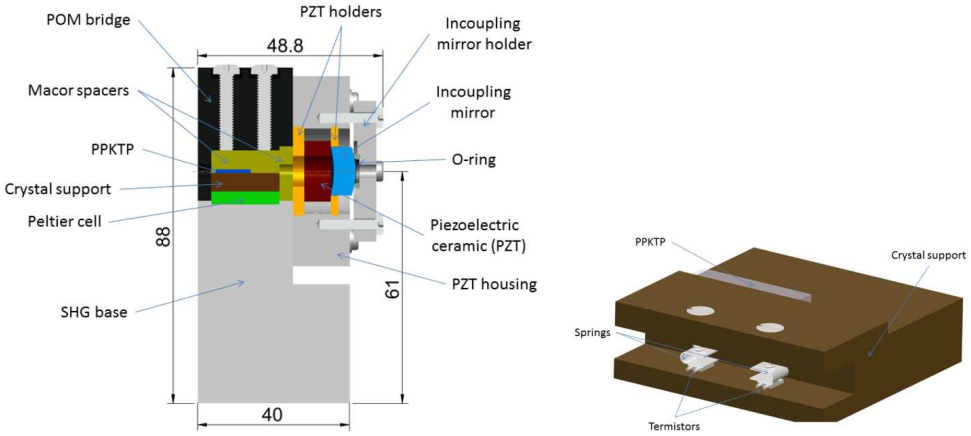

Figure 4.3: Left: SHG vertical section (orthogonal to the optical axis). Right: dry assembly of the SHG oven.

The cavity must be controlled in length, thus the incoupling meniscus is in contact with a piezoelectric (PZT) ring actuator. The elastic element that acts against the piezoelectric expansion is a viton o-ring. When the cavity is under construction, its length can be manually tuned, with an excursion of 3 mm, by moving the two brass spacer that forces the PZT in its position. The incoupling mirror and the crystal optical axis can be aligned by moving the PZT holder perpendicularly to the light propagation axis. Once the cavity is aligned, the incoupling mirror housing is blocked with four screws that fix it on the the SHG holder.

4.2.2 Cavity length and temperature stabilization

Fig. 4.4 shows in detail the integration scheme of the SHG in the squeezing optical bench and the layout of the two servo loop for its length stabilization. The resonator is held on resonance with the PDH technique that will be explained in App. A. The

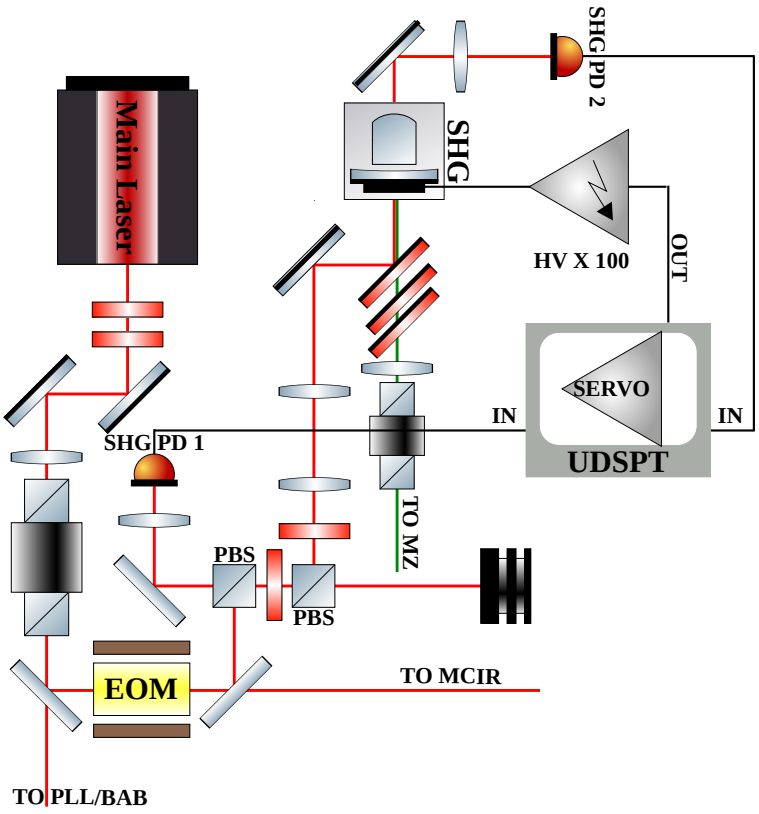

Figure 4.4: Optical scheme of the SHG cavity integrated in the squeezer bench.

laser light is phase modulated at 80 MHz with a resonant EOM that is driven with the channel 1 of the first DDS board which output level is set to 1 dBm and amplified of +24 dB with a medium power amplifier of Minicircuit manufacturer, Model ZHL-3A-S+. The PDH error signal is detected with the photodiode PD_{SHG1} placed in reflection to the cavity. It is equipped with an on board mixer and the LO signal is provided by the Channel 2 of the same DDS board (amplitude level set to +7 dBm). This channel is phase shifted to optimize the PDH error signal. A second photodiode PD_{SHG2} is placed in transmission to the cavity. This photodetector is used as trigger for the auto-locking procedure[2]. The two photodetector outputs are acquired and processed by a UDSPT board (see Sec. 7.2) that works with a sampling rate of 160 kHz. In the UDSPT board runs the code for the SHG control loop, that is closed sending the computed correction signal, amplified by a factor 100, to the piezoelectric actuator that moves the SHG incoupling meniscus.

[2] As it will be explained in Sec. 7.2.4 the locking condition is achieved with the following routine. A scansion of the cavity is performed by sending a triangular ramp to the PZT actuator. When the SHG is near the resonance, the SHG_{PD2} output signal overcomes a threshold the ramp is stopped and the loop is closed.

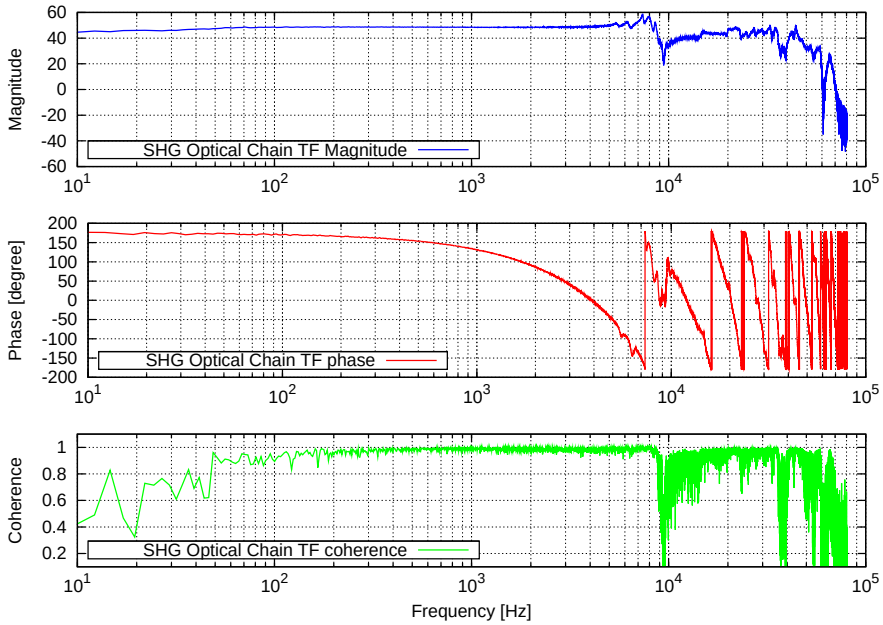

Figure 4.5: Optical chain transfer function of SHG cavity. Blue trace: magnitude. Red trace: phase. Green trace: coherence. The TF shows a almost constant gain from 1 Hz to 6 kHz. At higher frequencies the system shows some structures.

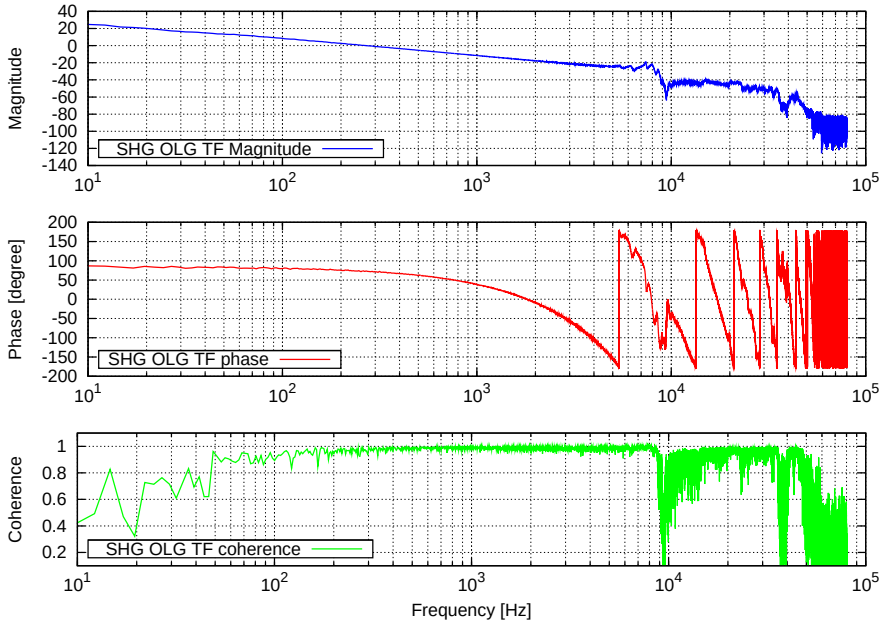

Figure 4.6: Open loop gain transfer function of SHG cavity. The servo loop is composed by a single pole at 1 µHz and a single pole at 5 kHz. Blue trace: magnitude. Red trace: phase. Green trace: coherence. The obtained unitary gain frequency is about 300 Hz.

Fig. 4.5 and Fig. 4.6 show respectively the measured optical chain transfer function

and the open loop gain transfer function. For simplicity with optical chain is intended the series composed by the HV-amplifier, the cavity and the photodiode. Here below, the technique used for transfer function measurement is summarized. The servo loop used to lock the SHG cavity is composed by two single poles, one at 1 µHz and one at 5 kHz and the resulting unitary gain frequency is at about 300 Hz.

Transfer function measurement

The SHG optical chain and open loop transfer function are measured, when the cavity is locked, with the system shown in Fig. 4.7. In particular, left side of Fig. 4.7 shows the open loop gain $L(\omega)$ measurement scheme. $L(\omega)$ is the overall transfer function and is composed by: the servo controller transfer function $SC(\omega)$, the high voltage amplifier transer function $HV(\omega)$, the cavity transfer function $CA(\omega)$ and the photo-detector transfer function $PD(\omega)$. When the system is locked, a signal $S(\omega)$ is injected in it by a summing amplifier and its response is measured simultaneously at two different nodes $A(\omega)$ and $B(\omega)$. The open loop gain is given by:

$$L(\omega) = -\frac{A(\omega)}{B(\omega)}.$$

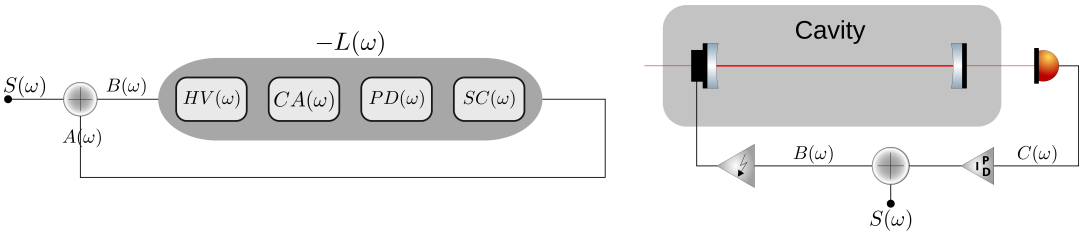

Figure 4.7: Right: scheme of the open loop gain transfer function measurement. Left: scheme of optical chain transfer function measurement.

The right side of Fig. 4.7 summarizes the optical chain transfer function measurement. This transfer function is composed by the product between the following transfer functions: $HV(\omega)$, $CA(\omega)$ and $PD(\omega)$. The aim of this measurement is the understanding how much an external disturbance, at a given frequency, affects the uncontrolled system. Therefore, in this measurement, the contribution of the servo controller is not included. The measurement is performed as follows: the disturbance $S(\omega)$ is injected into the system and its response is acquired at the nodes $B(\omega)$ and $C(\omega)$ placed before and after the servo controlled. The optical chain transfer function $(OC(\omega))$ is defined as:

$$OC(\omega) = \frac{C(\omega)}{B(\omega)}.$$

In both the setups the injected disturbance is a white noise which has to dominate all the other noise contribution. With the UDSPT boards these two measurements can be performed simultaneously, remotely and without hardware modifications by means of the following routine:

- the board is equipped by a digital random noise generator, that excites the system in a frequency range chosen by the user. The generated noise S is summed to the correction signal before the DAC;

- A, B and C signals are acquired simultaneously, where A is the servo correction signal, B is the output signal sent to the HV amplifier (correction signal summed to the disturbance) and C is the PDH error signal. If the noise S is not added A and B are the same signal;

- the PSD of the three signals is computed by exploiting the "pwelch" function of the "Matlab" numerical computing envirnoment. The optical chain and the open loop gain transfer functions are computed from the three PSD.

Temperature stabilization

The SHG cavity is based on a PPKTP nonlinear crystal, therefore its conversion efficiency strongly depends on the phase matching between the fundamental and the harmonic field. In this SHG, the optimal phase matching condition is achieved by tuning the nonlinear crystal temperature with a controller system. The temperature controller system and its performances will be deeply described in Sec. 7.1. In particular, in Fig. 7.3 is represented a photo of the controller board and in Fig. 7.4 are shown the performance of the system: it suppresses the room temperature fluctuations by a factor 35.

Scanning the crystal temperature, we have measured the phase matching curve of the SHG cavity that it is shown in Fig. 4.8. This measurement is performed as follows: the SHG fundamental input field power is set to 0.165 W and, for each temperature, the the green produced power is measured. The quasi-phase matching condition is reached at 304.6 K and around it the curve spans a wide maximum. Thus a variation of 0.1 K from such temperature causes an harmonic power variation less than 1 %. This is a confirm that the achieved temperature stabilization level, i.e. 12 mK of maximum excursion in a day of measurement, is good enough for the green pump beam production.

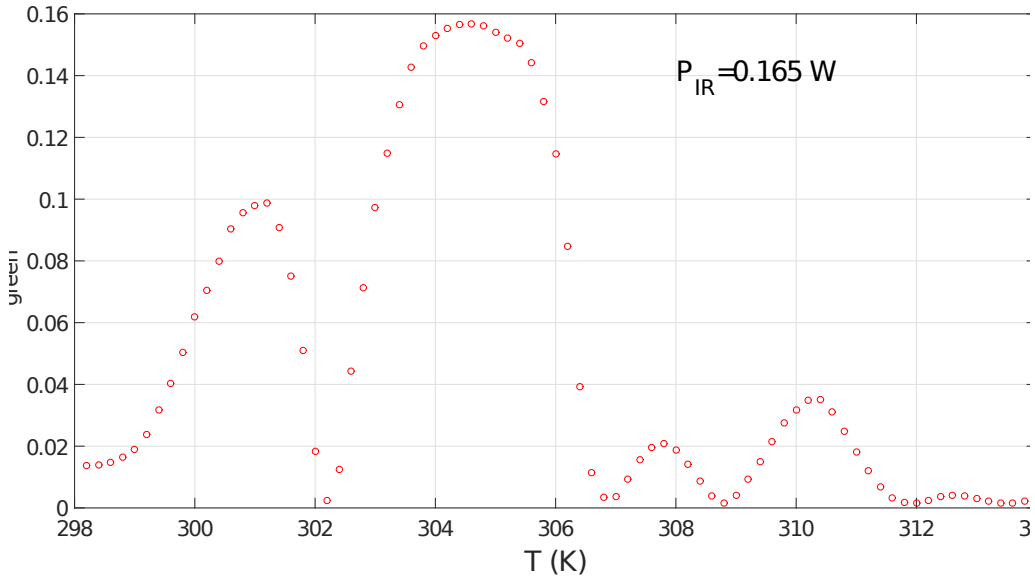

Figure 4.8: Produced green power at different crystal temperature with fixed fundamental input power [45].

4.2.3 Efficiency measurement

The SHG cavity is aligned as described in M. Leonardi thesis. After this alignment, the obtained mode matching between the fundamental field and the cavity is about 94 %. This is measured when the crystal temperature is set in order to have a negligible conversion efficiency. The mode matching is measured in the following way: the cavity length is scanned for more than two free spectral ranges (FSRs), the transmitted light is acquired, each Airy peak is fitted and the mode matching is computed as the ratio between the area of TEM_{00} peak and the total area of a FSR.

The SHG conversion efficiency is defined has the ratio between the power of the generated green field $P_{2\omega}$ and the fundamental power P_{ω}, normalized by the mode matching at SHG input [47]:

$$\epsilon = \frac{P_{2\omega}}{P_{\omega}}.$$

The SHG efficiency curve is measured with a fixed crystal temperature at 304.6 K and varying the fundamental input power in the range between 60 and 400 mW. Fig. 4.9 shows the conversion efficiency of the SHG cavity and the produced harmonic power as function of the fundamental input field. The conversion efficiency reaches a top value of $(99 \pm 1^{(stat.)} \pm 3^{(syst.)}\%)$, producing 324 mW in the harmonic green field with 326 mW input IR pump field. The systematic error in the efficiency measurement is due to the calibration error of the used power meter. Data above 0.35 W show a marked decrease of conversion ratio. This is caused by another competitive nonlinear process

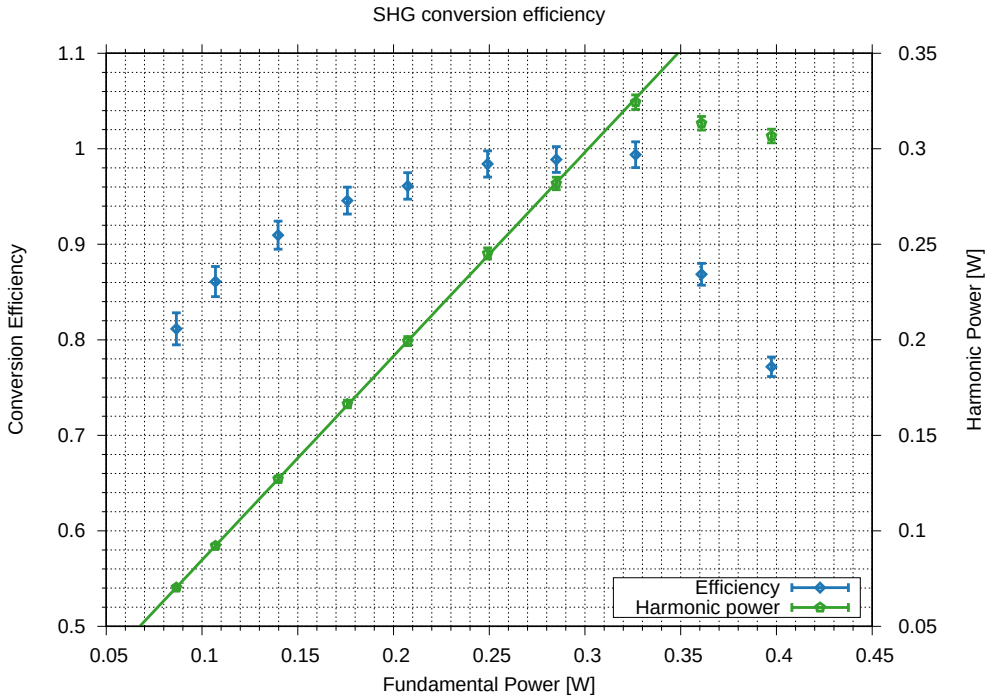

Figure 4.9: Conversion efficiency of SHG cavity at fixed temperature 304.6 K for different IR input power.

that limits the green power produced. This process is the degenerate subharmonic pumped parametric down conversion and occurs when the input power is larger than a threshold that is expected at about 0.34 mW [45] [48] [49]. In conclusion the green power produced by SHG cavity respects the requirement needed by the pump field of the OPO cavity.

4.3 Green mode cleaner resonator

Once generated, the green pump field is filtered by a travelling wave resonator, the green mode cleaner (MCG), in order to suppress the high order modes. The MCG is a triangular Fabry Perot optical cavity, designed by the INFN Napoli group, that is installed along the green light path as close as possible to the OPO cavity, with the following purposes:

- it acts as a low pass filter for the green field amplitude and phase noise. It has a roll-off frequency of f_c equal to the cavity half-width at half-maximum;
- it acts as a spatial mode filter, i.e. its transmitted beam mode contents is principally composed by the TEM_{00} mode while the high order modes are reflected

by the cavity.

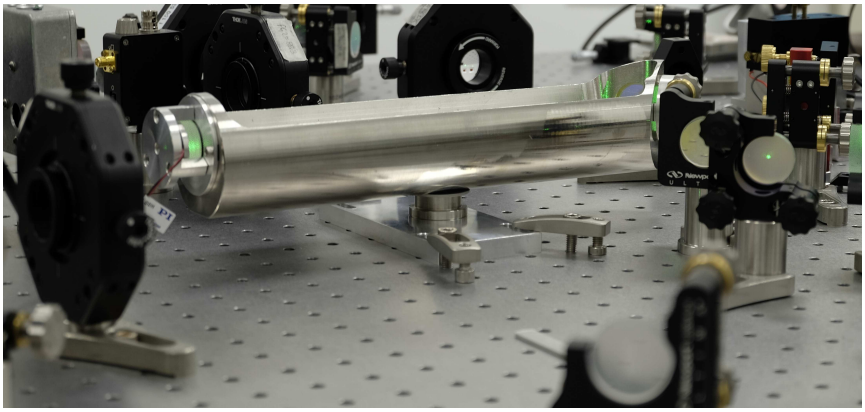

Figure 4.10: Photo of the green mode cleaner installed on the bench.

Fig. 4.10 is a picture of MCG installed on the squeezer bench. Its input and output mirrors are two plano-plano super-polished mirrors with power reflectivity $R = 0.995$, whereas the third mirror is plano-concave mirror with radius of curvature of 1 m and power reflectivity $R_1 = 0.9998$. The mirrors are assembled on a monolithic Invar[3] holder. This monolithic design and the material are adopted to ensure high mechanical stability and small length fluctuations due to thermal variations. The Invar spacer is designed to have a round trip length of 582.29 mm. Due to these optical and geometrical choices, the resulting MCG cavity has the following properties: its free spectral range is 514 MHz, its finesse is $\mathcal{F} = 613$ and the FWHM is 841 kHz both for s-polarized input beam. The cavity beam waist is 277 µm [44]. The cavity is locked on the green beam at frequency $2\omega_0$ actuating on a piezoelectric element mechanically connected to the concave mirror.

Fig. 4.11 shows the optical and control system layout of the squeezer green pump stabilization. As said in the introduction to this chapter, the green beam stabilization is performed by two active optical elements: the MCG cavity and the MZ interferometer that will be described in the next section. The control scheme evinces that the control loop of the MCG cavity and MZ interferometer are closed in cascade: the green power is stabilized by the MZ using as error signal the detected light by the photodetector PD_{MCG2}. This choice means that the MZ interferometer must be locked after the MCG cavity.

The MCG cavity is locked, as SHG, exploiting the PDH technique. The green input beam is phase modulated with an home made EOM which is resonant at 30 MHz.

[3]Invar or s FeNi36 is a nickel-iron alloy that shows a remarkably low coefficient of thermal expansion $\alpha = 1.2 \times 10^{-6}\,\mathrm{K}^{-1}$

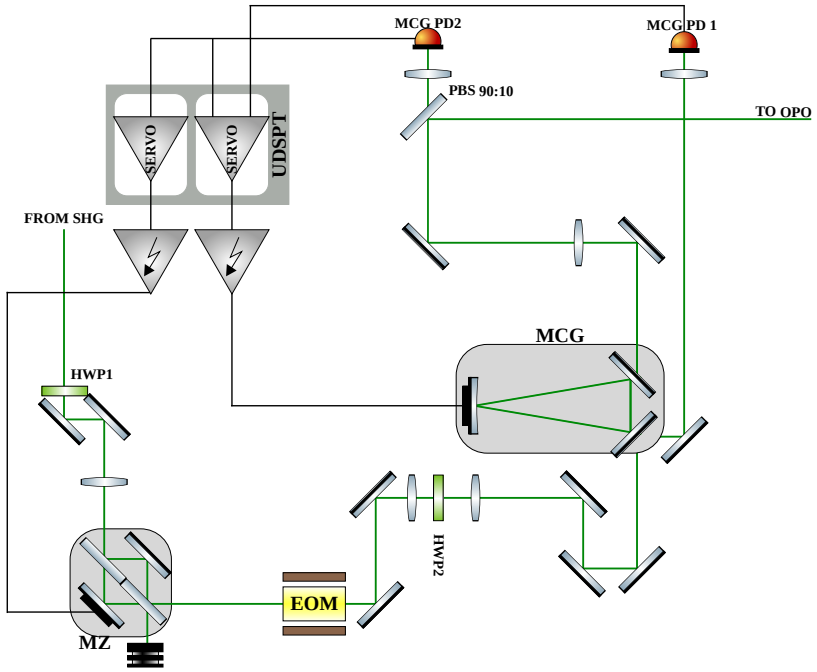

Figure 4.11: Optical scheme of the MCG cavity and MZ interferometer integrated in the optical bench

The modulator is realized by the optic and the electronic groups of EGO staff. The PDH error signal is detected by the photodetector MCG_{PD1} placed in reflection from the cavity. This is a Si photodiode mounted on circuit equipped by an RF trans-impedance amplifier and a mixer used to signal demodulation. The signals used to drive the EOM and as LO for the demodulation, both at 30 MHz, are generated by the same DDS board. The PDH loop is provided by an auto-locking procedure based on the signal detected by photodiode MCG_{PD2}. This photodetector is feed by the 10% of the MCG transmission beam extracted through a 90/10 BS.

4.4 Green pump power stabilization

This squeezer prototype is thought to be permanently employed in a gravitational wave observatory, therefore the generated degree of squeezing/antisqueezing must be stable on the timescale of months. According to Eq. 3.28 the squeezing/antisqueezing level depends on the pump power injected in the OPO cavity. Therefore a fluctuation of the harmonic power causes a variation on the produced squeezing level. The main source of green field power fluctuations are the fluctuations of the ML power used to pump the SHG cavity. In fact ML is not power stabilized thus the power variations of the 532 nm field are directly coupled to the ones of the 1064 nm field. Thus, the

long term stability of the squeezing level is provided by inserting a Mach-Zehnder interferometer, between the SHG and the MCG cavities, with the aim to control the pump level power injected into the OPO cavity.

4.4.1 Squeezing degree as function of the pump power

The fluctuations of the pump power has two consequences: first the squeezing/anti-squeezing variances depend on the ratio between the injected pump power and the OPO threshold power (see Eq. 3.28); second it induces thermal effects on the nonlinear crystal that cause a detuning of the s-polarized beam inside the squeezing cavity.

Fig. 4.12 shows how the squeezing and antisqueezing level produced varies, according to Eq. 3.28. For example, when the pump power changes of ±5%: the maximum variation of the squeezing level is less than 0.3 dB whereas the antisqueezing varies less than 1.2 dB therefore this effect is negligible in the long term fluctuations analysis.

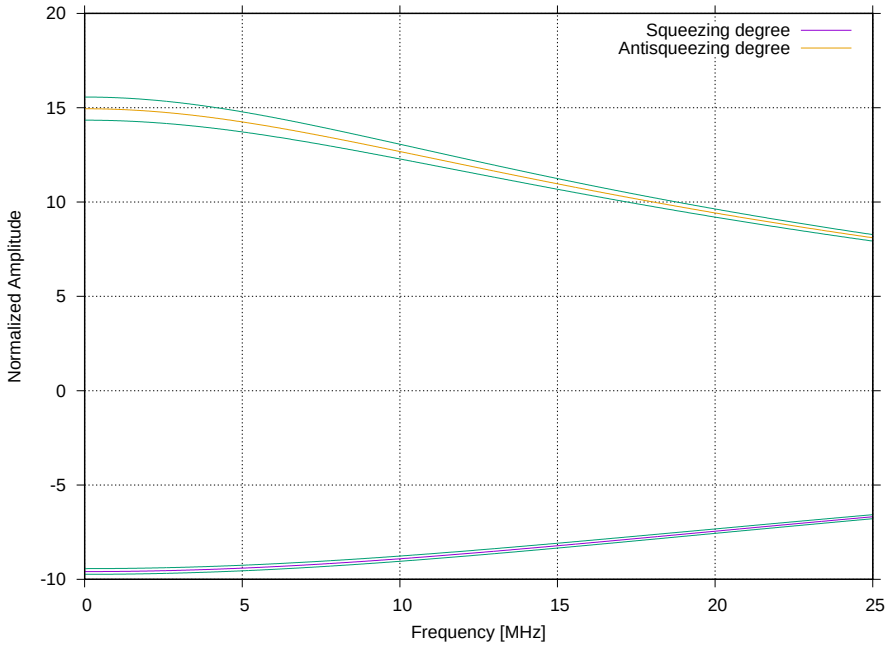

Figure 4.12: Simulation of the squeezing and anti-squeezing generated degree as function of the detection frequency. The pump power level chosen is an half of the threshold power. Squeezing is represented by violet line, whereas antisqueezing by orange line. Green lines indicates the effect of a ±5% fluctuation of the pump power.

In the following the thermal effects induced by green pump fluctuations are briefly described. For a deeper description of these phenomena the reader is addressed to reference [39]. The nonlinear crystal has a non negligible absorption coefficient at 532 nm , therefore a power change induces a temperature variation of the medium. This has several consequences:

- variation of the crystal refractive index that leads to the loss of the phase-matching condition.

- detuning of the OPO cavity respect to the s-polarized light. The OPO cavity is locked on the p-polarized AUX2 laser line, whereas the 532 nm pump beam and the generated squeezed vacuum states are in the orthogonal polarization. Because of the birefringence of the PPKTP nonlinear crystal, the condition in which the two orthogonal polarization are simultaneously resonant in the OPO is achieved by offsetting the AUX2 output frequency with respect to the ML one. Therefore a variation of the nonlinear crystal refraction index causes a loss of the coresonant condition that results in a detuning of the OPO respect to the s-polarized light;

- influence on the squeezing ellipse angle that causes disturbance in the coherent control system for its stabilization.

A theoretical stability requirement for the green power can be calculated exploiting the analysis presented in [39] that takes into account all the thermal effects. The result is that the deviation of the green power must be less than 1%, since within this value the squeezing degree and angle does not significantly change. This analysis is performed with the pump power set to about an half of the OPO threshold power [44].

4.4.2 Mach Zehnder interferometer

Fig. 4.13 shows a picture of MZ interferometer and its working principle scheme. This optical element is designed by INFN Napoli group.

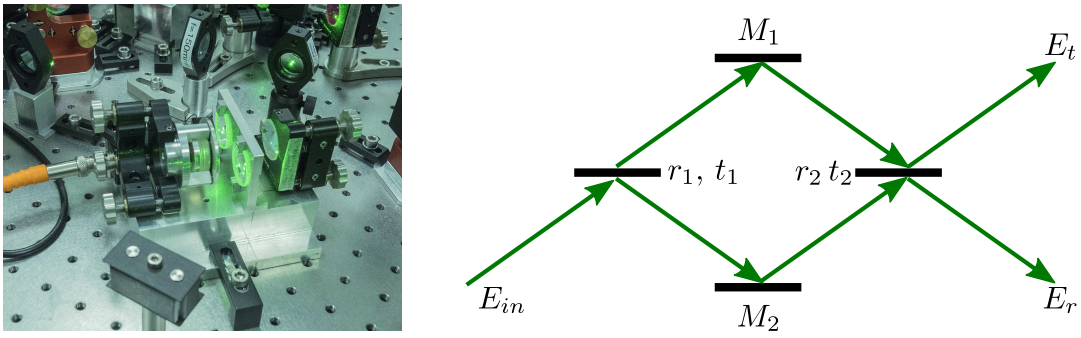

Figure 4.13: Left: photo of the MZ interferometer installed on the bench. Right: working principle of a MZ interferometer.

Referring to the right side of Fig. 4.13, the reflected E_r and transmitted E_t electric

fields can be computed as:

$$\begin{aligned} E_r &= \left(r_1 r_2 - t_1 t_2 e^{\imath\left(2\pi\frac{\Delta L}{\lambda}+\phi\right)}\right) E_{in} \\ E_t &= \imath\left(r_1 r_2 + t_1 t_2 e^{\imath\left(2\pi\frac{\Delta L}{\lambda}+\phi\right)}\right) E_{in} \end{aligned} \tag{4.1}$$

where r_1, r_2, t_1, t_2 are respectively the the amplitude reflectivities and transmittivity of the two beam splitters, ΔL is the length difference of the two beam paths, λ is the wavelength of the incoming field E_{in} and ϕ is the Gouy phase at the recombination point. The MZ used in this squeezer is in the configuration $\Delta L \ll z_R$, where z_R is the Rayleigh length of the incoming beam, therefore the Gouy phase ϕ can be neglected in the analysis.

The MZ is designed with equal arms length and with an unbalanced beams power along each arm; thus that the mean power of the transmitted differs to the one of the reflected electric field. It is composed by two superpolished mirror M_1 and M_2 with reflectivity $R > 0.9999$ and rms sourface roughness about 0.5 Å and by two two fused silica beam splitters, S_1, S_2 with power reflectivity $R_1 = R_2 = 0.1$ for p-polarized light and $R_1 = R_2 = 0.01$ for s-polarized light.

Fig. 4.11 shows the optical layout of the MZ and the MCG installed on the bench. The half-waveplate (HWP1) before MZ is used to adjust the polarization of its input electric field and thus to tune the transmitted field amplitude E_t. After MZ another half-waweplate $HWP2$ is placed with the aim to readjust its output polarization. The reflected beam is injected into MCG and used as OPO pump. The pump power is actively controlled with a piezoelectric actuator attached to one mirror. Acting on the PZT the difference path length ΔL changes and thus it is possible to stabilize its output power to fixed value. The error signal is provided by the photodetector PD_{MCG2} placed in transmission to the MCG cavity. The loop stabilizes the field power, i.e. the photodiode output voltage, to a fixed value.

Fig. 4.14 shows the MZ power reflection and power transmission, defined as $R_{MZ} = |E_r/E_{in}|^2$ and $T_{MZ} = |E_t/E_{in}|^2$ as function of ΔL. These two quantities are shown both for p and s polarized input field: for p-polarized light the mean reflection is $R_{MZ}^{mean} = 0.82$ while for s-polarized light $R_{MZ}^{mean} = 0.98$. Left plot shows the measured R_{MZ} for p-polarized light when the difference path length is changed with a triangular ramp on the piezoelectric actuator. These data are not in agreement with the expected curve because E_{in} is not perfectly p-polarized and therefore the fraction of the light reflected by the MZ interferometer is slightly different than the one expectedtuned[4]. In addition the two measured periods are not perfectly aligned

[4]This rotation of the incoming beam polarization was performed to allow the MZ response to be linear at higher reflected power.

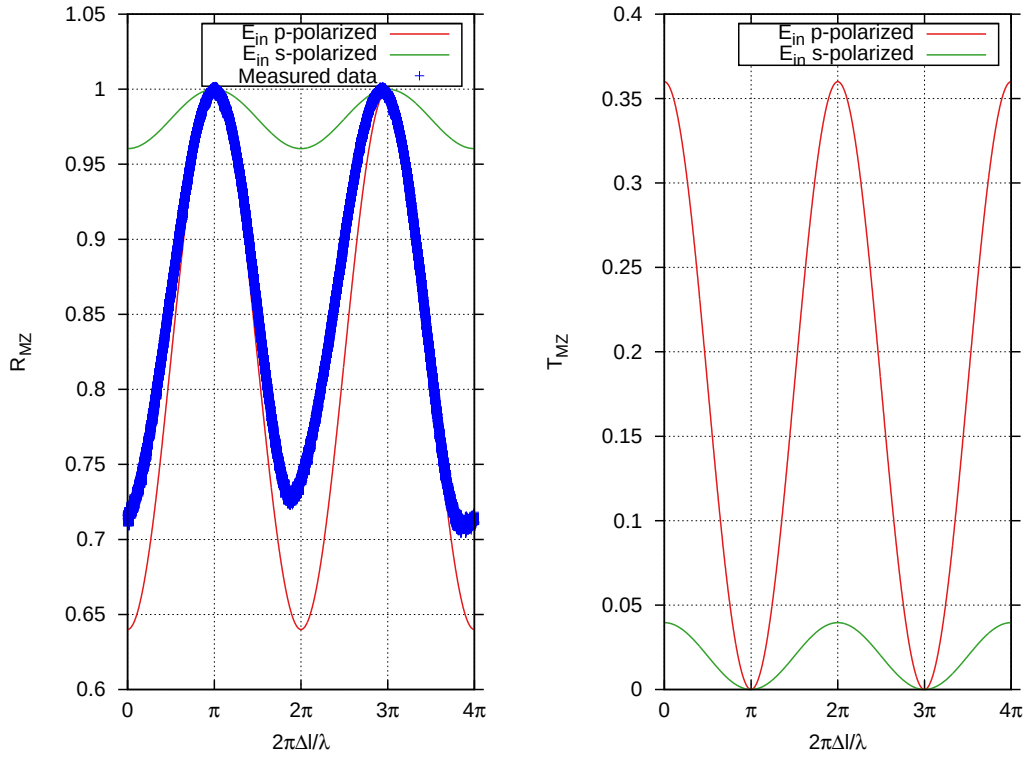

Figure 4.14: Left: plot of the power reflection both for s-polarization (green line), p-polarization (red line) and measured data with p-polarized E_in. Right: plot of the power transmission both for s-polarization (green line) and p-polarization (red line).

on the theoretical curves because of the PZT nonlinear response.

4.5 Squeezed beam diagnostic

After its production, the generated squeezing level is measured with a balanced homodyne detection scheme represented in the central part of Fig. 2.4. The homodyne detector setup is composed by a 50/50 beam splitter, a pair of photodetectors and two laser beams: the first is the field under measurement, in our case the squeezed light, and the second is the reference field, i.e. the local oscillator field. Moreover, as it is shown in Sec. 2.6.2, the relative phase between the LO field and the measured field determines the measured quadrature. Therefore in the LO beam path a piezoactuated mirror (PZTM1) is inserted.

Fig. 4.15 shows the homodyne detector setup installed in the squeezing optical bench. In order to minimize the detection losses the LO and the measured beam must have an high fringe visibility as it is said in Sec. 2.7.1. This condition is achieved if the two beams (LO and squeezed beam) have the same polarization and are mode

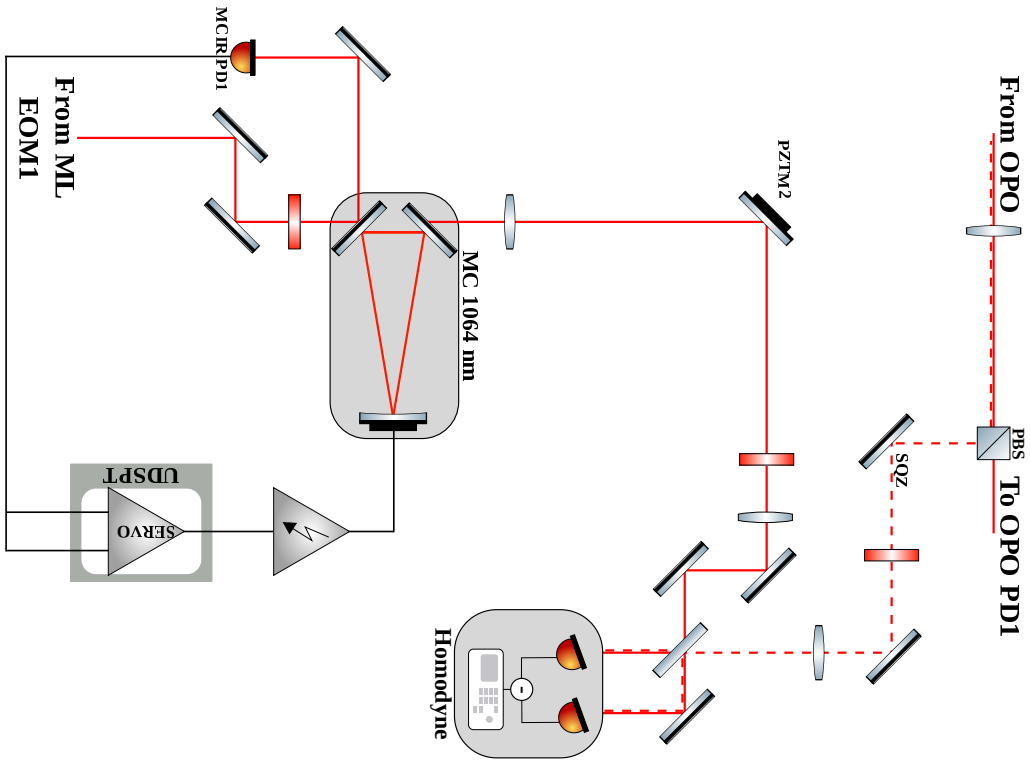

Figure 4.15: Optical layout of the homodyne diagnostic detector.

matched. The two beam waist positions and dimensions are equalized by using two matching telescopes one for each beam. The same polarization condition is obtained by placing in both the beam paths an half-wave plate used for a the fine polarization tuning. The OPO cavity acts as spatial filter on the squeezed field; thus a travelling wave triangular cavity is inserted in LO path, as close as possible to homodyne detector, that acts on it as spatial mode filter and grants a high spatial mode superposition of the two beams. In the following the MCIR triangular cavity and the homodyne detector are described.

4.5.1 Infrared Modecleaner MCIR

Fig. 4.16 shows a picture of the MCIR cavity installed on the optical bench and its 3D model. It consists in a triangular resonator whose plano-plano input and output mirrors have power transmittivity of 1.25% for p-polarized light and 700 ppm for s-polarized light[5]. These surfaces are oriented at an angle of 45(2)° with respect to the incoming optical beam. The third mirror is a super-polished plano-concave mirror with radius of curvature of 1 m and power transmittivity of 300 ppm for both the light

[5]This tabulated value is measured when the mirror surface is tiled by $45 \pm 2°$ with respect to the incoming beam

polarizations. The round trip length of the cavity is 545 mm [45]. The optical planar mirrors are mounted on a monolithic Invar spacer, whereas a PZT ring actuator is inserted between the curved mirror and the Invar holder. The result of this design is a triangular cavity with the following features: a finesse of $\mathcal{F}_s = 3330$ for s-polarization and $\mathcal{F}_p = 205$ for p-polarized light; a free spectral range of 550 MHz and a cavity-line width of 149 kHz for s-polarization and 2.23 MHz for p-polarization.

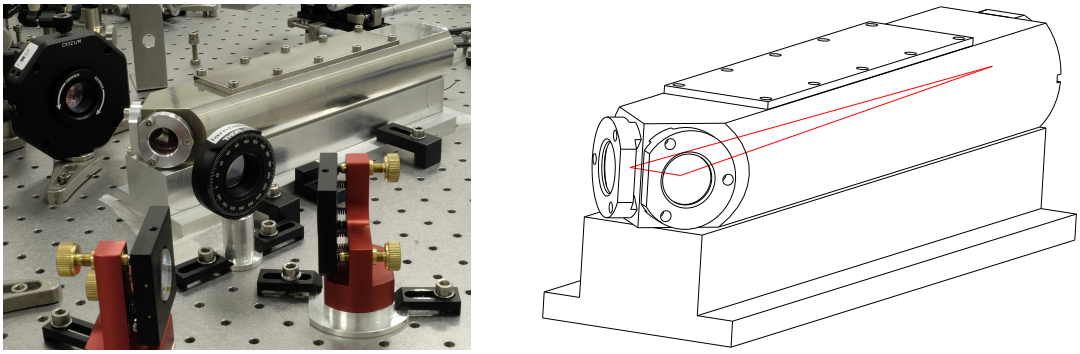

Figure 4.16: Left: photo of the infrared modecleaner cavity installed on the bench. Right: 3D model of the MCIR cavity.

The cavity is held on resonance on the ML beam using the PDH technique. Its input beam is phase modulated at frequency of 80 MHz with the same EOM used for the SHG servo loop. The error signal is taken from the photodiode $MCIR_{PD1}$ placed in reflection to the cavity. The demodulation, for PDH error signal extraction, is provided by one of the 4 channels of the DDS board used to drive the EOM and to demodulate the signal of SHG_{PD1} photodetector. This servo loop is based on only a photodiode, thus the signal used for the autolocking procedure is extracted from its DC monitor. The scheme of the loop is shown in Fig. 4.15. Fig. 4.17 and Fig. 4.18 show respectively its optical chain transfer function and its open loop gain transfer function. The servo loop used to lock in length MCIR cavity is composed by two single poles one at 1 mHz and one at 3 kHz and the obtained unitary gain frequency is at about 350 Hz.

4.5.2 Balanced homodyne detector

The working principle of an homodyne detector is described in Sec. 2.6.2. The design and development of the homodyne electronic board, installed in the squeezer in EGO site, is performed by the INFN Roma I group. As mentioned in Chap. 2 this detector can be designed with two completely different schemes:

1. **Variable gain scheme:** the two photodetectors are separately amplified by

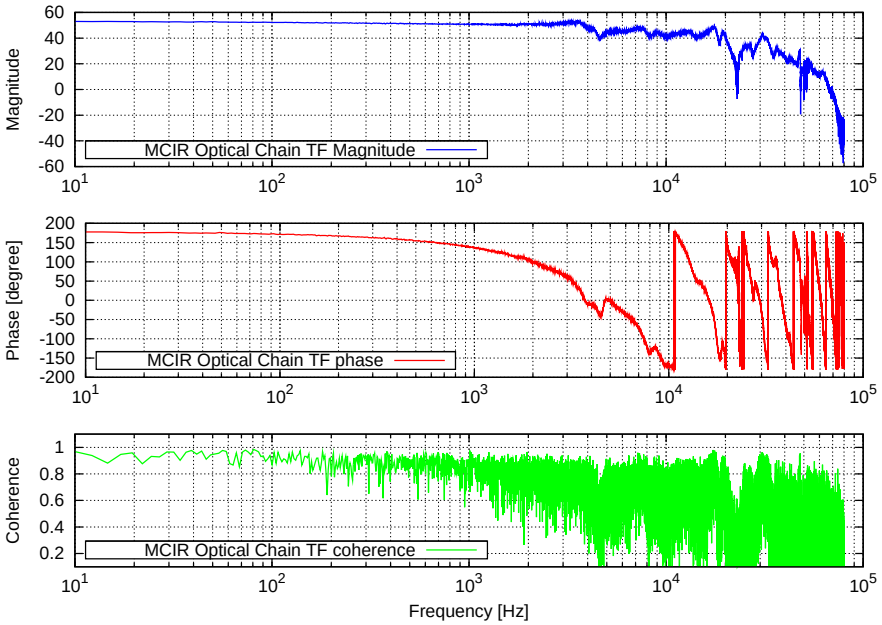

Figure 4.17: Optical chain transfer function of MCIR cavity. Blue trace: magnitude. Red trace: phase. Green trace: coherence. The TF shows a almost constant gain from 1 Hz to 10 kHz. After the system shows some structures.

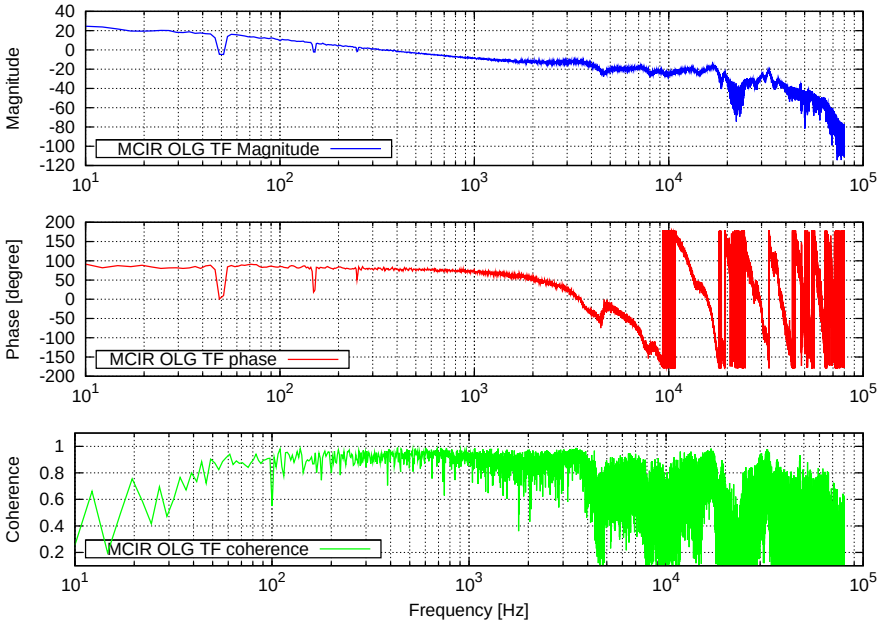

Figure 4.18: Open loop gain transfer function of MCIR cavity. The servo loop is composed by a single pole at 1 mHz and a single zero at 3 kHz. Blue trace: magnitude. Red trace: phase. Green trace: coherence. The obtained unitary gain frequency is about 350 Hz.

two transimpedance amplifiers with variable gain G. After the amplification

the two output signals are subtracted. In this system, the uneven optical power on the two photodiodes can be balanced electronically by acting on the transimpedance gain stages.

2. **Self subtracting current scheme:** the two photocurrents are firstly subtracted and the difference is amplified by an unique transimpedance stage. In this setup the balancing must be done optically by equalizing the light power on the two photodiodes.

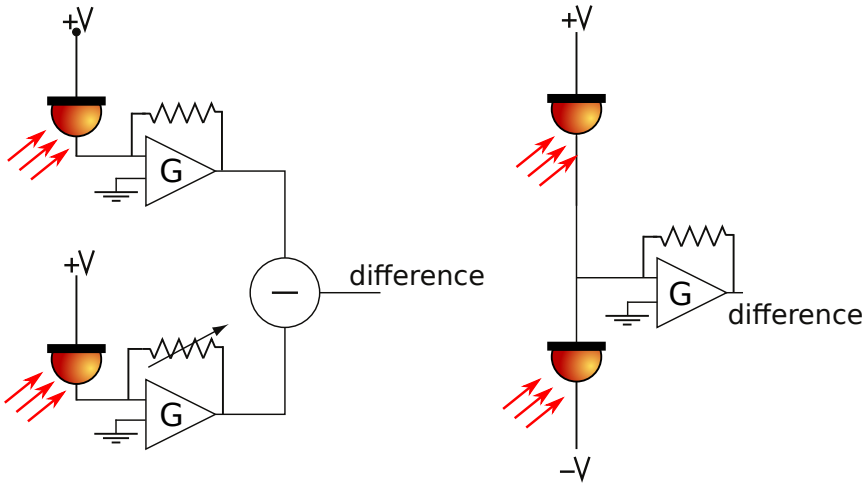

Figure 4.19: Left: homodyne detection with variable gain scheme. Right: homdyne detection with self subtracting scheme.

A sketch of the two detection schemes is shown in Fig. 4.19. Even if the first setup seems easier to manage, a gain difference between the two photodetectors causes a discrepancy between the measured squeezing level and the real produced squeezing level [30], therefore the second design is preferred for squeezing degree measurement. In addition with self subtracting scheme the classical noise sources are reduced because of the signal conditioning and amplification stages are common for both the detectors.

Principal features of the electronic board

Fig. 4.20 shows a conceptual scheme of the electronic board and a picture of the implemented setup. The two photodetectors work in reverse bias generated by an unique power supply. In this way the voltage fluctuations appears as a common-mode noise source for both the detectors. The board is equipped by five output channels: the photodiodes DC channels, $DC1$ and $DC2$, used during the detector alignment and as monitor of the total incoming power, the audio difference channel A_- that is band passed between 10 Hz to 110 kHz and it is used for the quadrature variance

measurement; the RF difference channel R_- that is band pass filtered between 1 to 120 MHz used for the quadrature variance measurement in the radiofrequency region and to provide the error signal for the squeezing ellipse angle stabilization; the audio sum channel A_+ filtered in the same way of A_- used to compute the Commod Mode Rejection Ratio of the detector. For additional information on the homodyne electronics, the reader is addressed to the Advanced Virgo Squeezer Techincal Design Report [44]. In the following the homodyne alignment procedure and characterization is described.

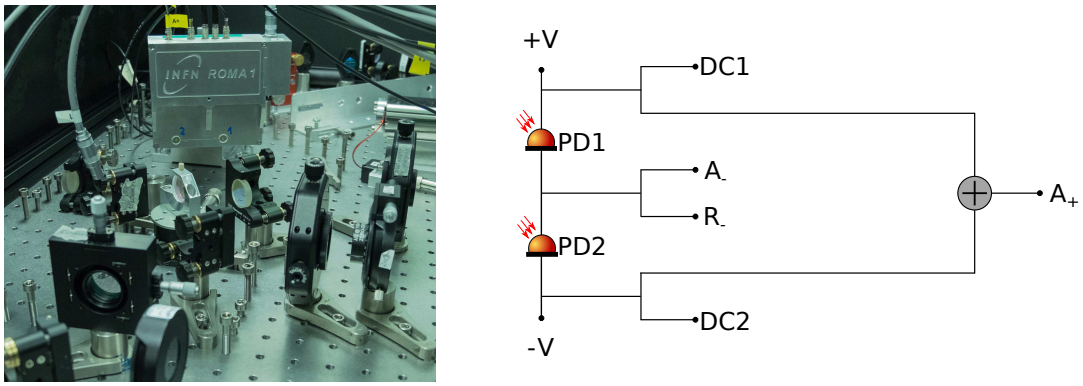

Figure 4.20: Left: homodyne detector conceptual scheme. Right: photo of the homodyne detector.

Photodiodes choice and detector alignment

For the optical quantum state detection the choice of the photodetectors must observe the following key features:

- a low dark current;
- an high quantum efficiency in order to reduce the detection losses;
- a wide area in order to minimize the clipping due to beam jitter effect.

In this work custom photodetectors made by the Fraunhofer Heinrich-Hertz-Institute are used because they active area has a diameter of 500 µm and they have quantum efficiency higher than 99% [30]. As it is shown in (Fig. 4.1 and in Fig. C.1) the homodyne detector is mounted tilted by 20° because the two photodetectors have an antireflection coating of $R < 0.05\%$ optimized for a light incident angle of 20°. As said before, in the self-subtraction scheme, the two photodiode input powers balancing must be performed optically and it must compensate the non identical quantum efficiency of the two photodiodes. It can be achieved in two ways: first the 50/50 beam splitter, in front of the homodyne, is slightly polarization sensitive, thus the

splitting ratio can be tuned changing the two input beam polarization acting on the half-waveplate placed along them beam paths. Second the splitting ratio depends on the BS orientation, thus it is placed on a graduated rotational stage that allows to fine adjust its position in a range of $\pm 2°$.

4.5.3 Homodyne detector characterization

The left plot of Fig. 4.21 shows the characterization of the photodiode DC1, i.e. the output voltage of DC1 as a function of the incoming LO power, that is measured by placing a power meter in front of the other photodiode PD2. DC1 shows a saturation at incident power of about 1.8 mW. The data points are fitted with a piecewise function shown in green. The first five points are fitted with a linear function with angular coefficient of $0.722(2)\,\mathrm{V\,mW^{-1}}$ whereas the last two points are fitted with a constant function $f(x) = a$ where $a = 1.328(6)\,\mathrm{V}$.

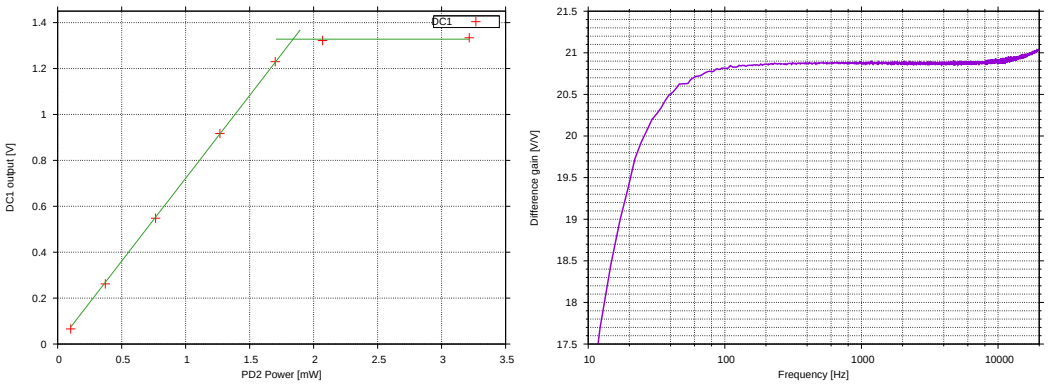

Figure 4.21: Left: measured output voltage DC1 as function of its incoming power measured in front of the photodiode PD2. The red points represents the data whereas the green line is a fit performed with a piecewise function: the first 5 points are fitted with a linear function, whereas the last two points are fitted with a constant function. Right: gain of difference audio A_- channel respect to sum audio A_+ channel as function of the frequency. From 100 Hz to 20 kHz the gain is constant and equal to 21.

The right plot of Fig. 4.21 shows the gain measurement of the difference audio channel A_- respect to the sum audio channel A_+. This measurement is performed by stopping the light path from the beam splitter to one of the two photodiodes, after that is performed the power spectrum of the two channels A_+ and A_-. The ratio between the square root of these two spectrum is the gain of the difference G_{A_-} respect to the sum channel expressed in [V/V]. G_{A_-} is flat between 100 Hz and 20 kHz and is equal to 20.875.

The photodiodes common mode noise arising from the LO technical noise can be suppressed balancing the optical power of the two beam splitter outputs. The

quantity that measures the common mode noise cancellation is called the *Common Mode Rejection Ratio* (CMRR) that is defined as the ratio of the power spectrum between the difference output A_- and the sum output A_+. In the computation of this quantity the difference PSD must be normalized for the measured gain G_{A_-}.

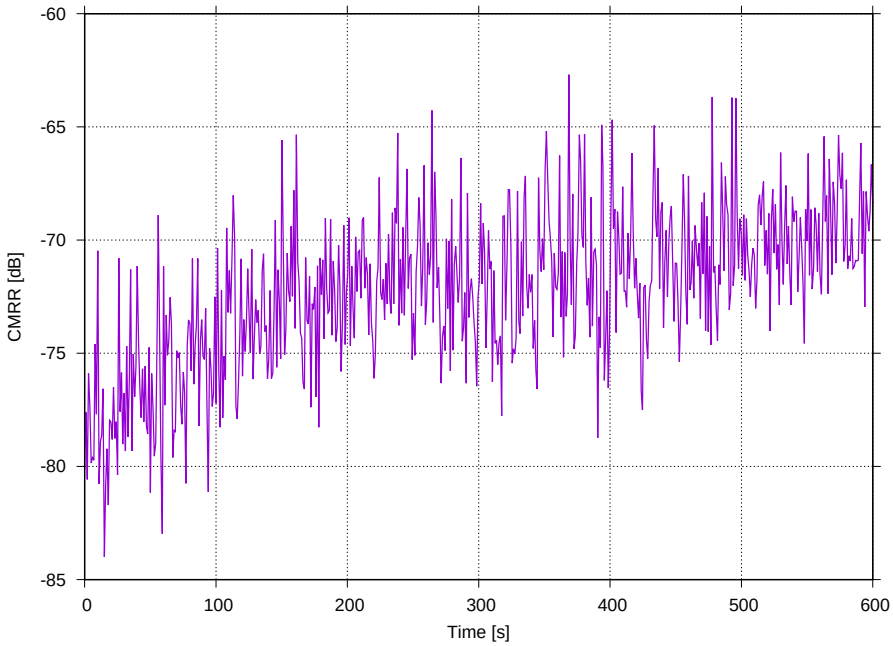

Figure 4.22: Degradation of the homodyne CMRR during the time. In the first 150 s the CMRR decreases of almost 10 dB.

The maximum CMRR achieved is around $-80\,\mathrm{dB}$. This operation is performed in two steps. Firstly a rough power balancement is done equating the DC1 and DC2 output voltages. After that an amplitude modulation of the laser at 110 Hz is turned on and the fine alignment is achieved by minimizing this frequency peak in the difference real time FFT without decrease the respective peak amplitude in the sum real time FFT spectrum. The obtained CMRR is checked for different modulation frequency applied to the ML. After the alignment a rapid degradation of the CMRR during the time is observed, see Fig. 4.22. This was measured with the following procedure: the optical power of the two beams after is balanced as well as possible obtaining a CMRR of 80 dB. After that the bench is covered and the alignment is not touched for the following 600 s. The amplitude modulation is not turned off and the A_+ and A_- channels are acquired for 600 s with a sampling frequency of 10 kHz. The obtained data strings are divided in substrings with the length of 1 s and for each string is computed the CMRR that is averaged in a frequency region of $\pm 10\,\mathrm{Hz}$ around the modulation peak. Fig. 4.22 shows that the CMRR degrades rapidly from

-80 dB to -70 dB in less then 3 minutes after that it is more stable. The reason of this behavior is not clear, further investigations are required.

Finally, the linear response of the homodyne detector as function of the incoming LO power is checked. Left side of Fig. 4.23 shows the power spectral density of the homodyne Radio difference channel R_- as function of the LO incoming power. The spectrum is quite flat in the range between 1 and 10 MHz for each incoming power. This measure is performed with a spectrum analyzer that was set with the following parameters: a resolution bandwidth of 300 kHz, a video bandwidth of 100 Hz and an input impedance of 50 Ω . For each PSD its RMS value between 1 and 10 MHz is also computed. The RMS value versus the the LO incoming is plotted in Fig. 4.23 right. In the plot are shown both the experimental data and a linear fit of them that evinces a linear behavior of the detector measured noise power as function of the incoming light power, as expected for a well designed homodyne detector.

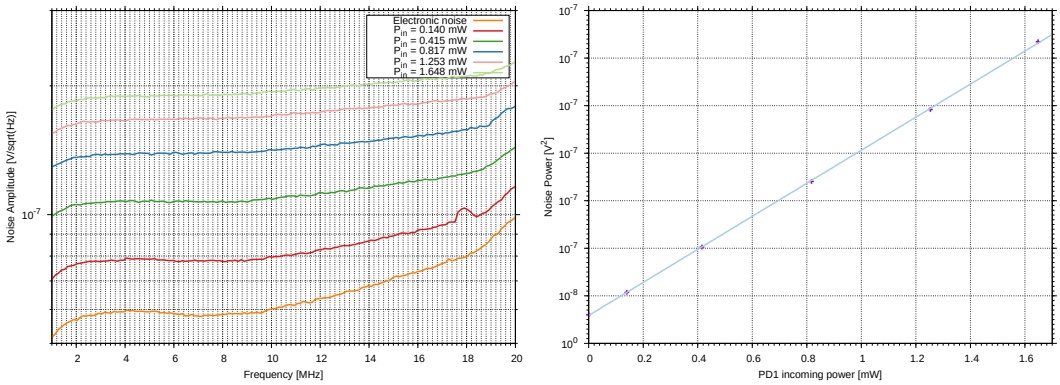

Figure 4.23: Homodyne characterization. Left: power spectrum of the radio difference channel as function of the LO incoming power. RMS value between 1 and 10 MHz of the radio difference channel as function of the incoming LO power.

4.6 OPO cavity and squeezing generation

The most important element installed on the bench is the squeezing cavity, i.e. the optical parametric oscillator (OPO). Fig. 4.24 shows a sketch of OPO optical elements (left side) and a photo of the cavity installed on the bench in the Virgo site. The mechanical design of the cavity is identical to the one used for the SHG, but with a different incoupling mirror. Its inner part has a radius of curvature of 25 mm, a reflectivity at IR wavelengnth $R = 92\%$ and $R = 20\%$ at green wavelength. Its outer external side is a planar surface with an infrared and a green reflectivity of $R < 0.2\%$

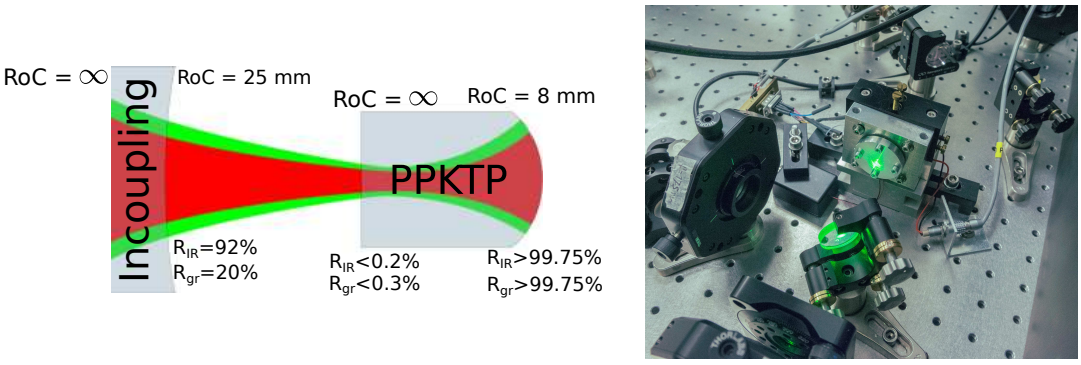

Figure 4.24: Left: OPO optical component scheme. All the reflectivity and curvature radii are reported. Right: photo of the OPO cavity installed in the optical bench in the Virgo site.

With these components the resulting cavity has at the fundamental wavelength: a finesse $\mathcal{F} = 75$, a free spectral range (FSR) of approximatively 3.74 GHz and a full width half maximum (FWHM) of approximatively 50.66 MHz; whereas at the green wavelength it has a finesse $\mathcal{F} = 3.7$, a FWHM of approximatively 1.01 GHz.

As for SHG cavity the OPO is equipped with an high performance crystal temperature stabilization with the aim to maintain the phase matching condition between the fundamental (squeezed) and the harmonic (pump) field. The mechanical building, the Peltier actuator and the controller board are the same used for the other cavity, whereas here the used sensors are two PT100 thermoresistors. The quasi-phase matching condition temperature is equal to 32 °C (see Fig. 4.26).

4.6.1 Cavity length stabilization

The scheme used in this work for OPO length locking was introduced in the development of the squeezer for GEO600 gravitational wave observatory [50]. It consists in the length locking of the OPO cavity in the p-polarization in order to no add technical noises in the squeezed light polarization (s-polarization). This result is obtained with the configuration shown in the light red and in the light blue regions of Fig. 4.25. The OPO's p-polarized locking beam is provided by the (AUX2) laser and has a power of about 170 mW. The OPO length locking is performed with the PDH technique actuating on the piezoelectric element that is connected to the cavity incoupling mirror. The AUX2 beam is phase modulated with an EOM driven at 78 MHz. The used EOM is broad band and is made resonant with a custom RLC resonator developed by the EGO electronic group. The PDH error signal is detected with the photodiode OPO_{PD1} placed in transmission from the OPO cavity. As the MCIR, the OPO length loop is based only on one photodetector, thus the signal used

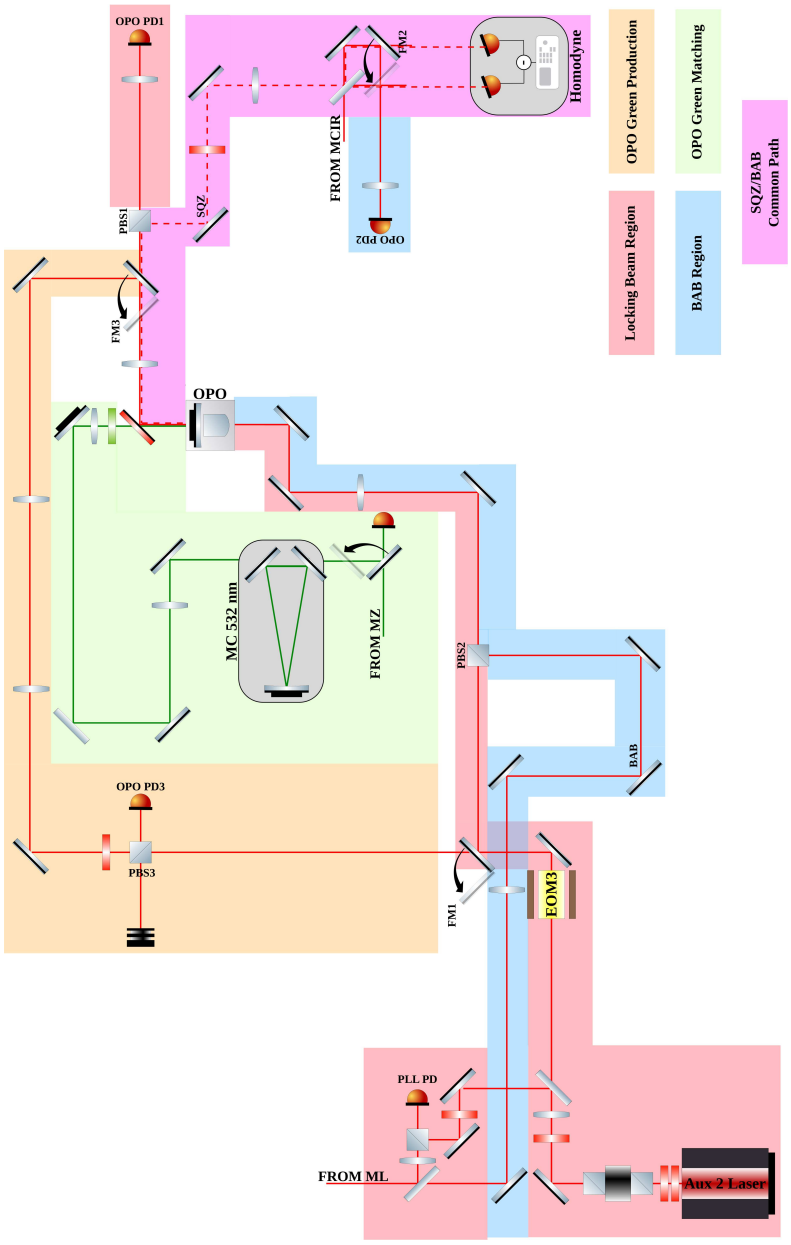

Figure 4.25: Optical layout of OPO region on the squeezing optical bench. A color code is used to divide the different region of this scheme. Light red: all the optical elements related to the length locking of OPO cavity. Light orange: all the optical elements used to configure the OPO cavity as a second harmonic generator. Light blue: bright alignment beam path. Light green: green pump matching with the OPO cavity. Violet: bright alignment beam and squeezed light common optical path.

for the autolocking procedure is extracted from its DC monitor.

When the OPO is locked on a p-polarized beam, due to the birefringence property of its nonlinear crystal, the s-polarized light does not resonate inside it. This problem is avoided by shifting the frequency of the AUX2 laser with a quantity $\Delta\omega$ respect

the frequency of the ML laser, exploiting an OPLL servo loop technique, that will be deeply explained in Chap. 6. In this way the p-polarized AUX2 beam at frequency $\omega_0 + \Delta\omega$ resonates inside the OPO simultaneously with the s-polarized ML beam at frequency ω_0.

A s-poalrized ML pick-off, the Bright Alignment Beam, is injected inside the OPO simultaneously to the p-polarized beam and superposed to it (see light blue region of Fig. 4.25. The BAB is used to measure how much the resonance condition of the two beams differs in frequency $\Delta\omega$. This is performed, with the green pump turned off, as follows: when both the beams are injected into the OPO, the cavity is scanned sending a triangular ramp tu the PZT actuator. With a photodetector, placed in transmission from the cavity, the resonance peak of the two polarizations are monitored. When the offset $\Delta\omega$ was set to 400 MHz the resonance peaks were superposed. This condition is the so called *co-resonance condition* and its frequency $\Delta\omega$ slightly decreases when the green pump is turned on. This effect is due to the power absorbed by the crystal. The OPLL error signal is the beat note between the two lasers taken from the photodiode PLL_{PD}. Because of the detection bandwidth of the used photodiode amplifier (PD_{PLL1}) is 100 MHz the OPLL servo loop is closed with an offset of 150 MHz and the other 200 MHz are obtained by moving the crystal temperature of one 1 °C from the phase matching condition temperature. In this way the OPO does not work in the optimal condition, but this will be fixed soon in the future changing the used photodiode PLL_{PD}.

When the green field is turned on, the crystal absorbs part of its power and the s/p polarization superposition frequency $\Delta\omega$ slightly changes. With the used electronic system this problem can be solved in two equivalent ways: by slightly changing the crystal temperaure or by changing the frequency offset of the OPLL servo loop. When PLL_{PD} will have an adequate bandwidth, the coresonance frequency can be tuned only acting on the OPLL offset frequency and without changing the crystal temperature from the phase matching condition.

The cavity locking, on the p-polarization using a second lasers, has a drawback: the fluctuations of the pump power induce a slightly change of the coresonance frequency $\Delta\omega$ that causes a detuning of the OPO cavity. For ths reason, a green power stabilization scheme is implemented on the bench, as it explained in Sec. 4.4.

Green pump matching

The locking beam of the OPO cavity can be also used for another purpose: the matching of the green pump beam with the squeezer cavity. In fact, a spatial overlap

between the pump field and the squeezer cavity eigenmodes is required for two reasons: first an higher matched amount of green allows to couple more green power inside the OPO and to reach an high parametric gain; second to reduce the interaction between the green field and the high order modes at the fundamental frequency inside the cavity. This interaction could cause to squeeze/antisqueeze higher order spatial modes and to decrease the achievable degree of squeezing in the TEM_{00} mode.

The matching of the green pump field is performed with a reverse scheme, i.e. by forcing the cavity to produce green light and by matching this generated green light to the MCG cavity. This is obtained by injecting an s-polarized IR beam inside the OPO through the flat side of the incoupling mirror, this beam is frequency doubled thanks to the presence of the nonlinear crystal. The setup used for this aim is shown in the orange shadowed part of Fig. 4.25: the locking beam is deflected with a mirror mounted on a flip-mount (FM1), its polarization is rotated from p to s with an half-waweplate and it is matched to the OPO cavity through a telescope. The OPO is held on resonance on this beam with a temporary PDH servo loop, whose error signal is extracted with the photodetector OPO_{PD2} placed in reflection from it. With this setup the OPO behaves as a SHG cavity and the green produced is matched with the MCG cavity using a telescope. This part of optical layout is shown in the green shadowed region of Fig. 4.25. The mode matching achieved is about 90% and it is measured with the photodiode OPO_{PD3} placed in transmission of the MCG.

Moreover, this configuration is exploited to measure the phase matching curve of the cavity. The curve is measured by fixing the IR input power and by changing the PPKTP crystal temperature. For each temperature value the cavity efficiency is measured. Fig. 4.26 shows the phase matching curve of the OPO cavity, used as SHG, for four different value of IR input power. The optimal phase matching condition is achieved at 32 °C.

4.6.2 Alignment beam

An s-polarized auxiliary beam, at the fundamental frequency ω_0, is injected into the OPO cavity through the curved face of the PPKTP crystal. This beam, called Bright Alignment Beam (BAB), is a pick-off of the ML source and has a power of 17 mW. It is injected in the OPO cavity superimposed on the locking beam exploiting a polarizing beam splitter PBS2 (see the blue region of the Fig. 4.25). This beam is employed for different purposes:

- the alignment of the squeezed light beam with respect to the interferometer or to the homodyne detector;

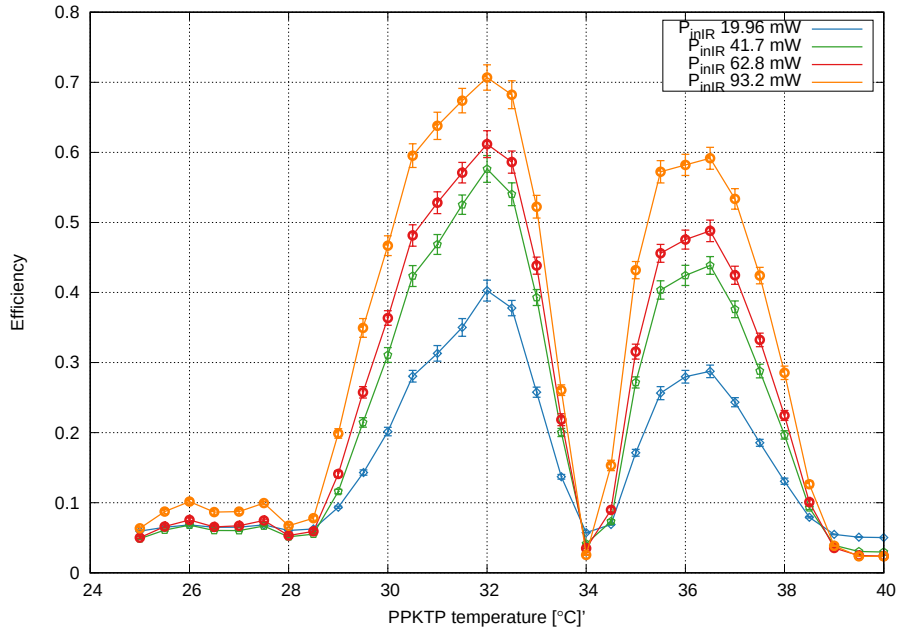

Figure 4.26: Phase matching curve of the OPO cavity when it is used as SHG cavity. The plot shows the curve measured at four different input powers.

- to measure the frequency offset $\Delta\omega$ between the resonance condition of the s-polarized and p-polarized beam inside the OPO cavity (see Sec.4.6.1);
- to measure the OPO pump power threshold by exploiting the DFG phenomenon.

The BAB is used only for service purposes, then it is shuttered when it is not used.

OPO threshold power measurement

The OPO threshold power is measured exploiting the classical parametric amplification process, in which the signal field is amplified/deamplified as it is explained in Sec. 3.2.1. This measurement is performed by injecting simultaneously the s-polarized BAB field, oscillating at frequency ω_0, and the green pump field, oscillating at frequency $2\omega_0$, inside the cavity. As it is shown in Eq. 3.27, the signal field can be amplified or deamplifed depending on the relative phase between the injected signal field and the pump field. Moreover the amplification/deamplification ratio, i.e. the nonlinear gain, depends on the ratio between the injected pump power and the threshold pump power, therefore by measuring this ratio at different green powers it is possible to determine experimentally the OPO pump threshold power.

This measurement is performed with the following procedure:

- the OPO is held on resonance using the p-polarized locking beam, generated by

the AUX2 laser. As explained above, this laser source is frequency locked to the ML using the OPLL technique. This time the OPLL beat note is detected using a photodetector with a bandwidth of (2 GHz). Now the coresonance condition of the s and p polarization into the OPO cavity is obtained only by shifting the AUX2 laser frequency by the quantity $\Delta\omega$ without acting on the OPO crystal temperature;

- the OPO crystal temperature is set at the phase matching temperature (32 °C);
- the green pump field is injected into the OPO cavity from the flat side of the incoupling mirror.
- for each pump field power the OPLL offset frequency is adjusted in order to compensate the crystal absorption, the green pump phase is changed by acting on its optical path length actuating on piezoelectric element attached to a mirror along the green field path (PZTM1).

With this procedure the BAB is or amplified or deamplified by the nonlinear process dependin on the BAB versus green phase difference. Therefore by measuring the BAB power in transmission from the cavity with the photodiode OPO_{PD2} in both the situations the amplification/deamplification ratio can be measured. Fig. 4.27 shows the OPO parametric gain as a function of the PUMP power. The scattered points represent the experimental data, whereas the lines represents a fit of the experimental data, in particular the blue points and line correspond to the OPO amplification regime, whereas the red ones correspond to the deamplification regime. The fit is performed using Eq. 3.27 where the free parameter is the pump threshold power that results equal to: 114 ± 2mW.

BAB alignment with the homodyne detector

In Sec. 2.7.1 it is shown how much the matching between the squeezing and the LO beam affects the homodyne detection efficiency. Therefore the two beams must have the same: waist position and dimension, spatial mode, polarization and propagation direction. This is achieved as follows. First the LO beam is prepared with a waist diameter of 31 µm. The waist position falls at the middle distance between the two homodyne photodetectors. Second the BAB is turned on and a matching telescope is designed in order to have the same waist position and dimension of the LO (violet part of Fig. 4.25. Then, the beam are overlapped on the beam splitter and are made co-propagating acting on the steering mirror along their optical paths. Once performed

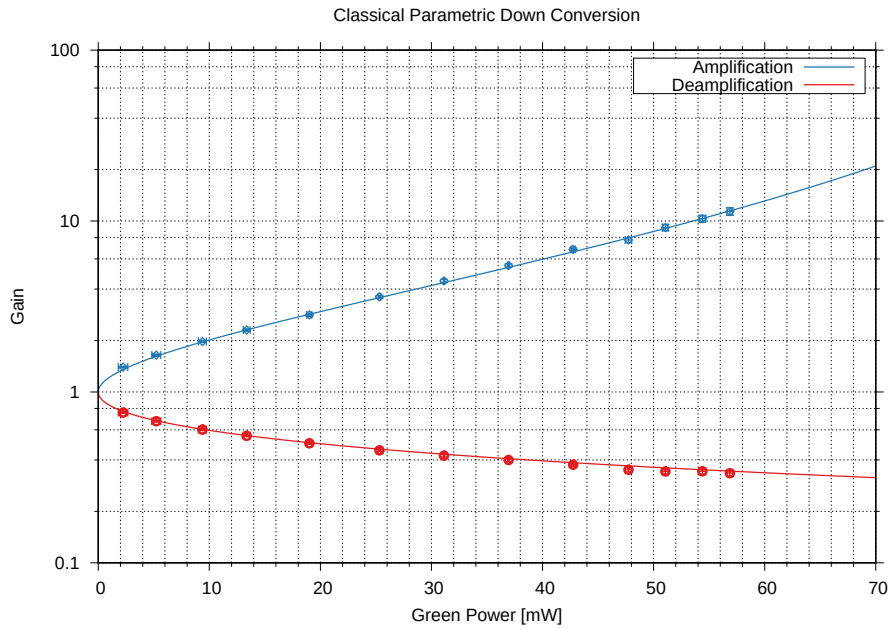

Figure 4.27: Parametric gain measurement of OPO cavity. The scattered points represent experimental data, whereas the line represents their fit. Blue: amplification regime. Red: deamplification regime.

this alignment, the interference fringe visibility $\mathcal{V}$, of the two beams, is measured as an estimator of the goodness of the obtained matching. The fringe visibility is measured using the photodetector OPO_{PD2}, after having equalized the powers of the two beams. This photodiode is used only for alignment purposes, thus it can be used by deflecting the transmitted beam by the homodyne BS with the flipping mirror FM2. A scan of the interference fringes is performed changing the LO beam phase by acting on the piezoelectric actuator linked to the mirror PZTM2, placed in its beam path. The visibility is given by the following equation:

$$\mathcal{V} = \frac{I_{max} - I_{min}}{I_{max} + I_{min}},$$

where I_{max} and I_{min} are respectively the maximum and the minimum of the measured fringes. Fig. 4.28 shows a plot of the best visibility achieved for the bench developed in Virgo. The scan is performed at 30 Hz and the obtained visibility value is of $\mathcal{V} = 97\%$.

4.6.3 First squeezed light states measurement

With the developed squeezer only a preliminary measurement of squeezed states was performed and it is sown in Fig. 4.29. The figure sows the noise powers at the Fourier frequency of 1 MHz with a resolution bandwidth of 300 kHz. The greem trace

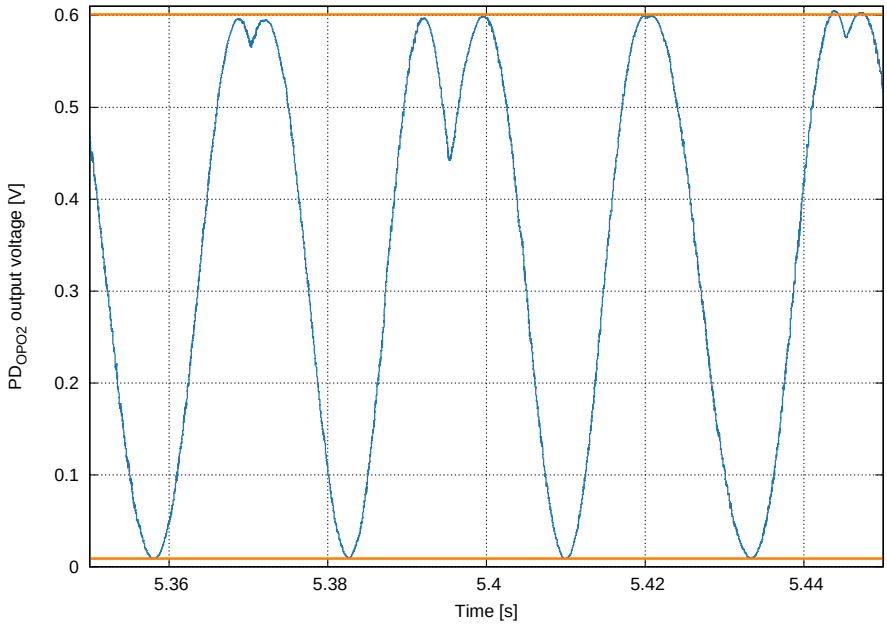

Figure 4.28: Visibility fringes after the matching between the LO beam and the transmitted BAB beam after OPO cavity.

corresponds to the shot-noise due to 3.6 mW of total LO power (1.8 mW per each photodiode of the homodyne detector) , measured when the squeezed light beam was shuttered. The blue trace shows the quantum noise reduction/enhancement due to squeezed/antisqueezed states injected into homodyne detector beam path through the beam splitter. These states are generated by pumping the OPO cavity with 69 mW of green field, whereas the relative phase between the signal and LO fields is adjusted by rapidly changing the pump field phase moving PZTM1 with a triangular ramp oscillating at 120 Hz. This frequency is chosen in order to change the green phase more rapidly than the natural oscillations of LO field phase that were not controlled during the measurement. The red trace is the detector dark noise that is approximately 11 dB below the LO shot noise level and its mean value is subtracted from the other two traces. In the figure the three traces are shifted to have the LO mesured mean value at 0 dB. This measure is performed with the same spectrum analyzer used for the homodyne detector characterization, i.e. model FSH4 of Rohde Schwartz manufacturer. The measure was acquired in time domain by setting the instrument in the zero-span mode, a time window of 20 ms and 300 kHz of resolution bandwidth. From the figure a raw estimation of squeezing and antisqueezing degree can be extracted, i.e. the reached squeezing degree is about -6 dB and the antisqueezing one is about 15.0 dB respect to the LO shot-noise level.

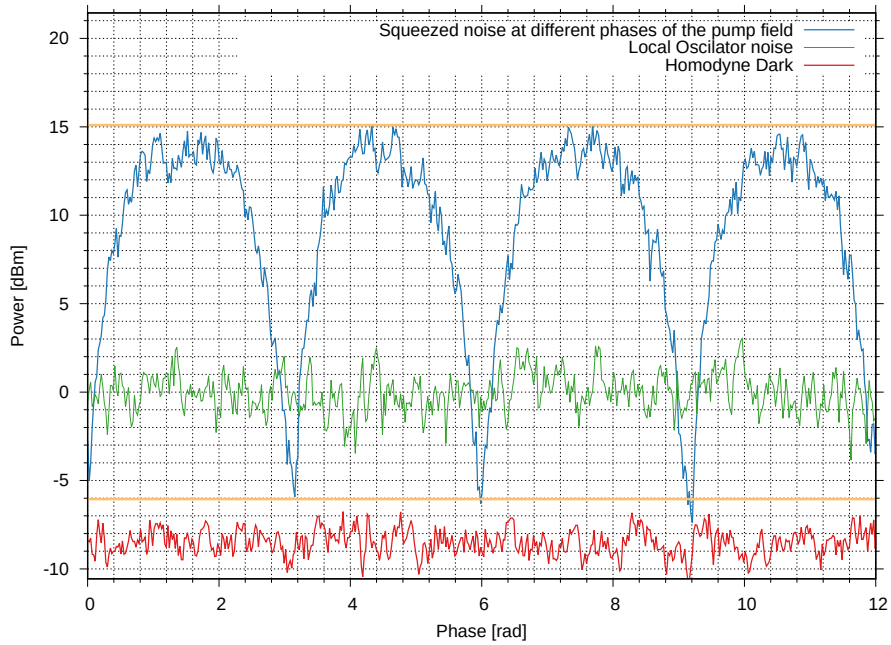

Figure 4.29: First characterization of squeezed light at 1 MHz of detection frequency, 300 kHz of RBW and 20 ms of acquisition time. Red trace is the homodyne dark noise, green trace is the LO shot noise and the blue trace is the reduced/enhanced noise by injecting squeezed/antisqueezed states into the beam path. The traces are normalized in order to set the mean value of LO (green trace) at 0 dB. Orange lines: the expected squeezing and antisqueezing degree computed by considering the parameters of the used OPO and 23% of optical losses.

The orange lines show the expected squeezing and anti-squeezing level computed using Eq. 3.28, where the real parameter of the OPO cavity are inserted and a guess on 23% of optical losses is made. Here below a summary of cavity parameter used for this computation:

$$\eta_{tot} = 0.77 \quad P_{th} = 115\,\mathrm{mW} \quad P = 69\,\mathrm{mW} \quad mm_{gr} = 0.9 \quad R_{inc} = 0.92,$$

where η_{tot} is the total optical efficiency and includes all the losses from the generation to the detection of squeezed light, P_{th} is the measured OPO pump power threshold, P is the pump power used during the measurement, mm_{gr} is the mode matching of the green beam to the OPO cavity and R_{inc} is the reflectivity of the incoupling mirror inner surface.

The squeezing measurement shown in this chapter is performed using the radiofrequency channel of the homodyne detector. A fast characterization is performed also with the A_- channel by acquiring it with UDSPT board for 2 s at a sampling frequency of 160 kHz in the same three configuration measured in the RF characterization: only LO on homodyne detector, LO and squeezed beam and the dark noise of the detector. The data in the time domain are filtered with an RMS filter computed

with Matlab, where the user must insert the center filter frequency and the resolution bandwidth in order to reply the behavior of the spectrum analyzer used in the RF analysis. With this technique 3-4 dB of squeezing are measured until $50 - 60\,\mathrm{kHz}$, but in the near future a more rigorous characterization of squeezed states must be performed.

To conclude the analysis of the first squeezing measurement, the origins of the estimated 23% of loss budget are discussed. As it is shown in Sec. 2.7 the squeezing degree is limited by the optical losses: the propagation efficiency η_{prop}, the photodiode quantum efficiency η_q, the OPO escape efficiency η_{esc} and the homodyne mismatch measured with the fringe visibility $\mathcal{V}$. Thus, in term of these factor, the overall optical losses $(1 - \eta_{tot})$ can be computed given the total efficiency η_{tot}:

$$\eta_{tot} = \mathcal{V}^2 \eta_q \eta_{esc} \eta_{prop}. \tag{4.2}$$

The homodyne visibility and its photodiode quantum efficiency are reported respectively in Sec. 4.5.2 and in Sec. 4.6.2 and are equal to $\mathcal{V} = 0.97$ and $\eta_q = 0.99$ for each photodiode. While the other two factors will be discussed separately.

The escape efficiency of a squeezed light source is defined as:

$$\eta_{esc} = \frac{T}{T + L},$$

where T is the transmission of the output coupler, in our case the incoupling mirror with $T = 0.92$, and L are the intracavity round-trip losses. These include the PPKTP losses due to the residual transmission through the HR-coated backside, i.e. 0.25% (see Fig. 4.24), the (negligible) absorption within the crystal 12 ppm C^{-1} [51], and the residual reflection of the AR-coated frontside, i.e. 0.2% (see Fig. 4.24), which must me taken in account two times. The total amount of the round-trip intra cavity losses can be estimated around 0.65%, thus the OPO escape efficiency is equal to 0.993.

The propagation losses occur due to the non perfect IR transmission of the harmonic beam splitter (T is measured equal to 99.5%) and the non perfect anti-reflective coating of the two lenses, which transmission is about 0.99. Moreover, in the beam preparation for the homodyne detector the beam diameter is been over-sized. In fact the prepared beam waist for the homodyne detector has a dimension of 31 µm and its position falls at the middle distance between the two photodetectors, thus one of the two homodyne photodiodes is placed about 1.5 cm before the minimum waist position and the other is placed about 1.5 cm after. Considering that the photodiode have a square active surface with dimension $500 \times 500\,\mu\mathrm{m}$ and that the waist dimension of the beam when it falls on the photodiode is equal to 167 µm, a fraction of the beam

power is clipped by the two detectors. The amount of lost beam power can be estimated with the following procedure. Starting from the function of a bi-dimensional Gaussian ($\mu_x = \mu_y = 0$ and $sigma_x = \sigma_y = \sigma$), i.e.

$$f(x,y) = \frac{1}{2\pi\sigma^2} e^{-\frac{1}{2}\frac{x^2+y^2}{\sigma^2}},$$

remembering that a photodiode is a quadratic detector, the probability distribution function ρ of $f(x,y)^2$ in radial coordinates (r and ϑ) is computed:

$$\rho(r) = 1 - e^{-\frac{r^2}{\sigma^2}}.$$

This result corresponds to the amount of power collected by each detector, therefore, by substituting in the last result σ with the beam waist at the detector position and r with the photodiode radius, one obtains the amount of power collected by the detector. This computation is performed considering the detectors surface area as circular, therefore σ correspond to an effective radius, i.e. the radius of the circle that has the same surface of the photodiode active area, i.e. $r = \frac{500}{\sqrt{2\pi}}\mu$m. Thus the fraction of power collected by each detector is equal to the 94.3%.

All the estimated contributes are inserted in Eq. 4.2 and it is obtained a total efficiency of the squeezing measurement equal to the 80%, i.e. the 20% of detection losses, i.e. a value comparable to the 23% obtained with the measurement shown in Fig. 4.29. In the future the optical losses can be easily decreased by redesigning the beam path from the OPO and LO to the homodyne detector in order to avoid the clipping and to have a visibility greater than the 99% and by replacing the used HBS with an high quality optics with transmission coefficient above 0.999. With these modification we will expect to have a total detection efficiency greater than 95%, i.e. in agreement with the requirement expressed at the beginning of this chapter.

4.7 Next steps of the optical bench

From September 2015, the Virgo squeezing working group is involved in the assembly from scratch a vacuum squeezing source in a clean room placed along the west arm of the Virgo interferometer. The bench is almost complete, i.e. all the cavities and the electronic are installed, but the optical line from AUX1 laser source that will be employed for the squeezing ellipse stabilization is not yet installed and it will be installed in the next months. Here below a lists of the following steps expected in the near future:

- a complete characterization of the produced squeezed light at radiofrequency (1 MHz) as function of the injected pump power in the OPO caivity. This must

be performed for a precise estimation of optical losses and phase noise that affect the system;

- the installation of the squeezing ellipse angle control line and the first lock of the coherent control loop in order to stabilize the ellipse phase jitter [50];
- a complete characterization of the produced squeezed light in the audio-frequency band (see first point);
- reduction of scattered light and optical losses, i.e. installation of the beam dumps and super-polished optics;
- optimization of all the servo loops in order to lock the cavities with a unitary bandwidth as big as possible;
- improvement of the green pump power stabilization level.

Chapter 5

Digital synthesis of radiofrequencies

Several RF channels with frequencies up to 100 MHz are required to put in operation the squeezer source. In particular the Virgo squeezer requires:

- 3 RF signals at 80 MHz: one for phase modulating the master laser's beam and two for demodulating the signal in reflection from the Second Harmonic Generator (SHG) and the Infrared Mode Cleaner (MCIR);
- 2 RF signals at 78 MHz: one for phase modulating the AUX2 laser's beam and one for the signal demodulation;
- 2 RF signals at 30 MHz: one for phase modulating the green beam and one for the the signal demodulation;
- 1 RF signal at 150 MHz: as offset of an Optical Phase Locked Loop (OPLL) between the master laser and the slave laser AUX2 with the aim of ensuring the coresonance condition of s and p polarizations into the OPO cavity;
- 1 signal at 7 MHz: as offset of an OPLL between the master laser and the slave laser AUX1 in order produce the frequency offset of the coherent control beam;
- 1 RF signal at 14 MHz: for the demodulation of the coherent control error signal;
- 1 RF signal at 7 MHz: for the demodulation of the homodyne RF difference channel to extract the error signal for the LO phase stabilization;
- 1 RF signal at 80 MHz: as offset of an OPLL between the master laser and the Virgo main laser.

Therefore a total of 12 signals between 7 MHz and 80 MHz are required for the squeezer's controls. The frequency range is not the only requirement in the clock generation but also a low residual phase noise is required. Moreover, for the remote management of the squeezed light source, the presence of a software, that allows to change the amplitude, pahse and frequency of each channel, is required.

Among the different possible solutions for RF generation we decided to use the direct digital synthesis (DDS) of clock [52]. This is a technique based on digital processing blocks for the generation of a frequency and phase tunable output signal that is referenced to a fixed frequency source called reference clock. Besides the cost-competitive and its integration in a single chip, other key features of Direct Digital Synthesizer (DDS) are: the micro-hertz frequency tuning resolution of the output frequency and its micro-radian phase tuning; the continuous frequency and phase hop without overshoots or settling times anomalies and the digital control of the chip that helps us in the development of the remote device's management.

This chapter is organized as follows: Sec. 5.1 discusses the principle of operation of a DDS single chip, Sec. 5.2 shows how the Virgo DDS system is implemented, finally Sec. 5.3 and Sec. 5.4 show the phase noise performances of the system.

5.1 DDS principle of operations

A DDS chip contains three principal elements: a phase accumulator, a phase to amplitude converter (sine look-up table) and a digital to analog converter (DAC), see Fig. 5.1. The input of a DDS chip are: the reference clock at Radiofrequency (RF) frequency ν_{ref}, the frequency tuning word and other set-up parameters. The output is a sinusoidal signal at a frequency $\nu_{out} < \nu_{ref}/2$.

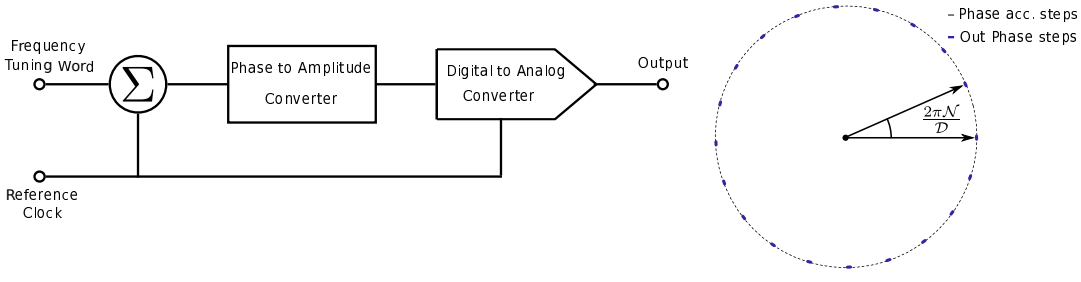

Figure 5.1: Left side: block scheme of a DDS chip. Right side: sketch of phase accumulator's operation

The first block of the scheme is the phase accumulator. The right side of Fig 5.1 illustrates the operation of this block. One can image the phase of the DDS output signal as a unitary vector rotating with constant speed around a phase wheel. A

complete revolution of this vector consists in one period of the output sine wave. The number of discrete phase points in the wheel is the resolution of the accumulator $\mathcal{D} = 2^p$ where p is the number of bits of the accumulator. At each reference clock rising edge the vector rotates of $\mathcal{N}$ steps in the wheel, where $\mathcal{N}$ is called the frequency tuning word of the DDS chip. If the phase overflows the length of the register the vector restarts the turn in the wheel. Therefore the position of the phase vector in the wheel, at the k-th cycle, can be written as:

$$n_k = (n_{k-1} + \mathcal{N}) \mod (\mathcal{D}). \tag{5.1}$$

This technique allows the chip to compute the phase of its output signal at each cycle of the reference clock. Therefore, if the reference clock frequency is ν_{ref}, the frequency ν_{out} of the DDS output is:

$$\nu_{out} = \frac{\mathcal{N}}{\mathcal{D}} \nu_{ref}.$$

The frequency resolution $\delta\nu$ of the phase accumulator is equal to the phase increment of a phase accumulator's bit, i.e. $\delta\nu = \nu_{ref}/\mathcal{D}$. So for example a 32 bit DDS with input frequency of 500 MHz has a frequency resolution of 0.116 mHz. The phase accumulator's output consists in the state variable n_k i.e the number of steps that the phase vector has done in the phase weel at the time t.

The phase to amplitude converter, i.e. the second block of DSS (see Fig. 5.1), is a sort of look up table where each value of the phase accumulator is related to the respective instantaneous amplitude of the output sine wave. Finally, the last block of the DDS chip is the Digital to Analog Converter (DAC) that converts values from the look-up table to an analog voltage [52][53][54].

This description explains only how the DDS chip generates its output frequency from the reference clock, but a real DDS is composed by other circuital elements that make it a powerful and versatile clock generator:

- a reference clock multiplier that allows to generate output frequency higher than the Nyquist theorem's limit $\nu_{ref}/2$;
- a voltage adder after the phase accumulator that allows to add an offset to the phase of the output signal;
- a digital multiplier between the look-up-table and the DAC that allows the user to change the output sine wave amplitude and to turn on an amplitude modulation;

- a memory for frequency phase and amplitude profiles that allows the user to change quickly from a waveform to another one.

5.1.1 Noise sources in a DDS

Sec. 5.1 shows that in a DDS chip the phase accumulator computes the state variable n_k, the look-up-table relates it to a part of the output sine wave and the DAC transposes the value of the look-up-table to an output voltage. There are two limits in these operations. Firstly, a DAC that works at high frequency has a limited number of bits q, for example the Analog Devices company uses a model with 14 bits as DAC with maximum resolutions. Secondly the read only memory (ROM) in which the look-up-table is stored is limited, for example if the phase accumulator has 32 bits and each accumulator steps corresponds to an entry with 8 bits of the look-up-table, the ROM would have more than 4 GB of memory to store the look-up-table. The solution to this problem is the *truncation* i.e. to use only a fraction of the phase accumulator bits. This is mandatory in any case because of the number of bit of the DAC is less than the resolution of the phase accumulator. These two limitations are the sources of two different kind of noises: the first is the quantization noise of the DAC and the second is the generation of spurious frequency lines in the DDS's output spectrum induced by the truncation [52][54].

Quantization noise

The resolution of a DAC is related to its number of bits q. This means that it can change its output voltage with a minimum step equal to the voltage of its less significant bit:

$$V_{LSB} = \frac{V_{FSR}}{2^q}$$

where V_{LSB} is the voltage of the less significant bit and V_{FSR} is the full scale range of the device. For example, Fig. 5.2 shows the reconstruction of a sinusoidal wave with a 4 bit DAC. One can see that the height of a single step is equal to V_{LSB} and the length in the horizontal axis is the sampling time. The distance between the original sine wave and the reconstructed on is called *quantization distortion*. Now we try to quantify the entity of the noise induced by the quantization. The quantization noise is supposed with a rectangular distribution between $\pm V_{LSB}/2$ as it is shown in left side of Fig. 5.3. The variance of the rectangular distribution is equal to:

$$\sigma^2 = \left(\frac{V_{LSB}}{\sqrt{12}}\right)^2 = \frac{V_{FSR}^2}{12 \cdot 2^{2q}}.$$

If the quantization noise is a purely random process, by virtue of the Nyquist theorem

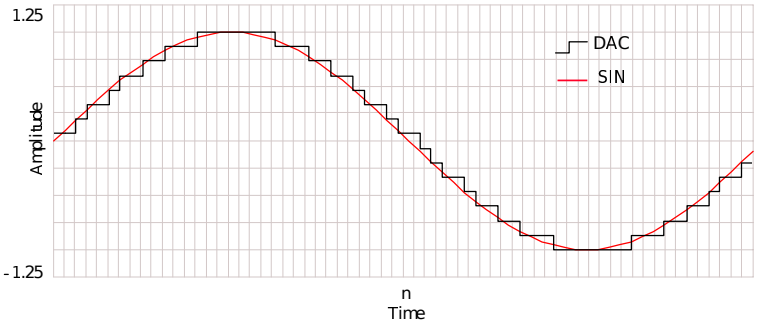

Figure 5.2: Comparison between the DAC output signal and the respective continuous time sine wave

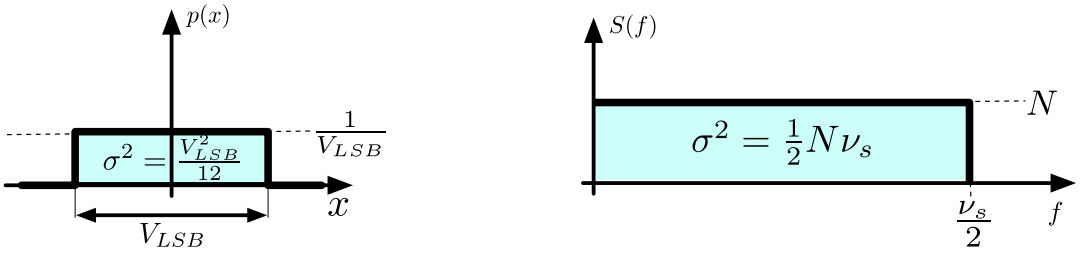

Figure 5.3: Left: probability distribution function of the quantization noise in a DAC. Right: power spectral density of the DAC's noise.

its noise spectrum is uniformly distributed between 0 Hz and one half of the sampling frequency (see the right side of Fig. 5.3). Moreover, the Parseval theorem states that the power calculated in the spectrum is equal to the power calculated in the time domain. So if N is the white noise level in the power spectrum it follows that:

$$N = \frac{V_{FSR}^2}{6 \cdot 2^{2q} \nu_{ref}}.$$

If the generated output uses all the scale of the DAC, the total RMS output power is equal to $V_{FSR}^2/8$ and, from the last equation, the white noise level can be rewritten in terms of DAC output phase noise:

$$PN_{DAC} = \frac{4}{3} \frac{1}{2^{2q} \nu_{ref}}.$$

For example, for a DAC with 14 bits and a reference frequency of 500 MHz the phase noise level due to the quantization error is equal to $-170\ \frac{\text{dBc}}{\text{Hz}}$. Sec. 5.3 explains what the phase noise is and how to measure it.

Finally, Fig. 5.2 shows that the reconstructed sine wave by the DAC is composed by sharp steps. Their presence causes the generation of high frequency spur components in the output spectrum. This kind of spurs is called *quantization spurs* and its contents is related to the DAC resolution. If the resolution of the DAC is increased,

the contents of spurs decreases because the distance between the generated sine wave and its mathematical representation decreases. Another trick to decrease the spurs content in the output signal is the oversampling.

Truncation and spurs generation

In this subsection a second kind of spurs is analyzed, i.e. the spurs generated by the elimination of the less significant bits from the phase accumulator register. Truncation spurs are the most important spurs source in a DDS generator. As explained above, the number of bits of the DAC and the one of the look-up-table is less than the resolution of the phase accumulator. From Eq. 5.1 the output of a look-up-table that uses all the bits of the phase registers is:

$$s[k] = \sin\left(2\pi\frac{\mathcal{N}\nu_{ref}}{\mathcal{D}}k\right) = \sin\left(2\pi\frac{\mathcal{N}\nu_{ref}}{2^p}k\right)$$

where p is the resolution of the phase accumulator. If only the first q most significant bits are used, the last expression can be rewritten as:

$$s[k] = \sin\left(\frac{2\pi}{2^q}\left[\frac{\mathcal{N}\nu_{ref}}{2^{p-q}}k\right]\right)$$

where the expression in the square brackets denotes the truncation. The last expression can be rewritten in term of a phase error ($e_p(k)$) due to the discarded bit:

$$s[k] = \sin\left(\frac{2\pi}{2^p}\left[\mathcal{N}k - e_p(k)\right]\right).$$

Therefore the resolution of the phase accumulator output sequence is decreased by a factor $e_p(k)$ that is a periodic function. The periodicity of this function can generate a series of spur lines in the spectum of the DDS output signal. A simple method to avoid this kind of spurs generation is a careful selection of the frequency tuning word $\mathcal{N}$. For example, there are spurs in the DDS output only if

$$GCD(\mathcal{N}, 2^p) < 2^{p-q}$$

where GCD is the greatest common divider. Conversely, in the opposite case the spurs generation does not happen.[52][53]

5.2 DDS system of Virgo squeezed light source

As explained in the introduction of this chapter, for the proper operation of the Virgo squeezer, at least 12 RF signals are needed with the following features: low

phase noise, output frequency between 7 MHz and 80 MHz and with a precise phase relationship in groups of at least three channels. Therefore boards were chosen that can output up to four different sinusoids synchronized in phase between them. For the development of such boards, I worked in collaboration with the electronic workshop of the INFN Padova. The work on the clock generator boards was divided in two phases. In the first one (until the installation of the third laser and the development of the coherent control loop) two Analog Devices AD9959 Evaluation Boards are used. In the second phase, a custom board based on 4 AD9910 chips of Analog Devices is developed. The first of these new board will be installed in the Virgo laboratory during the implementation of the coherent control loop. This section shows the features and the operation of the two different boards.

5.2.1 AD9959 Evaluation Board

As starting point we focused on the Evaluation Board of the AD9959 chip of Analog Devices which satisfies all our requirements. The most interesting features of AD9959 are [55]:

- 4 synchronized DDS channel @500 M Samples Per Seconds on a single chip;
- independent control of phase, frequency and amplitude of each channel;
- 32 bits resolution of the phase accumulator i.e. a frequency resolution of 0.12 Hz; 14 bit phase offset i.e. phase resolution of 0.02°;
- 4 integrated 10 bit DAC;
- RMS residual phase noise (at 75.1 MHz of output frequency and 500 MHz of reference clock): -135 dBc/Hz @ 1 kHz, -146 dBc/Hz @ 10 kHz, -154 dBc/Hz @ 100 kHz from the carrier.

The detailed block scheme of the chip is shown in Fig. 5.4. This chip is configurable in many ways by using the Serial Peripheral Interface (SPI) protocol: it has ten configurations registers in which an user can set the frequency, phase and amplitude tuning words, the value of the reference clock multiplier, amplitude phase modulation, etc. The main components of the AD9959 evaluation board are the quad-DDS chip and the microcontroller unit (CY7C68013 of Cypress). The microcontroller manages the configuration of the DDS with the SPI protocol and the communication to an external Personal Computer (PC) with the Universal Serial Bus (USB) protocol. Analog Devices provides an Evaluation Software that allows a user to manage all

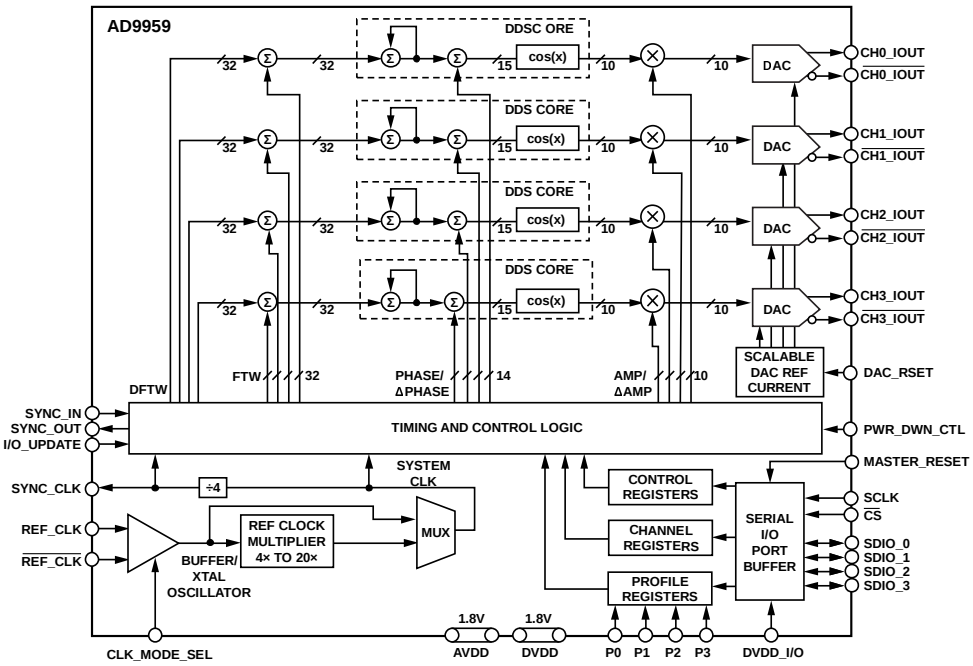

Figure 5.4: Block scheme of AD9959 chip from Ref. [55].

possible configurations of the DDS chip and to save or recall the current configuration of the chip. This software is a simple graphical interface for the communication between the PC and the microcontroller via the USB protocol [55] [56].

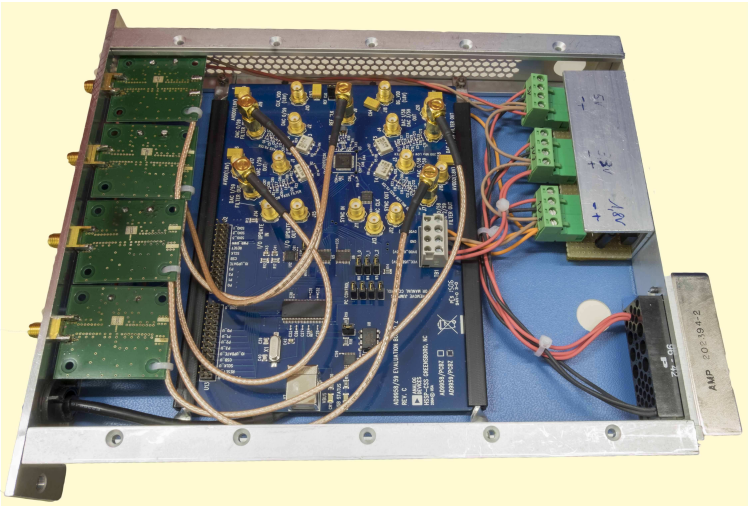

Figure 5.5: NIM box with the AD9959 evaluation board and the four monolithic amplifiers.

Fig. 5.5 shows an AD9959 evaluation board mounted in a NIM box. An amplifier (Minicircuit GALI-51+) is added in series at each output to have an output signal power level equal to +7dBm. The phase noise measurement of this board are shown in Sec. 5.4.

5.2.2 Quad DDS AD9910 Board

As second step we started the development of a 4 channel RF generator based on 4 AD9910 chips in collaboration with the electronic workshop of INFN Padova. The key improvements of the AD9910 DDS chip respect to the AD9959 are[55][57]:

- a single output with frequency up to 400 MHz @ 1 GSPS internal clock speed;
- 32 bits resolution of the phase accumulator i.e. a frequency resolution of 0.12 Hz; 16 bit phase offset i.e. phase resolution of 0.005°;
- integrated 14 bit DAC;
- RMS residual phase noise (at 75.1 MHz of output frequency and 1000 MHz of reference clock): -140 dBc/Hz @ 1 kHz, -150 dBc/Hz @ 10 kHz, -160 dBc/Hz @ 10 kHz from the carrier.

Fig. 5.6-left shows a part of the board layout: on the left the Aria G25, a low cost Linux Embedded SMD module. It is an embedded PC with a Linux operative system that integrates CPU, RAM, Ethernet and EMI components on a single SMD. This embedded module manages the configurations and the communication with the four AD9910 chips and the USB/Ethernet protocol for the parameter setting. In the center of the figure two of the four DDS chips are represented. The phase syncrhronization between the chips is ensured by a specific configuration of their registers and by synchronizing the updating signal from the microprocessor to all the chips. Unlike the evaluation board, each channel is a doublet: a signal with level of +7 dBm and a second signal with variable amplitude range granted by variable gain amplifier (Analog Devices AD8375). The amplifier's gain is changed with SPI protocol by using the software that runs on the Aria G25. Other two on board channels are implemented for distributing the reference clock. This features allows the use of a single reference clock when using more than one board; however this clock distribution does not ensure the phase syncronization of signals generated by different boards.

A C software running on Aria G25 allows the user to configure the four chips on the board. This is a command line software that listens to a command from a Linux shell and sends it to the right DDS chip. The command is composed by three inputs: which DDS chip to configure, the address of the register to configure, the value to send to the selected register in hexadecimal base. This software has two additional functions: it can read all the registers of the four chips and write it on a Linux's shell and finally it can read a default configuration from a file and send it to the DDS chips. The communication between the Aria G25 and a computer is performed by

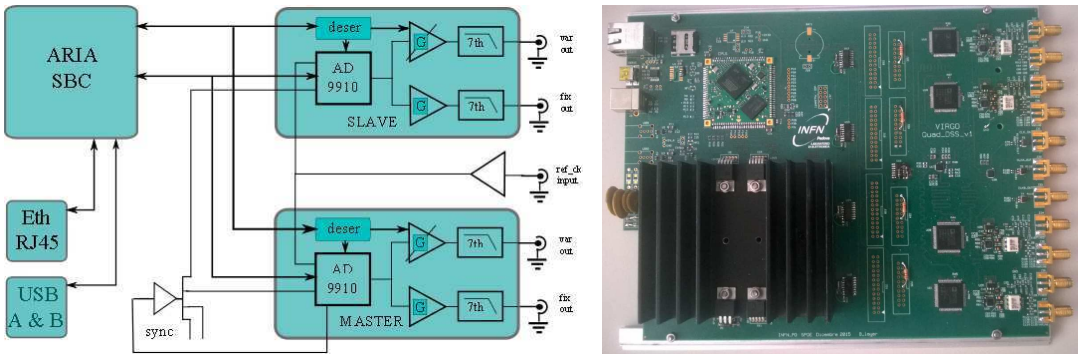

Figure 5.6: Left side: layout of two DDS generator based on AD9910 chip. Right side: photo of the quad DDS board developed in collaboration with the electronic workshop of the INFN Padova.

using the SSH protocol. Each DDS chip has 23 registers each of them is composed by

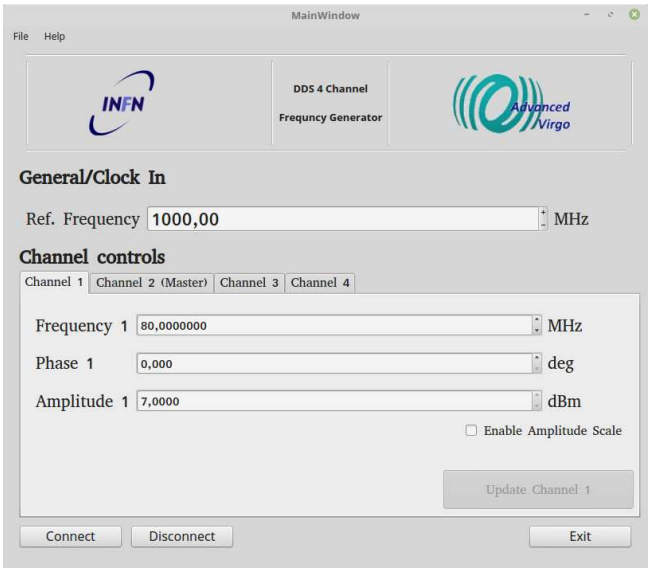

Figure 5.7: The Python GUI for the management of a 4 channel DDS board

32 or 64 bits: it is uncomfortable to send commands to the chips using the command line. Therefore I developed a graphical software that simplifies the communication between the PC and the Aria G25. The software is a Python script based on the Qt Graphical Library and its GUI is shown in Fig. 5.7. This software allows the user to set only a limited number of parameters: the frequency, the phase and the amplitude tuning words, and the gain of the variable gain amplifier. When the user runs the software it connects to the board via the Python library pxssh, then it asks to the board its actual configuration, finally it extracts the amplitude, frequency and phase parameters of each channel and prints them in the dedicated display. When the user changes one parameter the software computes the exadecimal string and sends it to

the C software that is running on the board.

5.2.3 Reference clock

Both the versions of the 4 channel RF generator presented in this chapter need an input reference clock. The principal requirements for the reference clock are: a phase noise level lower than the one of the DDS chip, an output frequency compatible with the DDS characteristics and finally an electrical tuning input channel that allows small output frequency shifts (as VCO). This third requirement is mandatory in the integration of the DDS board in the Virgo experiment, because with this channel it is possible to synchronize our RF system with the reference oscillator distributed in the Virgo interferometer.

The used reference clock is a thermally controlled crystal oscillator (Wenzel Associates model Sprinter Plus 501-27854-21) with the following features: output frequency 500 MHz, output level 13 dBm and phase noise equal to -105 dBc/Hz @ 100 Hz from the carrier, -135 dBc/Hz @ 1 kHz from the carrier and -150 dBc/Hz @ 10 kHz from the carrier. A limiting factor on the phase noise of the reference clock can come from its power supply: therefore a low noise power supply (Wenzel Associates, LNVR-18-12-2-1) is used in order to avoid noise excesses at the output of the reference clock.

5.3 Phase Noise

In any oscillating system the frequency stability plays an important role. Here the processes that affects the frequency of the system, with a duration less than one second, are studied. These processes could be periodic *spurs* or random *phase noise*. An ideal oscillator has no phase noise therefore its output spectrum consists in a single spectral line. As shown in Fig. 5.8, the phase noise broadens the spectral output line of the oscillator, whereas the spurs are additional spectral lines. Let us consider an ideal oscillator at frequency ω_0, its output is equal to

$$v(t) = \mathcal{R}\left[Ae^{i\omega_0 t}\right].$$

A real oscillator is affected by noise, i.e. amplitude fluctuations $a(t)$ and phase fluctuations $\varphi(t)$. Mathematically a real oscillator can be represented as:

$$v(t) = \mathcal{R}\left[(A + a(t))e^{i(\omega_0 t + \varphi(t))}\right]. \tag{5.2}$$

In this chapter, only the phase fluctuations are studied, therefore the amplitude fluctuations are neglected and the amplitude of the oscillator is considered equal

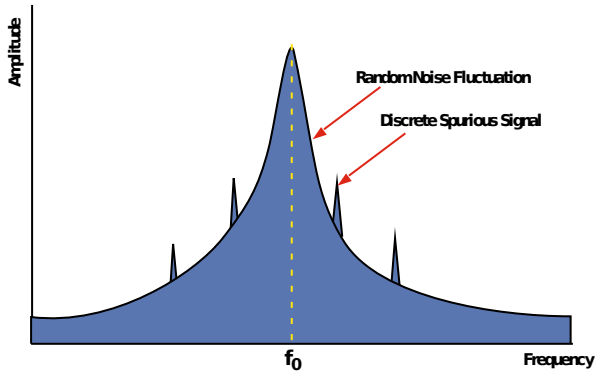

Figure 5.8: Spectrum of an oscillator with the carrier, phase noise and spurs.

to one. Eq. 5.2 is simplified as:

$$v(t) = \mathcal{R}\left[e^{i\varphi(t)}\right]$$

where, without loss of generality, only oscillations around $\omega_0 = 0$ are considered. The goal is to find an expression for the one-sided power spectral density ($S_{\varphi\varphi}(\omega)$) of phase fluctuations, i.e. the phase noise, as a function of the one-sided power spectral density ($S_{vv}(\omega)$) of the voltage process. The Wiener-Kinkine theorem is used. It states that the power spectrum of a stationary process is equal to the Fourier transform of its autocorrelation function. The autocorrelation function of the process is equal to:

$$c_{vv}(t-t') = \mathcal{R}\left[\left\langle e^{i(\varphi(t)-\varphi(t'))}\right\rangle\right] \approx 1-\frac{1}{2} < \varphi^2(t)+\varphi^2(t')-2\varphi(t)\varphi(t') >= 1-\sigma_\varphi^2+c_{\varphi\varphi}(t-t')$$

where zero average and small phase variations are considered, moreover $c_{\varphi\varphi}(t-t')$ is the autocorrelation function of the phase fluctuations. Finally by applying the Fourier transform:

$$S_{vv}(\omega) = (1-\sigma_\varphi^2)\delta(0) + S_{\varphi\varphi}(\omega)$$

The last result shows that the phase fluctuations remove a fraction σ_φ^2 from the spectral line of the oscillator and broadens it.

In the following subsection the principal phase noise measurement techniques are discussed.

5.3.1 Phase noise measurements

The output voltage of a real oscillator in time domain is represented by Eq. 5.2. Two fundamental classes of techniques are used to measure the contribution of the phase fluctuations: the first is a direct measurement of the oscillator's output with a spectrum analyzer and the second consists in the demodulation of the oscillations

at the carrier frequency and in the computation of the FFT of the demodulate signal [58][59]. The latter method is more complex than the former one but ensures a bigger dynamic range and a best resolution bandwidth.

Direct measurement of phase noise

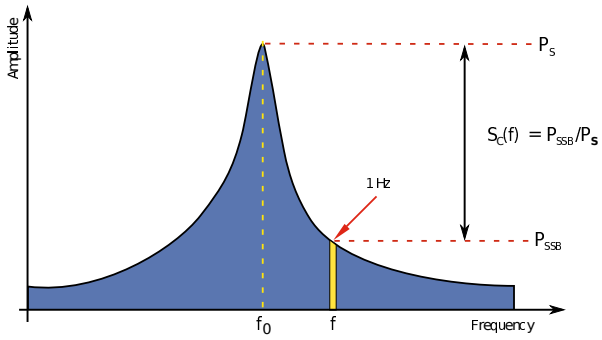

Figure 5.9: Typical signal of a non ideal oscillator measured with an RF spectrum analyzer.

Fig. 5.9 shows a typical spectrum of a non-ideal oscillator of frequency $f_0 = \omega_0/2\pi$. With a spectrum analyzer one measures directly the one side spectral density per unity of bandwidth of its input signal. The measured power is assumed equally distributed in the resolution bandwidth RBW of the instrument, with RBW $\ll f_0$. Usually the measured power is normalized per unit bandwidth by dividing for RBW, and per unit signal power by dividing for the carrier power P_s.

A spectrum analyzer filters the Fourier transform of the signal with a rectangular window with width equal to the resolution bandwidth RBW. Therefore the measured signal is the convolution of the window (ϑ) and the signal ($v(t)$) i.e.

$$v * \vartheta = \mathcal{F}^{-1}[\mathcal{F}[v * \vartheta]] = \vartheta.$$

The effect of the windowing consists in an enlargement of the peak, if the peak is width is narrower than the rectangular window width.

The phase noise is usually expressed in unit of dBc/Hz that are defined as the ratio per unit bandwidth of the power P_{SSB} of the signal at a frequency offset f from the carrier and the power P_s of the carrier signal at f_0, expressed in decibels see Fig. 5.9:

$$10 \log \left[\frac{P_s}{P_{SSB}(f)} \right]. \tag{5.3}$$

To normalize the measured power to unit bandwidth the quantity $20 \log[\text{RBW}]$ is subtracted from it. To normalize per unit signal power one takes the difference of the

resulting power in [dBc/Hz] and a Lorentzian fit of the carrier peak: the result is the phase noise of the non ideal oscillator under observation.

This is the fastest technique to measure phase noise; however usually spectrum analyzers have an inadequate dynamic range. I used this technique only for preliminary testing of devices, but all results exposed in this thesis are obtained with the technique explained in the following, i.e. phase noise measurement with the carrier demodulation.

Phase noise measurement with demodulation of the carrier

This technique consists in demodulating at its own frequency $f_0 = \omega_0/2\pi$ the output signal of the f_0 oscillator under test with a mixer. In principle one needs a second oscillator at f_0. Therefore at the two inputs of the mixer we have the following signals:

$$v_{lo}(t) = A_1 \sin(\omega_0 t + \varphi_1) \qquad v_{ref}(t) = A_2 \sin(\omega_0 t + \varphi_2).$$

where the pedix lo denotes the device under test and the pedix ref denotes the signal for the demodulation.

The mixer's output is:

$$v_{out}(t) = v_{ref}(t) v_{lo}(t) = \frac{K_{mix} A_1 A_2}{2} [\cos(\varphi_1 - \varphi_2) + \cos(2\omega_0 t + (\varphi_1 + \varphi_2))]$$

where K_{mix} is the mixer gain. The mixer is followed by a low pass filter with cutoff frequency $\ll 2\omega_0$, but bigger than the frequency region interested to the measurement. The output phases $\varphi_{1,2}$ of the two oscillators can be rewritten as:

$$\varphi_{1,2} = \phi_{1,2} + \phi_{n1,2}(t),$$

where the first term is a constant phase offset between lo and ref signals and the second consists in the phase fluctuations. Therefore the filtered output of the mixer can be rewritten as:

$$v_{out,flt} = \frac{K_{mix} A_1 A_2}{2} \cos[(\phi_1 - \phi_2) + (\phi_{n,1}(t) - \phi_{n,2}(t))].$$

This expression can be simplified if the phase of the demodulation signal is such that $\phi_1 - \phi_2 = \pi/2$ and considering that phase fluctuation of reference are negligible, i.e. $\phi_{n,2}(t) \ll \phi_{n,1}(t)$. So it follows that:

$$v_{out,flt} = \frac{K_{mix} A_1 A_2}{2} \sin[\phi_{n,1}(t)] \approx \frac{K_{mix} A_1 A_2}{2} \phi_{n,1}(t),$$

the sine is expanded for small phase fluctuations. By computing the power spectrum of this signal, one obtains directly the spectrum of the phase fluctuations i.e. the phase noise:

$$S_{\phi\phi}(\omega) = \frac{4S_{vv}(\omega)}{(K_{mix}A_1A_2)^2}.$$

Two aspects of this technique are crucial:

1. the reference clock must not drift in phase with respect to the device under test;

2. the phase noise of the reference clock must be negligible with respect to the phase noise of the device under test.

5.4 DDS measurements and results

This section describes the experimental setup used to perform the measurements of the phase noise performance of the two DDS boards. The phase noise is measured with the carrier demodulation technique by using two different setups. The first is a measurement of the residual phase noise of the system, whereas the second is a measurement of its absolute phase noise [60].

5.4.1 Residual phase noise

The aim of the residual phase noise technique is to extract the phase noise at the output of the oscillator under test and cancel the effect of external noise sources i.e. power supply, reference clock. The measurement setup is shown in Fig. 5.11: it is composed by two identical oscillators with the same reference clock and with a common power supply, a mixer, a low pass filter, a low noise amplifier and a spectrum anlayzer.

The signals of the two oscillators are sent to a mixer, whose output is composed by a DC component and component at twice the oscillator's frequency. The low frequency component contains information on the phase noise: it is extracted by a low pass filter at the output of the mixer. The filtered output is measured by using a low frequency FFT analyzer; often before the analyzer the signal is amplified by a low noise amplifier in order to overcome the noise floor of the spectrum analyzer. The use of two identical RF generators with the same power supply and reference clock allows the measurement to be independent of the phase noise from common noise sources: they are correlated and cancel each other. Differently, the uncorrelated part of the phase fluctuations of the two oscillators contribute equally to the measured

phase noise and therefore to extract the single contribution one needs to subtract 3 dB from the spectrum analyzer output.

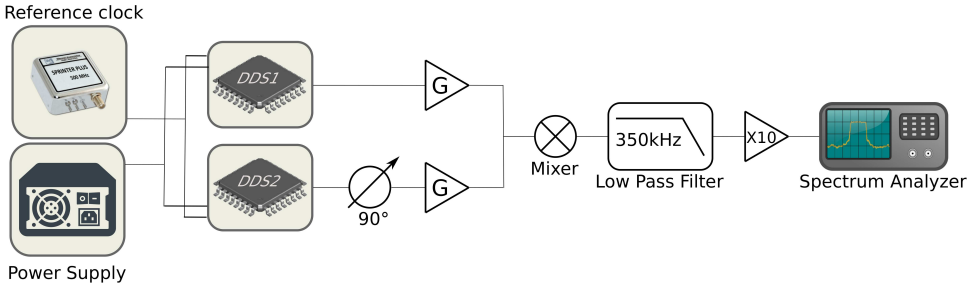

Figure 5.10: Experimental setup for residual phase noise measurement.

In detail, to measure the DDS residual phase noise I used: 500 MHz oscillator as reference clock, two channels of a DDS board as RF oscillators under measurement,one shifted by 90°with the phase tuning word, and a mixer (Minicircuit ZP1051+). The output of the mixer is filtered by a passive first order low pass filter with cutoff frequency of about 350 kHz and amplified by a factor 10 using a non inverting amplifier based on OP37 operational amplifier. To quantify the noise floor of the measurement, I used only one DDS channel: I split it in two signals in quadrature between them using a power splitter (Minicircuit ZMSCQ-2-50) and feed them to the mixer.

Fig 5.10 shows the measured residual phase noise between 2 DDS channels on the same board in the 2 hardware configurations (AD9959, AD9910) and their residual phase noise as from datasheet [57] [55]. The measurements are performed at 62.5 MHz: it consists in 1/8th of the reference clock and the choice of frequency tuning word does not cause the spur frequency lines generation. In the chip datasheets the phase noise is not given at our work frequency: to predict the noise value I used the value given at 98.6 MHz and transposed it to phase noise at 62.5 MHz by using the Egan's model for frequency divider [54][61]. Fig. 5.11 shows that the measured residual phase noise of AD9910 chip is 2dB higher then the expected one up to about 3 kHz and then the gap increases up to 9dB at 100 kHz. Moreover the measured residual phase noise of AD9959 chip is 1dB higher then tabulated one up to about 3 kHz and above this frequency the gap increases up to 13dB at 100 kHz. AD9959 has an output phase noise 5dB higher than one of AD9910 up to 3 kHz and above this frequency the gap increases up to 10 dB. The rms residual phase noise between 1 Hz and 100 kHz is 14 µrad for the AD9910 chip and 31 µrad for the AD9959 chip.

In the squeezing setup the residual phase noise enters in the performance of the Pound Drever Hall locking system of cavities and the coherent control loop. The residual relative phase error is 19 µrad RMS, i.e. well below the squeezing ellipse

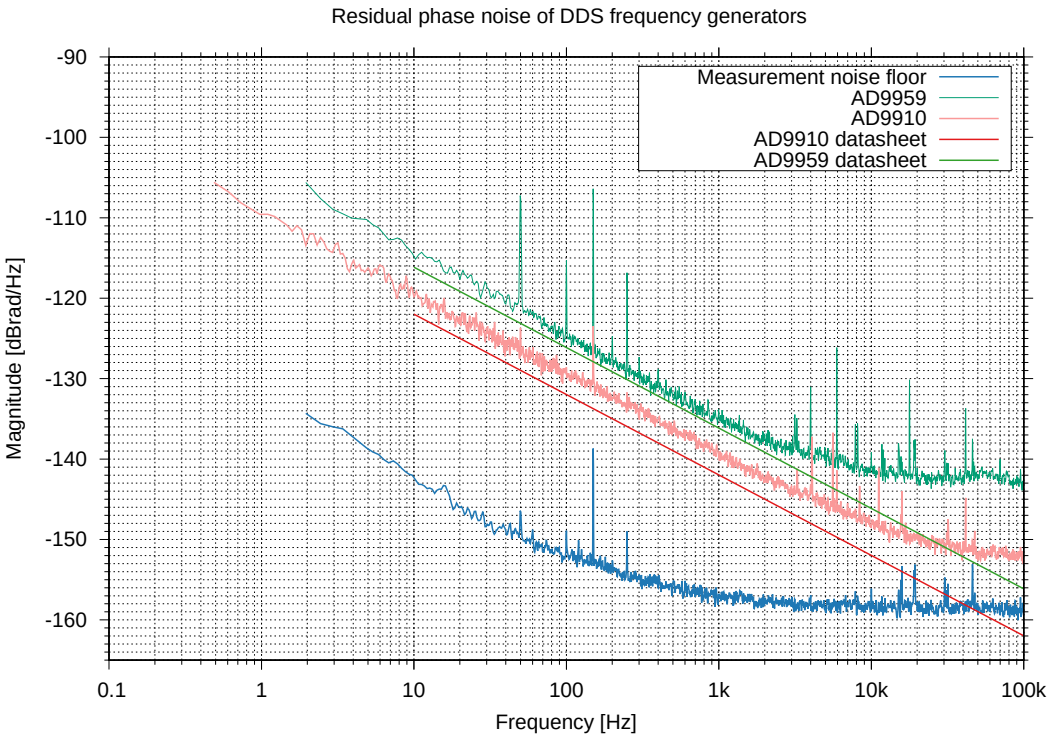

Figure 5.11: Residual phase noise at the output of the two DDS board at 65.5 MHz. In blue the measurement chain noise floor, in light red the AD9910 measured residual phase noise, in dark red the AD9910 tabulated phase noise, in light green the AD9959 residual phase noise and in dark green its tabulated one.

residual angular jitter requirement (about 1 mrad).

5.4.2 Absolute phase noise

The aim of an absolute noise setup is the measure of the phase noise respect to an ideal noiseless generator. Thus it includes the pure phase noise generated from the DDS chip and other noises from other sources, for example the reference clock and the power supply.

The used setup is similar to the one showed in Fg. 5.12 but instead of using two identical oscillators, the mixed signals come from the device under test and a reference oscillator with negligible phase noise and at fixed phase offset with respect to the oscillator under test. As reference oscillator I used a peak-off of the reference clock divided by 8: this grants a negligible phase noise and a constant phase offset with respect to DSS output. Fig. 5.12 shows the absolute phase noise at the output of the AD9959 evaluation board and of the the 4 channel AD9910 developed in INFN Padova Electronic Workshop. The figure shows that the absolute phase noise of

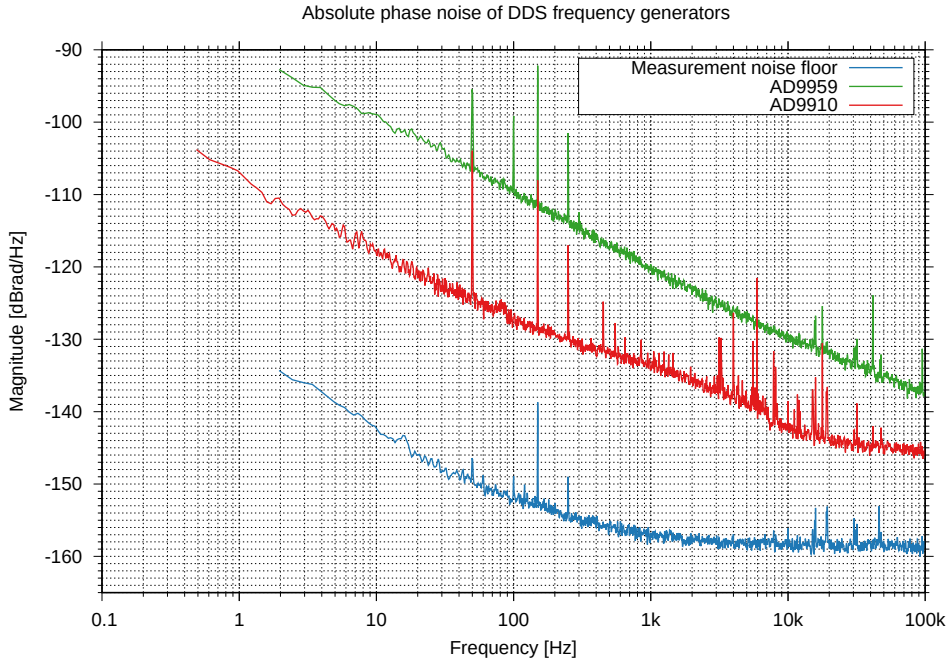

Figure 5.12: Absolute phase noise at the output of the two DDS board at 65.5 MHz. In blue the measurement chain noise floor, in red the AD9910 measured absolute phase noise, in green the AD9959 absolut phase noise

AD9910 is from 10 to 20 dB less than the noise of AD9959. The rms absolute phase noise between 1 Hz and 100 kHz is 27 µrad for the AD9910 chip and 117 µrad for the AD9959 chip.

To conclude this chapter, the performance of the developed DDS board are compared to other top level commercial devices. For example the top solution in the signal generation of the Rohde&Schwartz manufacturer is the model SMW200Ar[1]. This device has a single RF output which frequency can vary between 100 kHz and 3 GHz and has a tabulated phase noise less than -131 dBrad Hz^{-1}, measured at a frequency offset of 20 kHz from the carrier when the output frequency is set to 1 GHz. Using the Egan's model for frequency dividers, the tabulated phase noise can be transposed to the one measured at output frequency of 62.5 MHz and it becomes equal to -155 dBrad Hz^{-1}. Thus this commercial instrument is at least 10 dBrad $Hz^{-}1$ better than the custom developed quad DDS generator board. This Rohde&Schwartz generator can provide only a single output, but one of the requirement of the Virgo squeezer is to have 12 RF channels at 7 different frequencies that must be locked in phase between them at least in group of 3 channels. The developed DDS boards satisfy this requirement, whereas to implement this solution with the

[1] All the informations about this instrument can be founded at: `https://goo.gl/2mGaq9`.

commercial Rohde&Schwartz generator are needed 7 different instruments and needs an additional electronic to split channels and to add a phase offset to them. Each one of this instrument has a cost of about 50000 €, therefore the total cost of one of the better commercial solution is about 350000 €, whereas the total cost of our commercial solution about 5000 €i.e. 70 time lowers and its phase noise performance are adequate to the development of a squeezed light source.

Now, the attention is focused to another commercial signal generator, i.e. the model SMBV 100A of Rohde and Schwartz manufacturer[2]. Its output frequency range is the same of the previous, but now it has a recomputed output phase noise at 62.5 MHz equal to -145 dBrad Hz^{-1}, i.e. about 2 dB better than the custom quad channel DDS generator. This instrument has a single output channel and its cost is about 30000 €. Therefore the implementation of the squeezer RF setup with this commercial solution will cost about 200000 €, i.e. 40 times more than with the custom DDS boards.

[2]All the informations about this instrument can be founded at: `https://goo.gl/Fy2Zgv`.

Chapter 6

Phase Loked Loop

As mentioned in the previous chapters, the 1500W squeezer needs at least three frequency locked laser sources. This is achieved with the PLL technique. In particular the first PLL, between the main laser (ML) and the second auxiliary laser (AUX2), is required to ensure the coresonance condition between the s and p polarization of the light in the OPO cavity. The second PLL, between the Master Laser and the first auxiliary laser (AUX1), is required to inject a single sideband in the OPO cavity for the generation of the coherent control loop error signal; finally the last required PLL is between the main laser and the Virgo laser in order to generate the squeezed light states at the same frequency of the one of the Virgo main laser. This locking technique is called phase locked loop (Phase Locked Loop (PLL)) and usually it is used to lock in phase two RF oscillators.

This chapter will explain the principle of operations of a PLL servo loop: Sec. 6.1 analyzes the behavior of a PLL servo loop in the time domain, Sec. 6.2 describes different kind of phase detectors based both on digital and analog electronics, Sec. 6.3 analyzes the PLL transfer function, Sec. 6.5 shows a specific case of PLL i.e. the optical phase locked loop (OPLL), finally Sec. 6.6 shows the optical layout, the electronic setup and the performance of the OPLL developed for the Virgo squeezer.

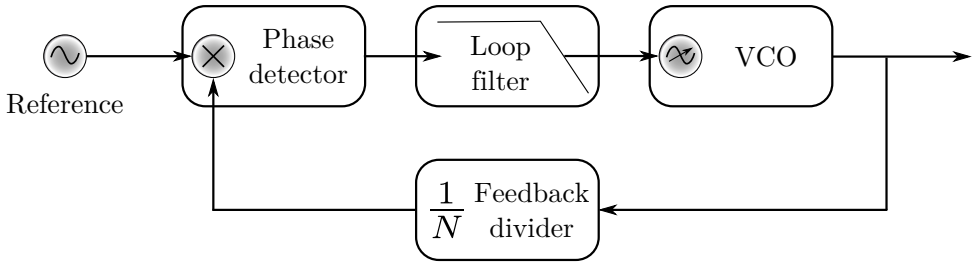

Figure 6.1: Generic layout of a PLL servo loop.

6.1 PLL principle of operation

A Phase Locked Loop (PLL) is a negative feedback system with the purpose to force a voltage controlled oscillator (VCO) to follow in frequency a reference oscillator at its input with a phase offset. When the PLL is locked the phase difference between is input and output is constant. The PLL feedback loop is composed by four main blocks: a Phase detector, a Loop Filter, a voltage controlled oscillator and a feedback divider as it is shown in Fig. 6.1.

While the frequency is the time derivative of the phase, to hold the two signals with a fixed phase offset it means that the two signal are held at the same frequency. This goal is achieved when the circuit's error signal i.e. the phase detector output is equal to zero. In this subsection, the phase evolution of the signals is analyzed block by block, in the time domain through all the subparts of the servo loop, and it is explained what means to say that the PLL is in an "unlocked state" or in a "locked state" [62][63][64].

The **phase detector** is the first block and the principal component of a PLL servo loop. It has two inputs: the reference oscillator and the Voltage Controlled Oscillator (VCO)'s output. The phase of its two inputs are respectively equal to:

$$\phi_{ref}(t) = \omega_{ref}t + \phi_{0ref} \qquad \phi_{vco}(t) = \omega_{vco}t + \phi_{0vco}. \tag{6.1}$$

The phase detector compares the phase of these two signals and has as output an error signal proportional to the phase difference between them:

$$v_{pd} = K_{pd}[\phi_{ref}(t) - \phi_{vco}(t)], \tag{6.2}$$

where the constant factor K_{pd} is the phase detector gain and is expressed in V rad^{-1}.

The phase detector output is the input of the **loop filter** that is a low pass filter for the error signal ($v_{pd}(t)$). Its output is the control voltage (V_{vco}) of the VCO.

The **voltage controlled oscillator (VCO)** is an RF oscillator controlled in voltage. Its output is a sinusoidal wave which frequency can be varied linearly from its natural frequency ω_0 with the following relationship:

$$\omega_{vco} = \omega_0 + K_{vco}V_{vco}, \tag{6.3}$$

where K_{vco} is the VCO gain coefficient expressed in rad s^{-1} V^{-1} and V_{vco} is its control voltage.

The **feedback divider** is a circuit element which divides the frequency of the feedback signal by the integer factor N. It is used to lock the system at a frequency

N times higher with respect to the reference frequency. Its input output relationship is the following:

$$\omega_{div} = \frac{\omega_{vco}}{N}. \tag{6.4}$$

Here below, starting from Eq. 6.1, Eq. 6.2 and Eq. 6.3, the PLL behavior with different initial conditions is studied. The computation is simplified by choosing $N = 1$ as feedback divider ratio and by neglecting the loop filer, i.e. the output of the phase detector is directly the input of the VCO ($v_{pd}(t) = v_{vco}(t)$).

Case 1: VCO output and reference signals with the same frequency and phase, i.e. $\omega_{ref} = \omega_{vco}$ and $\phi_{0ref} = \phi_{0vco}$. The phase detector output is equal to zero, thus the VCO oscillates at its natural frequency ω_0 and the PLL is said in "Locked state".

Case 2: VCO output and reference signals with the same frequency and different phase , i.e. $\omega_{ref} = \omega_{vco} = \omega_0$ and $\phi_{0ref} = 0$, $\phi_{0vco} > 0$. The phase detector output is $V_{pd}(t) = -K_{pd}\phi_{vco}$. The VCO output frequency is forced to be lower than its natural frequency. This implies that ϕ_{vco} varies in the time causing variations of v_{pd} and ω_{vco} until when the reference signal and the VCO will have the same frequency. This is mathematically expressed as follows:

$$\phi_{rf}(t) = \omega_0 t \qquad \phi_{vco}(t) = \omega_0 t + \phi_0,$$

thus the phase detector output voltage is equal to:

$$V_{pd}(t) = -\frac{K_{pd}\phi_0}{1 + K_{pd}K_{vco}t} \to 0 \quad \text{if t} \to +\infty.$$

Therefore for large t the PLL servo loops aligns its two inputs in phases.

Case 3: VCO output and reference signals have the different frequency and different phase , i.e. $\omega_{ref} > \omega_{vco} = \omega_0$ and $\phi_{0ref} = 0$, $\phi_{0vco} > 0$. As previous one can compute:

$$\phi_{rf}(t) = \omega_{rf} t \qquad \phi_{vco}(t) = \omega_{vco} t + \phi_0.$$

With these initial conditions, the VCO frequency and the phase detector output voltage are equal to:

$$V_{pd}(t) = \frac{K_{pd}[(\omega_{ref} - \omega_{vco})t - \phi_0]}{1 + K_{pd}K_{vco}t} \qquad \omega_{vco}(t) = \frac{\omega_0 + K_{pd}K_{vco}(\omega_{ref}t - \phi_0)}{1 + K_{pd}K_{vco}t}.$$

From these equation at $t = 0$ it follows that:

$$v_{pd}(0) = -K_{pd}\phi_0 \qquad \omega_{vco}(0) = \omega_0 - K_{pd}K_{vco}\phi_0,$$

whereas for $t \to \infty$ the servo loop forces the two signal to have the same frequency and phase, i.e.:

$$v_{pd} = \frac{\omega_{ref} - \omega_{vco}}{K_{vco}} \qquad \omega_{vco} = \omega_{ref}.$$

All these results are true only when the PLL is in its linear regime. i.e. the phase fluctuations around its locking point are small.

6.2 Different kind of phase detector

The phase detector is the core of a PLL system and it defines the the typology of PLL itself. If the phase detector is based on the analog electronic, the PLL is called, whereas if the phase detector consists in a digital mixing stadium the system is called Digital Phase Locked Loop (DPLL), finally if the PLL is built only by digital blocks it is called an All Digital Phase Locked Loop (ADPLL). Here below, the three principal kind of phase detector are studied: the analog mixer, the exclusive XOR phase detector and the phase frequency detector. The first is an analog phase detector, whereas the other two are digital.

6.2.1 Analog mixer phase detector

A typical example of analog phase detector is the mixer that multiplies its two input signals. If its two input signal are sinusoidal waves:

$$in_1(t) = A_1 \cos(\omega_1 t + \phi_1) \quad \text{and} \quad in_2(t) = A_2 \cos(\omega_2 t + \phi_2)$$

its output is equal to:

$$V_{mix} = in_1(t)in_2(t) = \frac{A_1 A_2}{2}[\cos[(\omega_1 + \omega_2)t + (\phi_1 + \phi_2)] + \cos[(\omega_1 - \omega_2)t + (\phi_1 - \phi_2)]].$$

When the PLL is locked the two inputs have the same frequency, i.e. $\omega_1 = \omega_2 = \omega$, so the output signal becomes:

$$V_{mix}(t) = in_1(t)in_2(t) = \frac{A_1 A_2}{2}[\cos[(2\omega t + (\phi_1 + \phi_2)] + \cos[\phi_1 - \phi_2]]. \tag{6.5}$$

By filtering the double frequency component with a low pass filter, an output signal proportional to the cosine of the phase difference of the two inputs is obtained. With the same notation of Eq. 6.2, Eq. 6.5 can be rewritten as:

$$V_{mix}(t) = K_{mix} \cos(\phi_1 - \phi_2).$$

An analog mixer is not a linear circuit element, but in this thesis the PLL is treated only considering small phase displacements around the locking point and the mixer output could be linearized as $V_{mix}(t) \approx k_{mix}[\phi_1 - \phi_2]$.

6.2.2 XOR type pahse detector

This digital phase detector is based on an Exclusive XOR gate (EXOR) gate, which output is equal to 0 when its two inputs have the same value whereas its output is equal to 1 when its two inputs have different values. Therefore if the two inputs of the EXOR gate are square waves with same amplitude, frequency and phase the output is always equal to zero, instead if the identical square waves have a phase difference equal to 180°the output is always equal to one. This gate can't discriminate the sign of this phase offset. Thus the XOR output characteristic is a periodic function with period equal to 180°.

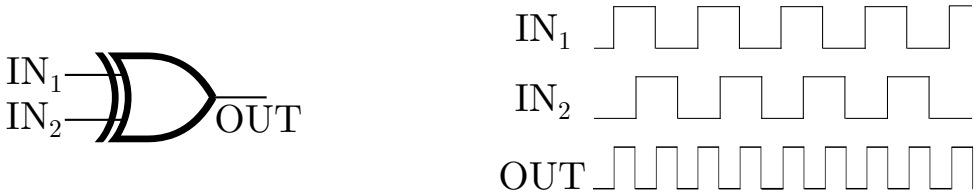

Figure 6.2: Left: the circuit symbol of a EXOR gate. Right: the inputs and the output signal of XOR gate phase detector when the phase difference between its inputs is 90°.

Moreover, when the phase difference between the two inputs is equal to 90°, the XOR output is a square wave with twice the frequency of the two inputs and a duty cicle of 50%. If the phase difference decreases the output duty cycle decreases; whereas if the phase difference increases the output duty cycle increases. Therefore the average of its output signal ($\bar{v}_{exor}$) is proportional to the phase difference between its two inputs:

$$\bar{v}_{exor}(t) = \frac{K_{exor}}{\pi}[\phi_1 - \phi_2].$$

The EXOR's gate output has the same form of the linearized analog mixer output, but for the EXOR gate this can obtained only putting a low pass filter in series to the gate in order to take only the mean value of its output.

6.2.3 Phase frequency detector

The Phase Frequency Detector (PFD) is a widely used architecture in the PLL servo loops. Differently from the EXOR gate, the phase detector produces two different outputs called Q_1 and Q_2 or UP and DOWN. A typical implementation of

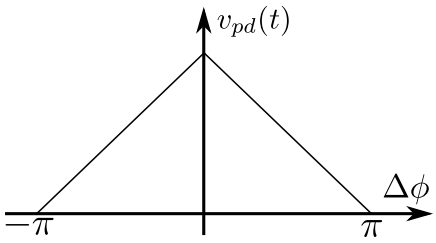

Figure 6.3: Averaged output of EXOR gate phase detector as function of the phase difference between its two inputs.

a phase frequency detector consist in two D-type flip flops. In series to the phase detector there is the charge pump as it is shown in Fig. 6.5. It consist in a positive current source enabled by the Q_1 output and a negative current source enabled by the Q_2 output. Before the description of the PFD principle of operation, the principle of operations of a D-type flip flop is summarized.

A D-type flip flop is a digital element with four inputs i.e. data D, clock, set S and clear or reset CLR, and two outputs called Q and $\bar{Q}$. The D-type flip flop is

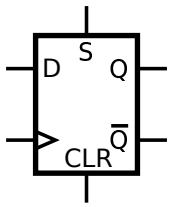

Figure 6.4: Circuit block of a D-type flip flop.

triggered or on the rising edges of its clock or on its falling edges. If S and CLR are forced to zero the flip flop behaves as a memory cell or a delay line, i.e. it captures its input during the right edge of the clock (rising or falling) and send it to the output Q and its opposite value to the output $\bar{Q}$. If D changes its state the output varies only after the right edge of the clock. If S and CLR are not simultaneously equal to zero, the input output relationship of the flip flop is given by the following truth table:

PFD principle of operation In this thesis, the used phase frequency detector are composed by edge triggered D-type flip flop with $S = 0$ and without considering the $\bar{Q}$ output. The outputs Q_1 and Q_2 are usually called respectively UP and DOWN. The input data D_1 and D_2 of the two flip flops are always high. The reference clock v_{ref} and the VCO output $v_{lo}(t)$ are respectively the clocks of the two flip flops U_1 and U_2 [62][65]. In series with the two flip-flops there is an AND gate which output enables the CLR port of U_1 and U_2. The PFD outputs are connected to a charge

Inputs				Outputs	
S	**CLR**	**D**	**CLK**	**Q**	**$\bar{Q}$**
0	1	X	X	0	1
1	0	X	X	1	0
1	1	X	X	1	1

Table 6.1: Truth table of D-type flip flop when S and R are not simultaneously equal to zero. X denotes a don't care condition.

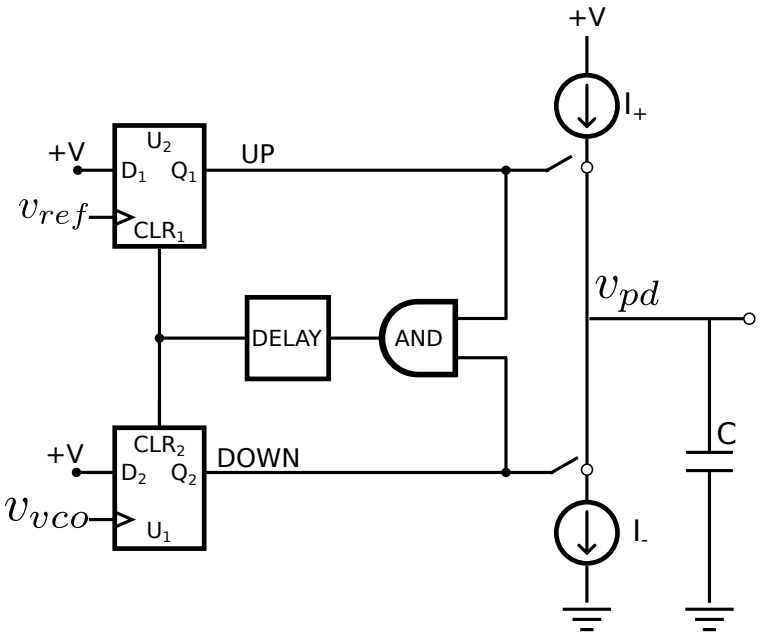

Figure 6.5: An example of phase frequency detector architecture.

pump composed by two current sources I^+ and I^- that are enabled by the UP and DOWN pulses. There are four possible output configurations for the couple of filp flops: $\mathbf{Q_1 = 1}$ and $\mathbf{Q_2 = 0}$ i.e. only output UP is HIGH, $\mathbf{Q_1 = 0}$ and $\mathbf{Q_2 = 1}$ i.e. only output DOWN is high, $\mathbf{Q_1 = 0}$ and $\mathbf{Q_2 = 0}$ both the output are low and $\mathbf{Q_1 = 1}$ and $\mathbf{Q_2 = 1}$, but this configuration is disabled by the AND gate connected to CLR port of flip-flops.

Now the behavior of the PFD is studied in the configuration in which $v_{ref}(t)$ has a frequency higher than $v_{lo}(t)$ as it is shown in the left side of the Fig. 6.6. Because of the frequency difference is high the UP output is most of the time in its high state and DOWN output is most of the time in its down state. In particular Q_1 becomes high after the first rising edge of $v_{ref}(t)$ and remains high until the first rising edge

of the other input. So the current source I_+ is almost always turned on and it causes an increase of the VCO frequency. Contrariwise, if the frequency of $v_{ref}(t)$ is much lower than frequency of $v_{lo}(t)$, PFD output is quite allways in its lower state and VCO frequency becomes lower.

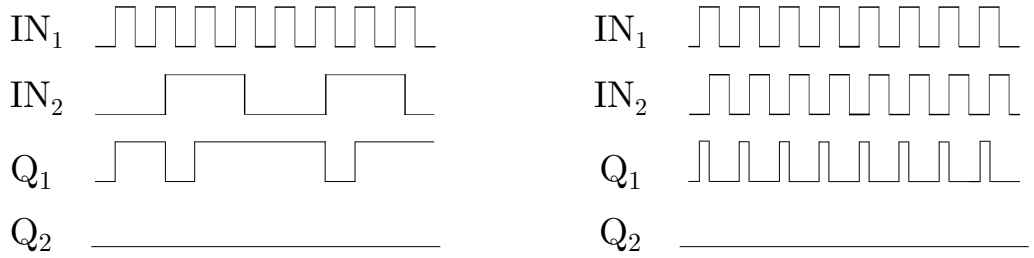

Figure 6.6: Behaviour of PFD output. Left: the two inputs have high frequency difference. Right: the two inputs have the same frequency but small phase offset. IN_1 and IN_2 are respectively v_{ref} and v_{vco}.

When the two PFD inputs have the same frequency but a small phase offset (for example the VCO oscillation has a phase delay respect to the reference oscillation), Fig. 6.6-right, the UP output is a series of pulses that switch on I^+ and the VCO is driven to become phase aligned with the reference. In this configuration the DOWN output is always equal to zero.

If the charge pump in series with the PFD is not considered and the output of PFD is assumed equal to the difference between the mean values of the UP pulses and the mean value of DOWN pulses, it has a linear characteristic between -2π and 2π i.e. 4 times bigger than linear characteristic of EXOR type phase detector. Moreover, the phase frequency detector has an output proportional to the frequency difference between its two inputs even if the PLL is in its unlocked state. This last property is a big advantage in the lock acquisition of a PLL that uses a PFD as phase detector.

Now, the behavior of the series composed by the PFD and charge pump is analyzed. The phase detector output signal has to be a voltage so a single capacitor after the charge pump is inserted as current to voltage converter, see Fig. 6.5. The charge pump outputs has three different output states:

- $\mathbf{Q_1 = 0}$ and $\mathbf{Q_2 = 0}$: the two current sources are turned off and the output is in an high impedance state;
- $\mathbf{Q_1 = 0}$ and $\mathbf{Q_2 = 1}$: the positive current source is turned off, the negative one is turned on and the output is I_-;
- $\mathbf{Q_1 = 1}$ and $\mathbf{Q_2 = 0}$: the positive current source is turned on, the negative one is turned off and the output is I_+;

This analysis is made with the following hypothesis: $\omega_{ref} > \omega_{vco}$. Each UP pulse adds charge to the capacitor C conversely each DOW pulse removes charge from the capacitor (See Fig. 6.5). The PLL is assumed as locked at frequency ω_{ref} so a pulse of the charge pump has a duration equal to:

$$t_p = \frac{|\phi_{ref} - \phi_{vco}|}{\omega_{ref}}.$$

T_{ref} is called the period of reference signal oscillations and so the average charge pump output current in a cycle of its input is:

$$\frac{I_p t_p}{T_{ref}} = I_p \cdot \frac{|\phi_{ref} - \phi_{vco}|}{\omega_{ref}} \frac{\omega_{ref}}{2\pi} = \underbrace{\frac{I_p}{2\pi}}_{K_{pd}} |\phi_{ref} - \phi_{vco}|.$$

Because of the current source I_- correspond to a connection with the circuit ground the above expression consists in the phase detector output current during a cycle. So the PFD output characteristic has the same form of analog mixer and EXOR output characteristic.

Before to conclude, the role of the delay element shown in Fig. 6.5 is explained. When the two signals are phase and frequency aligned the delay element between the AND gate and CLR port becomes essential. In fact if this element is not present the output of the charge pump could be in higher impedance state for long time. So the VCO drifts until it has a big phase error and then the PFD output drives again the charge pump with UP or down pulses to restore the lock condition. If this phenomenon is repeated many times one can see a sort of modulation of the VCO control voltage that is a subharmonic of $v_{ref(t)}$ frequency. Because of this signal could have low frequency it is no filtered by PLL's loop filter and it generates spurs in the VCO output spectrum. This phenomenon is calld "backlash" effect. If the delay element is inserted between the AND gate and the CLR port of flip flops this phenomenon not happens. Now, when PFD inputs have same phase and frequency I^+ and I^- current sources are alternative turned on with UP and DOWN output pulses with duration equal to the inserted delay.

6.3 PLL transfer function

The aim of this section is to find the phase transfer function of a PLL feedback system in the Laplace space, thus the transfer function of all its components is calculated separately by studying the relationship between their inputs and outputs phases [63][64]. As in the time domain, the analysis starts from the phase detector.

Its transfer function in the linear regime is equal to:

$$H_{pd}(s) = K_{pd}. \tag{6.6}$$

The following component, after the phase detector, is the loop filter with its generic transfer function $F(s)$; its output $v_{vco}(t)$ is the VCO's input. Remembering Eq. 6.3 the variation of the VCO frequency os $\Delta\omega_{vco} = K_{vco}v_{vco}$ and because of the frequency is the time derivative of the phase it follows that:

$$\Delta\omega = \frac{d\phi_{vco}(t)}{dt} \quad \Rightarrow \quad \phi_{vco}(t) = K_{vco}\int_{-\infty}^{t} v_{vco}(t')\,dt'. \tag{6.7}$$

The VCO transfer function in s-domain is indeed:

$$H_{vco}(s) = \frac{\phi_{vco}(s)}{v_{vco}(s)} = \frac{K_{vco}}{s} \tag{6.8}$$

The feedback divider divides the frequency of its input signal by a factor N, i.e. $\omega_{div} = \omega_{vco}/N$. Its transfer function is:

$$H_{div}(s) = \frac{\phi_{div}}{\phi_{vco}} = \frac{1}{N}. \tag{6.9}$$

Now a generic feedback system is considered, its open loop transfer function is denoted with $G(s)$ and its feedback transfer function is denoted with $B(s)$. By using the canonical equation of system analysis, one can write the closed loop transfer function $H(s)$ as the ratio between system output and input:

$$H(s) = \frac{V_{out}(s)}{V_{in}(s)} = \frac{G(s)}{1 + G(s)B(s)}. \tag{6.10}$$

Moreover, the error transfer function of a feedback system $E(s)$ is given by the ratio between the error signal $V_{err} = V_{in} - V_{out}$ and the input signal V_{in}:

$$E(s) = \frac{V_{err}(s)}{V_{in(s)}} = \frac{V_{in} - V_{out}}{V_{in}} = 1 - H(s) = \frac{1}{1 + G(s)B(s)}. \tag{6.11}$$

Referring to Fig. 6.1 and by using equations from Eq. 6.6 to Eq. 6.11 the PLL Open loop transfer function can be written as:

$$G_{pll}(s) = \frac{K_{vco}K_{pd}F(s)}{s}, \tag{6.12}$$

the closed loop transfer function is then equal to:

$$H_{pll}(s) = \frac{K_{vco}K_{pd}F(s)/s}{1 + K_{vco}K_{pd}F(s)/sN}, \tag{6.13}$$

finally the PLL error transfer function becomes:

$$E_{pll}(s) = \frac{s}{s + K_{vco}K_{pd}F(s)/sN}. \tag{6.14}$$

By using these three equation and by substituting $F(s)$ with the loop filter transfer function, one can study the behavior of a PLL feedback system. If the loop filter consist only in one capacitor i.e. a single pole the open loop transfer function becomes:

$$G_{pll}(s) = \frac{K_{vco}K_{pd}}{Cs^2},$$

where C is the capacitance. It is obvious that, in this condition, the PLL servo loop is not stable because the phase margin is equal to 0. The loop filter has to be at list an RC low pass filter in order to ensures a stable phase locked loop. In the PLL used in this work, $F(s)$ is realized with an analog second order loop filter composed by two capacitor and one resistor (see Fig. 6.7). It has the following transfer function:

$$F(s) = \frac{1 + sR_1C_1}{s^2R_1C_1C_2 + s(C_1 + C_2)}, \tag{6.15}$$

where C_1 and C_2 are the two capacitors and R_1 is the resistor.

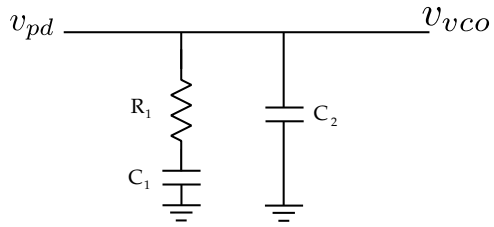

Figure 6.7: Loop filter layout used in Virgo PLL implementation.

6.4 Phase Noise contributions in a PLL servo loop

Fig. 6.8 shows a block diagram of the PLL servo loop including all the noise sources [62]. The phase noise sources at the input of the phase detector are the

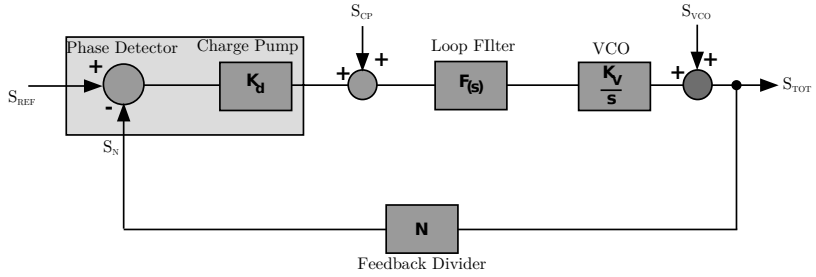

Figure 6.8: Phase noise sources in a PLL servo loop.

reference phase noise S_{ref} an the the noise due to the feedback divider S_N. The other two noise contributions are the noise of VCO S_{vco} and the output noise of the

charge pump S_{cp}. The total phase noise power spectral density (S_{tot}) at the output of the servo loop is the square sum of these contributions:

$$S_{tot}^2 = X^2 + Y^2 + Z^2$$

where X^2 is the noise power at the output due to S_N and S_{ref}, Y^2 is the noise at the output due to S_{cp} and Z^2 is the noise at the output due to S_{vco}. In order to write all the noise contributions at the output we use the transfer function computed in Sec. 6.3. The noise contribution X is obtained by multiplying the input noise of the phase detector with the closed loop transfer function of the circuit:

$$X^2(s) = (S_{ref}^2(s) + S_N^2(s)) \left(\frac{K_{vco} K_{pd} F(s)/s}{1 + K_{vco} K_{pd} F(s)/sN} \right)^2 . \tag{6.16}$$

At low frequencies, i.e. inside the loop bandwidth $X^2 \approx (S_{ref}^2 + S_N^2)N^2$ whereas at high frequencies this contributions is negligible. The charge pump output noise at the output will be:

$$Y^2(s) = (S_{cp}^2(s)) \left(\frac{1}{k_{pd}} \right)^2 \left(\frac{K_{vco} K_{pd} F(s)/s}{1 + K_{vco} K_{pd} F(s)/sN} \right)^2 . \tag{6.17}$$

At low frequencies, i.e. inside the loop bandwidth $Y^2 \approx (S_{ref}^2 + S_N^2)(N/K_{pd})^2$, whereas at high frequencies this contributions is negligible. Finally the contribution of the VCO at the output is:

$$Z^2(s) = (S_{vco}^2(s)) \left(\frac{1}{1 + K_{vco} K_{pd} F(s)/sN} \right)^2 . \tag{6.18}$$

The last expression shows that the PLL is an high pass filter for the VCO noise. Therefore the principal noise contributions in the loop bandwidth are the reference noise, the charge pump noise and the feedback divider noise, whereas outside the loop bandwidth the VCO noise is the principal source. As shown in Sec. 6.6.2, the principal phase noise contribution in the Virgo OPLL is the VCO's noise i.e. the lasers noise. Therefore we need an high loop bandwidth in order to suppress it as much as possible.

6.5 Optical Phase Locked Loop

An optical phase locked loop is a special kind of PLL with the goal to force two lasers to maintain a fixed frequency difference. The layout of this servo loop is very similar to the classical PLL servo loop. The difference is that the VCO is not a simple oscillator but it consists in the beat note of the two lasers detected by

a photodetector. At least one of the two laser must be tunable in frequency. In this section it is explained how an OPLL is implemented. Fig. 6.9 shows a detailed layout of an OPLL setup. This setup is divided in two blocks the optical part that substitutes the VCO and the electronic part that is identical to PLL scheme described above.

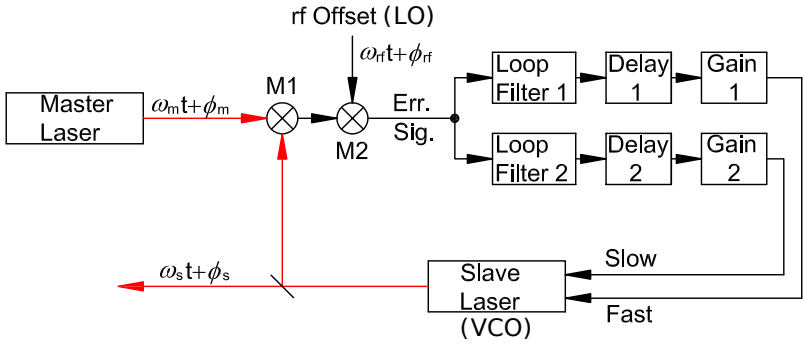

Figure 6.9: Typical OPLL servo loop.

In the simplest situation the optical part is composed by two lasers, a beam splitter and a photodiode. One of the two lasers, usually the most stable, is the *master laser* that is in free running. The other one, *the slave laser*, is forced by the servo loop to follow the first with a selectable frequency offset. The phase detector compares two signals: the first is the reference frequency, i.e. an RF signal oscillating at the offset frequency, the second is the *beat note* signal between the two lasers. The beat note is obtained by superposing the two laser beams on a beam splitter which output light is fed to to a photodiode. A photodiode is a quadratic detector, i.e. it is a current generator proportional to the power of the incident light. Its input is the sum of the two electrical field of the two lasers, therefore its output is composed by two components: the first oscillates at the sum of the frequency of the two lasers and the second oscillates at their frequency difference. The first is too fast and is averaged out by the detector, therefore the signal photocurrent is a sinusoidal wave at frequency equal to the frequency difference between the two lasers. To maximize the beat note amplitude the two beams must be overlapped, i.e. they must have the same beam waist dimension and position, their wavevectors must be parallel and the polarizations must be the same. The correction signal is fed to the piezoelectric control of the slave laser. In this work the used laser have a PZT tuning coefficient about $1\,\mathrm{MHz\,V^{-1}}$, the correction signal of the used phase detector has values in the range from 0 V to 10 V. The frequency drift of lasers is about $45\,\mathrm{MHz\,h^{-1}}$ if the room temperature is stabilized. This means that the range of the loop on the piezoelectric element of the laser (FAST servo loop) is not enough to ensures a long term stability

of the locking state. To overcome this problem an other servo loop (SLOW servo loop) is implemented. It acts on the laser's crystal temperature by means of a Peltier cell. The tuning range of this controller is in the order of $1\,\mathrm{GHz\,V^{-1}}$. The SLOW servo loop has the task to maintain the system locked for a long time (months). Sec. 6.6 shows the used electronic and the optical layout for the OPLL implementation.

6.6 The Virgo OPLL implemementation

For the locking of the Virgo squeezer, three OPLL servo loops must be designed and implemented. The first one, between the master laser and AUX2 laser, is employed to shift the AUX2 laser frequency by a quantity $\Delta\omega$ to have a simultaneous resonant condition of the two orthogonal light polarization into the OPO cavity. This condition is reached with a frequency offset of 150 MHz. The second OPLL, between the master laser and AUX1 laser, provides a frequency shift of 7 MHz of the light emitted by AUX1. This shifted beam is injected into the OPO with the aim to generate the error signal for the coherent control loop. The third PLL will be implemented in the integration of the squeezed light source in Virgo. It allows to lock the squeezer ML onto the Virgo main laser. Moreover, when the three OPLL are implemented, a hierarchical locking routine is needed to lock the three servo loops in the following order: firstly the PLL between the Virgo laser and the squeezer master laser, secondly the OPLL between the squeezer ML and AUX2 laser and finally the OPLL between the ML and the AUX1 laser. The electronic board of all the OPLL servo loop is designed to satisfy the following requirements:

- the OPLL frequency offset must be tunable in the range beetween 7 MHz and 150 MHz;
- a loop bandwidth up to 50 kHz;
- a residual phase noise less than 5 mrad measured between 1 Hz and 100 kHz;
- the loop has to maintain the locking state for long periods (in the order of months);
- the board must be equipped with an auto-locking routine and a communication protocol for its remote management.

In collaboration with University of Bologna and LENS electronic workshop we have developed a PLL board that satisfies all these requirements. We will describe it in Sec. 6.6.1

6.6.1 The PLL board

Fig. 6.10 shows a block diagram of the developed PLL circuit for the laser locking on the Virgo squeezed light source. The designed board implements two different servo loops that can be activated separately: the first is called fast servo loop and actuates on the piezoelectric element of the laser head, whereas the second, called SLOW loop, actuates on the Peltier element of the laser. The board is equipped by a microcontroller unit (model "Atmega328" of Atmel corporation) it performs the following tasks: the control of all the digital components mounted on the board, the management of the FAST and the slow servo loop, the USB communication with an external PC to exchange commands and informations used for the remote cotrol of the OPLL system. In the following the FAST and the SLOW servo loop are described separately.

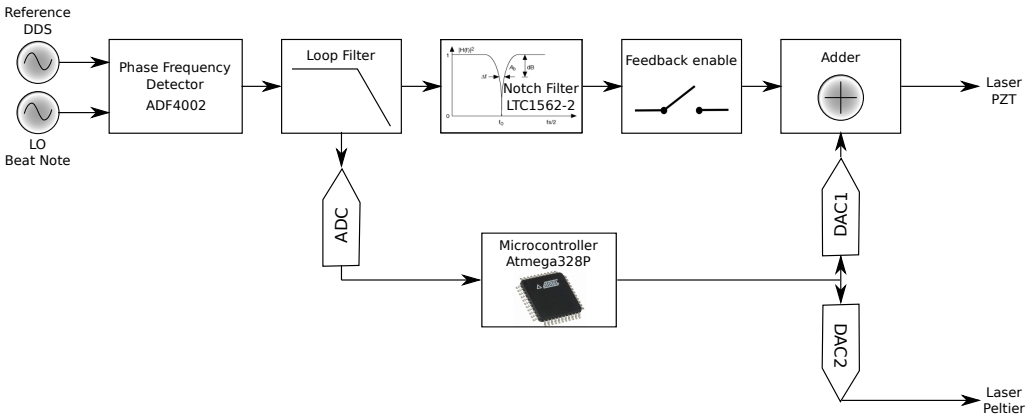

Figure 6.10: The optical setup of one OPLL developed for the Virgo squeezing optical bench.

The FAST servo loop is designed with the layout described in Sec. 6.1. The phase detector is a phase frequency detector, model ADF4002 of the Analog Devices company, that processes its two inputs: the reference signal and the beat note between the two lasers are processed [66]. The ADF4002 is a single chip that contains a PFD in series with a charge pump, its main features are listed in the following:

- its frequency working range for sinusoidal inputs is between 5 MHz and 400 MHz, whereas its amplitude working range is between -10 dBm and 0 dBm;
- it is equipped by a 14-bit reference divider R to lock the VCO at a sub-harmonic frequency respect to the reference by a facror R;
- it is equipped by a 13-bit feedback divider N to lock the VCO at a multiple frequency respect to the reference by a facror N;

- the charge pump gain can be changed with 8 different values;
- its output, the VCO control voltage v_{vco}, spans a range between 0 V and 5 V.

This chip is chosen a phase detector for two principal reasons: first, its frequency range is adequate for the OPLL needed to the squeezer development, second, a with PFD its simple to implement an auto-locking routine because it can detect frequency differences even if the system is not locked. After the PFD, the loop filter is implemented and it is composed by by two capacitor and one resistor as it is shown in Fig. 6.7. If it is required, an additional notch filter can be inserted in series with the loop filter, it has the aim to suppress the laser's piezoelectric resonances. This filter is designed with the the LTC1562 integrated chip of the Linear Technology manufacturer. The FAST servo loop is enabled/disabled exploiting a digital switch, managed by the microcoltroller, installed on the board. The filtered PFD output is summed with a tunable offset, between 0 and 4.5 V, before to send it to the actuator. This offset can be used to shift in frequency the beat note of few MHz.

The SLOW loop is digitally implemented inside the microcontroller unit. It has the task to maintain the FAST loop output at its central value, i.e. 2.5 V. Its implementation is discussed here below. One of the ATmega328 integraded ADC is engaged to sample the filtered PFD output with a sampling frequency equal to 10 Hz. This sampled signal is used as the error signal of a PID servo loop that holds it at its central value. The PID's output signal is sent to the Peltier actuator of the laser in order to change the temperature of the crystal. This servo loop ensures the long term stability of the OPLL maintaining it in the locking status for many days. The PID's output signals spans between ± 8.33 V and it is generated by using a 16 bits DAC. Therefore each bit corresponds to about 254 µV, the tabulated temperature tuning coefficient of the Laser is equal to $3\,\mathrm{GHz\,V^{-1}}$ so each bit shifts the laser frequency of about 800 kHz.

Another task of the microcontroller is the management of the communication with an external PC. This task is performed by exchanging ASCII character using the serial protocol. The board is then connected to the PC using the USB protocol and the Serial to USB communication is performed by means of the chip FT232 of FTDI company. It is a USB to serial UART interface (Universal Asynchronous Receiver-Transmitter). In this way the microconroller and the external PC communicates between them via the serial protocol and this chip manages the USB conversion. The complete schematic of this board is shown in App. refsec:schem:pll and Fig. 6.11 shows a picture of the board mounted in a the box installed in the squeezer clean room.

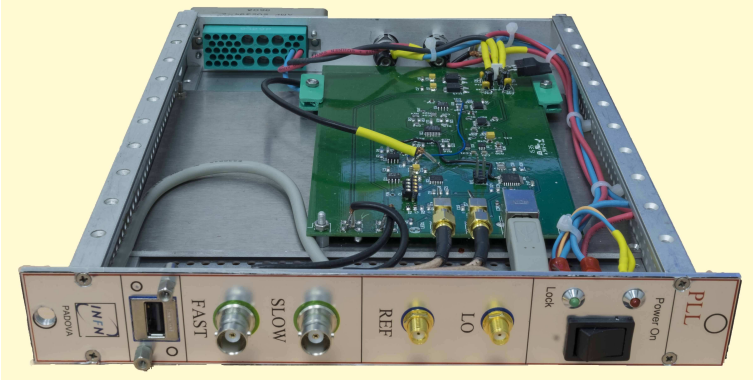

Figure 6.11: Photography of developed OPLL board mounted in a NIM crate.

Software interface

The firmware that runs on the Atmega 328 microcontroller is written in C language using avr libraries. It manges all the microcontroller's operations: at the startup of the board it initializes the SPI protocol, reads from the EEPROM the setting parameters and sets the registers of the ADF4002 and of the 16 bit DAC. In the endless loop the microcontroller samples the PFD output with a 10 bits ADC, computes the SLOW correction signal and listens to the serial port if a command is sent from an user to the board. With external commands it is possible to change many loop parameters: for the ADF4002 the value of N and R dividers, the charge pump gain and select the kind of multiplexer's output; for the FAST servo loop the on/off state, the sign and send an offset voltage to the laser's piezoelectric element; for the SLOW servo loop the on/off state, the sign, the PID controller's gains and send an offset voltage on the laser's Peltier element.

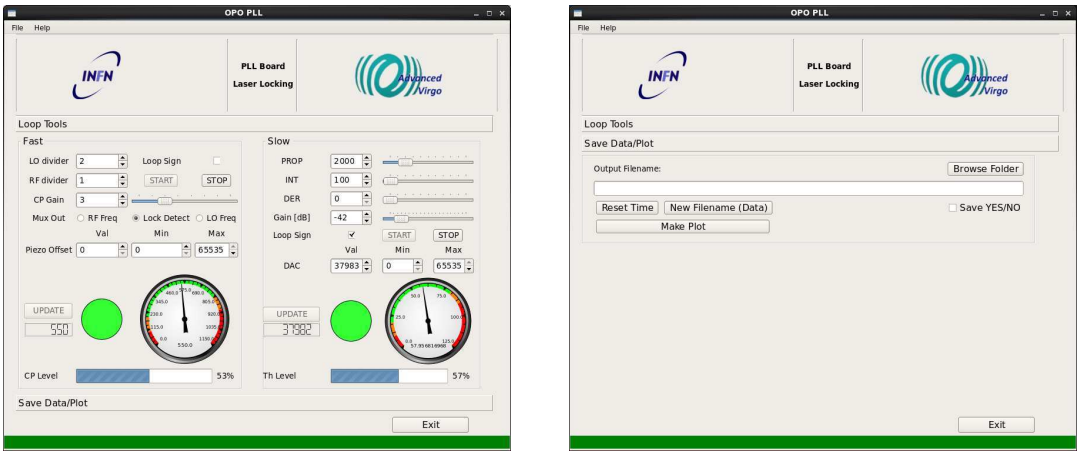

Figure 6.12: Screenshot of the python PLL graphical software. Left: the panel that manages the communication with the board. Right: the panel that manages the data acquisition

The board configuration via serial commands is uncomfortable for an users that works on the optical bench or manages it remotely. Therefore I have developed a graphical software that allows to manage the board without knowing the serial commands and the board's architecture. This software is written in Python 2.7 languages and the graphic part is based on Qt graphical libraries. A screenshot of the two different part of the graphical software is shown in Fig. 6.12. On the left side, the principal panel is shown, it is divided in two part: the first manages the FAST servo loop (left side of the panel) and the second manages the slow servo loop (right side of the panel). With the fast controller one can set the divider values, the charge pump gain, the loop sign and send an offset to the laser's piezoeletric element. Moreover in the bottom there is a led that shows if the loop is locked or not and a status bar that shows the PFD output value. With the slow controller an user can change PID parameters, PID gain, sign and its on/off status. Moreover in the bottom there is another led that shows if the loop is turned on or not and a status bar that shows how much the SLOW output is near to the set limits. On the right side of Fig. 6.12 it is shown the panel for the data storage which allows to select a folder, generate a filename with the gps time and, each second, writes on it the output values of the FAST and SLOW control loops.

6.6.2 Virgo squeezer OPLL setup

Fig. 6.13 shows the general optical layout of one of the three OPLL installed in the Virgo's squeezing optical bench. In this section all the loop parameters are summarized: the lasers specifics, the parameter used for the optimization of the OPLL phase noise and the obtained results.

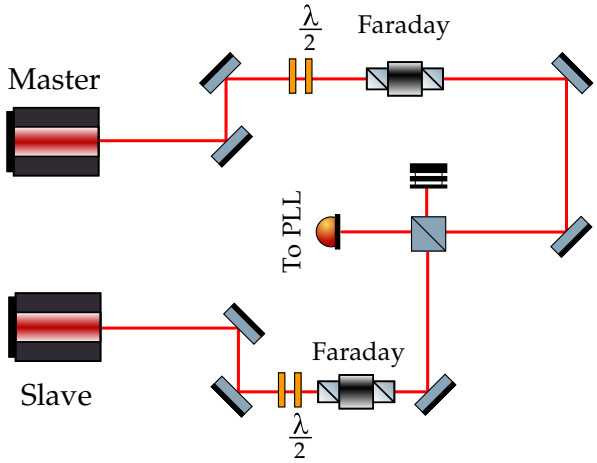

Figure 6.13: The optical layout of one OPLL in the Virgo squeezing optical bench.

PLL1: between the Master laser and AUX2 laser

The main Laser is a Mephisto of Coherent company with maximum output power of 1 W, whereas the slave laser is a Mesphsto S with maximum output power of 200 mW. The most interesting parameters of these two lasers are summarized in the following table:

Parameter	Value
Wavelength	1064 nm
Power	1 W
Thermal tuning coefficient	$3\,\mathrm{GHz\,K^{-1}}$
Thermal tuning range	30 GHz
PZT tuning coefficient	$1\,\mathrm{MHz\,V^{-1}}$
PZT tuning range	± 100 MHz

Table 6.2: Principal laser parameters.

The offset frequency $\Delta\omega$ that ensures the simultaneous resonance of s and p light polarizations into the OPO cavity is 150 MHz. Thie value of $\Delta\omega$ is set by changing the frequency of the PLL reference signal. This signal is generated with one channel of a DDS board. The DDS board output filter is designed to have a maximum output frequency of 100 MHz, therefore the OPLL is locked using a sinusoidal reference signal oscillating at 75 MHz and the feedback divider N set to 2. With this configuration the OPLL locks at the required frequency, i.e. twice the one of the reference clock. The PFD parameter of this servo loop are shown in the following table:

	Parameter	Value
011	R divider	1
	N divider	2
	Charge pump current	1.91 mA

Table 6.3: PFD parameter setted in the OPLL servo loop between the main laser and AUX2.

The other PLL input is the beat note and it is provided by the photodetector PLL_{PD}. The used photodiode amplifier is developed in collaboration with the University of Bologna and it is described in Sec. 7.3. The loop filter's topology is the one shown in Fig. 6.7 and its components are: $C_1 = 216$ nF, $C_2 = 33$ nF and $R_1 = 150\,\Omega$. These values are chosen to have an output phase noise less than 5 mrad and a unitary gain frequency of about 40 kHz.

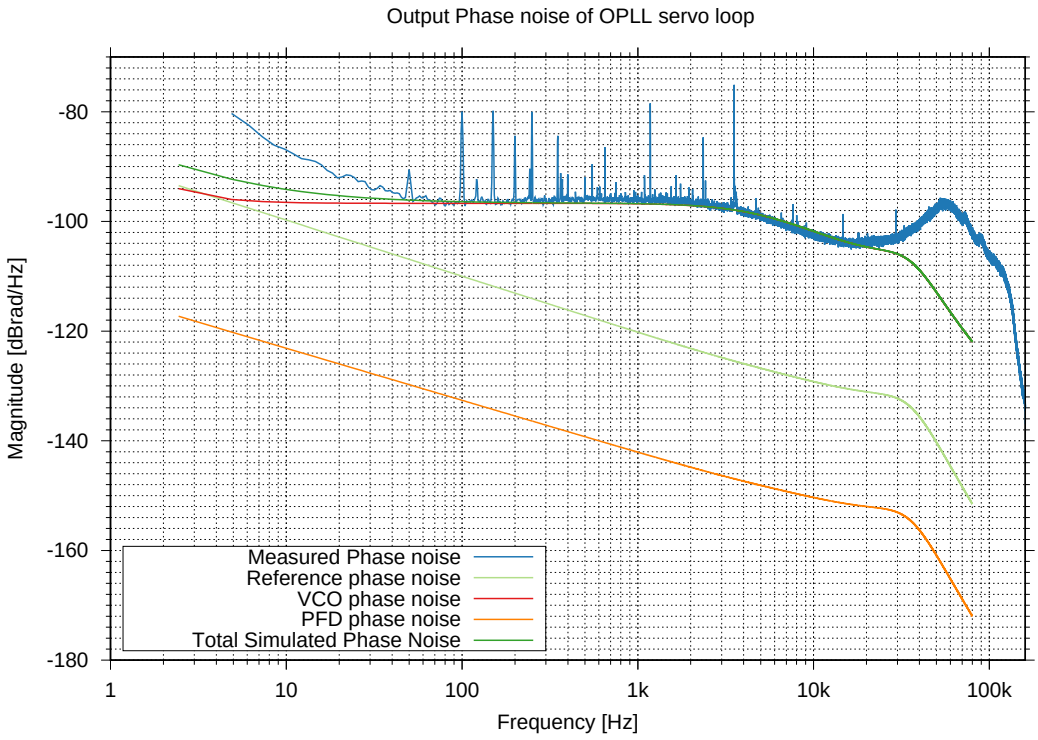

Figure 6.14: Simulated and measured PLL phase noise. In blue the measured phase noise of the PLL between the main laser and AUX2, in red the lasers phase noise, in hell green the reference phase noise, in orange the PFD phase noise and in dark green the total phase nose.

I have developed an OPLL simulator in Matlab computing environment that computes the servo loop open loop gain, closed loop gain and its output phase noise. It needs as inputs the VCO and phase detector gain, the value of the loop filter's componets and the input phase noise of all the PLL blocks. Fig. 6.14 shows the simulation and the measurement of the PLL's output phase noise. I have simulated separately all the contributions to the output phase noise and they are all negligible except the VCO's one, i.e. the two lasers phase noise. The phase noise measurement is performed in the same way of the DDS absolute phase noise measurement. Here, the beat note signal is demodulated by using a free channel of a DDS board at the same frequency. The figure shows that the measured phase noise follows the simulation curve until 20 kHz after that an excess of gain and a wrong estimation of the VCO transfer function causes the underestimation of the phase noise. The integral phase noise between 5 Hz and 160 kHz is equal to 3.2 mrad and the simulated unitary bandwidth is 31 kHz. The output phase noise and the unitary bandwidth values are determined by the FAST servo loop and in particular by the choice of the loop filter components and the charge pump gain. Otherwise in the PLL board is implemented a

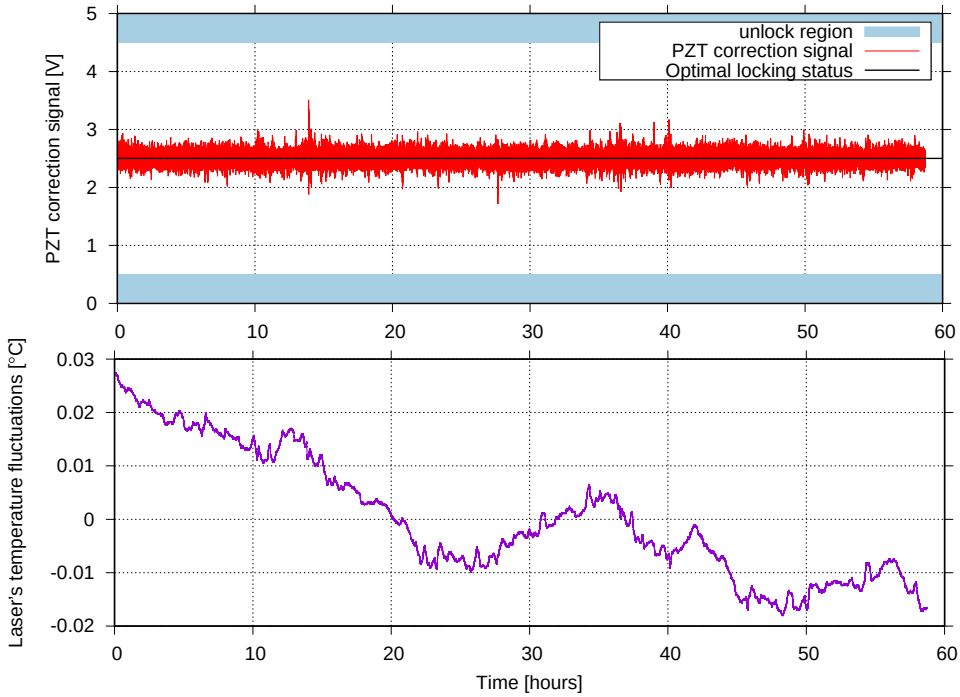

Figure 6.15: Long term stability of the PLL servo loop. In the upper plot shows 60 hours acquisition of the charge pump output. The bottom plot shows the acquisition of the slow correction signal.

PID servo loop to ensure the long term stability. The PID maintains the PLL locked acting on the laser's crystal temperature. Fig. 6.15 shows a 60 hours acquisition of the two outputs of the PLL board. The upper plot is related to the FAST output and it shows that the slow loop maintains it around its central value 2.5 V with a standard deviation of 100 mV, i.e. 100 kHz. The bottom plot shows how the SLOW loop acts on the laser's temperature. During the acquisition the SLOW loops causes a temperature variation of 0.045 °C that corresponds to a frequency drift of 135 MHz.

Chapter 7

Other electronics

This chapter treats all the other electronic and control systems of the Virgo squeezed light source. The chapter is structured as follows: Sec. 7.1 describes the temperature controllers of the OPO and the SHG cavities, Sec. 7.2 shows the ADC-DAC board used for the cavities length locking, the green power stabilization and the coherent control loop, finally Sec. 7.3 treats the other components i.e. the piezoelectric amplifiers, the RF photodiode amplifiers and the DC power supply.

7.1 Digital temperature controller

The two non linear cavities, OPO and SHG, must be maintained in the quasi phase matching condition to produce the non linear effect. This is reached at a precise temperature of the crystal. Therefore, in collaboration with the LENS electronic workshop, a temperature controller board is designed and developed. This board reads the crystal temperature with an NTC sensor and stabilizes it with a Peltier actuator. This section treats the principle of operation of these boards and their performances.

7.1.1 Peltier board: principle of operation

The crystal temperature is measured using a NTC thermistor (model TC-NTC2 of Laird manufacturer) located on the crystal holder (see Sec. 4.2.1). The NTC resistance is estimated with a digital resistance to voltage converter based on a stable voltage reference and a 24 bit $\Sigma - \Delta$ converter (AD7745 of Analog Devices). A digital PID filter is then computed using the microcontroller Atmega 328 of Atmel corporation. The correction signal is then transformed to an analogical signal and sent to a Peltier element by means of an H-bridge.

Temperature readout

In the circuit scheme (see App. B.2), the 4.096 V voltage reference (IC8) provides the reference voltage to the ADC (IC6), to the DAC (IC7) and to the voltage divider composed by the resistor R_1 and the NTC thermistor. The thermistor is not integrated directly on the board but it is connected to it with a 7 m cable. Therefore, the signal from this long cable is filtered by a couple of capacitors and coils to avoid RF peak up and noise that could generate aliasing in the ADC. The voltage divider is connected between the reference voltage and the ground and it is composed by a 9.1 kΩ low temperature coefficient (10ppm/°C) resistor and the NTC thermistor. The divider aim is to match the ADC input range and to provide a linearization of the NTC thermistor around the temperature of 37 °C.

A thermistor is a type of resistor whose resistance has a non linear relationship with temperature that follows the Steinhart Hart equation:

$$\frac{1}{T} = A + B\ln(R) + C\ln(R)^3$$

where the value of the A, B and C constants are tabulated on the thermistor datasheet. This equation can be rewritten as follows:

$$\frac{1}{T} = \frac{1}{T_0} + \frac{1}{\beta}\ln\left(\frac{R}{R_0}\right) \qquad R(T) = R_0\exp\left(\frac{\beta}{T} - \frac{\beta}{T_0}\right)$$

that is a Stenhart equation in which $A = 1/T_0 - ln(R_0)$, $B = 1/\beta$ and $C = 0$. If the thermistor is placed in series with a fixed resistor of value $R(T_0)$, the voltage divider ratio is equal to:

$$\rho(T) = \frac{R(T_0)}{R(T_0) + R(T)} = \frac{1}{\exp\left[\frac{\beta}{T_0}\left(\frac{T_0}{T} - 1\right)\right] + 1}.$$

The expansion of the ratio around $T = T_0 + \delta T$ when $\delta T \ll T_0$ up the third order is equal to:

$$\rho(T) \approx \frac{1}{2} + \frac{\alpha}{4}\left(\frac{\delta T}{T_0}\right) - \frac{\alpha}{4}\left(\frac{\delta T}{T_0}\right)^2 - \frac{\alpha(\alpha^2 - 12)}{48}\left(\frac{\delta T}{T_0}\right)^3 + \mathcal{O}\left(\left(\frac{\delta T}{T_0}\right)^4\right)$$

where $\alpha = \beta/T_0$. From the last equation it is straightforward to find the sensitivity of the voltage divider i.e.:

$$\frac{d\rho}{dT} = \frac{\beta}{4T_0^2}.$$

The voltage divider composed by the series of the TC-NTC2 thermistor and the 9.1 kΩ resistor has a linear characteristic around 36.85 °C in a range of ±7.5 °C with a sensitivity about 10 900 ppm/°C. Fig. 7.1 shows the linearized voltage divider output

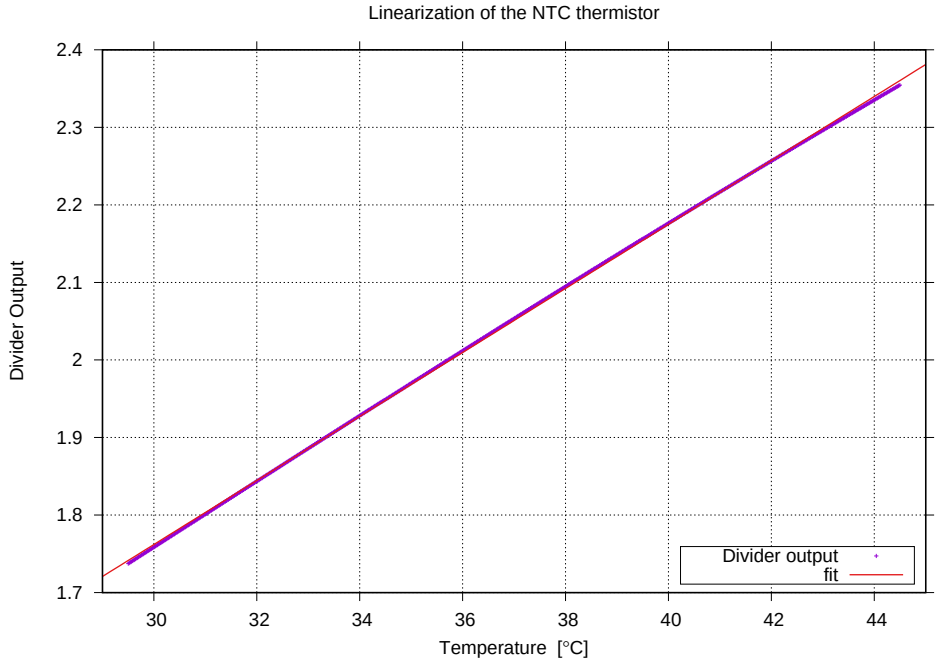

Figure 7.1: Linearized response of the NTC thermistor as function of its temperature. The pink line is the voltage divider output and the red line is its linear fit.

as a function of the thermistor temperature. A linear fit of the voltage divider output is performed, in the temperature range $30 - 45°$, and the value of its slope is equal to $41.25\,\mathrm{mV}\,°\mathrm{C}^{-1}$.

The output of the voltage divider is sampled with a $\Sigma - \Delta$ converter (IC8), i.e. a a kind of analog to digital converter. The used converter is the model AD7745 of Analog Devices company that has a resolution of 24 bits, thus it reads the output of the voltage divider with a resolution of 488 nV which corresponds to a temperature sensitivity of 11.5 µK [67]. Moreover, according to the datasheet, the ADC has an RMS noise of 2.1 µV when the sampling rate is set to 8 Hz that causes an RMS noise of about 50 µK per sample, whereas the ADC offset drift with temperature is negligible. A measure of the detector RMS noise is performed with the following procedure. A second 9.1 kΩ resistor is connected to the board in place of the thermistor, the value of the voltage divider output is sampled and the RMS value of the read voltage is computed and it is about 196 µK i.e. a factor 4 worse than the expected value.

In order to achieve an high degree of temperature stabilization the effect of the environmental temperature fluctuations has to be minimized. In this system, the main problem comes from the temperature susceptibility of the reference resistance at 9.1 kΩ and the parasitic resistance of the cable. In the design of the voltage divider a resistor with a low temperature coefficient, i.e. 10 ppm°C^{-}1, is chosen.

The variation of the divider resistor with temperature is measured by replacing the thermistor with another 9.1 kΩ then the board is heated and the temperature and the voltage divider output simultaneously are acquired. With a linear fit of these data a slope of 15 ppm°C^{-1} is obtained.

A second factor that influences the temperature readout is the parasitic resistance of the cables that are in series with the NTC. The thermistor is connected to the board with a cable composed by two copper terminals with diameter of 0.511 mm. The nominal resistance of the cable is 0.16 Ω m^{-1} and the temperature dependency of the copper resistivity is 0.43 %°C^{-1}. Therefore, if the temperature readout of the board, including these contributions, is simulated the obtained suppression of environmental temperature fluctuation is of the order of 1:800, however the measured suppression ratio is of the order of 1:36.

Temperature processing and stabilization

The second part of the board consists in the H-bridge that stabilizes the crystal temperature by controlling in current a Peltier cell. Once the ADC has sampled the voltage divider output, the microcontroller computes the corresponding temperature and implements a digital Proportional Integral Derivative (PID) with the aim to fix it to a set point. The controller has the following transfer function:

$$H(s) = K_p + \frac{K_i}{s} + K_d s$$

where K_p, K_i, and K_d are respectively the proportional, integral and derivative gains. The sampling rate of the ADC and the PID computation rate are set to 8 Hz. The computed correction signal is converted to an analog signal with a 16 bit DAC (IC7) and it is the control voltage of the current to voltage converters in the H-bridge. The H-bridge is powered at 6 V and drives in current the Peltier cell. The high side of the bridge is composed by two digital transitors (IC1) and (IC9) that are driven directly by the digital microcontroller outputs. Its low side is composed by a dual operational amplifier (IC4) that compares the DAC output voltage with the voltage across the resistors R2 and R19. The response of this circuit is 2 A/V, the maximum output of the DAC is 4 V that is in series with a voltage divider composed by the two couple of resistors R3 and R10 or R8 and R9. Therefore the DAC output is divided by a factor 4 and the maximum output current of the bridge is 2 A.

Communication with an external PC

The other tasks of the microcontroller are the initial configuration of the ADC, DAC and the communication with an external PC via the serial protocol. As in the PLL board an USB to RS232 converter is installed and it allows a bilateral communication between the board and an external PC. In the firmware is implemented a communication protocol based on the exchange of ASCII strings. The baudrate of the serial port is set to 9600. With ASCII commands an user can turn on/off the temperature stabilization, reverse the stabilization sign, change the temperature set point, set the three gains of the PID controller, ask to the board the status string. This string contains the last measured temperature, all the controller information (gains and status) and a monitor of the bridge output that is sampled at the output of the dual operational amplifier IC11.

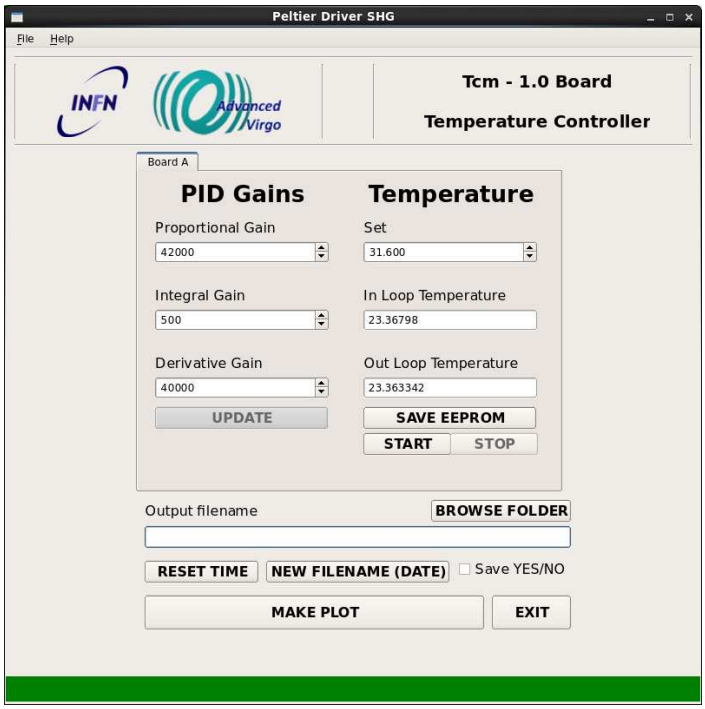

Figure 7.2: Graphical panel developed with Qt libraries for the management of a temperature controller board.

I have developed another graphical panel in Python programming language based on Qt graphical library for simplify the board management and temperature acquisition. A screenshot of the panel is shown in Fig. 7.2. The upper side of the panel is dedicated to the board management: on the left the controller gains can be changed, whereas on the right side it is possible toset the temperature, read the actual temperature from the board and turn on/off the temperature stabilization. The graphical

widget for the loop sign setting is hidden because the sign depends on the connection of the Peltier cell to the board so once fixed the sign it must not be modified. Moreover with a wrong sign it is possible to cool-down the crystal therefore it is safer to disable this controller. All the parameters are update in their respective widget with a pooling rate of 1 Hz. The bottom part allows the user to save in a file the temperature and the set point with a sampling rate of 1 Hz. When the user want save data he must choose the destination folder and the data are saved in a file with a name related to the gps time when the acquisition starts. The button make plot is connected to a Gnuplot script that opens the data file and shows the plot.

7.1.2 Installation of the board in the clean room and performances

Each cavity is equipped with a thermometer and a Peltier cell for the temperature stabilization and another thermistor for the acquisition of the out of loop temperature. Each board has only an ADC channel used for the NTC acquisition therefore two boards are used for each cavity one to perform the servo loop and one to read only the out of loop thermistor. A NIM module that contains two boards is assembled for each cavity. Fig. 7.3 is a photography of one of these modules. Its front panel

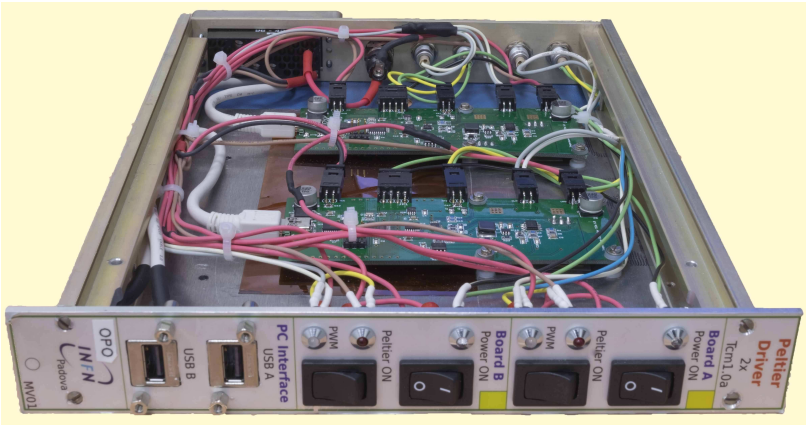

Figure 7.3: Photo of a NIM module that contains two temperature controller board used for the temperature stabilization of a non linear crystal.

is divided in three parts. The first two contain: the switches for power on/off the boards and the bridge separately and three status LEDs one that shows if the board is on, one that shows is the H-bridge power supply is on and and one bi-colours LED that shows if the bridge is cooling (green) or heating (red). The design of the board and of the NIM module allow to turn separately on the H-bridge and the readout electronics. The third part of the front panel is equipped with two USB port for the serial communication with the PC. On the rear panel there are the connectors for the

two thermometers and for the Peltier cell and a fuse.

As it is shown in Chap. 4 the PPKTP crystal is mounted in a sort of mini-oven composed by a copper element that is thermally connected to the Peltier cell and the two NTC thermistors that are mechanically attached on it. The Peltier element chosen is the model CP0.8-71-06L of Laird company and supports maximum voltage of 8.6 V and maximum current of 2.1 A. Fig. 7.4 shows the time charts of the room

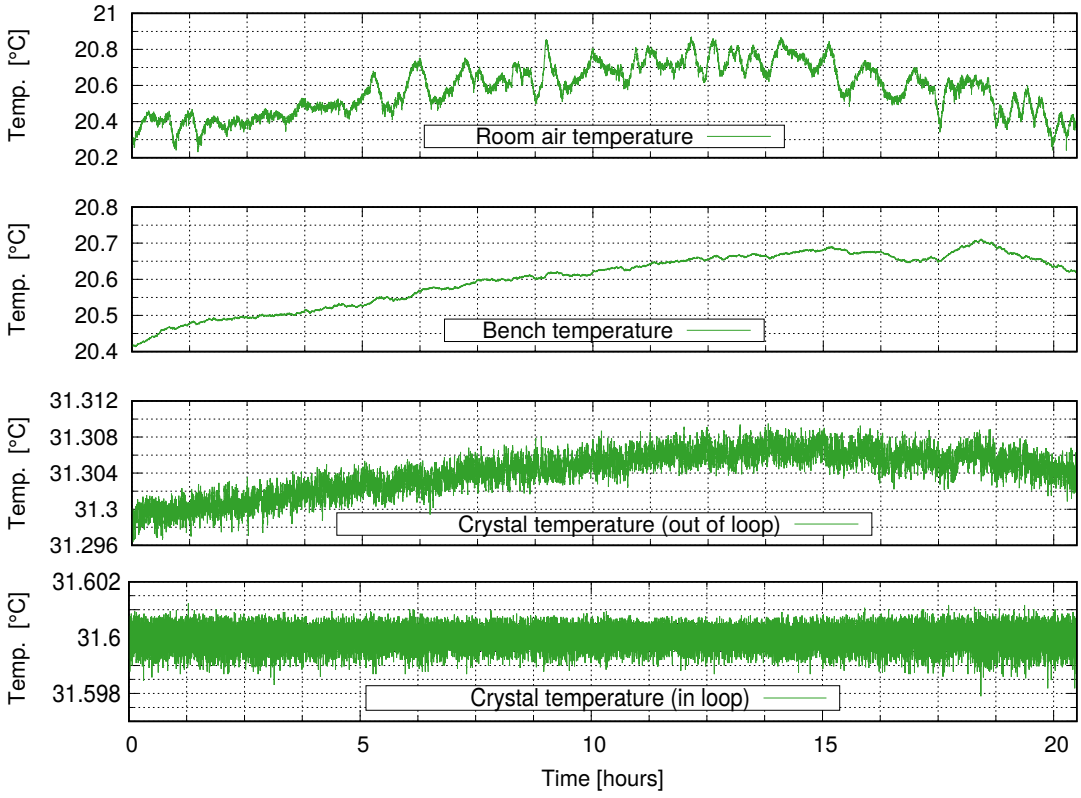

Figure 7.4: From the top time chart with a length of 20 hours of the temperature variations of the room temperature, bench temperature and crystal temperature both out of loop and in loop when the temperature controller is turned on.

temperature, bench temperature and crystal temperature both with the in loop and out of loop NTC thermistors. The four sensors are acquired for 20 hours. The first plot from the top is the air temperature measured in the box that covers the bench. The air temperature oscillates between 20.2 and 20.8 °C. The second plot represents the temperature on the bench measured with a thermometer placed near the master laser (about 30 cm from SHG cavity. The temperature on the bench has variations with a mean of 20.60 °C, a standard deviation of 0.07 °C and a maximum excursion of 0.3 °C. If the air temperature and bench temperature are compared one see that the bench acts on the temperature as a low pass filter. The last two plots are the in loop and out of loop crystal temperatures. The set point of the servo loop was set to

stabilize temperature at 31.6 °C, therefore the in loop temperature oscillates around 31.6 °C with a standard deviation of 347 µK. Conversely the out of loop temperature oscillates between 31.29 and 31.31 °C because the readout of the in loop thermistor depends on the room temperature as it is explained in Sec. 7.1.1. Therefore the system stabilizes the crystal temperature around 31.6 °C with a standard deviation of 2.4 mK, a maximum out of loop excursion of about 12 mK and a suppression of the bench temperature variations of a factor 35.

7.2 Servo loops based on UDSPT Boards

The last group of controllers used in the Virgo squeezed light source is composed by the following servos: the length locking of non linear cavities (SHG and OPO), the length locking of triangular cavities (Green Mode Cleaner (MCG) and MCIR), the green power stabilization with a Mach Zender Interferometer (MZ) interferometer and finally the squeezing ellipse angle stabilization with the coherent control loop. The cavities length locking is realized with the Pound Drever Hall technique, whereas the stabilization loops of the green power and the squeezing ellipse angle are PID controller with a selectable set-point. All these controllers are based on the UDSPT boards developed by the INFN Pisa group that are devices for signal conditioning and signal processing that mount two Field Programmable Gate Array (FPGA)s, a DSP and 6 Analog to Digital Converter (ADC) and 6 DAC each one. The INFN Pisa group has developed a command line software that allows to design quickly the digital controllers architecture by setting in the frequency domain the poles and zeroes position of each controller/filter. This section is structured as follows: Sec. 7.2.1 shows the features and the architecture of UDSPT boards and Sec. 7.2.4 describes how controllers are implemented using these boards.

7.2.1 Virgo UDSPT Board

As explained above, all the servo loops closed on a piezoelectric actuator are based on the Virgo UDSPT boards that are designed for the stabilization of the interferometer's superattenuators. The hardware, the firmware and the management architecture of these boards are completely thinked and developed by the Pisa INFN group. All the information about the boards are treated from [68] and [69].

UDSPT boards are high performance signal conditioning, signal conversion and signal processing platforms that allow users to implement real time control system. The design of these boards is very complex: they are composed by more than 250

components. Pisa group adopted a modular design in order to limit boards complexity and to help in the debugging and maintenance. Therefore each board is divided in dedicated areas: ADC, DAC, signal processing and the front-end for the analogic and digital inputs and outputs. Fig. 7.5 shows the layout of a board in the left side and a block scheme of each board in the right side.

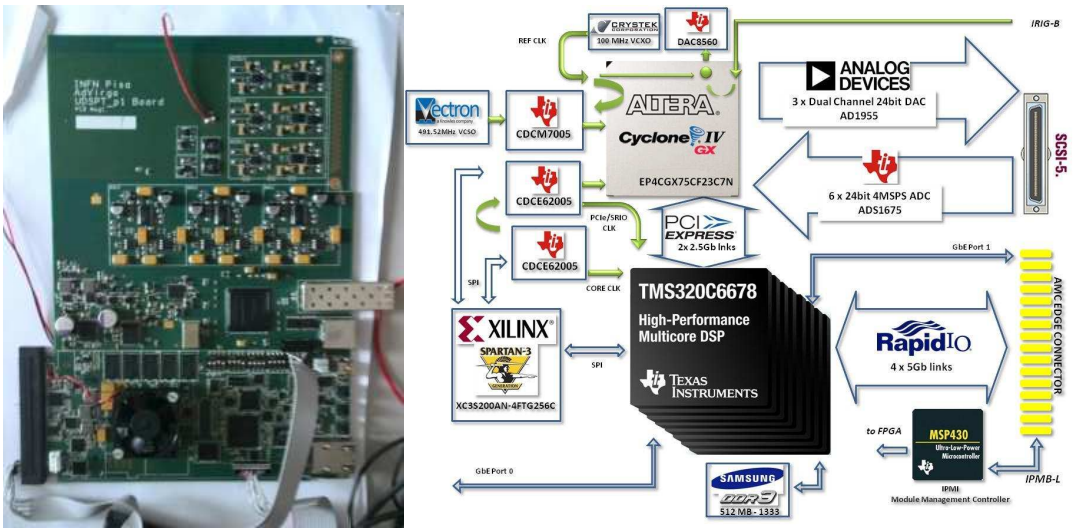

Figure 7.5: Left: a photo of a UDSPT board. Right: a block scheme of its layout and principal components.

UDSPT boards can works in two configurations: or as stand-alone devices or in cooperation with other boards. In the second configuration these boards are installed in a crate. The crate provides them the power supply, the Ethernet connection and the timing synchronization. As it is shown in Fig. 7.6 when boards work in cooperation mode each of them acquires sensors signals and acts on actuators, moreover different devices can exchange digitized signals between them via the RapidIO bus. Furthermore the system is connected in the Virgo Network that is used for different purposes: for boot code download that is a sort of basic OS at the board start-up, for data exchanging, for board programming and for board management. Finally one board in a crate is designed for real-time data exchanging with the Virgo Data Acquisition (DAQ) system by using an optical link. This system is used to visualize or store real time data with a maximum sampling rate of 10 kHz.

The following list summarizes the features of UDSPT boards:

- 6 differential ADC channels with resolution of 24 bit and 3.84 MHz of sampling rate;
- 6 balanced DAC channels with resolution of 24 bit and a sampling rate of

320 kHz;

- a Texas Instrument 8 core Digital Signal Processor (DSP) for the board management, signal conditioning and signal processing;
- two Gigabit Ethernet ports supporting 10/100/1000 Mbps data-rate one on the back connector and one on the front panel;
- two FPGAs one dedicated to the processing unit and one to interfacing data converters;
- the sampling frequency of converters is synchronized to an IRIG-B signal that is a board input;
- the board is powered at 12 V - 3 A power supply (external or by a crate);
- 5 channels at 5 Gbps of RapidIO on the board back plane, this is used for data exchanging between different boards that are placed in the same crate (only in cooperation configuration);
- an optical link with data rate of 1Gbps for digital input/output and communication with the Virgo Data Acquisition System.

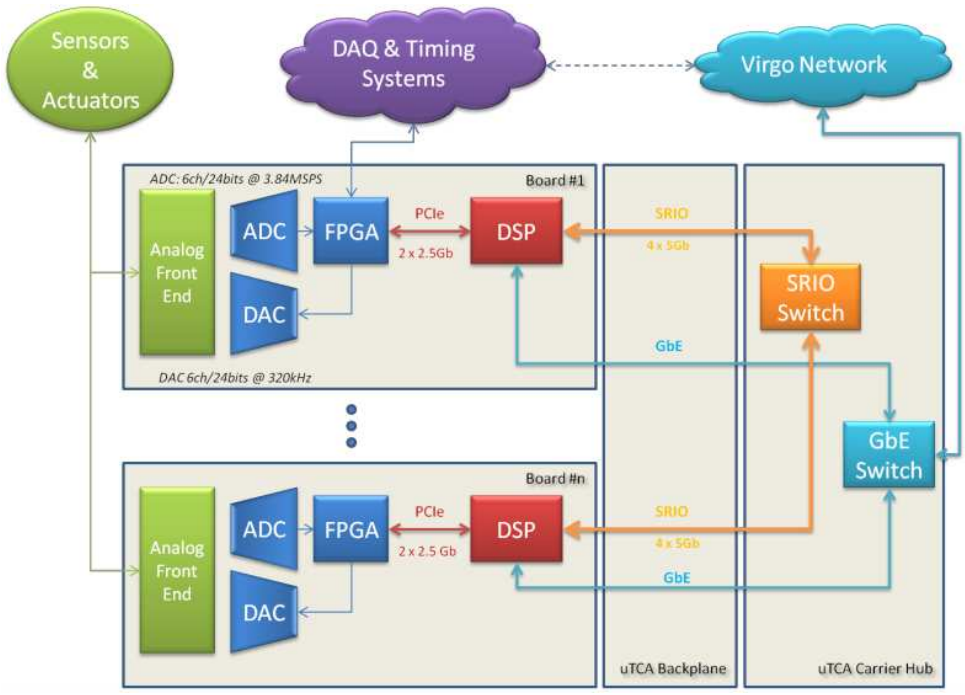

Figure 7.6: Layout of the signal path of the system: sensors acquisition, actuators driving, data exchanging between boards and boards timing synchronization

7.2.2 Boards management with “Damping” and “SAT supervisor”

The DSP has eight different cores but the user can act only on two of them i.e. core 4 and core 1. The other cores are dedicated to communication between different boards, to Virgo DAQ system, ADC and DAC and so on. The user writes code in these two cores by exploiting a command line software developed by INFN Pisa group. This software is called “Damping” and consists in an intuitive interface for signal manipulation and digital controller development without knowing the board architecture, the board firmware and digital control theory. The user manipulates signals by setting filters in which he can choose the frequency of zero and poles moreover he has available other blocks that help in the controller development such as: signal generators, signal multipliers, signal adders, Schmitt Trigger, etc.. When the “Damping” code is written it must be compiled and downloaded it into the board. The compilation generates a code for the cross-compiler that produces the DSP binary code. Because of the boards are connected to the Virgo network it is possible to write controllers remotely.

```
ADC1       MCIR_trans      NULL          no      1
ADC2       MCIR_err        NULL          no      1
FEED       MCIR_ramp
MCIR_ramp  MCIR_ramp       NULL          no      1
ADD        MCIR_sq_f                     no      0.5
SIG_GEN    MCIR_sq_tr square_trigger     no      1
ADD        MCIR_incr                     no      6.25e-06
ADD        MCIR_rcent                    no      0.55
ADD        MCIR_roff                     no      0
RELAY      MCIR_th_t  r_tramniss         no      1
MIX        MCIR_trian mix1               no      1
ADD        con_feedon                    no      1
MCIR_th_t  MCIRfeedon      NULL          no      -1
con_feedon MCIRfeedon      NULL          no      1
MIX        MCIR_ramp  mix_ramp           no      1
MCIR_ramp  MCIR_r_pzt      NULL          no      1.1
MCIR_rcent MCIR_r_pzt      NULL          no      0
MCIR_roff  MCIR_r_pzt      NULL          no      0.5
MIX        MCIR_err1  MCIR_dis_err1      no      1
MIX        MCIR_err2  MCIR_disablerr     no      1
MCIR_err2  MCIR_corr  feed1.flt          no      9          MCIR_gain  0.3       after
MIX        MCIR_r_fin MCIR_ramponoff     no      1
MCIR_r_fin MCIR_out        NULL          no      1
MCIR_corr  MCIR_out        NULL          no      1
```

Figure 7.7: An example of the “Damping” code used for MCIR cavity length locking.

When the control system is written compiled and downloaded it is possible to change some parameters without use “Damping” and re-compile every time the DSP code. INFN Pisa group has developed another software called “SAT Supervisor” written in C++ and in Python languages based on the Tango Controls software toolkit[1].

[1]For more details about Tango Controls toolkit read Sec. 7.4

With this software the user can turn on/off the boards, ask to them variable values, ask/change gain values, reset filters, change constant values and so on. Sec. 7.2.4 shows how I implemented the controls of all the cavities based on this hardware software environment.

7.2.3 ADC and DAC performances

I have measured the performance of one ADC and DAC channel of one of the three board used in the squeezing laboratory. For the ADC noise measurement I have connected its input with a 50 Ω termination, then the channel is acquired for 20 s and its FFT is computed using the Matlab function "pwelch". For the DAC noise measurement its output is set at 1 V, than it is amplified a factor 100 with a low noise amplifier (Model SR560 of Stanford Research manufacturer) and finally the signal is acquired wit the same ADC channel measured before. The full scale of the two converters is ±10 V. The two spectrum are shown in Fig. 7.8.

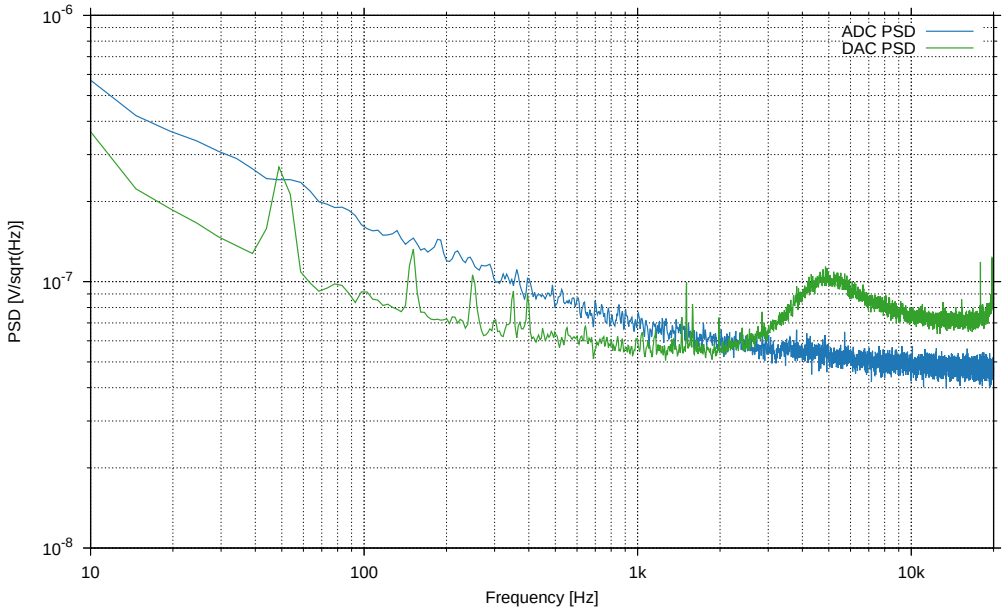

Figure 7.8: Noise spectrum of an ADC channel and a DAC channel of an UDSPT board measured in the squeezing laboratory.

7.2.4 Squeezer cavity locking implementation

We started the collaboration with INFN Pisa group in the summer 2015 and after a training period we installed the UDSPT boards system in the squeezing clean room in April 2016 . The system is composed by a crate, three UDSPT boards and three distribution boxes that are used to connect the three boards to their inputs

and outputs. One of the three board is designed as master board, i.e. it receives the timing synchronization from the Virgo DAQ system and is connected to it by using a mono-mode optical fiber for digital data exchanging. The master board controls the MCIR, SHG, MCG cavities and the MZ interferometer. A second board controls the OPO cavity and read the homodyne detector's audio channel; the last board manages the coherent control loop. The frequency of core 1 and core 4 of the three boards is set to 160 kHz.

The cavities are locked with the PDH technique shown in Sec. A and for each controller I used two input signals and one output signal. The first input is the output of a photodiode with low bandwidth (up to 200 kHz) placed in transmission to the cavity and used as trigger to have the information if the cavity is near of the resonance (peak) or out of resonance (flat). The second input is the PDH demodulated error signal extract from a photodetector with higher bandwidth up to 100 MHz placed in reflection from the cavity. The used photodiode boards are briefly described in Sec. 7.3. The PDH error signal is filtered by a digital controller and its output, amplified by a factor 100 (by means of the PZT high voltage amplifier), is sent to a piezoelectric actuator linked to one of the cavity mirrors. In this way the loop is closed and the cavity length can be changed and stabilized. The high voltage amplifier described in Sec. 7.3. The code running in the DSP implements a PDH servo loop with an auto-locking routine. The controller acts as follows. It scans the cavity with a triangular ramp with frequency of 0.5 Hz. The amplitude of the scansion is set in order to change the length of the cavity for about 2 free spectral range. Therefore if the trigger signal (photodiode in transmission) overcomes a selectable threshold, i.e. when the cavity is near the resonance, the ramp holds at the reached value and the servo loop is turned on and forces the error signal to remain around zero. Moreover I have developed another threshold based system that recognizes if the cavity loses the resonance condition, stops the servo loop and restart the slow ramp in order to re-lock automatically. The status of the loop (locked or scanning) is saved on a variable that is used for the development of an hierarchical auto-locking procedure of all the cavities.

The Mach Zender interferometer allows to set the green beam power at a fixed value. Therefore the architecture of its controller is completely different respect to cavity locking architecture. This loop have one input and one output. The output is amplified by a factor 100 and sent to the piezoelectric actuator attached to one of the MZ mirrors. The input signal comes from a photodiode (slow bandwidth) that measures a fraction of the green light transmitted by the MCIR cavity. The

architecture of this loop is very simple: the user chooses a set point which the control loop set stable at the photodiode output.

I have also added to the system the possibility to scan the cavities with a triangular ramp when the respective controller is turned off. The amplitude, the frequency and the offset of this ramp can be chosen remotely by the user.

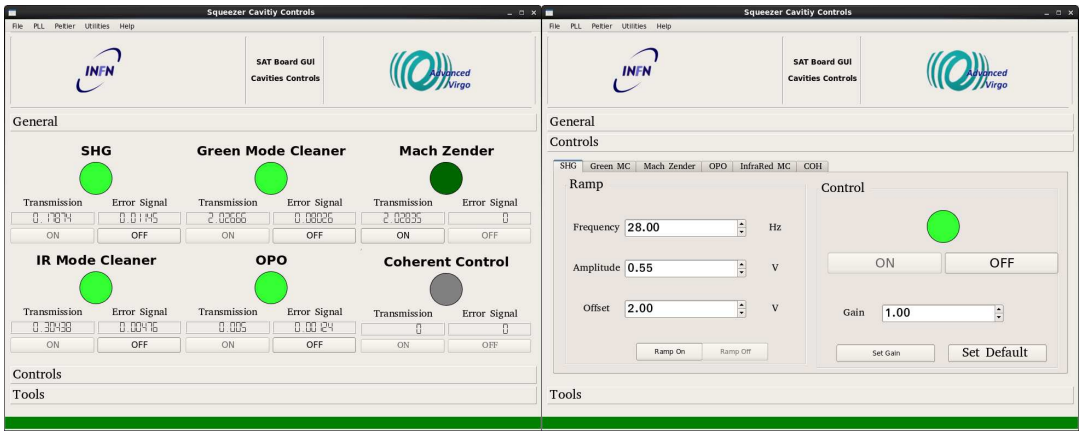

Figure 7.9: First two panels of the UDSPT board graphical tools for squeezer control.

I have developed a graphical software written in Python language based on Qt libraries for an easy management of all the controls based on the UDSPT boards. This graphical software exploits the system developed by INFN Pisa group, based on the Tango Controls toolkit. Fig. 7.9 and Fig. 7.10 show the graphical software for the cavity management. It is divided in three sub-panels. With the first panel the users can turn on/off each loop, have some displays that show the value of the two inputs sampled each second and a LED that shows if the cavity is locked (green), unlocked (red) or turned off (dark-green).

The second panel has a tab for each controller in which the users can turn on/off the loop, turn on/off the triangular scansion on the piezoelectric actuator, set the ramp amplitude, frequency and offset, the loop gain and if it is expected the set point.

Finally the third panel is a sort of tool box in which the user can restart the boards, reset each loop separately and has a fast visibility calculator when he work on the alignment of the homodyne detector.

In the right side of Fig. 7.10 a graphical panel for the management of all the photodiode offsets is shown. The performance of the loop, the open loops gain transfer functions and the cavity transfer functions are shown in Chap. 4. As said above the filters topology can be changed by modifying, with “Damping” software, the code that runs on DSP.

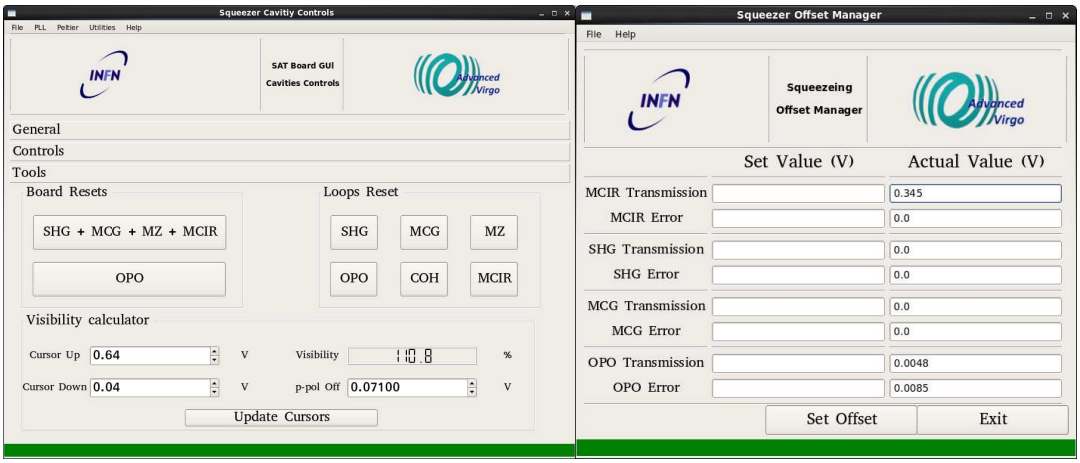

Figure 7.10: Left: third panel of the UDSPT board graphical tool for squeezer control. Right: Graphical tool for offset manager.

7.3 Photodiode amplifiers and power supplies

To implement the locking of all the cavities we developed some additional electronics i.e. photodiode boards with RF amplification and on board demodulation, low frequency photodiode boards and high voltage amplifiers for piezoelectric elements driving. In this section we will show briefly this support electronic used in the Virgo squeezed light source.

The high voltage amplifier board is designed by the EGO Electronic Workshop. It accepts only a positive inputs between 0 and 10 V which is amplified by a factor 100. Moreover, on the board is mounted a trimmer that allows to set an offset which is summed to the input signal. Finally the board is provided by an output monitor i.e. a signal equal to the output signal but divided by a factor 100. These boards have two different power supply, i.e. the high voltage up to 1000 V and the low voltage at ± 24 V. For the squeezer 7 high voltage amplifier are required: 2 for the stabilization of the squeezing ellipse orientation, 4 for the cavities locking and one for the MZ interferometer. The Electronic Workshop of Trento University has assembled a box that mounts six high voltage amplifier boards. Fig. 7.11 shows a photo of the box front panel that is equipped, for each board, by an LCD 7 segment display connected to the monitor output, a connector for the monitor output and a LED that turns on only when a current overload happens. On the rear panel are mounted the input and the output connectors. The box is stand alone because inside are mounted an high voltage power supply (700 V) and the low voltage power supply. The seventh channel is provided by a single board mounted in a NIM crate. This set-up has shown an high noise and spectral lines contents, thus after a series of tests we have understood

that the principal noise source was the ±24 V internal power supply that is replaced with a low noise external DC power supply line.

Figure 7.11: Box that contains six high voltage amplifiers

.

The RF photodiode boards are designed by LENS electronic workshop. The used photodiode is the model FD500 of Fermionics manufacturer. The board mounts a dual transimpedance amplifier with a total gain of 400. After the amplifier are placed the following elements: a transformer, a limiting amplifier with gain equal to 6 and and output level limitation such that the maximum output level is about 7dBm. The amplified signal is one of the two input of a class mixer (model ZRPD2+ mixer of Minicircuit company). Its second input is an external RF oscillating signal used to demodulate the photodiode output. After that the signal is filtered by a low pass filter with roll-off frequency of 4.7 MHz. The input impedance of the filter is 50 Ω whereas the output impedance of the mixer is equal to 500 Ω therefore another operational amplifier is used to match the impedance. The output of the board is differential and is generated by means of a fully differential amplifier with a gain equal to 4.6. The board is equipped by two additional output signals: the first is an RF monitor of the photodiode AC component before the mixer, whereas the second is connected directly to the photodiode output, before the transimpedance amplifier, and is used as monitor for photodiode alignment. The board is supplied at ±5 V and the photodiode bias is equal to 5 V.

The low frequency photodiode board are developed by EGO electronic workshop group. These boards mount a transimpedance amplifier, a low pass filter and are supplied at ±12 V. Each board has two outputs one which is single ended and it is useful during the detector alignment and one which is fully differential and it is connected to UDSPT boards. A photo of the low frequency and high frequency

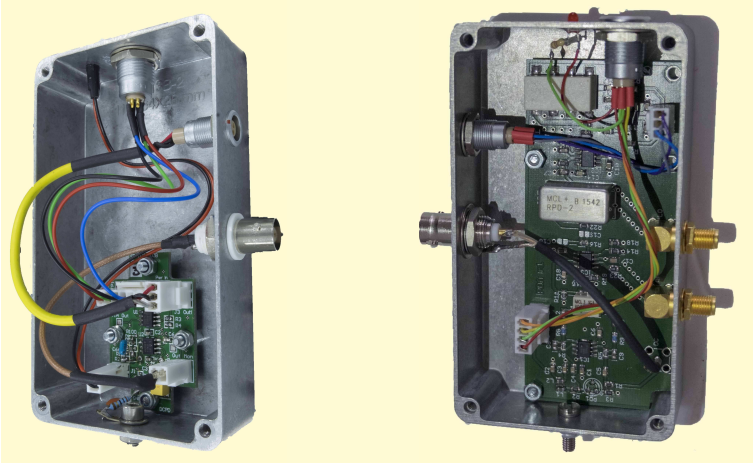

Figure 7.12: Custom photodiode amplifier used on the squeezer optical bench. Left: photo of a box that contains a low frequency photodiode. Right: photo of the box that contains an high frequency photodiode.

photodiode is shown in Fig. 7.12. The photodiodes configuration, placed all over the bench, is shown in Chap. 4. The power supply of all the photodiode boards is provided by EGO electronic workshop group.

7.4 Software hardware architecture

All the electronics and controls of the squeezer must be integrated in the Virgo Data Acquisition system and manageable remotely. In the Virgo experiment an homogeneous system of controls is developed by exploiting the Tango Controls toolkit. Tango controls is an open-source software toolkit thought to connect things together[2]. In Virgo Tango Controls is principally used to develop a distributed control system in which the devices are controlled and monitored in a distributed network. This toolkit is operating system independent and supports C++, Java and Python for all of the components. With Tango I have developed in Python programming languages a server of instrument that controls all the boards shown in this thesis, i.e. OPLL boards, DDS boards and temperature controller boards. For each kind of board I have written a device server that has the following features:

- it connects to the board by using the virtual serial port for the OPLL and temperature controller board or via the ssh protocol for the DDS board;

- it has a function that sends to the board a command and waits the answer. The

[2]Detailed information are on the Tango Cotrols toolkit offcial page at `http://www.tango-controls.org/`

command is sent as argument of the function;

- it asks to the board, each second, the value of its status variables and save it in the device server attributes;
- it controls each second if the board is connected.

The graphical software shown in Fig. 5.7, Fig. 6.12 and Fig. 7.2 are not connected directly to the boards but are clients of the "Tango" server that controls the different device servers of each board. The use of this toolkit ensures some benefits: when an user runs a graphical client it interacts with the server and not directly with the board in this way multiple board accesses are avoided. The EGO Computing Staff has developed some Python routines that send the Device Server's attributes to the Virgo DAQ system. In this way the status variable of each board are directly saved together with the other interferometer data. The UDSPT boards are managed by another Tango Controls server developed by the Pisa INFN group. The graphical client shown in Fig. 7.9 and in Fig. 7.10 is connected to this other server.

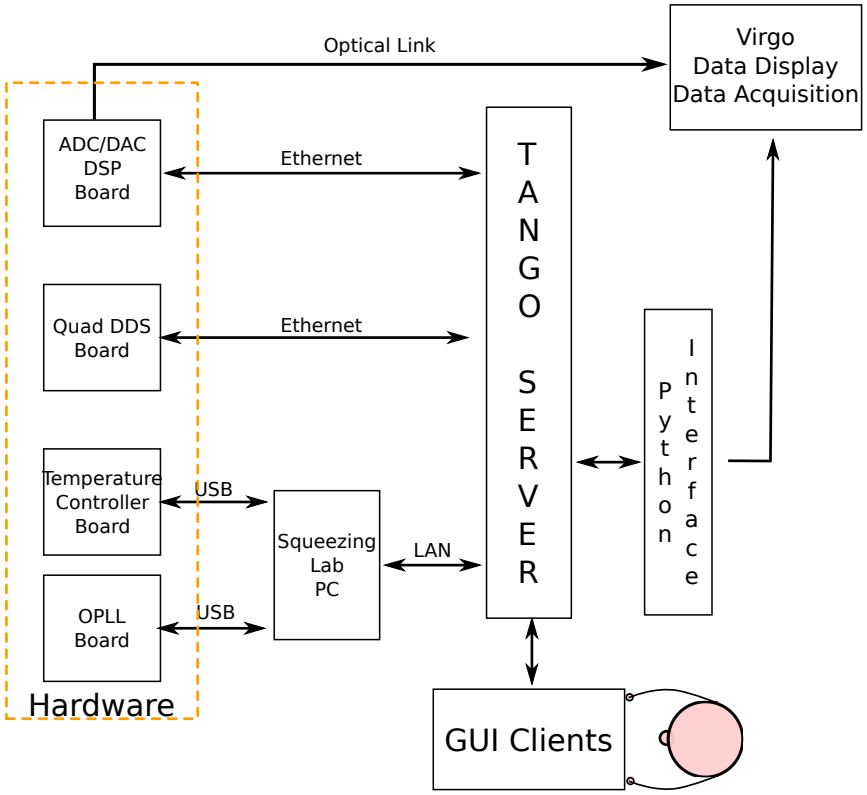

Figure 7.13: Schematic representation of the hardware/software interaction of all the electronic and controls.

Fig. 7.13 summarizes the architecture of the hardware/software interaction of the

squeezer control system. By starting from the user he interacts with the graphical clients that are connected to the two Tango Controls servers. These two servers send/receive data from the different boards. The user can observe online data or stored data by using the Virgo Data Acquisition system. The UDSPT board are directly connected to this system with the optical link whereas the other boards are integrated in it exploiting the Python based interface written by the Virgo computing Staff. In this way the user easily manages all the bench without knowing deeply a so complicated electronic system.

7.5 Locking performance of the control system

In conclusion to this part related to the electronic and control of the Virgo squeezer, the time needed to lock of all the squeezer servo loops is computed. The starting point of this analysis is a completely unlocked status of the squeezer and the final status is the one in which the temperature of the two nonlinear crystals is controlled, the PLL is locked, the MCG, OPO, SHG and MCIR cavities are controlled in length and the pump field power is stabilized with the MZ interferometer. The final state is achieved with a procedure divided in three steps. In the first the temperature of the OPO and SHG nonlinear crystal is stabilized in order to reach the phase matching condition, in the second the frequency of the AUX2 laser is locked to the one of the ML, whereas in the third all the cavity are locked.

Temperature control of nonlinear crystals. When the system is not controlled the starting temperature of the OPO and SHG PPKTP crystals is the room temperature, i.e. about 20 °C. The time needed to pass from the room temperature, to the SHG phase matching temperature, i.e. 31.5 °C is 30 s, whereas the time needed to reach the OPO phase matching temperature, i.e. 32 °C is 35 s.

AUX2 laser locking. The bottom part of the Fig. 6.15 analyzes the correction signal of the SLOW OPLL servo loop in a period with duration equal to 60 hours. During this time, its maximum excursion is equal to 0.045 V that corresponds to a variation of the laser crystal temperature of 0.045 °C that induces a laser frequency shift of about 135 MHz. It is assumed that, when the system is uncontrolled, the initial condition is worse than the measured value, i.e. the AUX2 laser is frequency is shifted by about 500 MHz compared to its frequency when the loop is closed. With the current parameters configuration, the thermal controller of the OPLL can move the laser frequency with a speed of about 15 MHz s^{-1}, therefore the OPLL needs less

than 35 s to pass from an uncontrolled state to the locking state. Otherwise, when the OPLL is already locked and for some reason it unlocks, for example when the beam is interrupted, it requires a couple of seconds to re-achieve the lock status.

Locking of the cavities and the MZ interferometer. The estimation of the locking time of all the active optical components is divided in two groups: the former is the generation and stabilization of the green pump field, whereas the second is the locking of the OPO and MCIR cavities. The components belonging to different groups can be locked independently. As explained in Chap. 4 the green pump line is composed by the SHG cavity, the MCG cavity and the MZ interferometer; these three elements must be locked in the order in which they were listed. A hierarchical autolocking procedure of the green pump is implemented and it is managed by some functions developed in the user GUI interface that ask to the UDSPT boards the status of the various loop with a polling rate of 1 Hz. Therefore, as it is implemented, this procedure needs at least one second to receive the status of the loop after the loop is turned on. The green pump locking time is divided as follows: at the time $t = 0$ the SHG loop is turned on, after less than 0.3 s the lock status is achieved; at the time $t = 1$ s the control interface receives the information of the SHG status and turns on the MCG cavity that achieves the lock after less than 0.3 s; finally at $t = 2$ s the interface obtains the trigger to turn-on the MZ interferometer and it achieves the locking condition in less than 0.1 s. Therefore the green pump line is locked in less than 2.1 s. In the future the hierarchical locking procedure will be transferred from the python code to the UDSPT firmware, here the time needed to understand if a cavity is locked will be about 6 µs, i.e. one cycle of the system which works at a frequency of 160 kHz, so the green line will be locked in less than 0.7 s. The OPO and the MCIR cavities can be turned on simultaneously and the system requires less than 0.3 s to achieve their locking condition, thus by turning on simultaneously the green pump line, the OPO and the MCIR cavities the system requires less than 2.1 s to lock all the active optical components.

If in the future a finite state machine, that manages an hierarchical auto-locking procedure of the whole squeezer, will be implemented, the time required to perform this operation, from a complete uncontrolled state, is about 35 s second to turn on simultaneously the OPLL and the two temperature controller of the PPKTP crystals, and other additional 2 s to lock all the optical cavities.

Chapter 8

Conclusions

During my PhD period I collaborated in the design and in the debugging of a relevant fraction of the electronic and controls of the Virgo squeezer. I also developed part of the firmware and the PC software for the remote management of these boards and finally I've wirtten a server of instrument with the Tango Controls toolkit for the integration of these boards in the Virgo DAQ environment.

The work I have done also include the integration of these devices on the optical bench and the initial characterization of the squeezer optical components. Using all the developed devices the first squeezed light has been produced and detected. The next step, at which I am currently working, are: the implementation of the coherent control system for the squeezing ellipse angle stablization and a systematic characterization and optimization of the squeezed light source.

The work I did was initially aimed at the development of a frequency independent squeezed vacuum source for the Virgo interferometer. However, in recent time, the AEI collaboration donated a last generation squeezer to Virgo, that will probably installed in Virgo from the upcoming O3 run. The motivation to continue the 1500W activities arises from the decision of the collaboration to exploit the 1500W facility into a tabletop EPR squeezing demonstrator.

In the following a detailed summary of the experimental part of my PhD thesis is presented. Chap. 4 describes the optical layout of the bench and the characterization of all the principal optical components. The already mounted part of the squeezer prototype is composed by two laser sources, two nonlinear cavities based on a PPKTP nonlinear medium, two triangular cavities a MZ interferometer and the homodyne detector. Sec. 4.2 describes the SHG cavity, its mechanics, how it is held on resonance and its performances. With this cavity we have obtained the world record of conversion efficiency of $99 \pm 1^{(stat.)} \pm 3^{(syst.)}$ with a fundamental field input

field wavelength at 1064 nm. Sec. 4.4 describes why we need an active green power stabilization that is achieved with a MZ interferometer. With this element we have obtained residual pump power fluctuations of 2%, this is not yet enough but in the near future the structure of the MZ servo loop will be optimized in order to achieve the requirement of 1% of residual fluctuations. The green pump spatial mode is filtered with a triangular cavity (MCG) described in Sec. 4.3. Sec. 4.5 characterizes the diagnostic homodyne detector that is based on the self-subtracting current scheme. Finally Sec. 4.5 describes the OPO cavity how it is held on resonance exploiting a second laser source AUX2. Sec. 4.6.2 shows the measurement of the OPO cavity pump power threshold that is equal to 115 mW. In Sec. 4.6.3 the first squeezing measurement is shown, where we have measured that with the injection of the generated squeezed states the shot noise level decreases of -6 dB and the with the injection of antisqueezed states it increases by 15 dB. Sec. 4.7 describes which are the next steps in the development of this squeezer prototype.

From Chap. 5 to Chap. 7 is described how the electronic and the controls are developed. Chap. 5 describes the generation of all the RF sinusoidal signals that is perfomed with a custom board based on a commercial DDS chip, the AD9910 of Analog Devices. Each board mounts four chip that have an RF output with a precise phase relationship between them. Their phase can be changed with a resolution of 0.005° and their frequency can be changed with a resolution of 0.12 Hz in the range between 5 MHz adn 150 MHz. To characterize the performances of these boards I have developed a phase noise measurement system that is described in Sec. 5.3.1. The resiudal rms phase noise, integrated between 1 Hz and 100 kHz, for each channel is equal to 14 µrad when the output frequency was set to 62.5 MHz.

Chap. 6 describes the OPLL servo loops and the boards developed for their realization. These are based on a commercial PFD chip (ADF4002 of Analog Devices) and are managed by a Microcontroller. The lasers phase/frequency locking is achieved with two loops one for fast fluctuations with a bandiwidth up to 50 kHz closed on the PZT actuator of the slave laser, and one for the stabilization of slow fluctuations with a bandwidth of few hertz closed on the Peltier actuator of the slave laser. The last loop ensures the long term stability of the system. The performances of these boards are shown in Sec. 6.6.2: the system remains locked for at least three days with a residual rms phase noise, integrated between 5 Hz and 160 kHz of 3.2 mrad.

Chap. 7 describes the crystal temperature stabilization system, the cavity stabilization system developed with the UDSPT board, the high voltage amplifier to drive PZT actuators and the photodiode amplifiers installed in the bench. In particular, in

Sec. 7.1 is shown the developed temperature controller board. It stabilizes the crystal temperature by actuating on a Peltier cell, whereas the temperature sensors are two thermistors. The board is based on a microcontroller unit of Atmel manufacturer i.e. the Atmega328, that implements a digital PID. This system stabilizes the SHG crystal temperature with a room temperature fluctuations rejection of a factor 35.

In the second part of the chapter, the implementation of all the loops, that control the active optical components of the squeezer, is shown. These loop are designed using the UDSPT board developed by the INFN Pisa group. In the implementation of these control loops I have performed the following activities: I have written the firmware that runs on the UDSPT boards using the Damping environment and I have developed a graphical interface that allows an user to manage easily the squeezer. The loop controlled by the UDSPT board can lock with a hierarchical procedure in less than 2.1 s and show a long term stability. In the future the design of these servo loops will be improved in order to increase their unitary bandwidth.

Appendix

Appendix A

The Pound Drever Hall Technique

The PDH technique was invented for stabilizing the frequency of a laser by locking it to a reference cavity [70]. In this thesis this technique is used to lock the length of all the optical cavities on the laser line. This locking method allows to build an error signal with different sign when the cavity is on either side of the resonance and it is equal to zero when the cavity is on resonance. A generic scheme of this technique is shown in Fig. A.1.

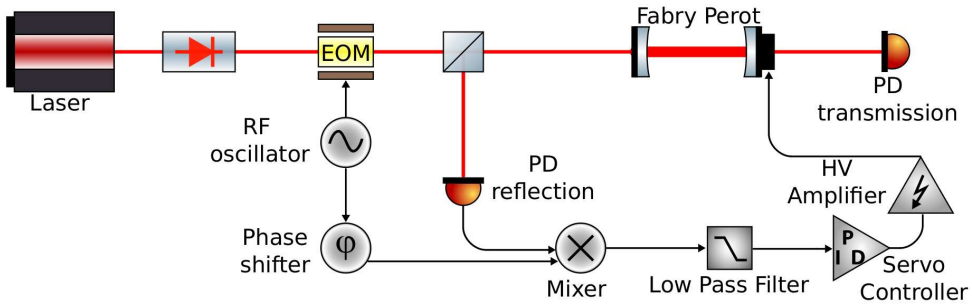

Figure A.1: Scheme of the cavity length locking to laser line with the Pound Drever Hall technique.

A PDH setup it is composed by a laser, an Electro Optical Modulator (EOM), a cavity with a piezoelectric actuator linked to one of the mirrors, a signals mixer, a servo controller, an high voltage amplifier and two photodiodes respectively one in reflection to the cavity and one in transmission. The laser light is phase modulated by the EOM at a fixed frequency ($\Omega/2\pi$) and injected in the optical cavity. The reflected light is detected with a photodiode and its output signal is demodulated with a mixer by using a local oscillator at the same frequency $\Omega/2\pi$. After the mixer, a low pass filter is inserted to extract only the signal components from DC to $100 - 200$ kHz.

The filtered signal is called PDH error signal which is processed by the controller and sent to the actuator with the aim to close the loop and stabilize the cavity. The PDH error signal is mathematically computed in the following subsection.

A.1 PDH error signal computation

The laser beam electric field can be written as $E(t) = E_0 e^{\imath\omega t}$. When it is phase modulated by an EOM the beam electric field becomes:

$$E_{inc}(t) = E_0 e^{\imath\omega t + \beta \sin(\Omega t)}$$

where β is the modulation depth and $\Omega/2\pi$ is the modulation frequency. The expression is rearranged with the Jacobi-Anger expansion:

$$E_{inc}(t) \approx E_0 e^{\imath\omega t} \sum_{-\infty}^{\infty} J_n(\beta) e^{\imath n\Omega t}$$

where $J_n(\beta)$ are the first kind Bessel functions. The last expression evinces that the modulated signal contains all the harmonics at the modulation frequency with an amplitude decided by the Bessel functions. If the modulation depth (β) is small we can consider only the 0 and ± 1 terms. Therefore the electric field, after the EOM, is rewritten as:

$$E_{inc}(t) \approx E_0 \left[J_0(\beta) e^{\imath\omega t} + J_1(\beta) e^{\imath(\omega+\Omega)t} - J_1(\beta) e^{\imath(\omega-\Omega)t} \right].$$

The last expression denotes that three different beams are incident on the cavity: the carrier with a frequency $\omega/2\pi$ and two sidebands with a frequency $(\omega \pm \Omega)/2\pi$. Therefore if P_0 is the total power, in this approximation, it arrives divided in three contributions, i.e. the carrier and the first order sidebands:

$$P_0 \approx P_c + 2P_s \qquad \text{where} \quad P_c = J_0(\beta)^2 P_0 \quad \text{and} \quad P_s = J_1(\beta)^2 P_0.$$

When a monochromatic beam enters in a Fabry-Perot cavity a fraction of it is reflected. The reflected beam has the same frequency of the incident beam and an amplitude proportional to its amplitude i.e. $E_{ref} = F E_{inc}$ where F is the reflection coefficient that depends on the properties of the beam and the cavity. For a generic two mirrors Fabry-Perot cavity, the reflected field is related to the incident field with the following relationship:

$$F(\omega) = \frac{-r_1 + (r_1^2 + t_1^2) r_2 e^{\imath\phi}}{1 - r_1 r_2 e^{\imath\phi}},$$

where $r_{1,2}$ are the reflection coefficients of the two mirrors t_1 is the transmission coefficient of the first mirror and ϕ is the phase delay that the light acquires in one round trip inside the cavity. The phase shift for each round trip is equal to:

$$\phi = \frac{2\omega L}{c} = \frac{\omega}{\Delta\nu_{FSR}},$$

where L is the cavity length and $\Delta\nu_{FSR}$ is the frequency width of a free spectral range. The reflected beam is given by the sum of three contributions each one obtained with the product of the beam electric field and the reflection coefficient at the right frequency:

$$E_{ref}(t) = E_0 \left[F(\omega)J_0(\beta)\mathrm{e}^{\imath\omega t} + F(\omega+\Omega)J_1(\beta)\mathrm{e}^{\imath(\omega+\Omega)t} - F(\omega-\Omega)J_1(\beta)\mathrm{e}^{\imath(\omega-\Omega)t} \right]$$

The reflected light is detected by the photodiode that measures its power i.e. $P_{ref}(t) = |E_{ref}(t)|^2$ that is equal to:

$$\begin{aligned} P_{ref}(t) = {} & P_c|F(\omega)|^2 + P_s\left[|F(\omega+\Omega)|^2 + |F(\omega-\Omega)|^2\right] + \\ & + 2\sqrt{P_cP_s}\left\{\Re[F(\omega)F^*(\omega+\Omega) - F^*(\omega)F(\omega-\Omega)]\cos(\Omega t) + \right. \\ & \left. + \Im[F(\omega)F^*(\omega+\Omega) - F^*(\omega)F(\omega-\Omega)]\sin(\Omega t)\right\} + (2\Omega\text{terms}) \end{aligned} \tag{A.1}$$

where the Ω terms are the result of the interference between the carrier and the sidebands and the 2Ω terms are the results of the interference between the sidebands. Only the contribution at frequency Ω contains information on the cavity position respect to the resonance condition. Therefore this frequency component is extracted by demodulating the photodetector output signal with a local oscillator oscillating at frequency Ω. The obtained signal is called PDH error signal. The relative phase between the photodetector signal and the LO phase must equal to 90° in order to maximize the error signal slope.

Depending on the ratio between the modulation frequency Ω and the cavity linewidth $\Delta\nu$ two different regimes are distinguishable from Eq. A.1:

- **Fast Modulation Regime:** when $\Omega \gg \Delta\nu$, the term $[F(\omega)F^*(\omega+\Omega) - F^*(\omega)F(\omega-\Omega)]$ is purely imaginary and its respective error signal is shown in the left side of Fig. A.2;

- **Slow Modulation Regime:** when $\Omega \ll \Delta\nu$, the term $[F(\omega)F^*(\omega+\Omega) - F^*(\omega)F(\omega-\Omega)]$ is purely real and its respective error signal is shown in the right side of Fig. A.2.

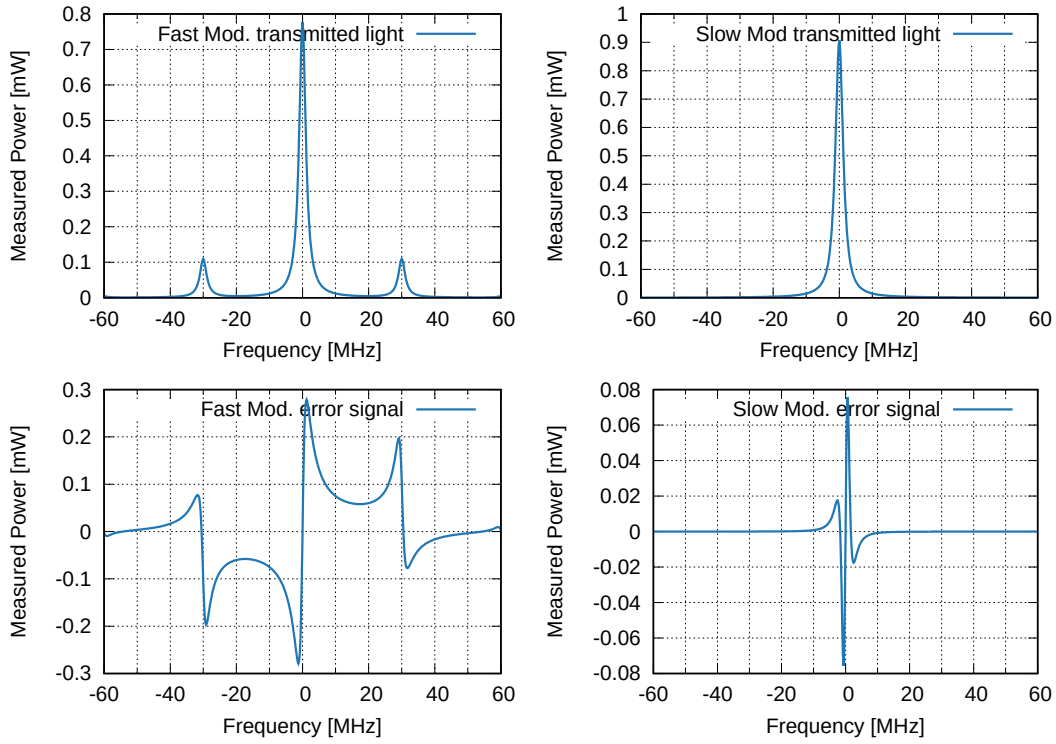

Figure A.2: Simulation of a Fabry-Perot cavity transmission signal (upper part) and error signal (lower part) in the PDH technique. The left side shows the two signals in the fast modulation regime and the right side shows the two signals in the slow modulation regime. The simulation is run by using Finesse optical simulator.

Fig. A.2 shows a simulation of a symmetric Fabry Perot Cavity with no losses in which is injected a phase modulated beam. The simulated cavity has a length of 0.8 m with two identical planar mirrors with reflectivity of 0.96%. Therefore, the simulated Fabry-Perot has a free spectral range frequency of 187.5 MHz a FWHL of 2.4 MHz and a finesse of 76.9. The two plots on the top show the transmitted power from the cavity as function of the frequency displacement from the resonance condition; whereas on the bottom is shown the PDH error signal. Left side of Fig. A.2 represents signals related to the fast modulation, i.e. the phase modulation frequency is 30 MHz; the right side shows the fast modulation regime, i.e. phase modulation frequency equal to 0.2 MHz. The PDH error signal, as expected, crosses zero axis when one beam, the carrier or a sideband, resonates into the cavity. Around these resonance condition the error signal is linear and the carrier slope is opposite respect the sidebands slope. Therefore with a choice on servo loop sign it is possible to stabilize the cavity or on a sideband or on the carrier frequency. Moreover the error signal sign depends on if the resonance frequency of the cavity is higher or lower than the laser frequency.

The Pound Drever Hall servo loops of the Virgo squeezed light source are in both the configurations: for example the MCIR cavity is locked in the fast modulation regime and the SHG and OPO cavities in the slow modulation regime, but the error signal is taken in transmission for the OPO cavity. Once generated, the PDH error signal is used as input of a servo loop that actuates on the piezoelectric attached to the cavity mirror in order to maintain the cavity on resonance by forcing the error signal to be equal to zero. The implementation of these servo loops is described in Sec. 7.2.1.

Appendix B

Electronic circuit diagrams

B.1 OPLL board

The circuit diagram of the OPLL board is displayed in Fig. B.1, Fig. B.2, Fig. B.3 and Fig. B.4. In particular Fig. B.1 shows the beat note and the local oscillator input stages and the phase frequency detector. The components C1, C10 and R6 are the loop filter components and have to be adapted to each OPLL control loop. Fig. B.2 shows the fifth order Bessel filter that attenuates 20 dB in the bandwidth between 100 and 200 kHz with the aim to suppress the laser's piezoelectric mechanical resonance. Moreover in this second sheet is placed the digital switch that allows to turn on/off the FAST loop. The third sheet in Fig. B.3 shows the ADC, the DAC and the operational amplifiers that prepare the FAST and the SLOW output signals. Finally the fourth sheet in Fig. B.4 contains all the voltage regulators and the microcontroller unit. This board is designed by Marco Prevedelli.

B.2 Temperature controller board

Fig. B.5 shows the circuit diagram of the Temperature controller board used for stabilizing the temperature of crystals inside the SHG, OPO cavities. The detailed explanation of this diagram is reported in Sec. 7.1.1. This board is designed by the LENS Electonic Workshop staff.

B.3 RF photoiode amplifier with on board demodulation

Fig. B.6 shows the circuit diagram of the photodiode RF amplifier. Its operation is explained in Sec. 7.3. This board is designed by Marco Prevedelli.

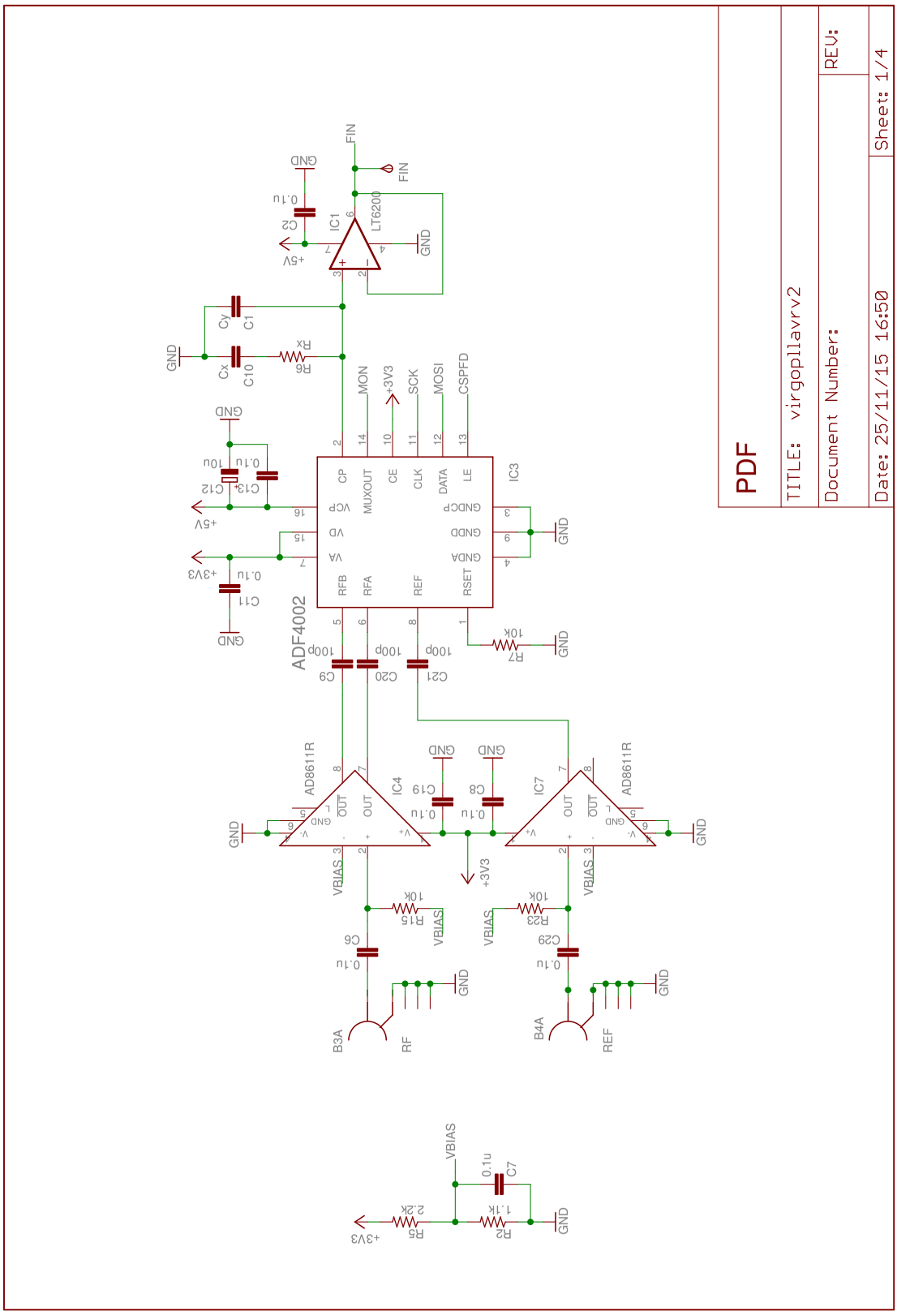

Figure B.1: OPLL circuit diagram sheet 1/4

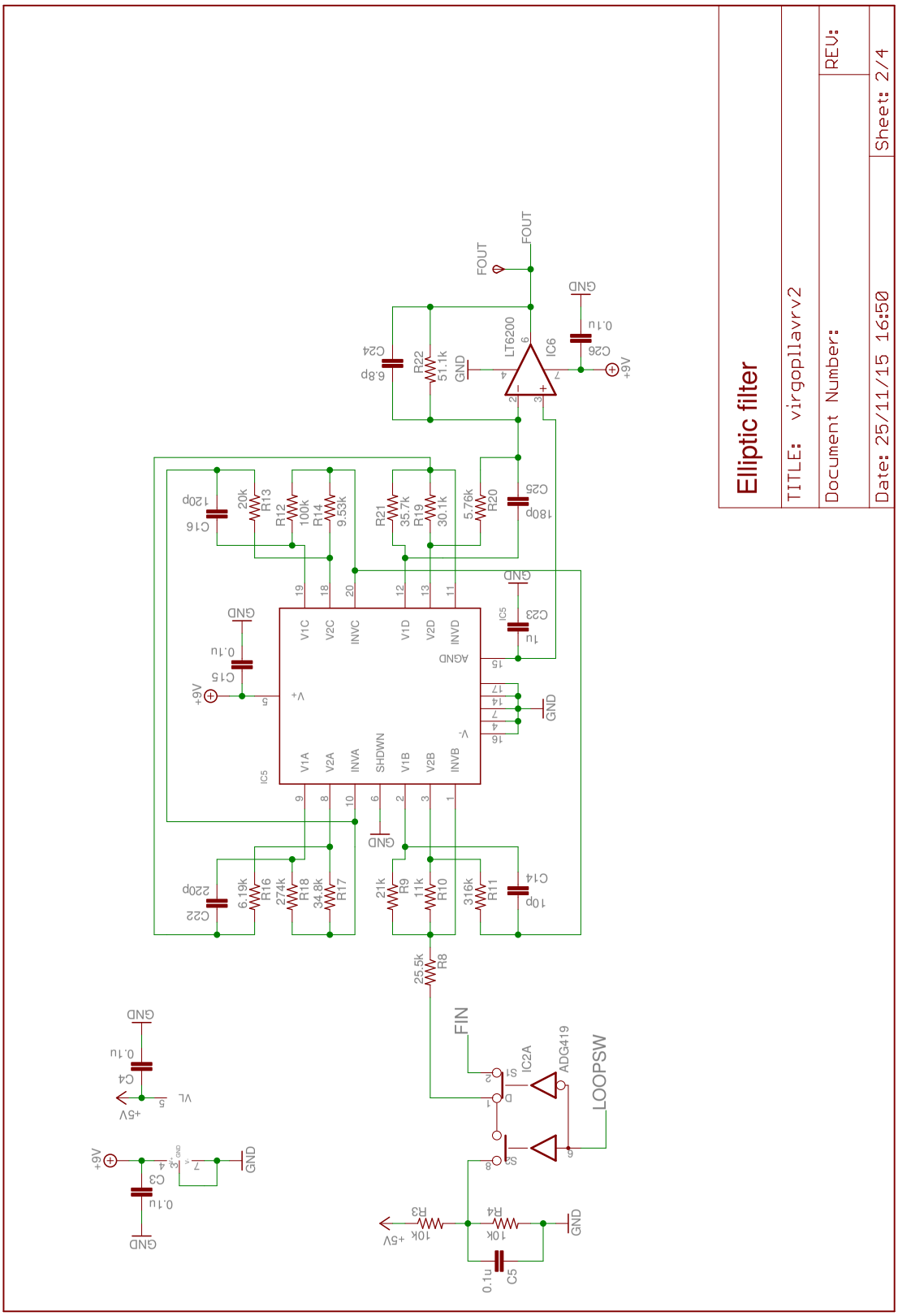

Figure B.2: OPLL circuit diagram sheet 2/4

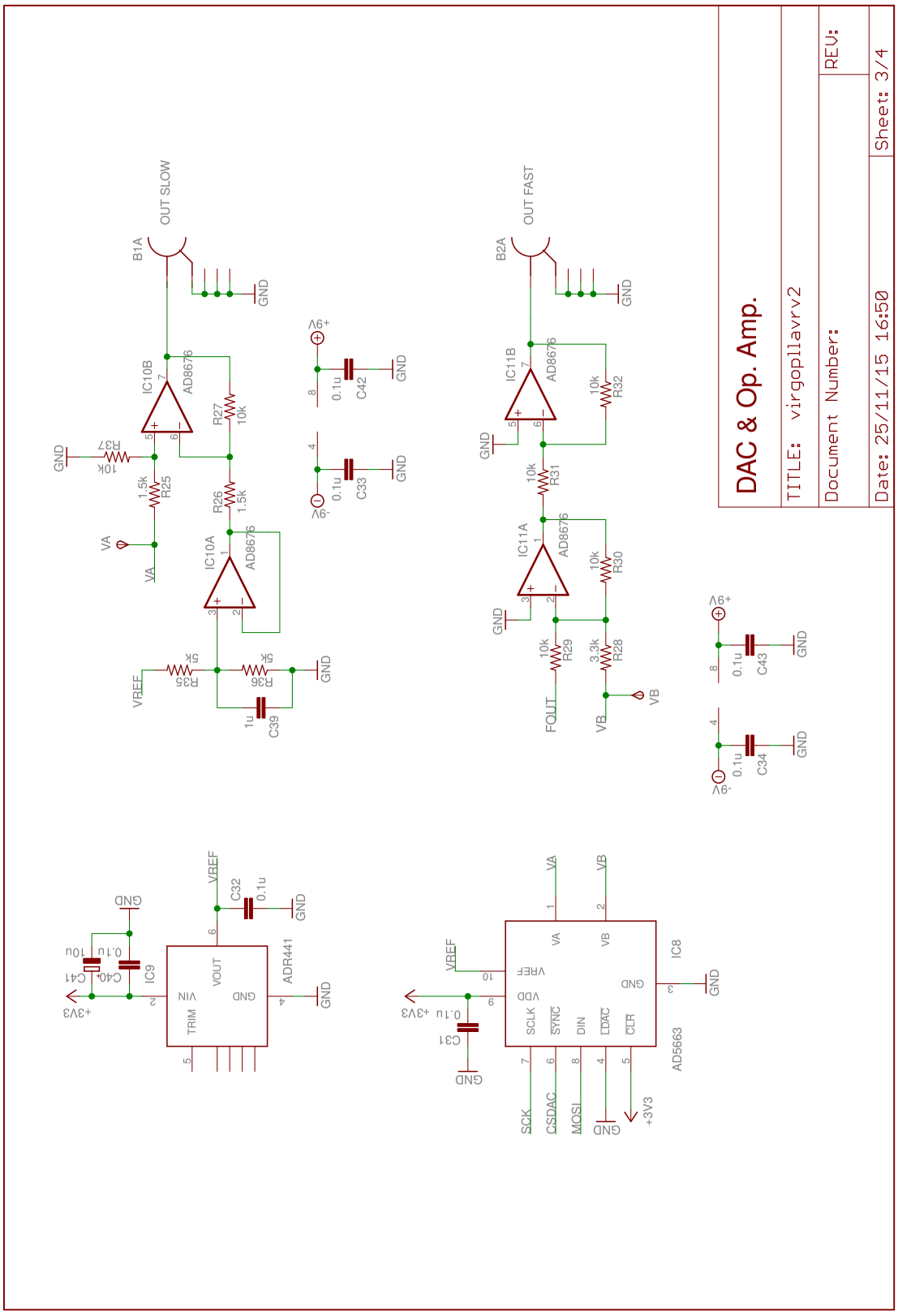

Figure B.3: OPLL circuit diagram sheet 3/4

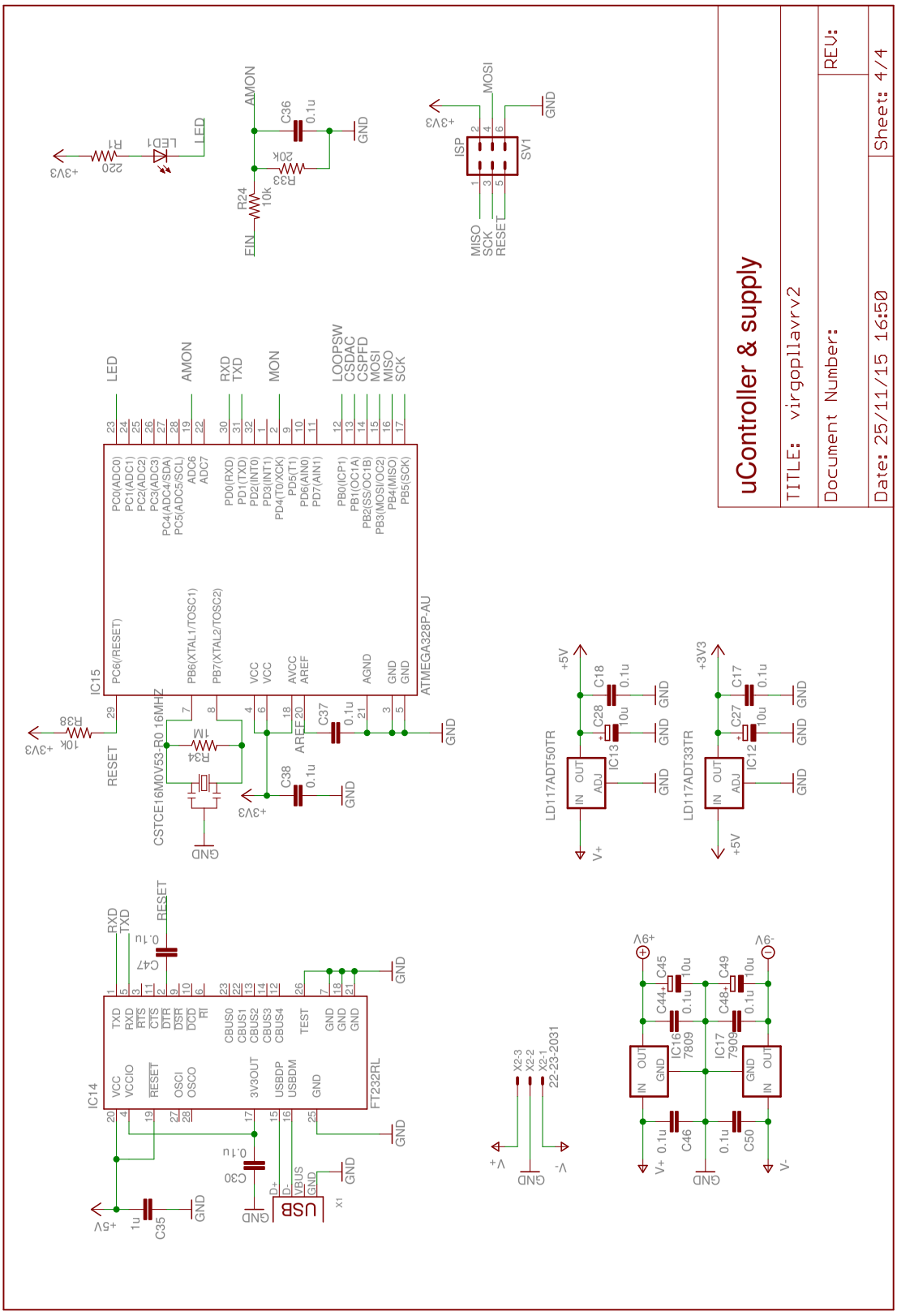

Figure B.4: OPLL circuit diagram sheet 4/4

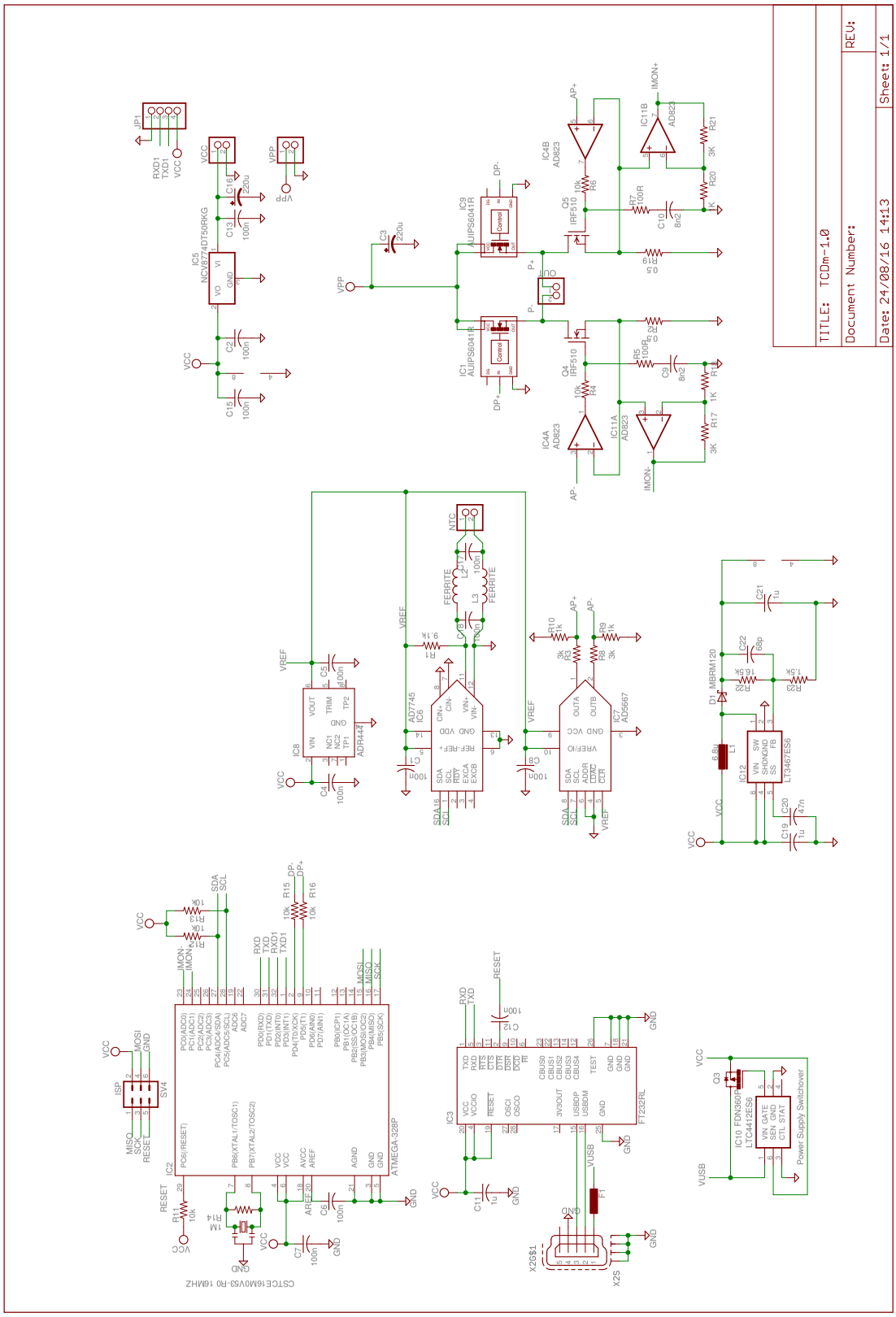

Figure B.5: Temperature controller circuit diagram sheet 1/1

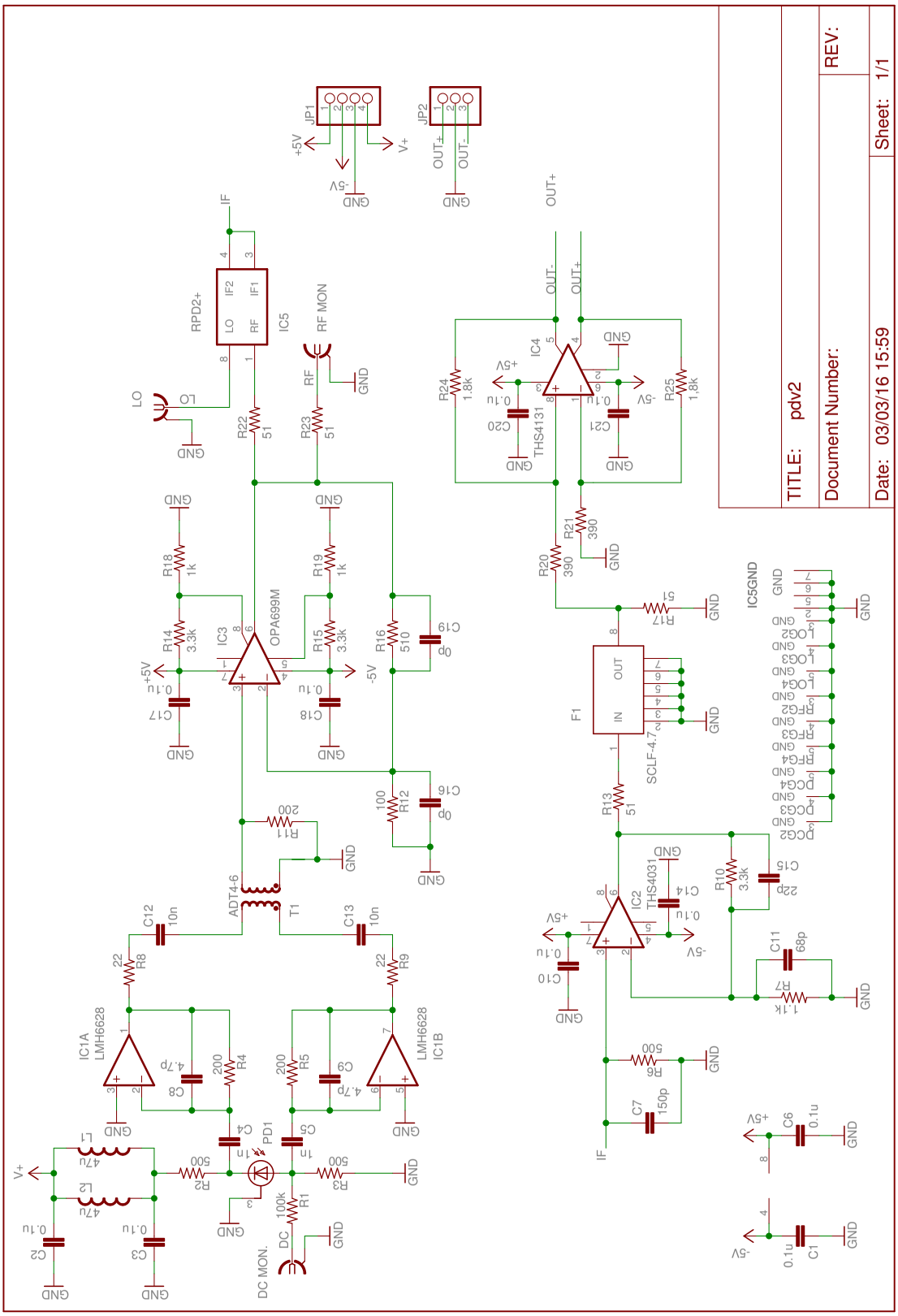

Figure B.6: High Frequency photodiode amplifier with on board demodulation circuit diagram sheet 1/1

Appendix C

Optical layout of the bench

Fig. C.1 shows the complete optical layout of the squeezed light optical bench developed in the Virgo interferometer site. It includes all the installed optical components. A detailed discussion of the setup is provided in Chap. 4.

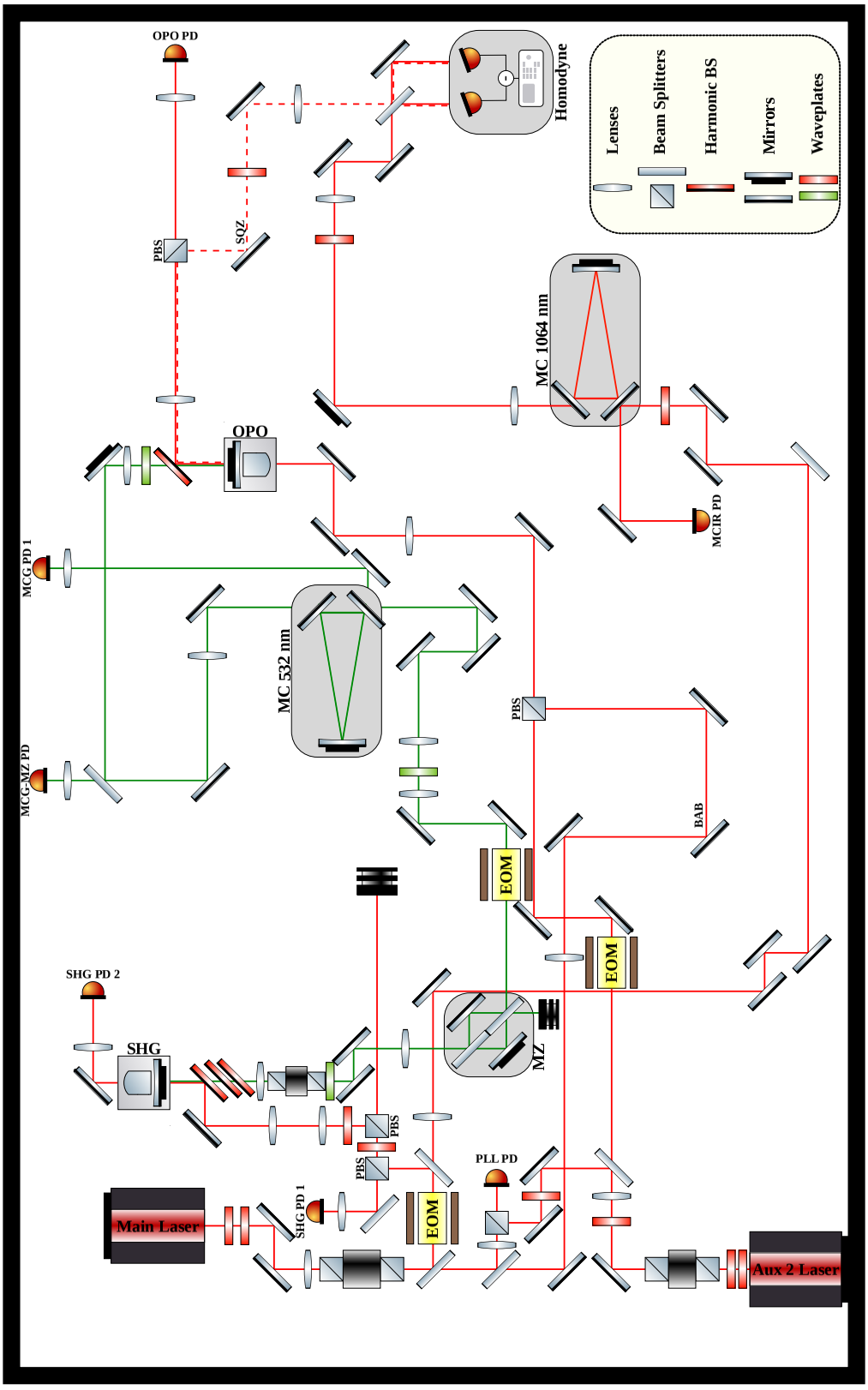

Figure C.1: Optical layout of the squeezed light bench.

Acronyms

ADC Analog to Digital Converter

ADPLL All Digital Phase Locked Loop

AUX1 Auxiliary Laser 1 Source

AUX2 Auxiliary Laser 2 Source

BAB Bright Alignment Beam

BS Beam Splitter

DAC Digital to Analog Converter

DAQ Data Acquisition

dBc Decibels relative to the carrier

DDS Direct Digital Synthesizer

DFG Difference Frequency Generation

DPLL Digital Phase Locked Loop

DSP Digital Signal Processor

EOM Electro Optical Modulator

EXOR Exclusive XOR gate

FPGA Field Programmable Gate Array

FSR Free Spectral Range

FWHM Full Width Half Maximum

HBS Harmonic Beam Splitter

HV High Voltage

HWP Half Wave Plate

IEEE Institute of Electrical and Electronics Engineers

LO Local Oscillator

MCG Green Mode Cleaner

MCIR Infrared Mode Cleaner

ML Main Laser Source

MZ Mach Zender Interferometer

NTC Negative Temperature Coefficient

OPLL Optical Phase Locked Loop

OLG Open Loop Gain

OPO Optical Parametric Oscillator

OR Optical Rectification

PBS Polarizing Beam Splitter

PC Personal Computer

PD Photodiode

PDH Pound Drever Hall

PFD Phase Frequency Detector

PID Proportional Integral Derivative

PZT Piezoelectric

PLL Phase Locked Loop

RBW Resolution Bandwidth

RF Radiofrequency

SFG Sum Frequency Generation

SHG Second Harmonic Generator

SPI Serial Peripheral Interface

TF Transfer Function

USB Universal Serial Bus

VCO Voltage Controlled Oscillator

Bibliography

[1] M. Maggiore. *Gravitational Waves: Volume 1: Theory and Experiments*. Gravitational Waves. OUP Oxford, 2008.

[2] P.R. Saulson. *Fundamentals of Interferometric Gravitational Wave Detectors*. World Scientific, 1994.

[3] R. Flaminio, A. Freise, A. Gennai, et al. Advanced virgo white paper. Technical report, 2005.

[4] F. Acernese et al. Status of the advanced virgo gravitational wave detector. *International Journal of Modern Physics A*, 32(28n29):1744003, 2017.

[5] B. P. Abbott et al. Gw170814: A three-detector observation of gravitational waves from a binary black hole coalescence. *Phys. Rev. Lett.*, 119:141101, Oct 2017.

[6] T. V. Collaboration. Advanced virgo technical design report. Technical report, 2012.

[7] M. Granata, M. Emeline, C. Nazario, et al. Mechanical loss in state-of-the-art amorphous optical coatings. *Phyisical review D*, 93(1), JAN 27 2016.

[8] F. Acernese, F. Antonucci, F. Aoudia, et al. Measurements of superattenuator seismic isolation by virgo interferometer. *Astroparticle Physics*, 33(3):182 – 189, 2010.

[9] P Amico, L Bosi, L Carbone, L Gammaitoni, F Marchesoni, M Punturo, F Travasso, and H Vocca. Monolithic fused silica suspension for the Virgo gravitational waves detector. *Review of scientific instrument*, 73(9):3318–3323, SEP 2002.

[10] Drever and R. W. P. Laser interferometer gravitational radiation detectors. *AIP Conference Proceedings*, 1983.

[11] Jean-Yves Vinet, Brian Meers, Catherine Nary Man, and Alain Brillet. Optimization of long-baseline optical interferometers for gravitational-wave detection. *Phys. Rev. D*, 38:433–447, Jul 1988.

[12] Brian J. Meers. Recycling in laser-interferometric gravitational-wave detectors. *Phys. Rev. D*, 38:2317–2326, Oct 1988.

[13] Jan Harms and Ho Jung Paik. Newtonian-noise cancellation in full-tensor gravitational-wave detectors. *Phys. Rev. D*, 92:022001, Jul 2015.

[14] Gregory M Harry, Andri M Gretarsson, Peter R Saulson, Scott E Kittelberger, Steven D Penn, William J Startin, Sheila Rowan, Martin M Fejer, D R M Crooks, Gianpietro Cagnoli, Jim Hough, and Norio Nakagawa. Thermal noise in interferometric gravitational wave detectors due to dielectric optical coatings. *Classical and Quantum Gravity*, 19(5):897, 2002.

[15] A. Gillespie and F. Raab. Thermally excited vibrations of the mirrors of laser interferometer gravitational-wave detectors. *Phys. Rev. D*, 52:577–585, Jul 1995.

[16] V.B. Braginsky, M.L. Gorodetsky, and S.P. Vyatchanin. Thermo-refractive noise in gravitational wave antennae. *Physics Letters A*, 271(5):303 – 307, 2000.

[17] A Rocchi, E Coccia, V Fafone, V Malvezzi, Y Minenkov, and L Sperandio. Thermal effects and their compensation in advanced virgo. *Journal of Physics: Conference Series*, 363(1), 2012.

[18] K. Goda. *Development of Techniques for Quantum-Enhanced Laser-Interferometric Gravitational-Wave Detectors.* PhD thesis, University of California at Berkeley, 2001.

[19] M. Evans et al. Observation of parametric instability in advanced ligo. *Phys. Rev. Lett.*, 114:161102, Apr 2015.

[20] Carlton M. Caves. Quantum-mechanical noise in an interferometer. *Phys. Rev. D*, 23:1693–1708, Apr 1981.

[21] W. G. Unruh. *Quantum Optics, Experimental Gravity, and Measurement Theory.* New York:Plenum, 1983.

[22] F. Arcense, S. Aoudia, et al. Einstain grawitational wave telescope conceptual design study. Technical report, 2012.

[23] Eric Oelker, Tomoki Isogai, John Miller, Maggie Tse, Lisa Barsotti, Nergis Mavalvala, and Matthew Evans. Audio-band frequency-dependent squeezing for gravitational-wave detectors. *Phys. Rev. Lett.*, 116:041102, Jan 2016.

[24] Ma Y., Miao H., Pang B. H., Evans M., Zhao C., Harms Y., Schnabel R., and Chen Y. Proposal for gravitational-wave detection beyond the standard quantum limit through epr entanglement. *Nature Physics*, 13, Oct 2017.

[25] J.J. Sakurai. *Advanced Quantum Mechanics*. A-W series in advanced physics. Addison-Wesley Publishing Company, 1967.

[26] M. Fox. *Quantum Optics: An Introduction*. Oxford Master Series in Physics. OUP Oxford, 2006.

[27] C. Gerry and P. Knight. *Introductory Quantum Optics*. Cambridge University Press, 2004.

[28] D. Meschede. *Optics, Light and Lasers: The Practical Approach to Modern Aspects of Photonics and Laser Physics*. Physics textbook. Wiley, 2007.

[29] C. Cohen-Tannoudji, B. Diu, and F. Laloe. *Quantum Mechanics, 2 Volume Set*. Wiley, 1992.

[30] A. Vahlbruch. *Squeezed Light for Gravitational Wave Astronomy*. PhD thesis, Albert Einstiei Institue, 2007.

[31] Carlton M. Caves. Quantum-mechanical radiation-pressure fluctuations in an interferometer. *Phys. Rev. Lett.*, 45:75–79, Jul 1980.

[32] H.A. Bachor and T.C. Ralph. *A Guide to Experiments in Quantum Optics*. Wiley, 2004.

[33] R.W. Boyd. *Nonlinear Optics*. Nonlinear Optics Series. Elsevier Science, 2008.

[34] C. W. Gardiner and M. J. Collett. Input and output in damped quantum systems: Quantum stochastic differential equations and the master equation. *Phys. Rev. A*, 31:3761–3774, Jun 1985.

[35] Benjamin Caird Buchler. *Electro-optic Control of Quantum Measurements*. PhD thesis, The Australian National University, 2001.

[36] Sheon S. Y. Chua. *Quantum Enhancement of a 4km Laser Interferometer Gravitational-Wave Detector*. PhD thesis, The Australian National University, 2013.

[37] Ligo Scientific Collaboration et al. A gravitational wave observatory operating beyond the quantum shot-noise limit. *Nature Physics*, 7:962–965, 2011.

[38] Ligo Scientific Collaboration et al. Enhanced sensitivity of the ligo gravitational wave detector by using squeezed states of light. *Nature Photonics*, 7:613–619, 2013.

[39] A. Khalaidovski. *Beyond the Quantum Limit - A Squeezed-Light Laser in GEO 600*. PhD thesis, Albert Einstiei Institue, 2011.

[40] D. Verkindt. Data display users manual. Technical report, LAPP, 08 2008.

[41] L. Rolland for the DAQ team. Daq status. Technical report, LAPP, 05 2017.

[42] F. Carbognani. Metatron: state machine-based automation for virgo @ aug 2017 lvc meeting in geneva. Technical report, Ego, 09 2017.

[43] Coherent Lasers. *Mephisto/Mephisto S*.

[44] Advanced Virgo Squeezeing Working group. Advanced virgo squeezer technical design report. Technical report, 2015.

[45] M. Leonardi. *Developed of a squeezed light source prototype for Advanced Virgo*. PhD thesis, Università degli studi di Trento, 2016.

[46] K. Dooley, H. Vahlbruch, and E. Schreiber. Experiences with degradng squeezer compoents at geo600. Technical report, 2015.

[47] E. S. Polzik and H. J. Kimble. Frequency doubling with knbo3 in an external cavity. *Opt. Lett.*, 16(18):1400–1402, Sep 1991.

[48] R.L. Byer W.J. Kozlovsky, C.D. Nabors. Efficient second harmonic generation of a diode-laser-pumped cw nd:yag laser using monolithic mgo:linbo/sub 3/ external resonant cavities. *EEE journal of quantum electronics*, 24:913–919, 1998.

[49] Classical and quantum properties of the subharmonic-pumped parametric oscillator. *Optics Communications*, 138(1):158 – 171, 1997.

[50] Henning Vahlbruch, Simon Chelkowski, Boris Hage, Alexander Franzen, Karsten Danzmann, and Roman Schnabel. Coherent control of vacuum squeezing in the gravitational-wave detection band. *Phys. Rev. Lett.*, 97:011101, Jul 2006.

[51] Henning Vahlbruch, Moritz Mehmet, Karsten Danzmann, and Roman Schnabel. Detection of 15 db squeezed states of light and their application for the absolute calibration of photoelectric quantum efficiency. *Phys. Rev. Lett.*, 117:110801, Sep 2016.

[52] Analog Devices. *A Technical Tutorial on Digital Synthesis*, 1999.

[53] J. Vankka. *Digital Synthesizers and Transmitters for Software Radio*. Springer US, 2005.

[54] C. E. Calosso, Y. Gruson, and E. Rubiola. Phase noise and amplitude noise in dds. In *2012 IEEE International Frequency Control Symposium Proceedings*, 2012.

[55] Analog Devices. *AD9959 - 4-Channel, 500 MSPS DDS with 10-Bit DACs*, 2007-2016. D05246-0-7/08(E).

[56] Analog Devices. *AD9959 - Evaluation Board for 4-Channel 500 MSPS DDS with 10-Bit DACs*, 2005. EB05698-0-10/05(0).

[57] Analog Devices. *AD9910 - 1 GSPS, 14-Bit, 3.3 V CMOS Direct Digital Synthesizer*, 2005-2008. D06479-0-10/16(E).

[58] Temple B. Decker D. *Choosing a Phase Noise Measurement Technique. Concepts and Implementation.* Agilent Technologies, 2000.

[59] Gheen K. *Phase Noise Measurement Methods and Techniques.* Agilent Technologies, 2012.

[60] Cavey J. Brandon D. *The Residual Phase Noise Measurement.* Analog Devices, 2008.

[61] Egan W. F. Modeling phase noise in frequency dividers. *IEEE Transactions on Ultrasonics, Ferroelectrics, and Frequency Control*, 37(4):307–315, 1990.

[62] O'Brein P. Curtin M. Phase-locked loops for high-frequency receivers and transmitters. *Analog Dialogue*, 33, 1999.

[63] F.M. Gardner. *Phaselock Techniques.* Wiley, 2005.

[64] W.F. Egan. *Phase-Lock Basics.* Wiley - IEEE. Wiley, 2007.

[65] Analog Devices. *Fundamentals of Phase Locked Loops (PLLs)*, 2009.

[66] Analog Devices. *ADF4002 - Phase Detector/Frequency Synthesizer*, 2006-2015. D06052-0-9/15.

[67] Analog Devices. *AD7745 - 24-Bit Capacitance-to-Digital Converter with Temperature Sensor*, 2005. C05468-0-4/05(0).

[68] A. Gennai. Real time control of suspended masses in advanced virgo laser interferometer. Technical report, INFN Sezione di Pisa, 06 2016.

[69] A. Gennai. Scs electronics and software for squeezing cavities control. Technical report, INFN Sezione di Pisa, 05 2017.

[70] E. Black. Notes on the pound-drever-hall technique. Technical report, California Institute of Technology, 04 1998.

Acknowledgements

It is my pleasure to thank all the people who, during the last three years, have contributed to this work in many different ways. First of all I want to thank my advisor, Jean-Pierre Zendri, for the opportunity he gave me to work in a group in which I found ideal working condition. Moreover I thank him for all the support he gave me and his technical and scientific advices. During this period I had another mentor, Livia Conti, who has taught a great deal, thus I want to thank her for the support and patience.

I would now like to give a special thanks to Matteo Leonardi. He started this project two years before I joined this working group, thus thanks to his experience and his numerous contributions, my work has been made easier. I will thank the other members of the Virgo Padova group: Giacomo, Marco, Claudia and Gabriele for making this period so enjoyable and productive. During all the integration of the optical and electronic components in the Virgo site I worked with all the members of the squeezing working group: Jean-Pierre Zendri, Livia Conti, Marco Bazzan, Giacomo Ciani, Valeria Sqeuino, Martina De Laurentis, Imhran Kahn, Fiodor Sorrentino, Mateush Bawaj, Sibilla Di Pace and Luca Naticchioni. I hope they had as much fun working with me as I had working with them.

During the developement of the electronic and controls almost none of my contributions is achieved working alone. Therefore I thank Alberto Gennai, Diego Passuello for their support in the integration of the UDSPT board in the squeezing clean room and their support during the implementation of the control systems based on the board developed by their group. Moreover, I thank Giovanni Cerretani for his help in my learning of Damping tool, Tango Control Toolkit and his advices during the implementation of the graphical software for the squeezer management. Thank you to Matteo Pegoraro, Alessandro Griggio and the INFN Padova Electronic workshop for the design and development of the boards dedicated to the radiofrequencies synthesis and the help given me in their characterization, optimization and in the software development. Thank you to Marco Prevedelli for the help given in the design of the

PLL and Peltier controller boards and for all the useful discussions and for the long emails full of useful tips and clarifications. Finally thank you to Luciano Modenese for the help given in the debugging of most part of the board that we have developed and their integration in the NIM crates.

I'm also very grateful to all the EGO people. They gave us support and contributions in many fields. In particular the infrastructure team support us with all the problem related to the clean room, the computing team help us in the integration of the developed software in the Virgo Environment, the optic group for the development of the resonant EOM used in the green path and the useful discussion, finally the electronic group for the development of the low frequency photodiode amplifiers, the high voltage power supply, the resonant circuit for one of the EOM, the help in the cabling and for all the suggestion given during the installation of the electronic components.

Dear reader, for the final few lines, please allow me to switch back to my mother tongue.

Ringrazio i miei genitori per il supporto economico e il sostegno morale datomi durante tutto il mio percorso di studi, per esserci sempre stati e per avermi dato la forza di andare avanti. Ringrazio le mie nonne Anna e Albertina e mia sorella Nicoletta per aver sempre creduto in me e per avermi sempre spinto a provare a fare meglio. Infine, ma non ultimo per importanza, ringrazio Agnese per avermi sopportato soprattutto nei momenti peggiori e per essere stata la mia forza trainante durante gli ultimi otto anni del mio lungo percorso di studi.